A FUNDAMENTAL STUDY OF CHAR COMBUSTION:

CHANGES IN PARTICLE MORPHOLOGY DURING OXIDATION

Thesis by

P. S. Northrop

In Partial Fulfillment of the Requirements

for the Degree of

Doctor of Philosophy

California Institute of Technology

Pasadena, California

1988

(Submitted May 16, 1988)

This thesis is dedicated to my parents, who always encouraged me to do the best I could; and to Dharlene, who will help me encourage our son to to his best.

...And seek not the depths of your knowledge
with staff or sounding line.
For self is a sea boundless and measureless.
Say not, "I have found the truth," but rather,
"I have found a truth."
Say not, "I have found the path of the soul."
Say rather, "I have met the
soul walking upon my path."
For the soul walks upon all paths.
The soul walks not upon a line, neither
does it grow like a reed.
The soul unfolds itself, like a lotus of
countless petals.

–Kahlil Gibran
The Prophet, 1923

ACKNOWLEDGEMENTS

I must first thank my advisor, Professor George Gavalas, for his patience and guidance. I am indebted to him for his constructive criticism and counsel. I also would like to thank my co-advisor, Professor Richard Flagan, who helped me with many worthwhile suggestions.

I gratefully acknowledge the Department of Energy for their financial support of this work; I also wish to thank the National Science Foundation for a three-year Fellowship, which allowed me to pursue my research freely.

I was aided by several people in the Department of Chemical Engineering: in particular, I thank George Griffith for his creative solutions to problems in the laboratory.

I wish to acknowledge the following people for their help: Siegfried Jenner and Gabor Faludi of the Glass Shop, who fabricated the adsorption apparatus; Pat Koen of the Department of Biology, who helped me obtain many scanning electron micrographs; Larry Henling of the Analytical Laboratory, who performed elemental analyses on several char samples.

Interaction with fellow graduate students is always appreciated. In particular, I wish to thank my friend Ranajit Sahu for very fruitful collaboration. My learning from him was not confined to the area of engineering alone. I also wish to thank Dr. Yiannis Levendis, without whom the single particle experiments would not have been possible.

Finally, special thanks are due to Dharlene, who helped me through the difficult times.

ABSTRACT

This thesis presents a study of the morphological changes that occur in selected coal chars during oxidation at low temperature (725K-875K) and at high temperature (1400K-1600K). Gas adsorption and mercury porosimetry were the primary means by which these changes were monitored. An attempt was made to relate the observed reactivity of the char in oxygen to the evolving porous structure of the char. Initial pore structure was varied by using three different raw coals: a lignite, a subbituminous and high volatile A bituminous coal. In the case of the bituminous coal, pore structure was varied further by using different pyrolysis temperatures. Of course, while there were differences in the physical structure of the chars, there were differences in the chemical structure as well. In order to account for this, the chemical nature of the chars was monitored, using elemental analysis and oxygen chemisorption.

The results of this study indicate that, at low temperatures, the rate of oxidation of the subbituminous and bituminous chars is proportional to the BET surface area beyond 20% conversion. The lignite char did not show such simple behavior because of the presence of large amounts of ash. For the high-temperature case, reaction appeared to be confined to the exterior of the particle and to the interior of the macropores.

Time-temperature histories of individual lignite char particles were obtained with a two-color pyrometer. A simplified model of single- particle-char combustion was used in conjunction with statistical analysis to infer kinetic parameters from the experimental time-temperature traces.

TABLE OF CONTENTS

LIST OF FIGURES

LIST OF TABLES

CHAPTER 1

INTRODUCTION

1.1 Motivation

The U.S. has a great reserve of energy in the form of coal. The most common use of coal is as pulverized fuel (particles $<100\mu$m in diameter) for steam generating power plants. Though its use has leveled off recently, it is likely that future demand will increase as oil becomes scarce. Therefore, we must recognize the need for better understanding of the combustion of solid fuels today.

1.2 Background

"Coal" is a rather general term that refers to carbonaceous sedimentary rock which has resulted from the decomposition of vegetable matter that died eons ago. Because of the great number of plant species that existed and the wide variety of conditions under which they coalified, coal structure and composition varies significantly, even within a seam.

Coals are broadly classified according to the extent of their coalification. Anthracites are the oldest; they have the highest carbon content and the highest heating value. Bituminous coals have lower carbon contents and heating values, while lignites have the lowest carbon contents and heating values. There are significant variations in carbon content, volatile matter, moisture and mineral matter between different coals within the same classification.

When pulverized coal is blown into a boiler, it first undergoes pyrolysis. During pyrolysis, the large organic molecules of the coal break apart and subsequently recombine to form more stable species (Anthony and Howard (1976)). Volatiles are expelled as tars (small organic molecules) or light gases, such as H_2O, CO or CO_2.

The combustible volatiles produced during this time burn in the gas phase almost immediately.

The resulting solid material, **char**, is richer in carbon and ash and poorer in hydrogen and oxygen than its precursor. Chars have extensive porous networks into which oxygen can diffuse and react. The structure depends not only on the raw coal but also on the size of the particle, the rate at which it is heated, the maximum temperature attained, and the pressure and composition of the gas phase during pyrolysis. For studies on the physical changes that occur during char formation, see Lightman and Street (1968), Street *et al.* (1969), or Pohl *et al.* (1978).

While the expulsion and subsequent oxidation of the volatiles are rapid, char burnout takes much longer (Laurendeau (1978)). Thus, the burnout of char can be regarded as the rate-limiting step of the process. Therefore, it plays an important role in determining the size of a coal combustor and the efficiency of combustion.

Prediction of burnout time and particle temperature is necessary for proper design of combustors. This requires accurate rate information. The kinetics of char oxidation have been the subject of numerous investigations, both theoretical and experimental. Smith (1982) provides an excellent review of this literature.

Low-temperature (350-650°C) oxidation experiments are potentially useful for predicting high-temperature behavior; hence, many workers have concentrated their efforts on understanding the kinetics of low-temperature char oxidation. Jenkins *et al.* (1973) used a thermogravimetric analyzer to study oxidation of over twenty different chars in air at 500°C. They found that char reactivity increased with decreasing rank. Snow *et al.* (1960) had already shown that higher hydrogen contents

in carbon blacks resulted in higher reactivities. Thus, Jenkins *et al.* concluded that the enhanced reactivity of the chars derived from lower rank coals is at least partly due to their higher hydrogen content. Dutta and Wen (1977) studied the oxidation of several chars in air at temperatures of 424-576°C. They concluded that reactivity of a given char in oxygen depends on the changes in pore structure during oxidation; however, they did not observe a direct relationship between reactivity and surface area. Tseng and Edgar (1984) studied oxidation of a lignite char at temperatures of 425-900°C and found that char reactivity depended strongly on pyrolysis conditions. Of course, the physical structure of the chars also depends on pyrolysis conditions. The conclusion of these studies is that low-temperature oxidation rates for various chars differ widely (Smith (1978)), and that much of the variation in observed reactivity is due to the influence of the porous structure of the char.

Attempts have been made to take into account the effect of the physical properties of char on observed reaction rates. For example, intrinsic reaction rates are based on the total surface area of char. While this accounts for some of the variation of reactivity between chars, large differences in the intrinsic rates of oxidation of chars derived from different coals still exist.

The presence of ash also affects observed reaction rates of chars at low temperatures. Jenkins *et al.* (1973) used demineralized chars in an attempt to understand the role of ash during low-temperature combsution. They demonstrated that ash has a catalytic effect on char oxidation. Hengel and Walker (1984) have shown that calcium is a particularly active catalyst.

Tong *et al.*(1982) used oxygen chemisorption to determine the "active" surface

area (ASA) of pyrolytic carbon and found good correlation with observed oxidation rate. Radovic *et al.*(1983) applied this technique to several chars. They found that reactivity is proportional to ASA. They also found that increasing severity of pyrolysis conditions reduced the ASA.

High-temperature combustion is more difficult to study, both experimentally and theoretically. Workers at BCURA in the U.K. and at CSIRO in Australia have made significant contributions in experimental studies of high-temperature combustion. Field (1969) studied the high-temperature combustion of char derived from a low-rank coal, using a laminar flow furnace to obtain particle temperatures of 1200-2000K. He found evidence that oxidation takes place inside the particles.

Smith and Tyler (1972) studied the oxidation of a pulverized semianthracite in the range 1400-2200K. Their results also indicate that internal burning takes place at these high temperatures. Smith and Tyler (1974) also studied the reactivity of a porous brown coal over a wide range of temperatures. They found that for particles 49μm and larger, pore diffusional limitations were important at temperatures above 760K.

In a landmark study of high-temperature combustion, Ayling and Smith (1972) measured the temperature of a stream of burning char particles by using a pyrometer to capture radiation emitted from the stream. By independently determining carbon conversion, they used mass and energy balances to deduce that carbon monoxide is the primary product of the heterogeneous reaction. More recently, Mitchell and McLean (1982) and Jorgensen and Zuiderwyk (1985) have used pyrometry to study the combustion of individual particles.

In order to define more precisely the role of porosity on combustion, better descriptions of the porous structures and more data on pore diffusion are needed.

Several methods have been used to better understand the nature of porous materials. These methods are generally applicable to chars. It is from these types of experiments that we hope to obtain the detailed information on particle structure necessary for a better fundamental understanding of char combustion.

Gas adsorption remains the most popular means of solid characterization. While many types of adsorptives have been used, the most commonly used being nitrogen and carbon dioxide. Nitrogen adsorption at 77K is used in conjunction with BET theory to determine overall surface areas; nitrogen adsorption can also be used to obtain pore volume distributions (pore radii of 16 to 150 Å) through capillary condensation. Carbon dioxide at 298K is used with the Dubinin-Polyani theory to determine micropore volumes and surface areas (pore diameters less than 30 Å).

Walker and Kini (1965) used a variety of adsorptives on several raw coals. They concluded that carbon dioxide is superior because it is free of activated diffusion effects. Marsh and Rand (1971), using both nitrogen at 77K and carbon dioxide at 293K to study a variety of carbonaceous materials, reached a similar conclusion. However, Reucroft and Patel (1983) have indicated that carbon dioxide induces swelling in coals, thus leading to questionable values of surface area.

Pope (1984) describes a novel technique of pore characterization that utilizes the *rates* at which gases adsorb on a lignite coal. He concluded that swelling of the sample makes interpretation difficult.

Mercury porosimetry is a useful means of determining pore-size distributions of the larger pores (pore radii of 32 Å to 3 μm). Debelak and Schrodt (1979), using both capillary condensation of nitrogen and mercury porosimetry, found good agreement between the two methods over the range of overlap.

Spitzer and Ulicky (1976) have described a low-angle x-ray scattering technique for measuring surface area associated with microporosity. This method has the advantage of being able to detect blind pores. Bale *et al.* (1986) have used this technique to study the changes in particle morphology of a lignite coal after heat treatment.

In addition to experimental advances, much theoretical work has been done on pore structure and reactivity of chars. Simons (1979) modeled char structure with a pore tree model. Bhatia and Perlmutter (1980) and Gavalas (1980) independently developed random pore models to describe internal porosity of chars.

Others have considered single particle combustion. Among these are Sotirchos and Amundson (1984), who have developed a detailed model of transient char combustion at high temperatures.

Few have attempted to unify these facets of char combustion.

1.3 Research Objectives

The purpose of this research is to better understand char combustion through a detailed analysis of the evolving physical structure of char during oxidation. Experimental and theoretical studies of the microstructure and of pore diffusion and reaction within this microstructure were performed.

Three raw coals were examined in this study: a high volatile A bituminous

(PSOC 1451), a lignite (PSOC 1443) and a subbituminous (PSOC 1488). Chars were generated from size-classified samples of these coals by pyrolysis in an inert atmosphere in a drop-tube furnace. The chars were partially oxidized at low temperature (675-825K) and at high temperature (1400-2000K). These partially oxidized chars were subsequently characterized, both chemically and physically.

Physical characterization included the following: i) nitrogen adsorption at 77K to obtain a "total" surface area and pore-size distribution (for pores with radii less than 150 Å), ii) mercury porosimetry to obtain particle density and pore size distribution (for pores with radii greater than 32 Å) and iii) scanning electron microscopy to visualize the surface.

Chemical characterization included: i) oxygen chemisorption to determine "active" surface area and ii) elemental analysis to determine C:H ratios.

Experiments on high-temperature reactivity were also done using a two-color pyrometer. In this series of experiments, entire time-temperature histories for many particles under different ambient conditions were obtained. A simple model of single particle combustion was developed to derive kinetic parameters from the traces. Because of the particle-to-particle variability, a statistical approach was necessary.

A more realistic model was also developed to describe the high-temperature combustion of single char particles. Physical parameters derived from materials that were partially oxidized at low temperature were used to predict high-temperature behavior of the same material. The results of this model were compared to experimental data obtained in this study.

1.4 Organization

Chapter 2 describes the experimental equipment and techniques used in the characterization of the chars. Interpretation of the data obtained from these experiments is also discussed. Chapter 3 describes studies on the low-temperature (400-600 °C) reactivity of chars and the changes in the pore structure that occur during reaction. Chapter 4 presents the results of studies of the high-temperature oxidation of coal chars, including observations on the evolution of the structures of chars with reaction. Chapter 5 shows the results of single-particle oxidation studies. A statistical method for deducing reaction kinetic parameters by analysis of single particle reaction data is also described in Chapter 5. Chapter 6 presents the models which were used to describe single particle combustion. Chapter 7 summarizes the major conclusions from this study. Appendix I lists some of the physical and chemical properties of the coal, including its proximate and ultimate analyses, heating values, elemental composition, and composition of ash.

REFERENCES

Anson, D., Moles, F.D., and Street, P.J. (1971). Structure and Surface Area of Pulverized Coal During Combustion. *Comb. Flame*, **16**, 265.

Anthony, D. and Howard, J. (1976). Coal Devolatilization and Hydrogasification. *AIChE J.*, **22**, 625.

Ayling, A.B., and Smith I.W. (1972). Measured Temperature of Burning Pulverized Fuel Particles and the Nature of the Primary Reaction Product.

Bale, H.D., Carlson, M.L., and Schobert H.H. (1986). Thermal Modification of the Pore Structure of a North Dakota Lignite. *Fuel*, **65**, 1185.

Bhatia, S.K. and Perlmutter, D.D. (1980). A Random Pore Model for Fluid-Solid Reactions: I. Isothermal, Kinetic Control *AIChE J.*, **26**, 379.

Debelak, K.A. and Schrodt, J.T. (1979). Cómparison of Pore Structure in Kentucky Coals by Mercury Penetration and Carbon Dioxide Adsorption. *Fuel*, **58**, 732.

Dutta, S. and Wen, C.Y. (1977). Reactivity of Coal and Char. 2. In Oxygen-Nitrogen Atmosphere. *Ind. Eng. Chem.*, **16**, 31.

Field, M.A. (1969). Rate of Combustion of Size-Graded Fractions of Char from a Low-Rank Coal Between 1200K and 2000K. *Combust. Flame*, **13**, 237.

Gavalas, G.R. (1980). Analysis of Char Combustion Including the Effect of Pore Enlargement. *Comb. Sci. Tech.*, **24**, 197.

Hamor, R.J., and Smith, I.W. (1973). Kinetics of Combustion of a Pulverized Brown Coal Char Between 830 and 2200K. *Combust. Flame*, **21**, 153.

Hengel, T.D. and Walker, P.L., Jr. (1984). Catalysis of Lignite Char by Exchangeable Calcium and Magnesium. *Fuel*, **63**, 1214.

Jenkins, R.G., Nandi, S.P. and Walker, P.L., Jr. (1973). Reactivity of Heat-Treated Coals in Air at 500oC. *Fuel*, **52**, 288.

Jorgensen, F.R.A. and Zuiderwyk, M. J. (1985). Two-Color Pyrometer Measurement of the Temperature of Individual Combusting Particles. *J. Phys. E: Sci. Instrum.*, **18**, 486.

Laurendeau, N.M. (1978). Heterogeneous Kinetics of Coal Char Gasification and Combustion. *Prog. Energy Comb. Sci.*, **4**, 221.

Lightman, P. and Street, P.J. (1968). Microscopial Examination of Heat Treated Pulverized Coal Particles. *Fuel*, **47**, 7.

Loewenberg, M., Bellan, J., and Gavalas, G.R. (1987). A Simplified Description of Char Combustion. *Chem. Eng. Comm.*, **58**, 89.

Marsh, H. and Rand, B. (1971). Microporosity in Carbonaceous Materials. *Proc. of Third Conf. on Indust. Carbon and Graphite Soc. of Chem. Ind.*, London, England, 172.

Mitchell, R.E., and McLean, W.J. (1982). On the Temperature and Reaction Rate of Burning Pulverized Fuels. *Nineteenth Symposium (Int.) on Combustion, the Combustion Institute*, p. 1113.

Pohl, J.H., Kobayashi, H., and Sarofim, A.F. (1978). The Effects of Temperature and Time on Pulverized Coal Particles. *Combustion Institute Technical Meeting*, Boulder, CO.

Pope, C.G. (1984). Lignite Porosity by Kinetics of Gas Adsorption. *Fuel*, **63**, 1681.

Radovic, L., Walker, P.L.,Jr., and Jenkins, R.G. (1983). Importance of Carbon Active Sites in The Gasification of Coal Chars. *Fuel*, **62**, 849.

Reucroft, P.J. and Patel, K.B. (1983). Surface Area and Swellability of Coal. *Fuel*, **62**, 279.

Simons, G.A. (1979). The Structure of Coal Char: Part I. Pore Branching. *Comb. Sci. Tech.*, **19**, 217.

Smith, I.W. and Tyler, R.J. (1972). Internal Burning of Pulverized Semi-anthracite: The Relation Between Particle Structure and Reactivity. *Fuel*, **51**, 312.

Smith, I.W. and Tyler, R.J. (1974). The Reactivity of a Porous Brown Coal Char to Oxygen Between 630 and 1812K. *Comb. Sci. Tech.*, **9**, 87.

Smith, I.W. (1978). The Intrinsic Reactivity of Carbons to Oxygen. *Fuel*, **57**, 409.

Smith, I.W. (1982). The Combustion Rates of Coal Chars: A Review. *Nineteenth Symposium (Int.) on Combustion, the Combustion Institute*, p. 1045.

Snow, C.W., Wallace, D.R., Lyon, L.L. and Crocker, G.R. (1960). *Proc. of the Fourth Conf. on Carbon*, Pergamon Press, New York, 79.

Sotirchos, S.V. and Amundson, N.R. (1984). Dynamic Behavior of a Porous Char Particle Burning in an Oxygen-Containing Environment. *AIChE J.*, **30**, 537.

Spitzer, Z. and Ulicky, L. (1976). Specific Surfaces of Coals Determined by Small Angle X-ray Scattering and by Adsorption of Methanol. *Fuel*, **55**, 21.

Street, P.J., Weight, R.P., and Lightman, P. (1969). Further Investigations of Structural Changes Occurring in Pulverized Coal Particles During Heating. *Fuel*, **48**, 343.

Timothy, L.D., Sarofim, A.F., and Beer, J.M. (1982). *Nineteenth Symposium (Int.) on Combustion, the Combustion Institute*, p. 1123.

Tong, S.B., Pareja, P., and Back, M.H. (1982). Correlation of the Reactivity, the Active Surface Area and Total Surface Area of Thin Films of Pyrolytic Carbon. *Carbon*, **20**, 191.

Tseng, H.P. and Edgar, T.F. (1984). Identification of the Combustion Behavior of Lignite Char Between 350 and 900°. *Fuel*, **63**, 385.

Tseng, H.P. and Edgar, T.F. (1985). Combustion Behavior of Bituminous and Anthracite Coal Char Between 425 and 900°. *Fuel*, **64**, 373.

Walker, P.L.,Jr. and Kini, K.A. (1965). Measurement of the Ultrafine Surface Areas of Coals. *Fuel*, **44**, 453.

CHAPTER 2

METHODS OF PHYSICAL CHARACTERIZATION OF POROUS MATERIALS

2.1 Introduction

A variety of techniques have been developed to study porous materials. Since coals and chars are porous, most of these methods are applicable to the study of these materials. Mahajan (1981) describes many of these techniques in detail.

This chapter deals with two of the most important methods used to elucidate the internal morphology of char: gas adsorption and mercury porosimetry.

2.2 Gas Adsorption

Gas adsorption is a useful tool for probing solids on the molecular level; however, obtaining the data can be a tedious process. A novel technique for obtaining adsorption isotherms is described in Subsection 2.2.1.

Various interpretations of adsorption data have been put forward; Subsection 2.2.2 discusses some models of these interpretations.

2.2.1 Experimental Method

The standard technique of obtaining adsorption isotherms involves dosing the solid of interest with a known volume of gas, then allowing the system to equilibrate. The system pressure is measured, and the process is repeated. Finally, the system volume is determined so that the amount of gas adsorbed at each step can be calculated. While this method gives good results, it is time consuming. Alternative methods have been proposed, but a method developed by Innes (1955) was found to be amenable to automation. The following paper describes the technique and apparatus used for obtaining the gas adsorption isotherms used in later chapters.

MEASUREMENT OF GAS ADSORPTION ISOTHERMS BY CONTINUOUS ADSORBATE ADDITION

P. S. Northrop* **G. R Gavalas***

and

R. C. Flagan**

Chemical Engineering*

Environmental Engineering Science**

California Institute of Technology

Pasadena, California 91125

Published in *Langmuir*, **3** (1987), 300

ABSTRACT

A technique of measuring gas adsorption isotherms by continuous addition of adsorbate gas to the sample is described. Flow rates in the range of 0.01-1 ml STP/min. can be obtained by means of orifices of diameter 1-10 microns. The continuous flow technique is compared with the customary incremental addition of the adsorbate gas for two sorbents, a γ-alumina and a high volatile bituminuous coal.

INTRODUCTION

Gas adsorption is the standard technique for measuring the surface area of porous and finely dispersed solids. When extended to the range of capillary condensation, gas adsorption also provides information about pore size distribution for pore openings with diameters below about twenty nanometers.

The conventional method for obtaining a gas adsorption isotherm involves the following steps: First, the sample is outgassed under vacuum at a specified temperature. It is then isolated from the remainder of the system and cooled to the requisite temperature, which is often the normal boiling point of the adsorbate. A container of precisely known volume is filled with the adsorbate gas to the desired pressure. The container is then opened to the sample volume and after the lapse of specified time, the pressure is recorded. The sample holder and the container are then isolated, the container is refilled, and the procedure is repeated.

The amount of gas adsorbed at each pressure level is simply the difference between the amount of gas introduced into the system and the amount occupying the "dead volume" as calculated by the pressures before and after each equilibration (Brunauer *et al.*(1938)). This incremental addition of gas provides a discrete set of points along the isotherm and will be referred to as the "discrete" technique. This technique of generating points along the isotherm gives good results, but can be very tedious and time consuming.

An alternative to this method has been reported by Innes (1951) and Lange (1963). Both used a continuous flow of adsorbate into their systems and monitored system pressure. Innes used a mass-flow controller to admit a steady flow of gas,

while Lange used a small capillary. When the ratio of upstream pressure to downstream pressure is above its critical value, choked flow is established in the capillary, and the flow rate is independent of downstream pressure. The flow rates achieved in these two reports were limited by the capability of the mass-flow controller or the size of the capillary to a minimum of approximately 4.0 ml STP/min. More recently, Dollimore *et al.*(1973) and Bosch and Peppelenbos (1977) have described gas-adsorption systems that are based on the same principle.

Thin metal foils with laser-drilled openings as small as 1 micron are commercially available. These can be used to obtain flow rates as low as 0.01 ml STP/min. Special, high-vacuum leak valves can achieve even lower flow rates; however, these valves are quite expensive. The rate of gas introduction into the sample cell must be sufficiently low to ensure quasi-equilibrium between the gas phase and the adsorbed phase. In this paper, we report the development of an instrument based on the continuous flow technique. Important experimental issues concerning the dependence of flowrate on downstream pressure and the effect of the temperature profile in the sample holder are addressed.

APPARATUS AND PROCEDURE

A schematic of the apparatus is presented in Figure 2.1. The adsorbate (usually high-purity nitrogen) passes through a filter to remove any dust particles and then flows through the orifice. Commercially available orifices (Melles-Griot, Irvine, CA) with diameters from 1 to 50 microns were used. The thin foils were mounted in

special holders as shown in Figure 2.1. were used. For most of the experiments, we have used a 10-micron diameter orifice with an upstream pressure of 0.2MPa to obtain a flow rate of about 1.3 ml STP N_2/min. A multiport valve does, however, allow selection of different orifices according to the particular sample. An option for connection of an orifice to vacuum is included to facilitate desorption isotherm measurements. The baratron gauge shown in Figure 2.1 measures system pressure to a precision of 0.1 torr on full scale. It has been interfaced to a microcomputer-based data-acquisition system, so that the pressure can be recorded at regular intervals, typically every 10 seconds. This system can also be used to carry out measurements by the customary discrete technique.

The sample is outgassed successively by a mechanical pump and a diffusion pump and then isolated from the vacuum system by closing the stopcock (Figure 2.1). A small Dewar flask containing liquid nitrogen is placed around the sample tube. The level of liquid nitrogen in the Dewar is maintained constant by periodically replenishing the liquid lost by evaporation. During the period when the sample is cooling to liquid nitrogen temperature, nitrogen flows through the orifice and other lines (except the sample volume, which remains isolated) and exits through the vacuum line. At the start of the run, the valve to vacuum is closed, the stopcock to the sample volume opened, and data acquisition is initiated.

When the adsorption measurements are complete, the desorption isotherm can be measured by switching to the appropriate orifice, using the multiport valve. At the end of the desorption run, the system is re-evacuated. The dead volume of the system, including the sample tube, is obtained by filling it with helium. The

pressure is measured, and the valve to the calibration volume is opened (see Figure 2.1). The pressure after expansion is recorded. This procedure is repeated twice. The dead volume is calculated, using the ideal gas relation. Finally, the orifice is calibrated immediately after the run, as there are minute, day-to-day fluctuations in the flow rate.

DATA REDUCTION

The amount of gas adsorbed is simply the difference between the amount of gas that has passed through the orifice and that which occupied the dead volume:

$$n = \int_0^t Q(t)dt - P(t)/R \int_0^{V_T} dV/T, \tag{2.1}$$

where Q is the molar flow rate of gas, t is the time, P(t) is the pressure, R is the gas constant and V is the volume of system plus sample tube. Using this relation, the number of moles of gas adsorbed is determined as a function of pressure. The BET and capillary condensation analyses can then be carried out on the resulting isotherm.

The number, n, of adsorbed moles is usually the difference between two larger numbers; therefore, it is essential that these numbers be measured as accurately as possible. The pressure P(t) has a maximum error of $\pm 0.05\%$, while the error in the integral is $\pm 0.1\%$. The flow rate Q is sensitive to upstream pressure fluctuations and temperature variations. Figure 2.2 shows the 95% confidence interval for flow rate as a function of downstream pressure. The maximum deviation from the average is about $\pm 0.5\%$. For a sample with a total area of 1.0 m^2, the standard error in the

area measurement is nearly $\pm 15\%$. For samples with larger area, the relative error is proportionally smaller. Reducing the volume of the sample holder and various lines will provide improved accuracy for small samples.

The desorption data are treated in a similar manner. In this case, the amount of gas remaining adsorbed is given by

$$n = n_0 - \int_0^t Q(t)dt - \frac{P(t)}{R}\int_0^{V_T} \frac{dV}{T}, \tag{2.2}$$

where n_0 is the initial number of moles in the system (adsorbed plus gas phase). The first integral is the number of moles removed from the system up to time t. The molar flow rate Q(t) is a function of the system pressure P(t) obtained by suitable calibration. The second integral is the gas in the dead volume, as in Equation (2.1).

RESULTS

Compressible flow theory provides that flow through an orifice or a tube becomes choked and remains independent of downstream pressure when the upstream-to-downstream pressure ratio exceeds a critical value. This result, however, applies only in the usual continuum limit when the Knudsen number, $\mathrm{Kn} = \frac{\lambda}{d} << 1$, where λ is the mean free path of the gas molecules and d is the orifice diameter. With orifices as small as 1-10 microns, the Kn becomes of order one or higher, depending on downstream pressure. Hence, standard compressible flow theory is not expected to apply. Figure 2.2 shows that the flow rate is a weak function of downstream pressure, even when the upstream-to-downstream pressure ratio is far above the critical value for choked flow. This behavior necessitates careful calibration of flow

rate versus downstream pressure for the specific orifice and upstream pressure employed.

A high surface area γ-alumina was employed as the first test material to compare the continuous and discrete techniques. One continuous flow run and one discrete run were performed, providing isotherms shown in Figure 2.3. The total isotherm was obtained in two hours, using the continuous flow method; the twenty points of the discrete method took 15 hours. The agreement between the two methods is very good up to pressure of 400 torr; however, in the regime of capillary condensation, the uptake of gas measured by the continuous method is somewhat lower than in the discrete measurements. This is not surprising, as time is required to establish equilibrium between the gas phase and liquid in the capillaries. Better equilibration can be obtained with the continuous method by reducing the orifice size.

The BET model is usually applied to a relative pressure range (P/P^0, where P^0 is the vapor pressure of adsorbate) of 0.04 to 0.30. For nitrogen at 77K, the upper limit corresponds to about 250 torr. In this range, the 10 micron orifice gave good equilibration and good agreement with the discrete technique. The calculated surface areas were 182 m^2/g for the continuous run and 178 m^2/g for the discrete addition.

Figure 2.3 also shows isotherms obtained for a high volatile bituminous coal. In this case, the continuous run took one hour, while the discrete addition took more than 12 hours. The disparity between adsorption isotherms for this microporous material is not surprising. Diffusion of gaseous nitrogen within the microporous

structure of coal is an activated process and, hence, very slow at the temperature of liquid nitrogen (Walker and Kini (1965)). The BET surface area was $1.5 m^2/g$ for the continuous run, and 3.7 m^2/g for the discrete run.

CONCLUSIONS

Measurement of adsorption isotherms by continuous gas flow at rates below 1 ml STP/min. can be carried out using suitably small orifices on thin metal foils (orifice diameter 1-10 microns). The method requires measurement of the flow rate as a function of downstream pressure, since this does not obey the usual compressible flow relationships. The continuous flow method provides BET surface areas in good agreement with the customary discrete method and requires less run time and is less laborious.

ACKNOWLEDGEMENT

This work was supported by DOE Grant DE-FG22-83PC60801.

2.2.2 Interpretation of Gas Adsorption Data

While gas adsorption data are easy to obtain, their interpretation is not necessarily straightforward. Many models of gas adsorption exist; however, they can only approximate physical reality. The most common (and most doubtful) assumptions are that the surface is homogeneous and that there are no specific adsorbent-adsorbate or adsorbate-adsorbate interactions. Molecular sieve effects are not generally considered. As a result, these models have limited validity.

The BET model is probably the most widely used form for inverting gas adsorption data. The reason for this is that, in spite of its simplicity, it accurately describes multilayer adsorption for a wide variety adsorbates and adsorbents. Thus, BET surface area is a standard parameter used in the characterization of a solid.

The Dubinin-Polyani theory was developed to describe adsorption into microporous adsorbents, primarily carbonaceous materials. The theory is based on a micropore filling mechanism rather than on a surface adsorption mechanism. This method has gained wide acceptance because the carbon dioxide molecule has a smaller minimum dimension than nitrogen, and adsorption takes place at higher temperature, thus reducing the possibility of limitation via activated diffusion.

In addition to total surface area and total micropore volume, gas adsorption can be used to infer pore-volume distributions over a wide range of pore sizes. Capillary condensation is particularly useful for determining pore-volume distributions; however, information on pore structure can be obtained from the entire isotherm. The following paper discusses some of the merits and drawbacks of several means of pore-volume distribution inversion.

A CRITICAL ANALYSIS OF GAS-SOLID PHYSISORPTION

P. S. Northrop* Ranajit Sahu§

R. C. Flagan† G. R. Gavalas*

Depts. of Chem. Eng.*, Mech. Eng.§,

Env. and Mech. Eng.†

California Institute of Technology

To be submitted to the *Journal of Colloid and Interface Science*

ABSTRACT

The internal morphology of three porous solids (γ-alumina, a partially oxidized synthetic char and PSOC-190 coal) was studied in detail, using gas adsorption. Four gases (nitrogen, argon, carbon dioxide and Freon-21) were used to observe specific adsorbent-adsorbate interactions in each solid. BET surface areas and C values were determined in each case. Several methods of determining pore volume distributions (Cranston-Inkley, Yan-Zhang and Brunauer's Modelless method) from the isotherms were examined and compared. The pore-size distribution in the micropore range was interpreted according to the MP and Medek methods. Micropore volumes were obtained from the Dubinin-Radushkevich-Kaganer method. The results of these analyses were used to construct a consistent picture of the internal structure of these solids. Suggestions are made regarding the applicability of these methods in specific situations.

INTRODUCTION

Gas adsorption is widely used to probe the internal structure of porous solids because physical adsorption is reversible (except for porous solids, which exhibit hysteresis), non-destructive, and readily measured. The amount of gas adsorbed on a solid surface depends on the temperature of the system, the partial pressure of the particular adsorptive, and the nature of the solid. The extent of adsorption is usually measured as a function of pressure of the adsorptive at a fixed temperature. For this reason, the resulting plot of quantity adsorbed versus pressure is known as an isotherm.

Since physical adsorption does not depend strongly on chemical interactions, various gas-solid pairs give qualitatively similar isotherms. Brunauer *et al.* (1940) identified five basic types of isotherms. Porous solids usually give type III isotherms, but also pseudo type I and more rarely type V. For types III and V, enhanced adsorption at pressures greater than 40% of the saturation pressure is attributed to capillary condensation of adsorbate in the small pores of the solid. This region of the isotherm contains information about pore-size distribution.

Desorption isotherms do not coincide with adsorption isotherms for porous materials. This hysteresis in the adsorption-desorption cycle is attributed to differences in the physical state of the gas-solid system during the processes of evaporation and condensation. The pore shape may be inferred from the hysteresis, although the irregular shapes of the pores in most materials of interest make such inferences questionable.

The dynamics of adsorption and the molecular nature of the solid surfaces

in porous materials are not well understood. Even less is known about capillary condensation. A number of models have been developed in the attempt to elucidate the nature of the underlying porous structure of the solid (Wheeler (1946), Brunauer *et al.* (1938), Kaganer (1959)). In these models, the pore shape is assumed *a priori.* Pores are often assumed to be cylindrical or slit-shaped. The purpose of this paper is to examine a few of these models and to apply them to isotherms of several gas-solid pairs. The models will be evaluated in light of what is known about the solid and the gas. With sufficient information about the adsorbing gas, it should be possible to draw conclusions about the fundamental nature of the solid consistent with all observations. In particular, it may be preferable to infer the pore morphology of a given solid based on its interactions with a number of different gases rather than a single one. Some attempts in that direction shall be made in the present study.

The analysis of particle morphology in the microporous region is extremely difficult because of the presence of strong overlapping pore potentials from pore walls. Moreover, the concept of rigid pore geometry is too limiting for a realistic description of the structure at molecular dimensions. Some of the more common methods for analyzing the pore structure in this regime are examined in the present analysis.

EXPERIMENTAL PROCEDURE

All isotherms were obtained using a system into which a continuous flow of adsorbate was introduced. This technique has been described in detail by Northrop *et al.* (1987) and will be only briefly described here. The adsorptive was admitted through a 10 μm diameter orifice. The flow rate was very carefully calibrated for a

given set of conditions by monitoring the pressure increase in a well-defined volume. Generally, flow rates were kept at about 1.0 cm^3(STP)/min.

During the experimental run, the system pressure variation with time was measured with an MKS Baratron 270A Digital pressure gage, whose output signal was recorded in a microcomputer based data acquisition system.

Following the measurement of an adsorption isotherm, the "dead-volume" of the system including the sample tube was measured by introducing a known volume of helium. Knowledge of the system dead-volume and pressure at a given time allowed calculation of the amount of adsorptive in the gas phase. The difference between the amount of adsorptive introduced through the orifice and the amount remaining in the gas phase was the amount adsorbed. The system can also be used to obtain desorption isotherms, but only the adsorption branch was measured in this series of experiments.

Four different adsorbates were examined on three porous adsorbents. The gases used were: nitrogen at 77K, argon at 77K, carbon dioxide at 195K, and Freon-21 at 273K. Carbon dioxide at 298K was also used to obtain data for the Dubinin-Radushkevich-Kaganer (DRK) theory. The solids examined were: a γ-alumina, a partially oxidized synthetic char, and a raw coal (PSOC-190). The unique interactions of each adsorptive-adsorbent pair are important in determining the type of isotherm for that pair. Table 2.1 lists some of the physical properties of the adsorptives used.

DATA INVERSION

While the primary interest is in adsorption on porous materials, it will be

useful first to consider multilayer adsorption on flat surfaces. Many models have been developed to explain physical adsorption on a free surface (Halsey (1948), Young and Crowell (1962), Sircar (1985)). However, none of these has been as successful as the theory developed by Brunauer *et al.* (1938).

The BET theory is based on the assumptions of a homogeneous surface and no adsorbate-adsorbate interaction. These assumptions are difficult to justify, yet the model gives a good fit to experimental data for a wide variety of gas-solid pairs over a limited range of relative pressures (P/P^0, where P^0 is the vapor pressure of adsorptive at the system teperature). Furthermore, the theory predicts the amount of adsorbate required to form a layer one molecule thick over the surface. Knowledge of the molecular cross-sectional area allows calculation of an overall surface area. The model also gives a measure of the strength of the gas-solid interaction through the C value, where $C = \exp\{(\epsilon - \epsilon_v)/RT\}$, ϵ is the energy of adsorption per mole of adsorbate, and ϵ_v is the energy of vaporization per mole. The BET surface area and C value are useful for comparison between experiments. The measured values for all gas-solid pairs studied are summarized in Table 2.2.

Condensation occurs in porous solids at pressures below the vapor pressure of the adsorbate due to the surface tension induced pressure difference across the curved meniscus of the condensed vapor. The relationship between the size of the capillary and pressure is given by the Kelvin equation

$$\ln(P/P^0) = 2\gamma\bar{V}\cos\theta/\mathrm{LRT}, \tag{2.3}$$

where γ is the surface tension, $\bar{V}$ is the molar volume, θ is the angle of contact, R is the gas constant and T is the absolute temperature. L is a measure of the width of

a pore; for a cylinder, it is the radius, while for a slit it is half the distance between walls.

Using a model for capillary condensation in cylindrical pores that included multilayer adsorption, Wheeler (1946) deduced that the specific pore volume V(r) was related to the volume of nitrogen desorbed over a small segment on the desorption branch of the isotherm v(r) by

$$v(r) = \left(\frac{(r - t(r))}{r}\right)^2 V(r) + dt/dr \int_r^{r_0} \frac{2(r' - t(r'))}{r'^2} V(r')dr'. \qquad (2.4)$$

where r is the radius of the pore, and t is the thickness of the adsorbed layer of gas. The first term on the right accounts for liquid evaporated from the pore cores, while the second term represents the amount of gas desorbed from free surfaces. This relation applies to the adsorption branch of the isotherm as well.

The thickness of the layer was obtained from what is known as a t-curve (Lippens and deBoer (1965)). This is simply a plot of the volume of adsorptive per unit of BET surface area at monolayer coverage versus the relative pressure for a non-porous substance. Thus, it is a relation between the mean thickness of the adsorbed layer and the relative pressure. This relation has a weak dependence on the C value. Therefore, in order to obtain the most accurate t values, a t-curve from a solid with a C value similar to that of the solid in question should be used (Lecloux and Pirard (1979)).

In principle, both the Kelvin radius and the average thickness of adsorbate can be calculated for a given relative pressure. The appropriate values can then be used in (2.4), which can be expressed as a Volterra integral equation of the second kind. Wheeler was not able to come up with an iterative scheme for calculating V(r).

Several authors have developed methods for calculating $V(r)$. Among them are Pierce (1953), Dollimore and Heal (1964), and Cranston and Inkley (1957). The inversion method of Cranston and Inkley was difficult to carry out when it was first introduced. However, the calculations are quite easy on a computer. For a finite adsorption step from pressure P_1 (corresponding to radius r_1) to P_2 (radius r_2), the amount of nitrogen adsorbed is

$$v_{12} = \int_{r_1}^{r_2} \frac{(r' - t_1)^2}{r'^2} V_{r'} dr' + (t_2 - t_1) \int_{r_2}^{\infty} \frac{V_{r'}(2r' - t_1 - t_2)}{r'^2} dr', \tag{2.5}$$

where t_1 and t_2 are the adsorbed layer thicknesses at the respective pressures and $V_{r'}$ is the volume of pores with radii in the interval r_1 to r_2. Cranston and Inkley have shown that V_{12} can be approximated by

$$V_{12} = R_{12} \left(v_{12} - 4(t_2 - t_1) \sum_{r_2 + \frac{\Delta r}{2}}^{r_{max}} \frac{(r - 1/2(t_1 + t_2))}{2r^2} V_r \Delta r \right), \tag{2.6}$$

where

$$R_{12} = \frac{r_2 - r_1}{\int_{r_1}^{r_2} \left[(r - t_1)^2 / r^2 \right] dr}. \tag{2.7}$$

Yan and Zhang (1986) have also developed a means of calculating pore volume distribution based on Wheeler's model. The volume of pores of mean radius R_i is given by

$$\Delta V_i = R_i \left(\Delta v_i - 2\Delta t_i \sum_{j=1}^{i-1} \frac{\Delta V_j}{\bar{r}_j} + 2\bar{t}_i \Delta t_i \sum_{j=1}^{i-1} \frac{\Delta V_j}{\bar{r}_j^2} \right), \tag{2.8}$$

$$i = 1, 2, \cdots, n$$

where i refers to the pore group and the overbar denotes average values. They have shown that this method gives results similar to the results of the Cranston-Inkely method. In fact, the only difference is that R_{12} is essentially a log mean of r_1 and r_2, while R_i is an arithmetic mean. Yan-Zhang's method is more compact, however.

A rather different line of thought was used by Brunauer *et al.* (1967) to develop their "modelless" theory. This model is based on the thermodynamic identity

$$\gamma dS = \mu da. \tag{2.9}$$

This equation relates change in surface area (dS) of the adsorbate to the free energy change (da) energy change through the surface tension γ and the chemical potential μ. Integration yields

$$S = \frac{1}{\gamma}\int A_n da = \frac{1}{\gamma}\int \mathrm{RT}\ln(P/P^0)dn, \tag{2.10}$$

where R is the ideal gas constant, T is the absolute temperature, P^0 is the vapor pressure, dn is the incremental number of moles of adsorbate and A_n is the free energy of adsorption. The method is called modelless because it uses the hydraulic radius as a characteristic length parameter for the cores rather than assuming a particular pore geometry. The hydraulic radius is defined as follows:

$$r_h = V/S, \tag{2.11}$$

where V is the volume of adsorbate and S is the wetted surface area. Again, both the gas evaporating from (or condensing into) the cores and the gas desorbing from (adsorbing on) open surfaces must be accounted for.

An example of the calculations is as follows: for relative pressure from 1 to 0.95, $V_1 = (n_{1.0} - n_{0.95})\nu$, where ν is the molar volume of liquid. Then, S_1 is obtained from (2.10). The definition of hydraulic radius is used to obtain a measure of average core size in this range of relative pressures. For the next step, $V_2 = (n_{0.95} - n_{0.90})\nu - V_2'$. The second term is the correction for gas that is desorbing from

the free surface. If the pores are assumed to be parallel slits, $V_2' = 10^{-4}(t_1 - t_2)S_1$, for t in Å, S in m^2 and V in cm^3. The correction for cylindrical pores is more complicated, but it does not change the result significantly.

As it stands, the modelless method describes the size and volume distributions of the cores. In order to compare its results with those of other inversions, the pore size and pore volume distributions are needed. However, in going from **cores** to **pores**, some assumption regarding geometry must be made; hence, the resulting method is no longer modelless. In the present analysis, the average thickness of the adsorbed layer calculated at the appropriate partial pressure was added to the core hydraulic radius to determine the pore radius. The core volume was also increased by an amount $S_i t_i$ to determine the pore volume. These modifications were made in order to facilitate comparision of the now "modelless" method with the other schemes.

The procedures above pertain to pores in which capillary condensation takes place. For nitrogen at 77K, the lower limit of applicability of the Kelvin Equation (2.3) occurs at a relative pressure of about 0.4, which corresponds to a core radius of 16 Å. For smaller dimensions, the concept of bulk surface tension becomes harder to justify. Of course, smaller pores may be present in the solid. Thus, it is necessary to consider analyses which deal with these micropores.

One such method is known as the MP method (Mikhail *et al.* (1968)). This theory is rooted in the concept of the t-curve described above. A v-t curve is a plot of the liquid volume uptake versus a mean thickness of the adsorbed layer, which is obtained from a t-curve. It is important that a t-curve from a solid of similar C

A v-t plot for a non-porous adsorbent will be a straight line with a slope equal to the surface area (Lippens and deBoer (1965)). A v-t plot of a microporous adsorbent will be concave downward at low relative pressures, as shown in Figure 2.21 (oxidized char). The reason for this is that, at the lowest pressures, adsorption occurs over the entire surface. As more adsorption occurs, some of the micropores become filled with adsorbate, making less surface is available for adsorption. This is reflected in the v-t curve by a decrease in slope, and hence, apparent surface area.

Actually, the surface area in pores of this size cannot be strictly defined because the pore dimensions are similar to the size of individual molecules. Whether the pore is cylindrical or slit-shaped, the total area "covered" by a molecule will be quite different from that which it covers on a free surface.

Radushkevich (1949) developed a theory for micropore *volume* analysis based on the micropore filling theory of Dubinin. Kaganer (1959) extended it to predict surface area. The following assumptions are made concerning microporous materials:

i.) The potential distribution in the porous solid is of the form

$$N = N_0 \exp(-K{E_0}^2), \tag{2.12}$$

where N is the number of moles of gas adsorbed, N_0 the total molar capacity of the solid, E_0 is the energy of adsorption of a reference adsorbate and K is a constant characteristic of the solid.

ii.) All adsorbates can be scaled to a single reference adsorbate

$$N = F(E/\beta), \tag{2.13}$$

where $\beta = E/E_0$.

The work required for isothermal compression of a gas from P to P_0 is

$$E = \mathrm{RT} \ln(P_0/P). \tag{2.14}$$

Substitution of (2.13) and (2.14) into (2.12) gives

$$N = N_0 \exp(-K(\mathrm{RT})^2 \ln^2(P_0/P)/\beta^2), \tag{2.15}$$

or, taking logarithms,

$$\log N = \log N_0 - 2.303K(\mathrm{RT}/\beta)^2 \log^2(P_0/P). \tag{2.16}$$

A plot of $\log N$ vs. $\log^2(P_0/P)$ should give a straight line. The number of moles at monolayer coverage can be calculated from the intercept of this line. Given a molecular cross-sectional area, the total surface area for the sample can be calculated. Again, the numerical value of the area of a molecule sitting on a particular surface is debatable.

Medek (1977) extended this theory to determine pore-volume distributions. Working from Dubinin's Equation (2.12), he assumed that the potential inside of a pore could be expressed as $\phi = kr_{eq}^{-3}$, where k is a constant and r_{eq} is the equivalent radius of the pore. Substitution into (2.12) yields:

$$N/N_0 = \exp\left(-(\kappa/E)^n r_{eq}^{-3n}\right), \tag{2.17}$$

where κ is related to k and the exponent n is close to 2 (but treated as a parameter in the Medek analysis). This expression is differentiated to get a pore-volume distribution.

RESULTS

Isotherms

The isotherms for nitrogen, argon, carbon dioxide at 195K and Freon on γ-alumina are shown in Figure 2.4. They are plotted as a function of relative pressure, so that they can be compared on a single plot. All isotherms on the γ-alumina are typical Type IV isotherms. This indicates that the solid is porous, with most pores being in the meso- to macro-pore range (i.e. more than 16 Å in diameter). The similarity between the nitrogen and argon isotherms is to be expected, since both molecules are similar in size. The small difference in shapes is an artifact of the experimental procedure. There is little difference in the absolute rates of gas admission in the two cases; however, the argon has less time to equilibrate with the sample since the run is stopped when its vapor pressure is reached (about 200 torr at 77K). Carbon dioxide (196K) and Freon also produce similar isotherms. Since these molecules are larger, the total molar amounts adsorbed are smaller. Multiplication of the respective molar volumes shows that the total pore volume is nearly 0.40 cm^3/g in all four cases. The isotherm for carbon dioxide on γ-alumina at 298K is shown in Figure 4. It appears as though there is Type I behavior followed by further adsorption. It is possible that at very low relative pressures, carbon dioxide is adsorbed only by the most active sites. At higher pressures, adsorption takes place over the entire surface.

The nitrogen, argon and carbon dioxide at 195K isotherms on oxidized glassy carbon char are classic examples of pseudo-Type I isotherms (see Figure 2.5), indicating that the char contains a very large number of micropores. Once these

micropores are filled, there is very little subsequent adsorption. The amount of argon adsorbed is higher than that of either nitrogen or carbon dioxide. This is surprising because argon has the largest minimum dimension of the three. Furthermore, its atoms are spherically symmetric and have no quadrupole moment, while the others do possess quadrupole moments.

While the Freon also produces a Type I isotherm, it is evident that there are two distinct regimes of adsorption (as manifested by the different slopes). This indicates that the char-Freon interaction is site specific and points to the existence of two distinct types of adsorption sites. Given the large size of the Freon molecule, one would expect that it may not be able to penetrate the smallest pores. This is not apparent from the total pore volumes measured by the different gases (in cm^3/g): 0.039 (N_2), 0.033 (CO_2), 0.05 (Freon) and 0.06 (Ar). The Freon molecules may be oriented on the surface, or have strong affinity to be in the adsorbed phase. Figure 2.7 shows the resulting isotherm for carbon dioxide at 298K on the partially oxidized char.

The nitrogen and argon isotherms on PSOC-190 (Figure 2.6) showed rather unusual behavior. At the lowest pressures, there was very little adsorption. However, when the relative pressure reached a critical value (0.04 for N_2 and 0.08 for Ar) adsorption increased significantly. The reason for this appears to be non-equilibration between the gas and adsorbed phases at low pressure. It is not due to pressure drop in the bed, as the particle size was 425 μm and the bed was free flowing. Equilibration is not a limiting factor for carbon dioxide or Freon. This may be due to the higher temperature of the system. The uptake of carbon dioxide was significantly

greater than that of any other adsorbate. Freon gave a typical type IV isotherm.

BET plots

The BET plots for nitrogen, argon, carbon dioxide at 195K and Freon on γ-alumina are shown in Figure 2.8. All are approximately linear, and give reasonably consistent surface areas. The areas were calculated, using molecular cross-sectional areas obtained from Lowell and Shields (1984), and Gregg and Sing (1982). The computed specific areas for this method are 207 m^2/g (N_2), 174 m^2/g (Ar), 200 m^2/g (CO_2) and 205 m^2/g (Freon).

Figure 2.9 shows the BET plots for the same adsorbates on oxidized char. It is interesting to note the similar shapes of the nitrogen, argon and carbon dioxide plots. The upward deviation at higher relative pressures is due to there being so little additional adsorption in this region. Once the micropores of the solid are filled with adsorbate, the solid appears virtually non-porous. The specific areas were found to be: 400 m^2/g (N_2), 573 m^2/g (Ar), 430 m^2/g (CO_2) and 433 m^2/g (Freon).

In Figure 2.10 the BET plots on the coal are shown. The specific areas were: 23.1 m^2/g (N_2), 22.8 m^2/g (Ar), 147.5 m^2/g (CO_2) and 151.6 m^2/g (Freon).

The C values for these isotherms (as calculated from the BET plots) are shown in Table 2.2.

Pore Volume Distributions

The inversions described above (Cranston-Inkley, Yan-Zhang and Modelless — subsequently referred to as CI, YZ and ML, respectively) were applied to each of the isotherms to determine the pore-volume distributions in each case. Pore-

volume distributions were chosen instead of pore-surface-area distributions for the following reasons: (a) Fundamentally, the concept of surface area in porous (or microporous) solids is nebulous on close scrutiny. Surface areas are useful only as a comparison between different materials; therefore, their intrinsic value has been questioned by many researchers (Debelak and Schrodt (1979)). (b) Geometrical assumptions, often simplistic, must be made to derive surface area distributions from the experimental data. (c) Most inversions naturally lend themselves to pore-volume distribution determinations.

In this section, all plots are in the form dV/dlog r vs. log r. The reason for this is that it is easy to visually integrate to obtain total void volume.

The CI and YZ distributions showed virtually identical results, as shown in Figures 2.11-2.14. As discussed earlier, these methods are based on the same fundamental equation. In order to observe the effect on the calculation, two approximations for the thickness have been used in each method: (a) a polynomial fit to the thickness curve ($C \sim 130$) and (b) the Halsley expression ($C \sim 100$). For a given expression of thickness, the two methods gave indistinguishable results (Fig. 2.11 and 13 or Fig. 2.12 and 14). This shows that the method of calculation of mean radius (log mean vs. arithmetic mean) is unimportant. Figure 2.15 shows thickness as a function of relative pressure for these two approaches. Note that the appropriate range of relative pressure is 0.4 to 0.95. The use of the Halsey thickness resulted in total pore volumes, which were about 5% lower than those from the polynomial approximation. The reason for this is that the Halsey thickness was slightly smaller than that calculated by the polynomial approximation.

Pore-volume distributions were obtained for nitrogen, argon and Freon on γ-alumina and raw coal using the CI method (see Figures 2.16 and 2.17). The char did not show appreciable pore volume in this range of sizes, so it is not considered here. For the γ-alumina (Fig. 2.16), the distributions from the nitrogen and Freon isotherms were strikingly similar, but the distribution from argon differs significantly. While total pore volumes (equal to area under the curve) are similar, the argon distribution is skewed toward larger pore sizes. As mentioned above, the argon had less time to equilibrate with the sample; hence, adsorption took place at artificially high relative pressures. This shows the importance of allowing adequate times for equilibration. The similarity of the nitrogen and Freon results may seem surprising. However, if the pores are sufficiently large, and if the interaction with the surface is similar, the result is reasonable. Freon has a higher dipole moment, but that appears to have little influence on the surface interaction. This suggests that the nature of the adsorption is non-specific, and that the adsorbent is relatively passive.

The similarity of the nitrogen and Freon results may seem surprising. However, if the pores are sufficiently large, and if the interaction with the surface is similar, the result is reasonable. Freon has a higher dipole moment, but that appears to have little influence on the surface interaction. This suggests that the nature of the adsorption is non-specific, and that the adsorbent is relatively passive. It is also possible that the Freon interaction is very strong on a local level. This interaction may be so localized that there is no overall orientation effect.

The pore-volume distributions for PSOC-190 are shown in Figure 2.17. Here,

the nitrogen and argon distributions differ for the same reasons as described above. Freon, on the other hand, gives a much larger total pore volume. It appears as though Freon has a strong specific interaction with the coal. This may lead to orientation of the adsorbate, which in turn may lead to enhanced adsorption.

The modelless method was applied only to the nitrogen isotherms. The resulting distributions are shown along with those of CI (Figures 2.18-2.20). Recall that the hydraulic core radii calculated by the method were augmented by the adsorbed layer thickness as calculated by the Halsey equation. The two methods cannot be directly compared, because CI has assumed a cylindrical pore geometry, while the modelless method uses a hydraulic radius. Since the hydraulic radius of a cylinder is half of its radius, the radii from the modelless method could be multiplied by two to obtain some type of comparison.

Microporosity Analysis

The v-t plots for nitrogen on the porous solids are shown in Figure 2.21. The slope for the alumina (for t=3 to 5 Å) gave an area of 211 m^2/g, which was quite close to the BET area. The v-t plot gave an area of 34 m^2/g for the PSOC-190. This area was significantly higher than the corresponding BET area. This is an unusual case, where the two methods do not agree even though the v-t plot does not show significant microporosity.

The area for the char had to be estimated from the slope of a line passing through the origin tangent to the plot. This resulted in an area of 750 m^2/g, which was much greater than the nitrogen BET area.

The v-t plots show that only the char has significant microporosity. Therefore,

the MP analysis was applied only to the char. The result is shown in Figure 2.22. According to this analysis, a vast majority of pores have radii between 3.5 and 5 Å. This is consistent with the pseudo type I isotherm obtained for this material.

The DRK Theory was applied to the isotherms of carbon dioxide at 298K (see Figure 2.23). Strictly speaking, this theory was developed for carbonaceous solids with micropores. Since the assumptions are not too stringent, the theory was applied to the alumina as well. The plot for PSOC-190 was quite linear; those for γ-alumina and oxidized char were less so. The region of lower log$N$ was used in the calculation of specific area. The areas calculated by this method were: 161 m^2/g for alumina, 1400 m^2/g for char, and 162 m^2/g for PSOC-190. The values for γ-alumina and PSOC 190 are similar to those calculated from the BET method for CO_2 at 196K. The area for char is extremely high.

The Medek method was applied to these isotherms in addition to those of Freon. Figures 2.24-2.25 show the results of the Medek method CO_2 and Freon on the porous solids. The form of the curve is the same in all cases; only the magnitude and position of the maxima are different.

DISCUSSION

For the materials studied, the continuous flow method gives isotherms similar to those obtained by the traditional method in a fraction of the time. Some discrepancies were noted, however. These were due to non-equilibartion of the gas phase with the adsorbed phase.

The adsorptives used in this study were selected because of their different molecular characteristics. Nitrogen, generally regarded as the "standard adsor-

bate," is non-polar and axially symmetric. Argon, another commonly used adsorptive, is also non-polar, but is spherically symmetric. Carbon dioxide has a strong quadrupole, and is easily polarizable. Freon is larger than the others, and possesses a permanent dipole.

In spite of these differences, there was little effect on the overall form of the isotherm for a given adsorbent. The only significant exceptions were Freon on char and carbon dioxide on PSOC-190. The Freon isotherm was not nearly as steep as the others at low pressure. This was probably due to slow diffusion of large Freon molecules into the small micropores, as explained above. The large amount of carbon dioxide adsorbed on the raw coal was likely due to specific adsorbate-adsorbent interaction, the small minimum dimension of the carbon dioxide molecule, and the higher temperature at which adsorption took place.

The areas calculated for the microporous char are rather questionable. The models used assume that the adsorbate molecule sits on a locally flat surface. However, when a molecule is in a pore that has a diameter on the order of molecular dimensions, it will cover a much larger area. The discrepancy between the nitrogen and argon areas shows that the way in which the molecules are packed into the pores is an important consideration.

It was interesting that the DRK model gave an area for γ-alumina that was consistent with the other methods. As previously mentioned, the model was developed from a theory of micropore adsorption. The v-t method indicated that the alumina has few micropores, but the alumina is rich in oxygen. It is possible that the carbon dioxide interaction with oxygen-containing groups is similar in magni-

tude to its interaction with the walls of a micropore. That the total area obtained by this method is close to those of the others may be fortuitous.

The Medek method gave curves that appeared to be self-similar for all adsorbents and adsorptives. Furthermore, it showed significant microporosity for the alumina, which is rather questionable. It appears that this method simply transforms a given isotherm into a log normal curve.

Alumina is the most studied and relatively "well-characterized" materials of the solids considered in this study. Using the present experimental findings, conclusions can be drawn regarding its morphology based on a "unified" analysis of surface area, pore volume and pore volume distribution. The BET surface area was around 200 m^2/g for all gases except argon, which gave a lower value, possibly because of non-equilibration effects. The v-t plot gave a surface area that was very close to the BET values; it also indicated an absence of micropores. While the Medek method gave a micropore distribution, its validity is doubtful.

Considering the similarity of the nitrogen and Freon CI pore-volume distributions, they are likely to give a reasonable picture of the true porosity. The modelless method is difficult to interpret without having some idea about pore shape. Unfortunately, it is difficult to infer anything about pore shape without a desorption isotherm.

The partially oxidized synthetic char is not a common material, but it gives isotherms similar to many other microporous substances, like molecular sieves or activated charcoals. In this case, the micropores were large enough so that diffusion of adsorbate into the pores was not an issue. Not surprisingly, the lack of larger

pores precluded the use of CI and YZ. The MP method gave what appears to be a reasonable distribution for the micropores. The Medek method gave distributions with much larger pore volumes and radii.

The PSOC-190 is a typical bituminous coal. As with many raw coals, reliable determination of particle morphology is difficult at best. The existence of micropores that are of the order of molecular dimensions causes molecular sieve effects to be extremely important. Also, diffusion into pores of this size may be via an activated process. To counter these effects, an adsorptive with small minimum molecular dimension and high critical point is generally used for determining the isotherm. Anderson *et al.* (1965) suggest that carbon dioxide at 196 or 298K is the adsorptive of choice for these materials. However, applying the BET analysis to the carbon dioxide isotherm (196K), it is seen that, while the adsorptive uptake is quite high, the C value is quite small (Table 2.2). Since the C value indicates the strength of the gas-solid interaction, the only conclusion that can be drawn is that CO_2 adsorbs strongly on itself.

CONCLUSIONS

Examination of the isotherms shows that the form of the isotherm is essentially independent of the type of adsorptive (for the small molecules used here) for a given solid.

The BET areas were generally consistent with areas calculated by other methods for non-microporous solids. When micropores are present, the agreement was not as good. Of course, interpretation of area on this level is fraught with uncertainty.

The equivalent methods of CI and YZ appear to be the most suitable means of obtaining pore-volume distributions in the mesopore range. The modelless method is also quite useful; however, additional information regarding pore shape must be obtained in order to formulate a reasonable picture of the internal structure.

The MP analysis is the method of choice for pore-volume distributions in the micropore range. The Medek method is somewhat questionable.

ACKNOWLEDGEMENTS

This work was supported by DOE Grant No. DE-AC2284FC70915.

2.3 Mercury Porosimetry

Mercury does not wet most substances, so it demonstrates capillary depression in pores of these substances. As a result, pressure must be applied to force mercury into these pores. Washburn (1921) developed the relationship between the radius r of pore intruded by mercury (assuming cylindrical pores) to applied pressure P:

$$r = -2\gamma \cos\theta / P, \tag{2.18}$$

where γ is the surface tension of mercury and θ is the angle of contact. Usually, γ is taken as 480 dyne/cm and θ is around 140°. Scholten (1967) has shown that various workers have obtained different values for these quantities on different solids. For carbon, θ may be as high as 155°(Lowell (1982)). There is some question as to whether these values are valid in the smallest pores (Kiselev (1958)).

Cumulative pore volume is measured as a function of applied pressure. Using the Washburn Equation (2.18), total volume intruded is obtained as a function of pore radius. Differentiation of this curve yields a pore-volume distribution.

2.3.1 Experimental Apparatus

The apparatus used for this series of experiments was an Autoscan-33 porosimeter manufactured by Quantachrome Corporation. It is capable of generating pressures up to 33000 psi in its high-pressure cavity. This corresponds to a pore radius of approximately 32 Å.

The porosimeter has a companion mercury-filling apparatus. Here, the sample is outgassed to a pressure of less than 100 μm Hg. The sample tube is then filled with mercury and weighed. The volume of mercury in the tube can be easily found

from the density of mercury at that temperature. The difference of the volume of the tube (measured in the same way) and the volume of the mercury is the volume of the sample not penetrated by mercury. From this, particle density can be calculated.

The filled sample tube is then placed in the high- pressure cavity. The porosimeter pressurizes to 33000 psi in about ten minutes; depressurization takes the same amount of time. Volume is plotted versus applied pressure on an X-Y recorder.

2.3.2 Interpretation of Results

Figure 2.26 shows a trace of pressure versus volume for 0.2581g of a lignite coal (PSOC 1443). The solid curve is obtained from pressurization, while the dashed curve is from the depressurization part of the cycle. The depressurization curve does not retrace the path from the first half of the cycle; this is known as hysteresis. Not all of the mercury extrudes; this is known as entrapment. In most cases, subsequent intrusion-extrusion cycles result in little additional entrapment.

As previously mentioned, pore-volume distribution plots are obtained by differentiation of the cumulative volume versus pore-radius curve. The pore-volume distributions shown in Figure 2.27 were derived in this manner from the raw data in Figure 2.26.

It must be pointed out that compressibility of the solid has not been accounted for. Scholten (1967) suggests a value of 10^{-11} cm^2/dyne for raw coal. This would account for a significant amount of "intrusion" above 25000 psi. Note also that the pore volume distributions shown here are based on the assumption that the pores are non-intersecting cylinders. The porosity in most substances is not so ideal.

Hysteresis has been used as a qualitative measure of non-ideality of pore structure. It was generally believed that "ink bottle" pores were the cause of hysteresis. Relatively high pressure would be required to penetrate the neck of the pore; extrusion would not occur until a significantly lower pressure existed in the bulk. However, it is improbable that all substances have this type of porosity.

Lowell and Shields (1981) have shown that hysteresis may be simply accounted for in some cases by adjusting the angle of contact θ so that the extrusion curve retraces the intrusion curve. There is evidence to support the idea that advancing and receding contact angles are different (Penn and Miller (1980)). While this may eliminate much of the disparity between intrusion and extrusion curves, it will generally fail to eliminate it completely; furthermore, entrapment remains unaccounted for.

Several explanations of the phenomenon of entrapment have been put forth. For example, Kamakin (1961) suggested that very long equilibration times are required for extrusion from pores that are less than 75 Å in radius. Lowell (1980) has proposed that mercury columns may break because of potentials existing in the fine pores.

Entrapment may also be explained by merging of opposing menisci. This may be particularly true for granular materials, which have a significant volume of interparticle voidage. If these voids are completely filled, no menisci will be present. Thus, there would be no means by which the mercury could be pushed back out, even at the lowest pressures. Since different materials trap different amounts of mercury, entrapment data should be used to aid in the characterization of the solid.

Entrapment data are easily obtained by performing a second intrusion. The difference between the first and second intrusion curves yields the volume of mercury entrapped as a function of pressure. Figure 2.28 compares the pore-volume distributions derived from the first and second intrusion curves for this sample. There is significant entrapment over the entire range of pore sizes, particularly in the largest voids. These voids probably represent space between particles. It is possible that the porous structure of the material was altered after the first intrusion, as Sarakov (1963) has shown that certain porous carbons may be damaged upon pressurization.

The second intrusion curve represents the porosity in which "reversible" intrusion and extrusion take place. Figure 2.29 shows the pore-volume distributions from the first extrusion and subsequent intrusion. The intrusion curve shows greater porosity in the 1000 Å range, while the extrusion curve displays higher pore volume in the 50000 Å range.

Mann *et al.* (1980) developed a two-dimensional random network model to predict pore-volume distributions based on mercury porosimetry. Pores of differing radii but of equal length are placed in a grid. A simulation is carried out whereby increasing pressure is applied to the mercury, causing it to penetrate smaller and smaller pores. Extrusion is also simulated. These simulations are carried out on different grids until the experimental traces are matched. The advantage of this model is that it predicts hysteresis and entrapment. The disadvantage is that there is no systematic means of obtaining the appropriate network. Because of this limitation, it will not be considered further.

Kadlec (1984), working from the Gibbs condition of thermodynamic equilibrium, has shown that micropores (pore radii 8-12 Å) may fill by a vapor transfer mechanism at the same time at which transitional pores (pore radii 20-100Å) are filling with liquid. The consequence of this is that the amount of transitional porosity is overestimated.

2.4 Conclusions

The result of these considerations is that because of the uncertainties involved in the interpretation of these characterization experiments, it is not possible to obtain a true picture of the solid on a microscopic level. However, the surface areas and pore-volume distributions obtained from these methods are useful for comparing solids of similar nature.

REFERENCES

Anderson, R. B., Bayer, J. and Hofer, L.J.E. (1965). Determining Surface Areas from CO_2 Isotherms. *Fuel*, **44**, 443.

Anson, D., Moles, F.D., and Street, P.J. (1971). Structure and Surface Area of Pulverized Coal During Combustion. *Comb. Flame*, **16**, 265.

Bosch, H. and Peppelenbos, A. (1977). Automatic and Low-Cost Determination of BET Surface Areas. *J. Phys. E. Sci. Instr.*, **10**, 608.

Brunauer, S., Emmett, P.H., and Teller, E. (1938). Adsorption of Gases in Multimolecular layers. *J. Am. Chem. Soc.*, **60**, 309.

Brunauer, S., Demming, L.S., Demming, W.S. and Teller, E. (1940). On a Theory of the van der Walls Adsorption of Gases. *J. Amer. Chem. Soc.*, **62**, 1723.

Brunauer, S., Mikhail, R.S. and Bodor, E.E. (1967). Pore Structure Model Without a Pore Shape Model. *J. Coll. Int. Sci.*, **24**, 451.

Cranston, R. and Inkley, F. (1957). The Determination of Pore Structures from Nitrogen Adsorption Isotherms. *Adv. in Cat.*, **9**, 143.

Debelak, K.A. and Schrodt, J.T. (1979). Comparison of Pore Structure in Kentucky Coals by Mercury Penetration and CO_2 Adsorption. *Fuel*, **58**, 732.

Dollimore, D. and Heal, G.R. (1964). An Improved Method for the Calculation of Pore Size Distribution from Adsorption Data. *J. Appl. Chem.*, **14**, 109.

Dollimore, D., Rickett, G. and Robinson, R. (1973). The Design and Operation of a Simple Volumetric Adsorption Apparatus. *J. Phys. E. Sci. Instr.*, **6**, 94.

Gregg, S.J. and Sing, K.S.U. (1982). *Adsorption, Surface Area and Porosity*, Academic Press, New York.

Halsey, G.D. (1948). Physical Adsorption on Non-Uniform Surfaces. *J. Chem. Phys.*, **16**, 931.

Innes, W.B. (1951). Apparatus and Procedure for Rapid Automatic Adsorption, Surface Area and Pore Volume Measurement. *Anal. Chem.*, **23**, 759.

Kadlec, O. (1984). The General Equation of the High Pressure Mercury Porosimetry. *Ads. Sci. Tech.*, **1**, 177.

Kaganer, M. G. (1959). A New Method for Determining the Specific Surface of Adsorbents and Other Finely Divided Substances. *Russ. J. Phys. Chem.*, **33**, 352.

Kamakin, N. N. (1961). In *Methoden de Strukturuntersushung an Hochdispersen und porosen Stoffen.* Akademie-Verlag, Berlin.

Kiselev, A. V. (1958). In *Methods of Investigation of the Structure of Highly Dispersed and Porous Bodies.* USSR Academy of Science Press.

Lange, K. R. (1963). Adsorption Isotherms by a Rapid Flow Method. *J. Coll. Sci.*, **18**, 65.

Lecloux, A. and Pirard, J.P. (1979). The Importance of Standard Isotherms in the Analysis of Adsorption Isotherms for Determining the Porous Texture of Solids. *J. Coll. Int. Sci.*, **70**, 265.

Lippens, B.C., deBoer, J. H. (1965). Studies on Pore Systems in Catalysts V. The t Method. *J. Cat.*, **4**, 319.

Lowell, S. (1980). Hysteresis in Mercury Porosimetry. *Powder Tech.*, **25**, 37.

Lowell, S. (1982). Contact Angle Measurement for Mercury Porosimetry. *Quantachrome Powder Tech. Note*, **15**.

Lowell, S. and Shields, J.E. (1981). Contact Angle in Mercury Porosimetry. *J. Coll. Int. Sci.*, **83**, 192.

Lowell, S. and Shields, J.E. (1984). *Powder Surface Area and Porosity*, Chapman and Hall, New York.

Mahajan, O.P. (1981). Coal Porosity in *Coal Structure*, R. A. Meyers, Ed., Academic Press, New York.

Mann, R., Androutsopoulos, G.P. and Golshan, H. (1980). Application of a Stochastic Network Pore Model to Oil-Bearing Rock with Observations Relevant to Oil Recovery. *Chem. Eng. Sci.*, **36**, 337.

Marsh, H. and Rand, B. (1971). Microporosity in Carbonaceous Materials. *Proc. of Third Conf. on Indust. Carbon and Graphite Soc.*, London, England, 172.

Medek, J. (1977). Possibility of Micropore Analysis of Coal and Coke from the Carbon Dioxide Isotherm. *Fuel*, **56**, 131.

Mikhail, R.S., Brunauer, S. and Bodor, E.E. (1968). Investigations of a Complete Pore Structure Analysis I. Analysis of Micropores. *J. Coll. Int. Sci.*, **26**, 45.

Northrop, P.S., Flagan, R.C. and Gavalas, G.R. (1987). Measurement of Gas Adsorption Isotherms by Continuous Adsorbate Addition. *Langmuir*, **3**, 300.

Penn, L.S. and Miller, B. (1980). Measurement of Advancing and Receding Contact Angles in Mercury. *J. Coll. Int. Sci.*, **77**, 574.

Pierce, C. (1953). Computation of Pore Sizes from Physical Adsorption Data. *J. Phys. Chem.*, **57**, 149.

Pope, C.G. (1984). Lignite Porosity by Kinetics of Gas Adsorption. *Fuel*, **63**, 1681.

Radushkevich, L. V. (1949). A Method for Micropore Volume Determination. *Russ. J. Phys. Chem.*, **23**, 1410.

Reucroft, P.J. and Patel, K.B. (1983). Surface Area and Swellability. *Fuel*, **62**, 279.

Sarakov, A.I. (1963). Some Comments on the Accuracy of the Method of Mercury Porsimetry. *Russ. J. Phys. Chem.*, **37**, 242.

Scholten, J.J.F. (1967). Mercury Porosimetry and Allied Techniques in *Porous Carbon Solids* R.L. Bond, Ed., Academic Press, New York.

Sircar, S. (1985). New Isotherm for Multilayer Adsorption of Vapours on Non-Porous Adsorbents. *Ads. Sci. Tech.*, **2**, 23.

Smith, I.W. and Tyler, R.J. (1972). Internal Burning of Pulverized Semi-anthracite: The Relation Between Particle Structure and Reactivity. *Fuel*, **51**, 312.

Smith, I.W. and Tyler, R.J. (1974). The Reactivity of a Porous Brown Coal Char to Oxygen Between 630 and 1812K. *Comb. Sci. Tech.*, **9**, 87.

Street, P.J., Weight, R.P., and Lightman, P. (1969). Investigations of Structural Changes Occurring in Coal Particles During Heating. *Fuel*, **48**, 343.

Walker, P.L.,Jr. and Kini, K.A. (1965). Measurement of the Ultrafine Surface Areas of Coals. *Fuel*, **44**, 453.

Washburn, E.W. (1921). The Dynamics of Capillary Flow. *Phys. Rev.*, **17**, 273.

Wheeler, A. (1946). *Catalyst Symposium, Gibson Island AAAS Conference.*

Yan, J. and Zhang, Q. (1986). Pore Structure Analysis of Porous Particles by an Equivalent Model. *Part. Charact.*, **3**, 20.

Young, D.M. and Crowell, A.D. (1962). *Physical Adsorption of Gases*, Butterworths, London.

ADSORBATE	SHAPE	σ ($\AA^2$)	α $10^{24}(cm^3)$	μ	q	V_{liq} (cm^3/g mol)	γ (dynes/cm)
N_2	SPHERO–CYLINDRICAL	16.2	1.73	NO	YES	34.65	8.5
Ar	SPHERICAL	14.2	1.62	NO	NO	28.53	14.2
CO_2	SPHERO–CYLINDRICAL	19.5	2.59	NO	YES	36.36	25.7
FREON-21	IRREGULAR	40.0	7.4	YES	YES	73.15	18.0

Table 2.1. Selected properties of adsorptives.

ADSORBATE : NITROGEN

	A_{BET} (m^2/g)	C_{BET}	V_{C-t} (cm^3/g)	V_{M-L} (cm^3/g)	A_{V-t} (m^2/g)	A_{DRK} (m^2/g)
γ-ALUMINA	207	260	0.409		211	
OXIDIZED SYN-CHAR	400	LARGE	0.009		508	
PSOC-190 COAL	23	100	0.043		34	

ADSORBATE : ARGON

	A_{BET} (m^2/g)	C_{BET}	V_{C-t} (cm^3/g)	V_{M-L} (cm^3/g)	A_{V-t} (m^2/g)	A_{DRK} (m^2/g)
γ-ALUMINA	174	52.5	0.546			
OXIDIZED SYN-CHAR	573	LARGE	0.026		714	
PSOC-190 COAL	23	46	0.06			

ADSORBATE : FREON-21

	A_{BET} (m^2/g)	C_{BET}	V_{C-t} (cm^3/g)	V_{M-L} (cm^3/g)	A_{V-t} (m^2/g)	A_{DRK} (m^2/g)
γ-ALUMINA	205	47	0.377			
OXIDIZED SYN-CHAR	433	14	0.206		446	
PSOC-190 COAL	152	8.5	0.162			

ADSORBATE : CO_2 AT 196 K

	A_{BET} (m^2/g)	C_{BET}	V_{C-t} (cm^3/g)	V_{M-L} (cm^3/g)	A_{V-t} (m^2/g)	A_{DRK} (m^2/g)
γ-ALUMINA	200	113	0.166			161
OXIDIZED SYN-CHAR	430	LARGE	0.099		579	1400
PSOC-190 COAL	148	14.3	0.08			162

Table 2.2. Experimental results for various adsorbate-adsorbent pairs.

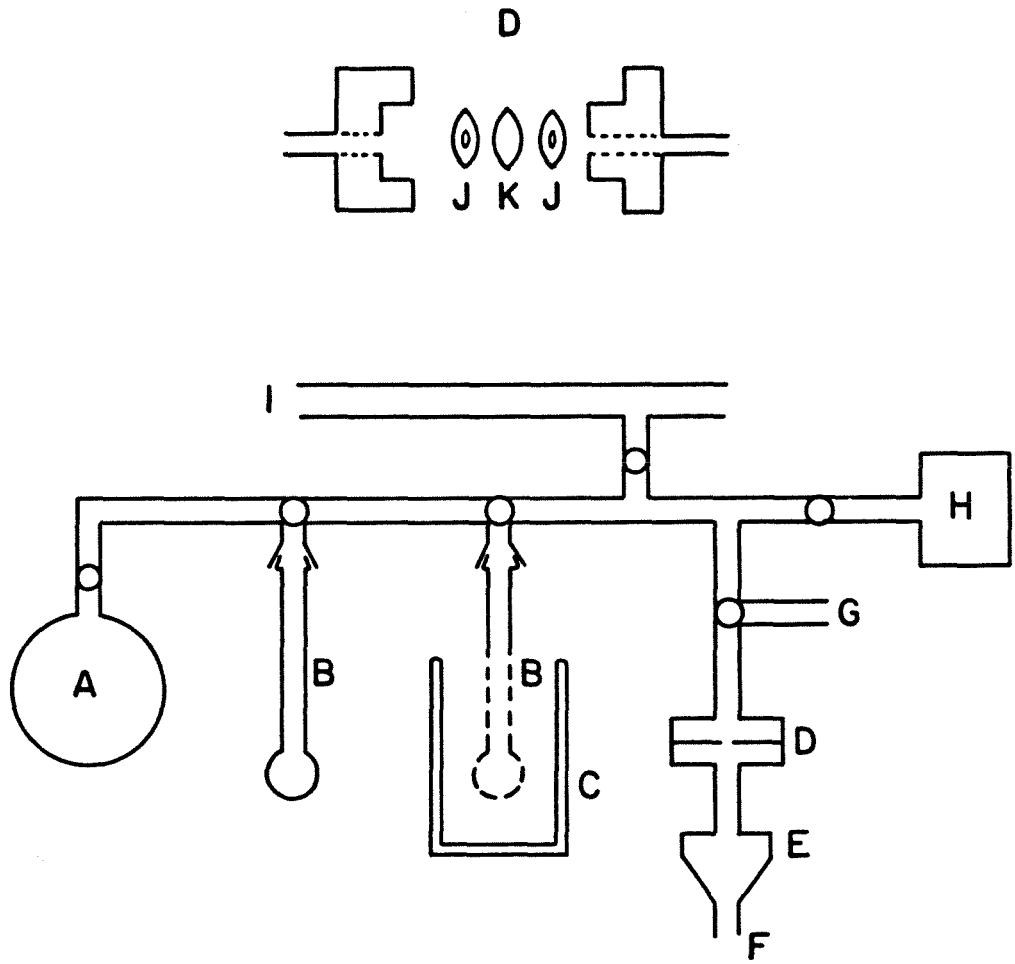

Figure 2.1. Schematic of gas adsorption apparatus.

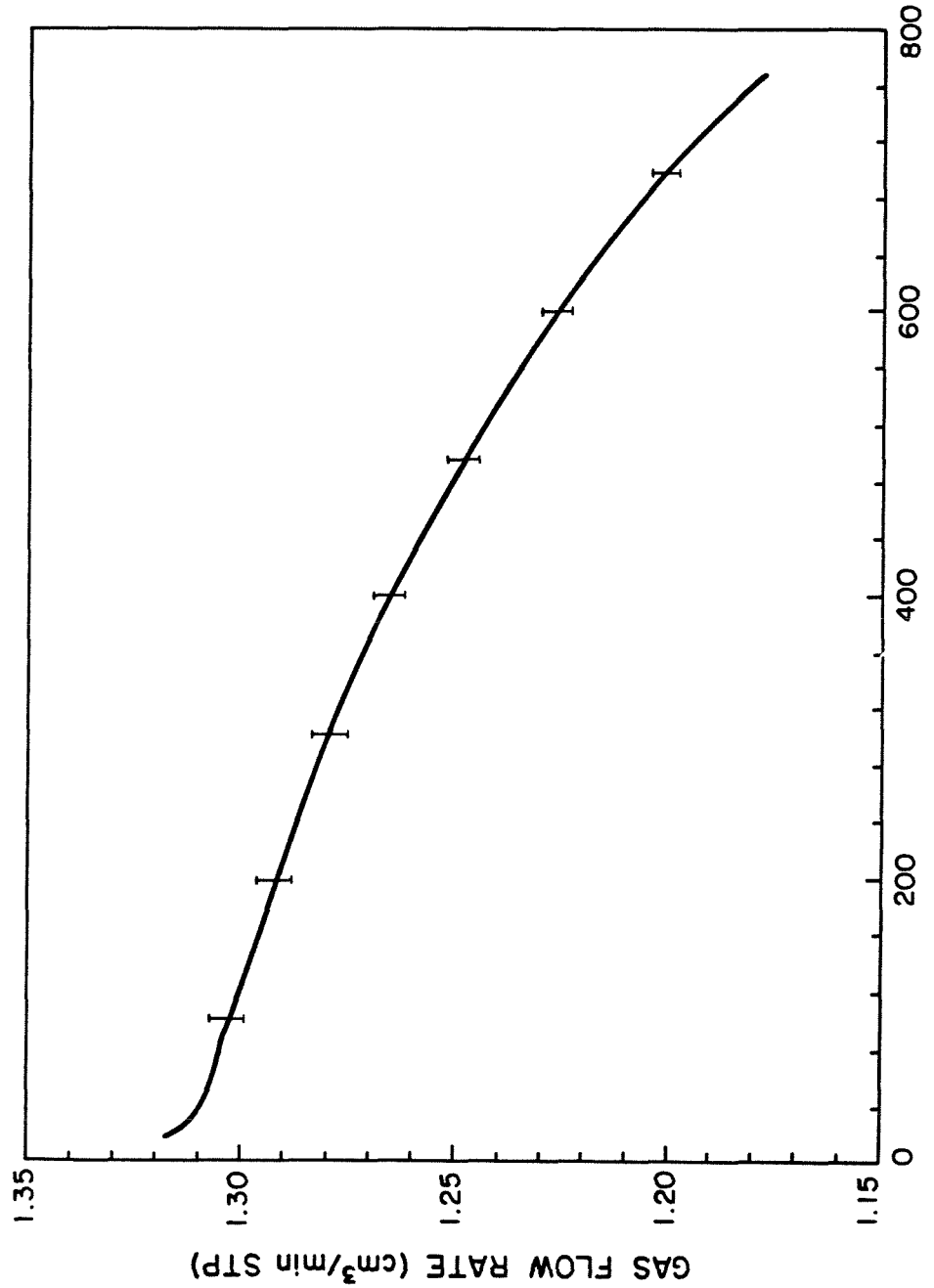

Figure 2.2. Flow rate of nitrogen through a 10 micron orifice at a fore pressure of 0.2 MPa as a function of downstream pressure.

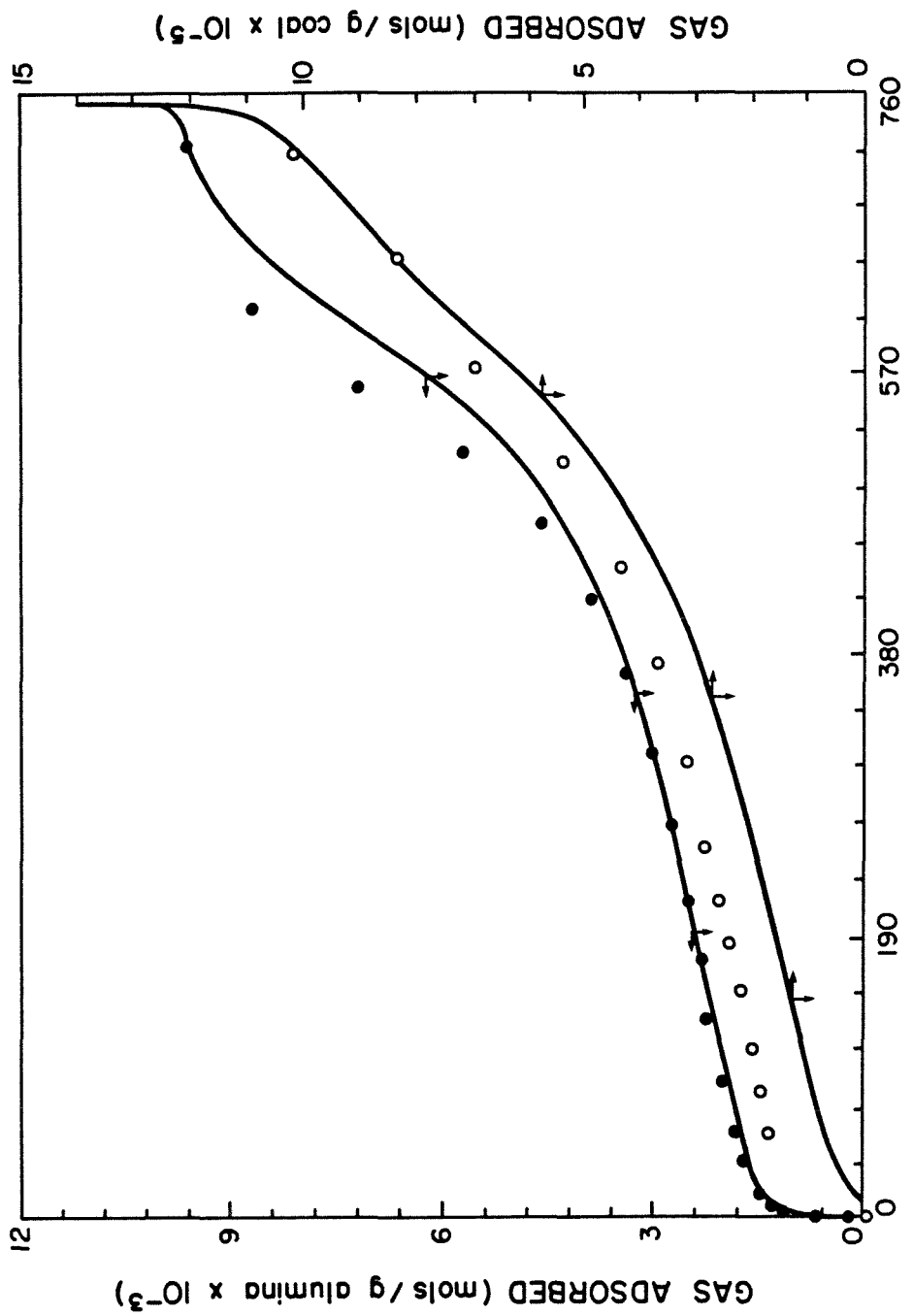

Figure 2.3. Comparison of continuous and traditional isotherms.

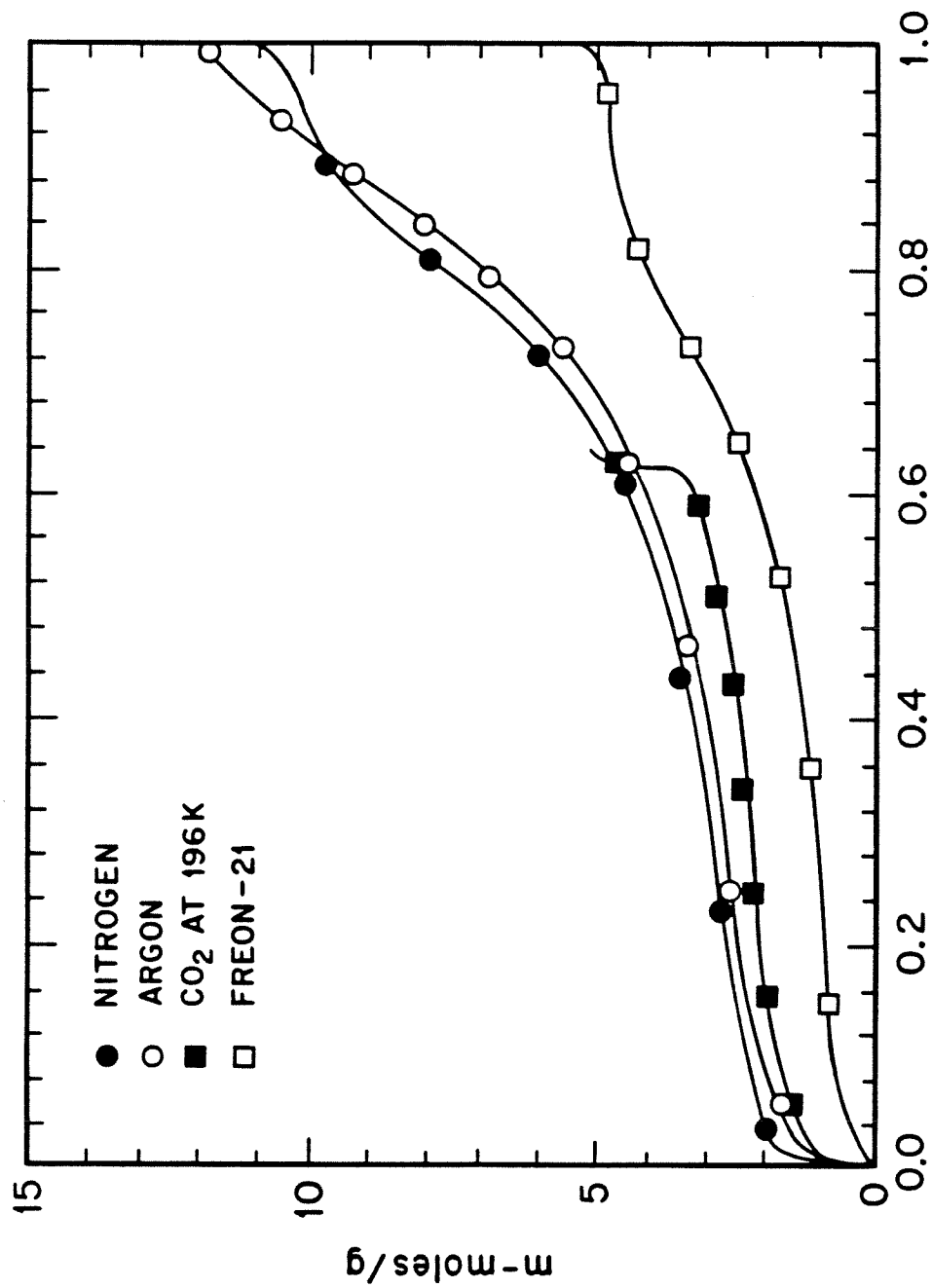

Figure 2.4. Nitrogen, argon, carbon dioxide (196K), and Freon-21 isotherms on γ-alumina.

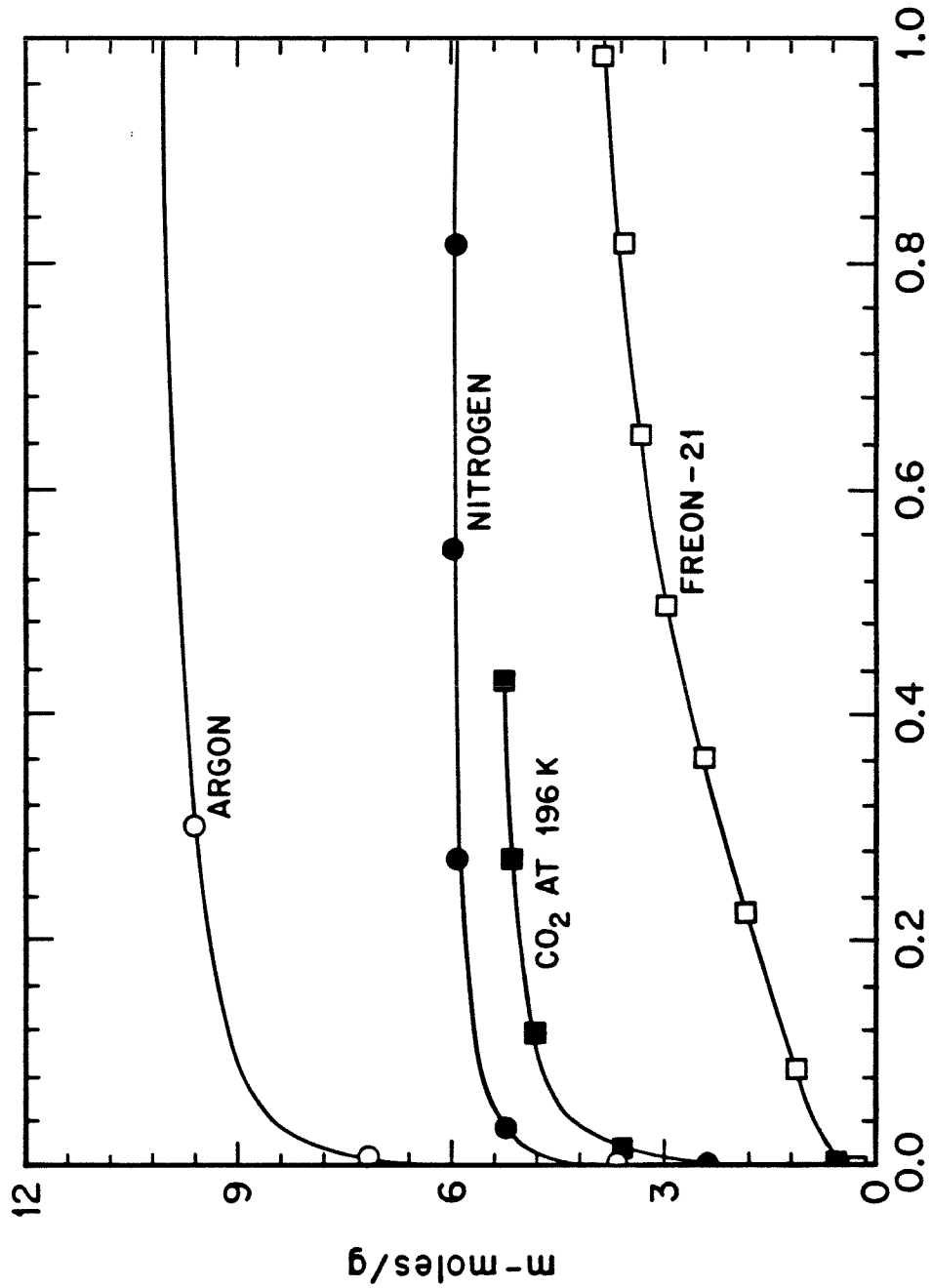

Figure 2.5. Nitrogen, argon, carbon dioxide (196K), and Freon-21 isotherms on oxidized char.

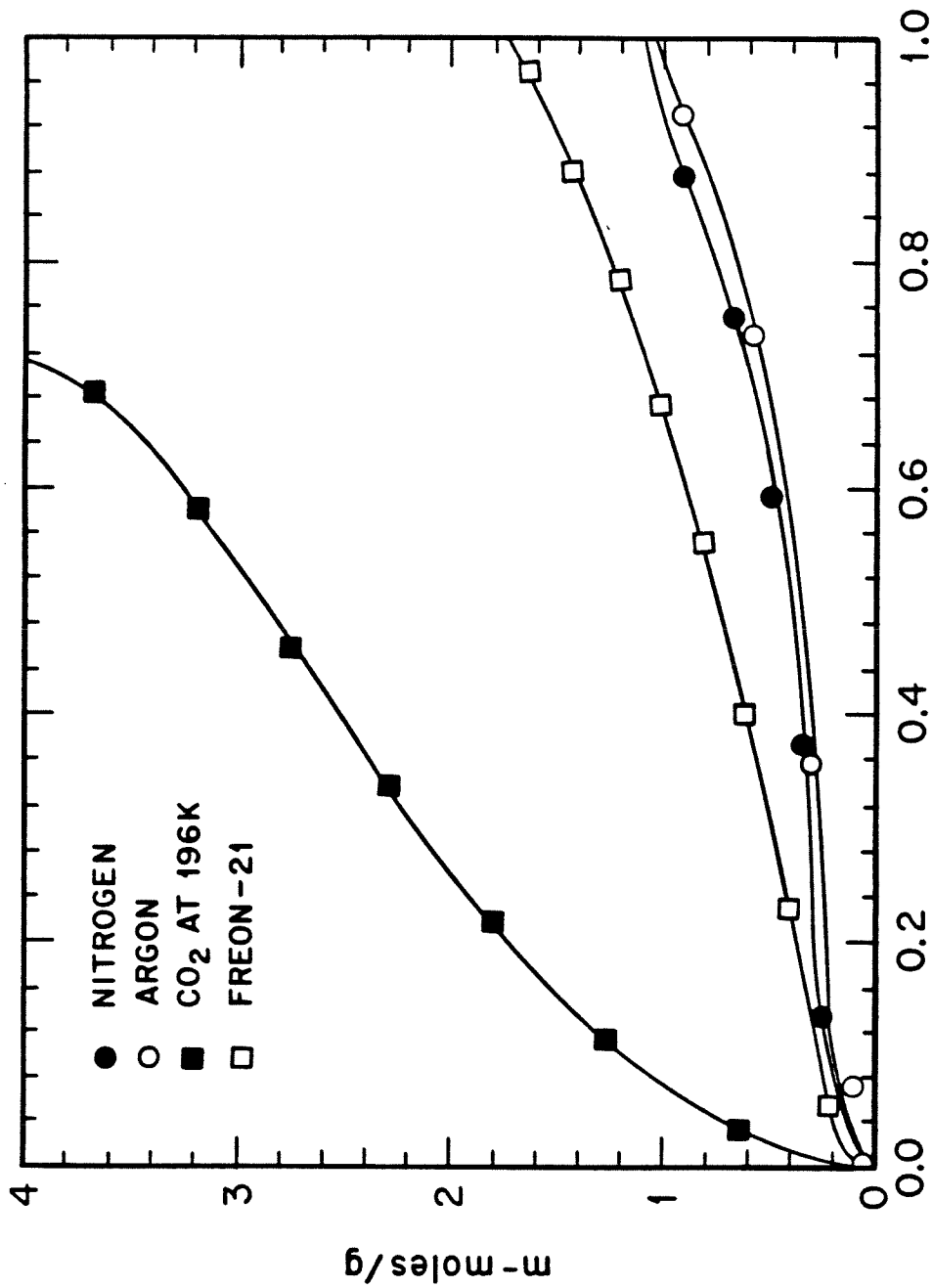

Figure 2.6. Nitrogen, argon, carbon dioxide (196K), and Freon-21 isotherms of PSOC-190 Coal.

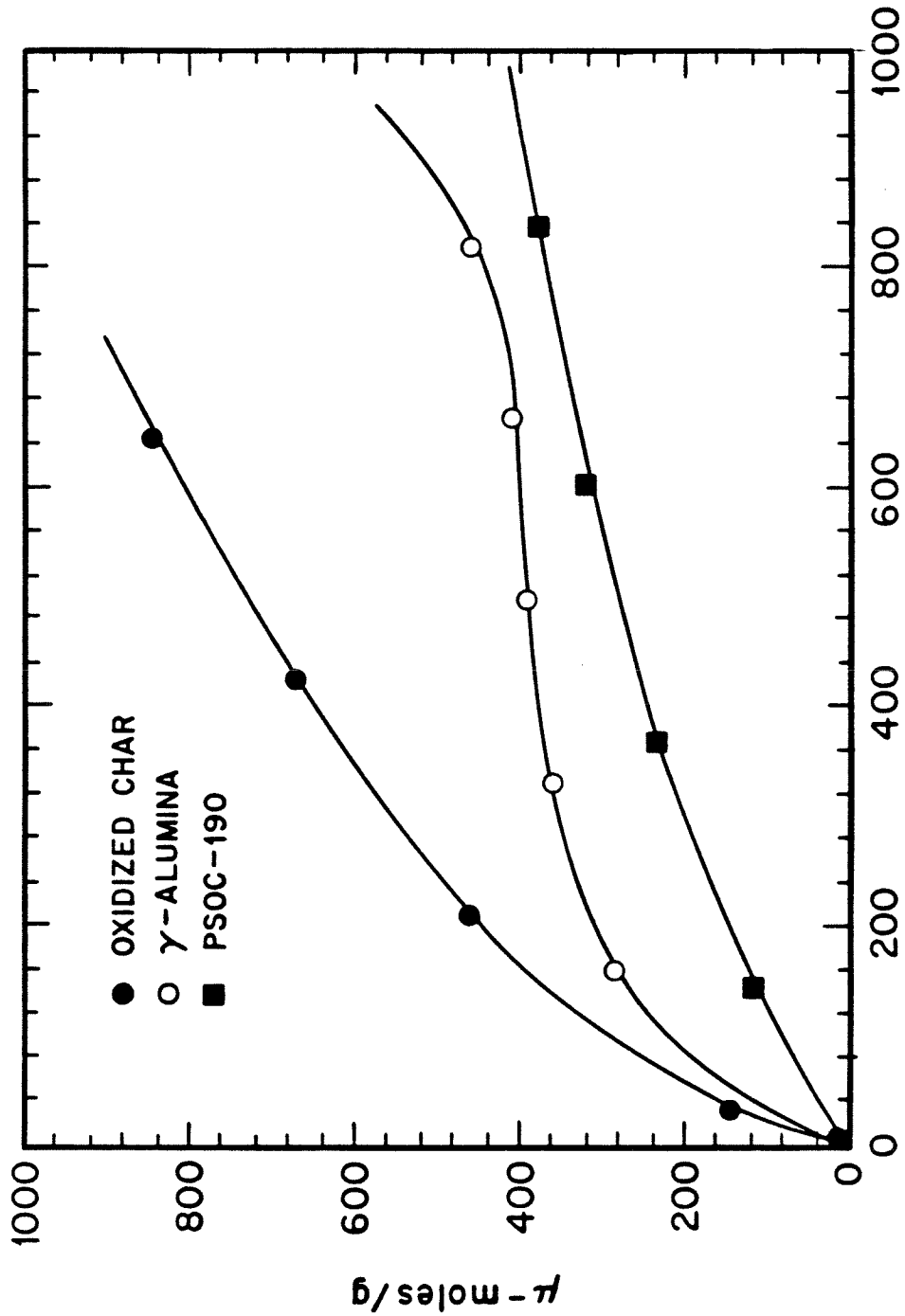

Figure 2.7. Carbon dioxide isotherms at 298K on γ-alumina, oxidized char and PSOC-190.

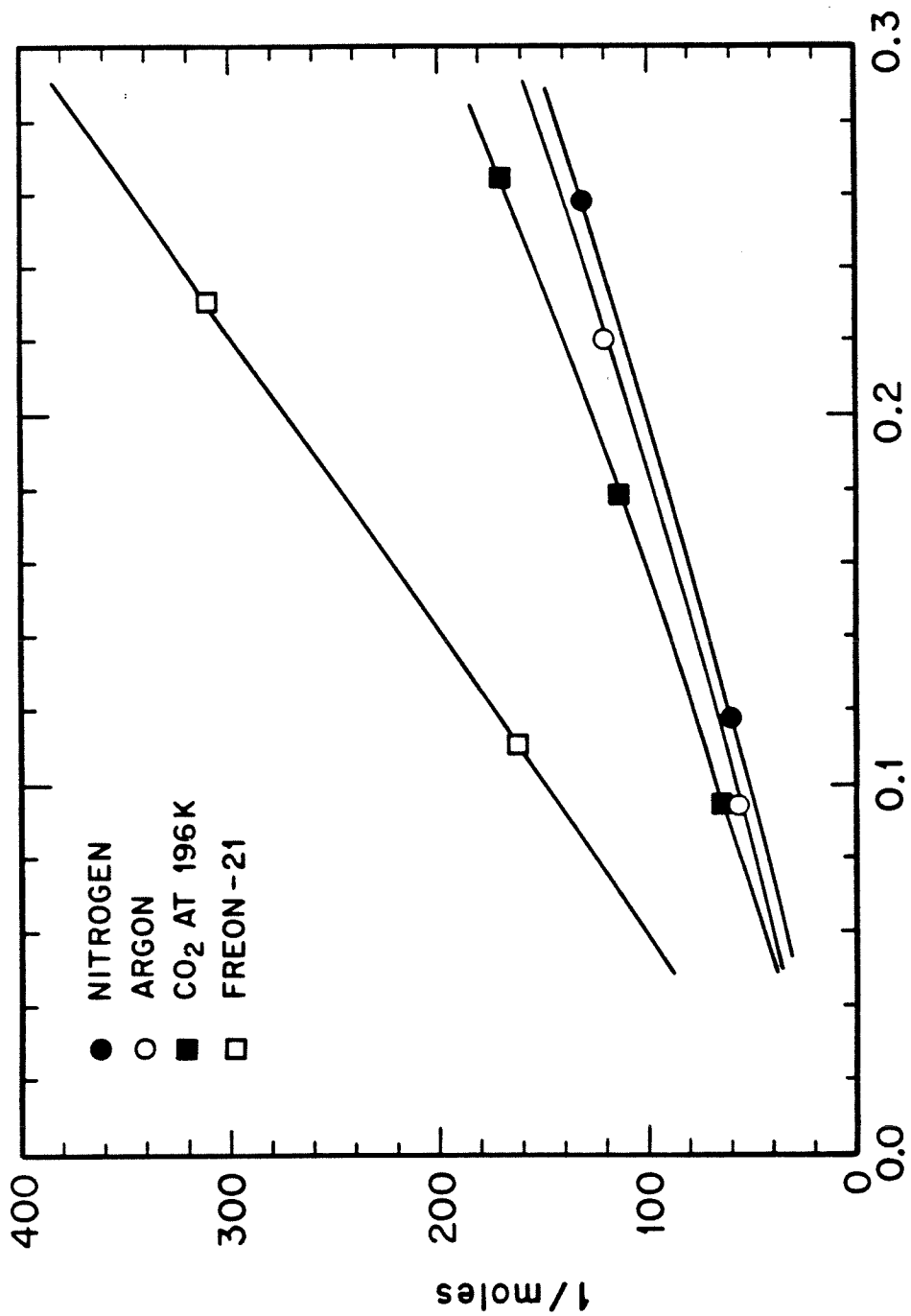

Figure 2.8. BET plots for γ-alumina.

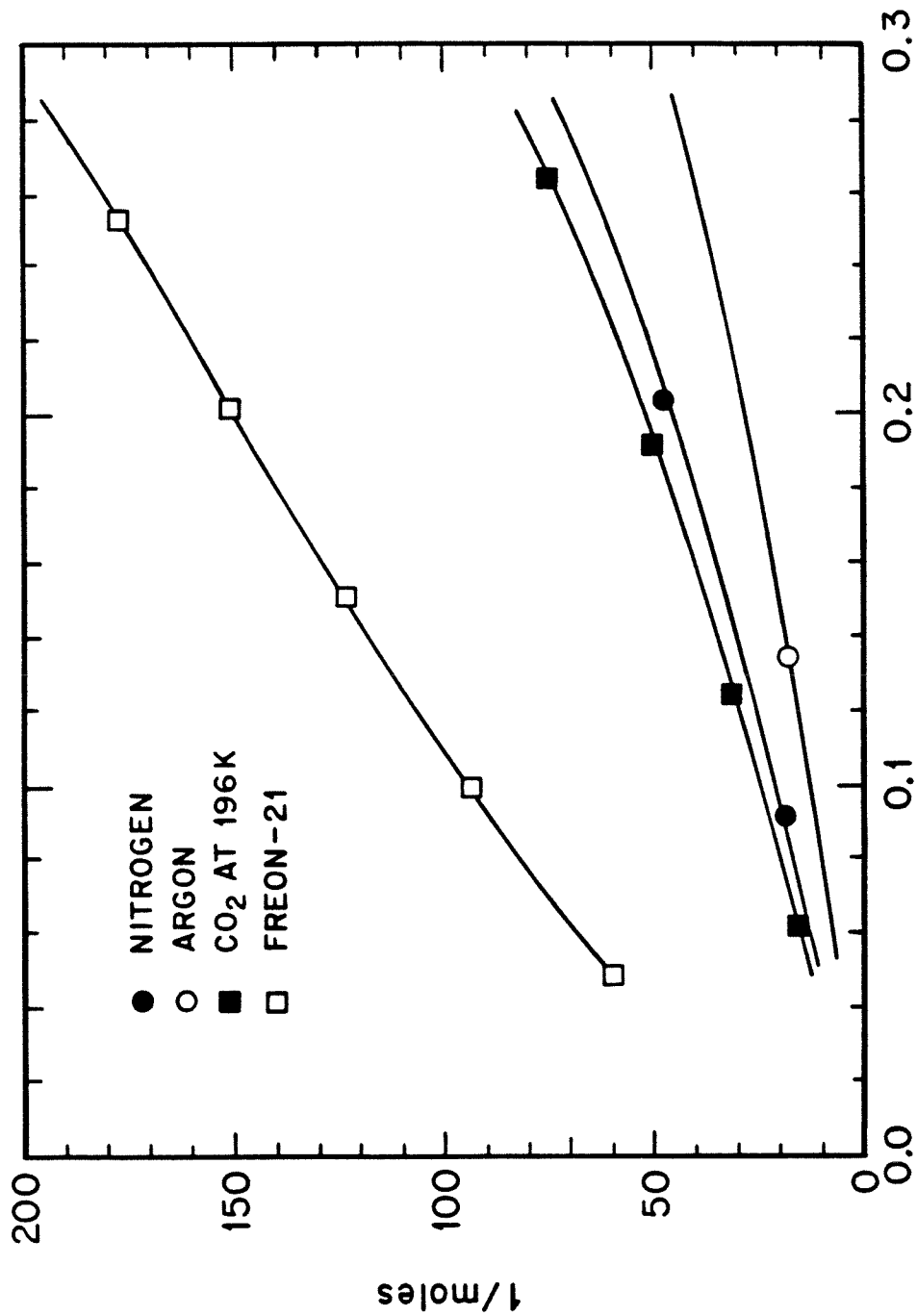

Figure 2.9. BET plots for oxidized char.

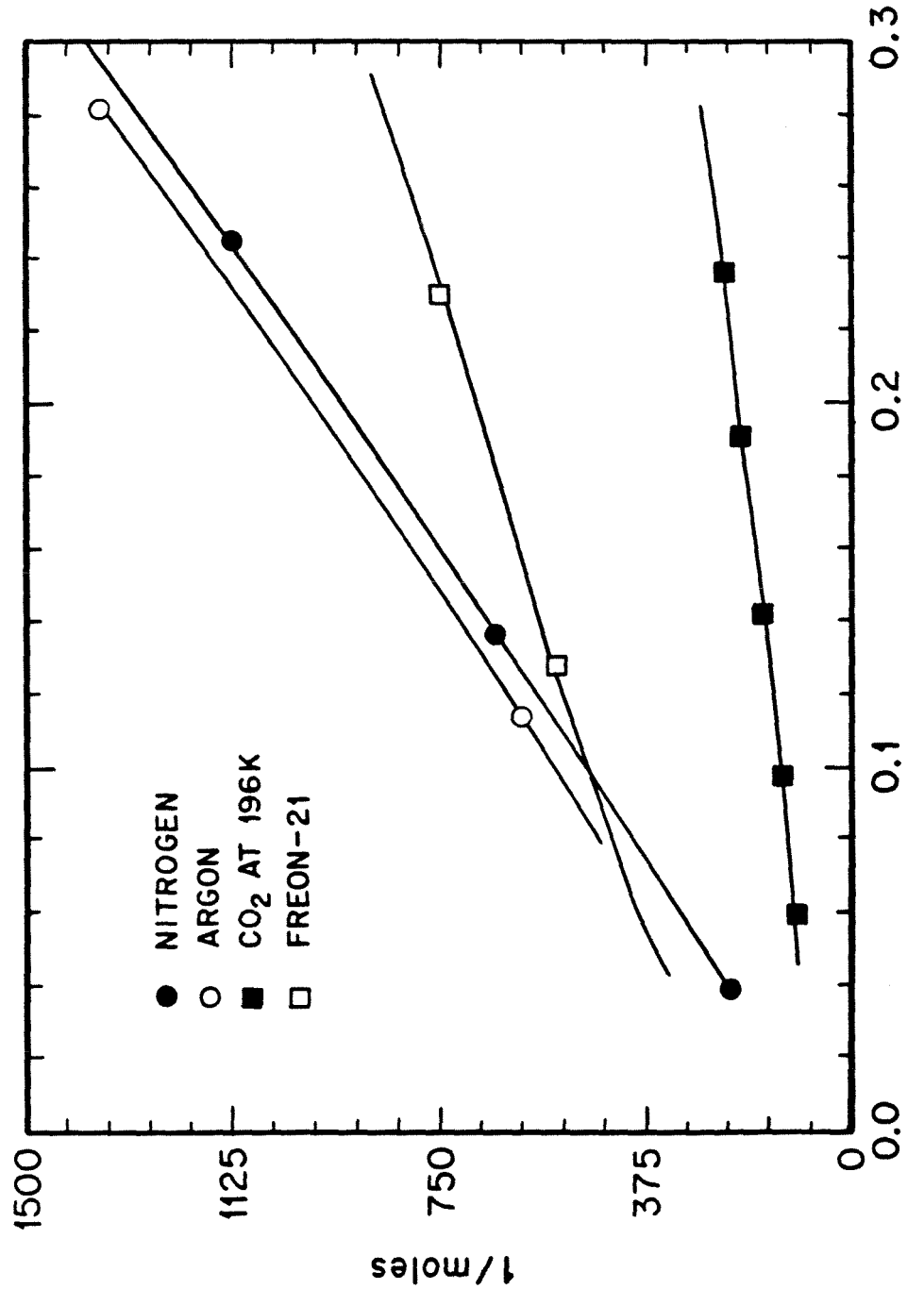

Figure 2.10. BET plots for PSOC-190 coal.

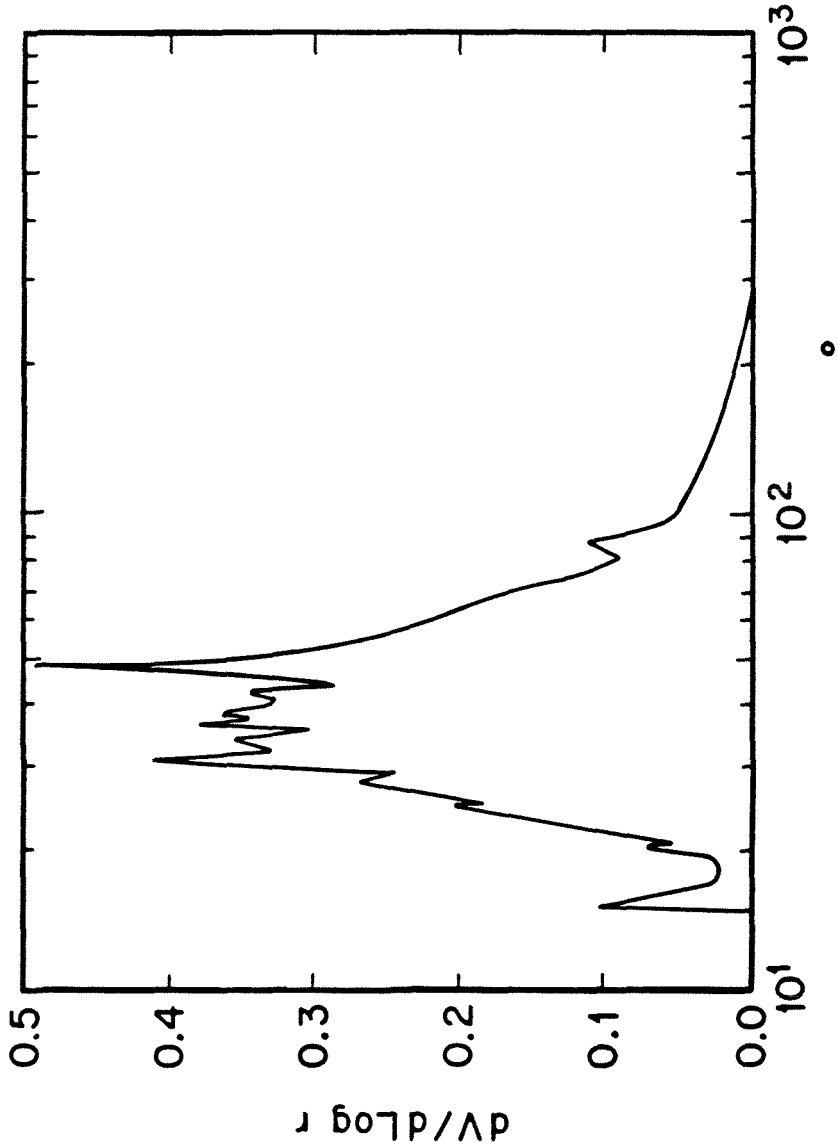

Figure 2.11. Pore volume distribution of γ-alumina from nitrogen: CI with polynomial thickness.

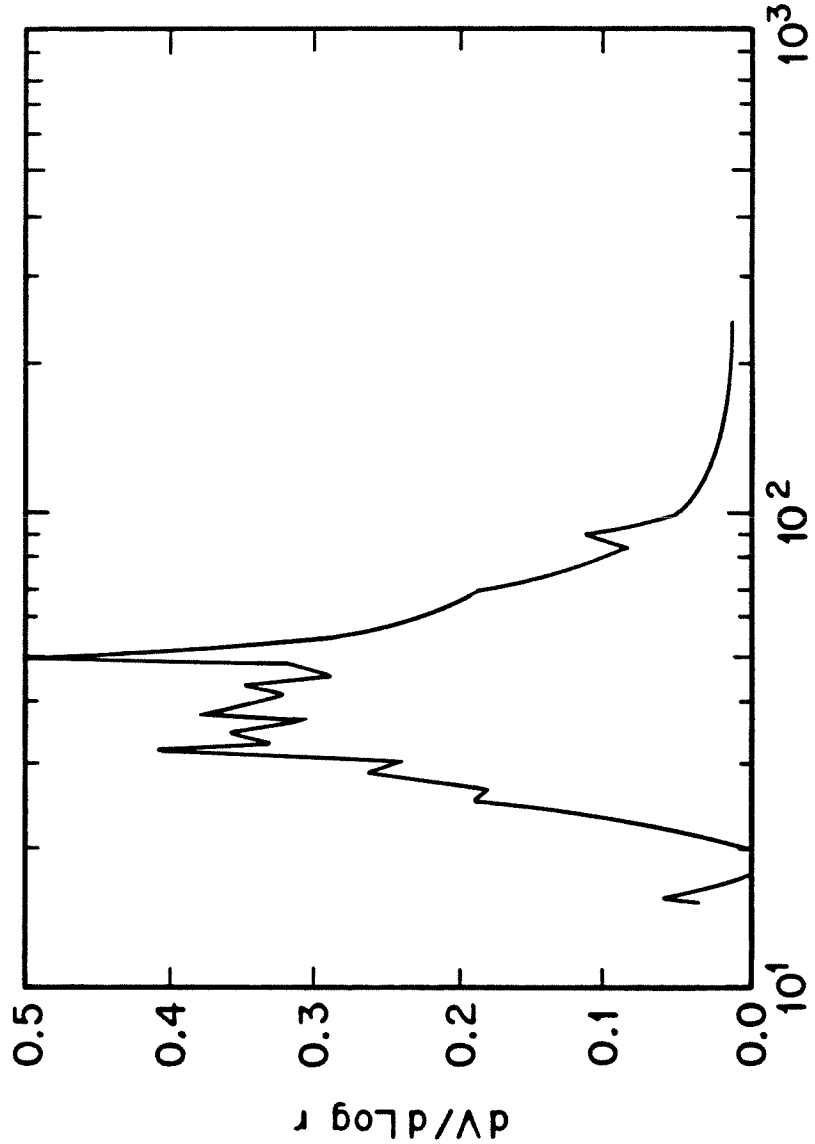

Figure 2.12. Pore volume distribution of γ-alumina from nitrogen: YZ with polynomial thickness.

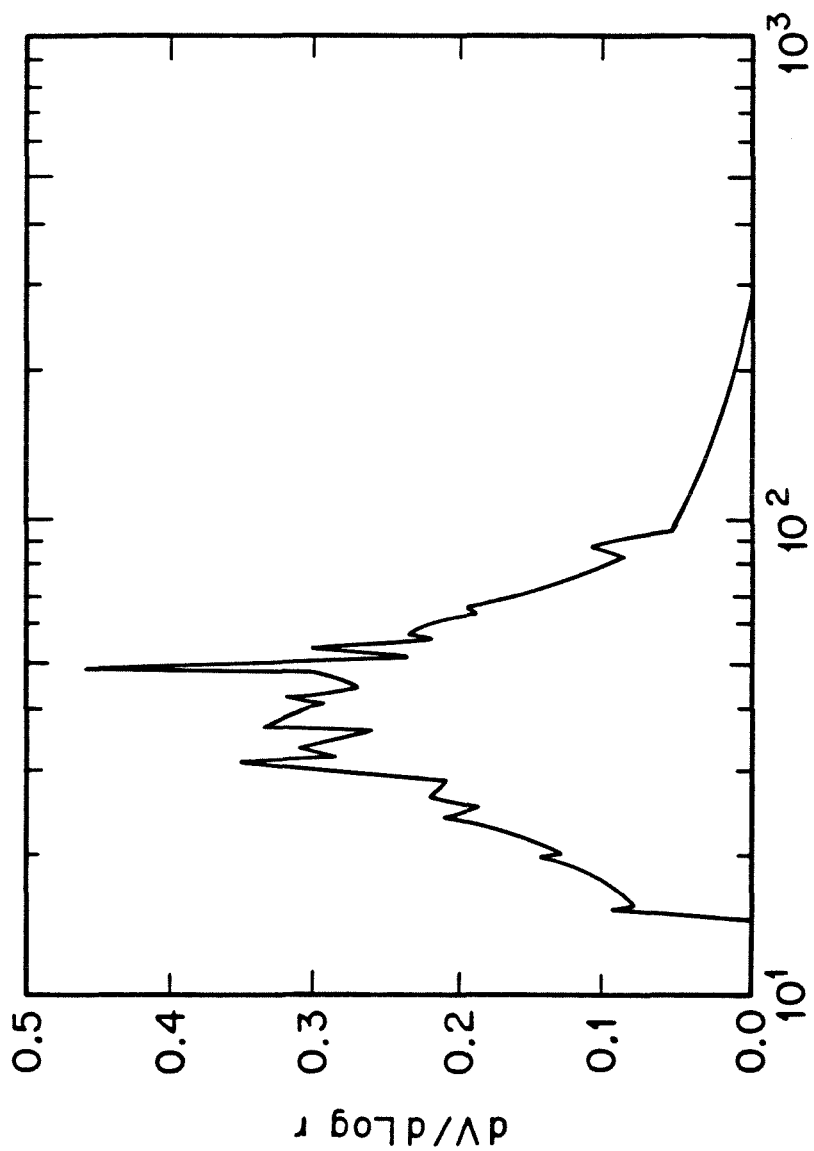

Figure 2.13. Pore volume distribution of γ-alumina from nitrogen: CI with Halsey thickness.

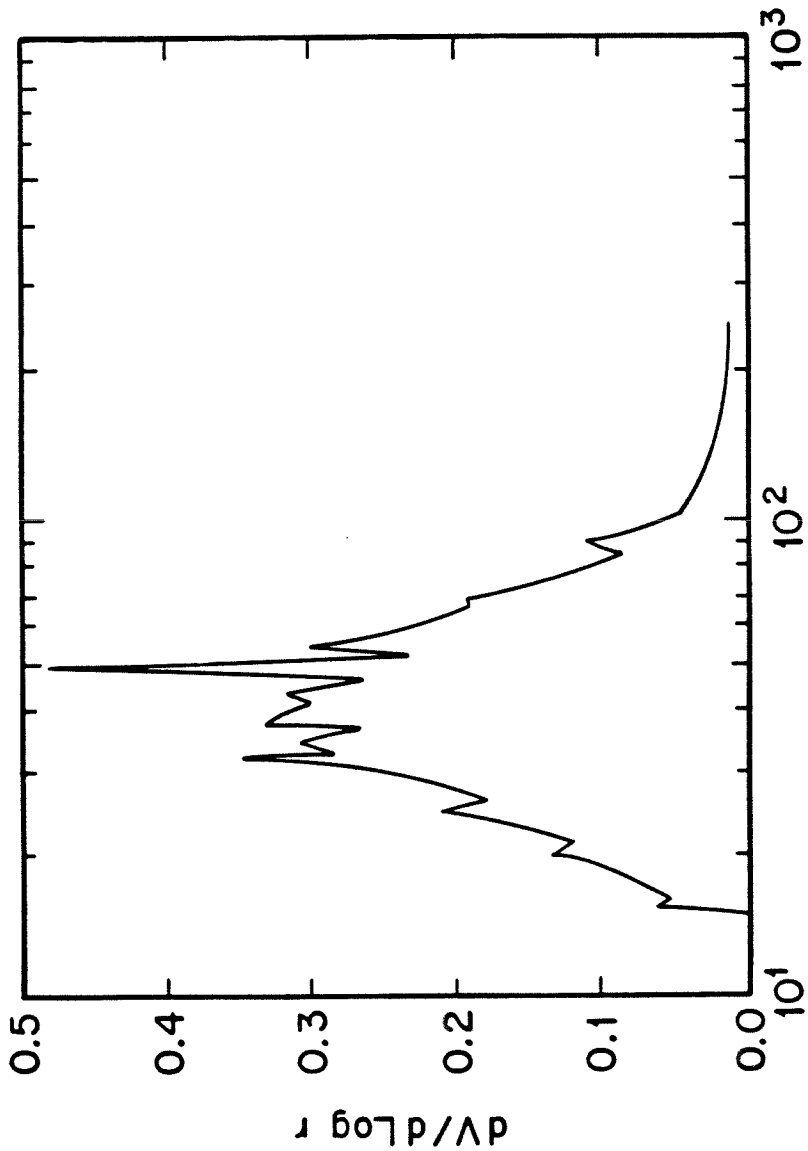

Figure 2.14. Pore volume distribution of γ-alumina from nitrogen: YZ with Halsey thickness.

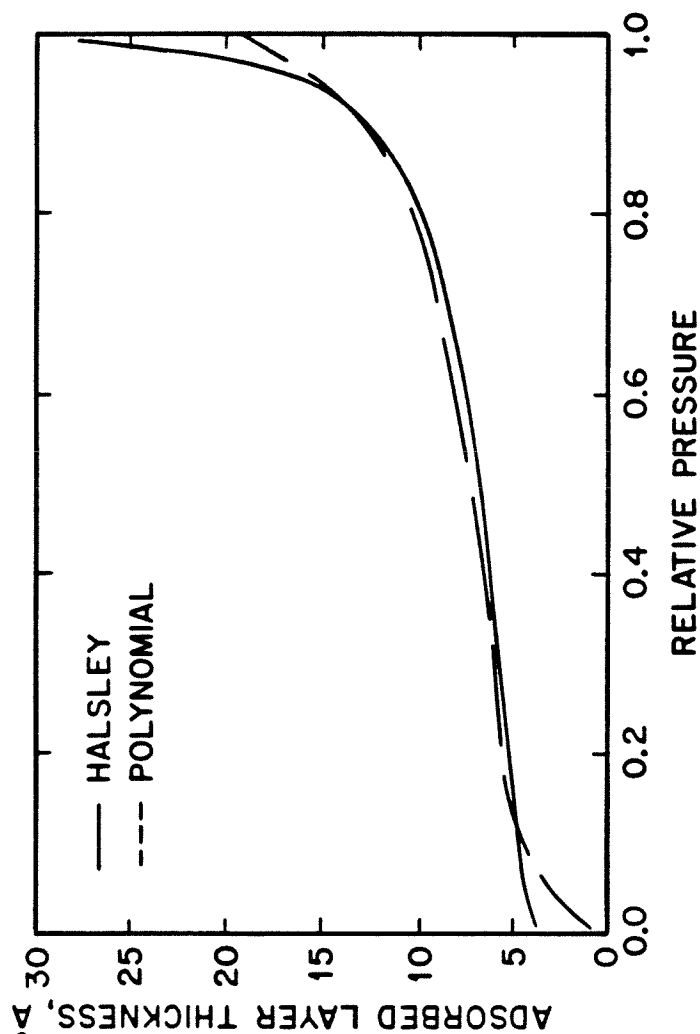

Figure 2.15. Comparision of polynomial and Halsley thicknesses as a function of relative pressure.

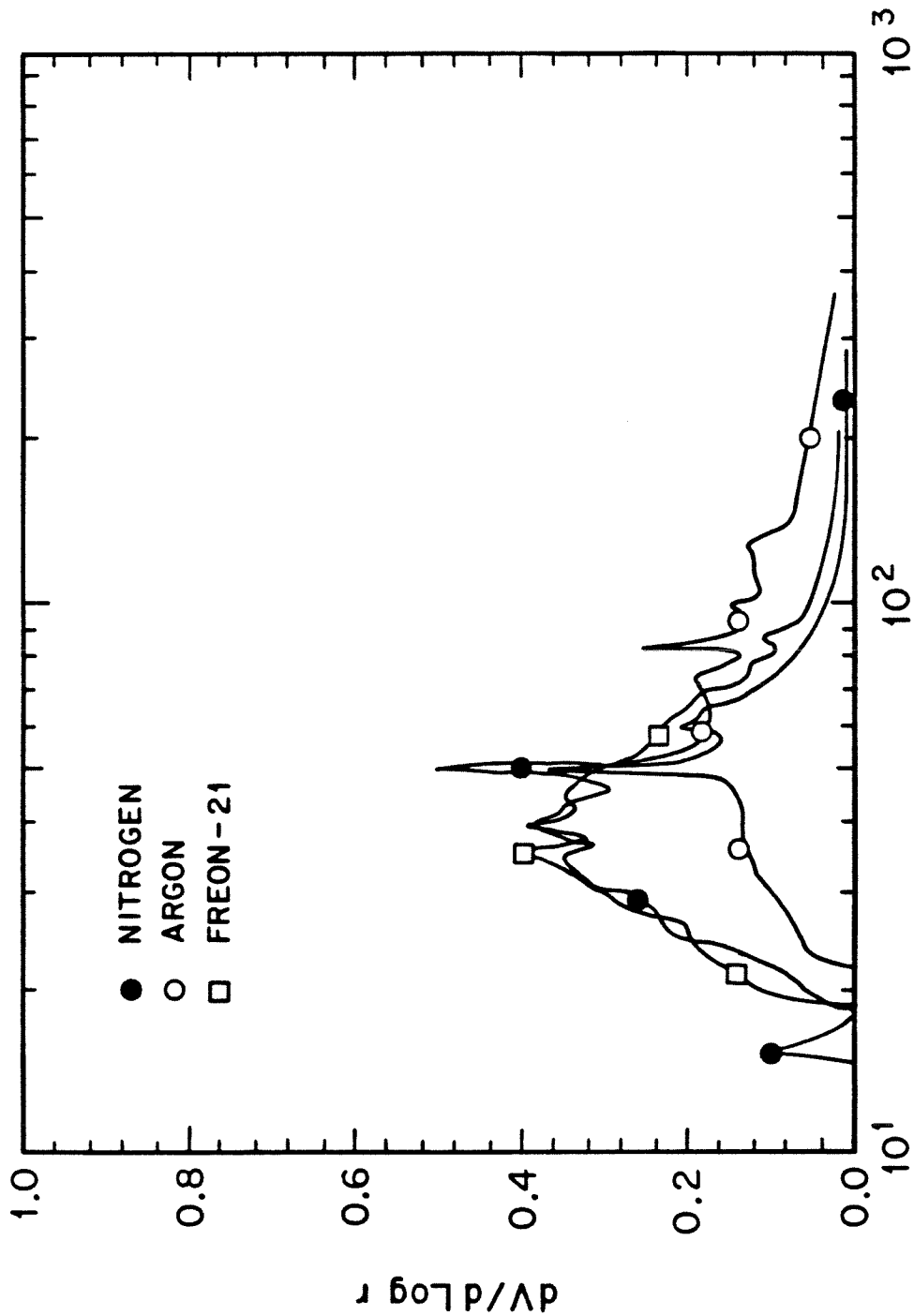

Figure 2.16. Pore volume distributions from different gases computed from CI for γ-alumina.

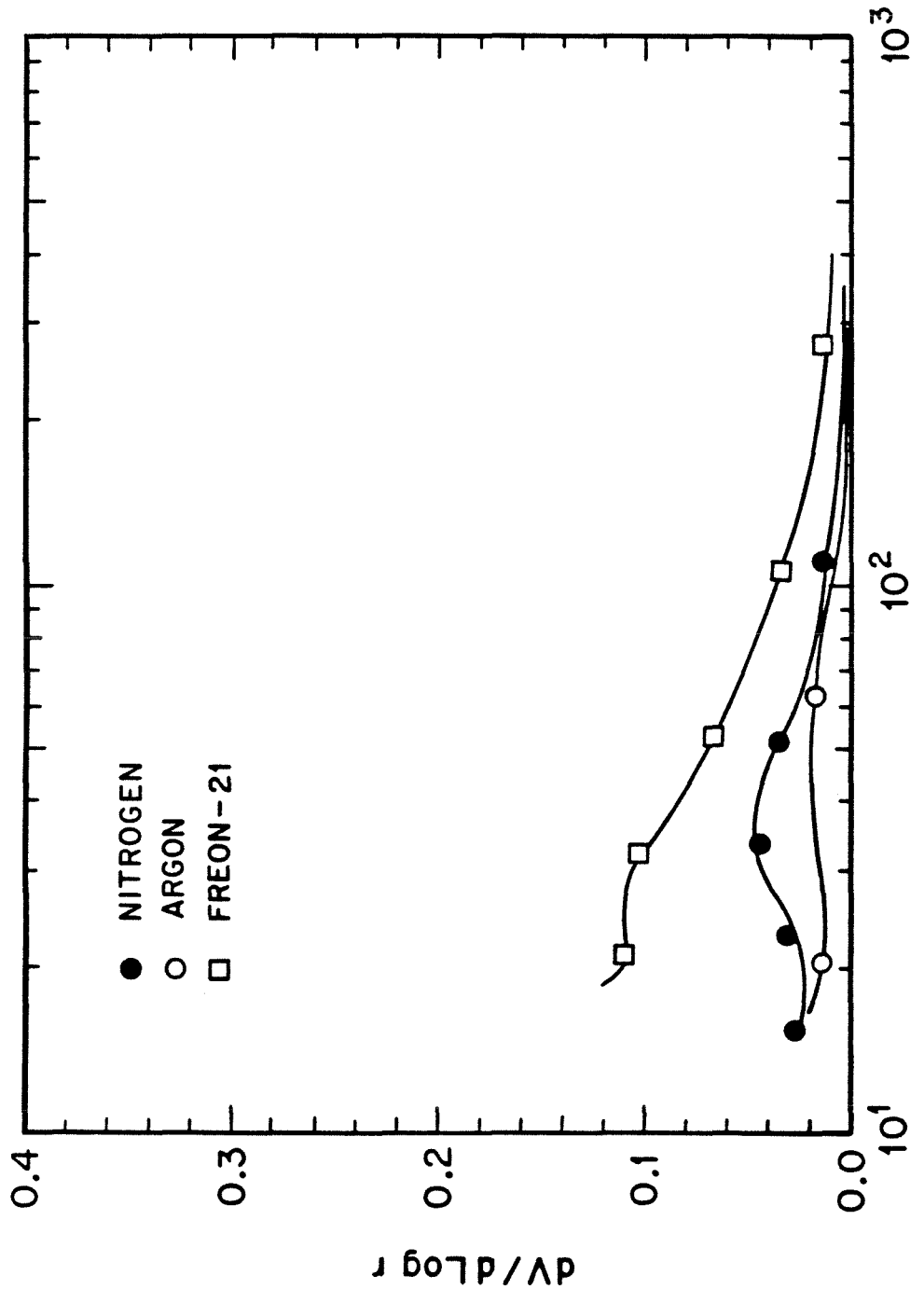

Figure 2.17. Pore volume distributions from different gases computed from CI for PSOC-190 coal.

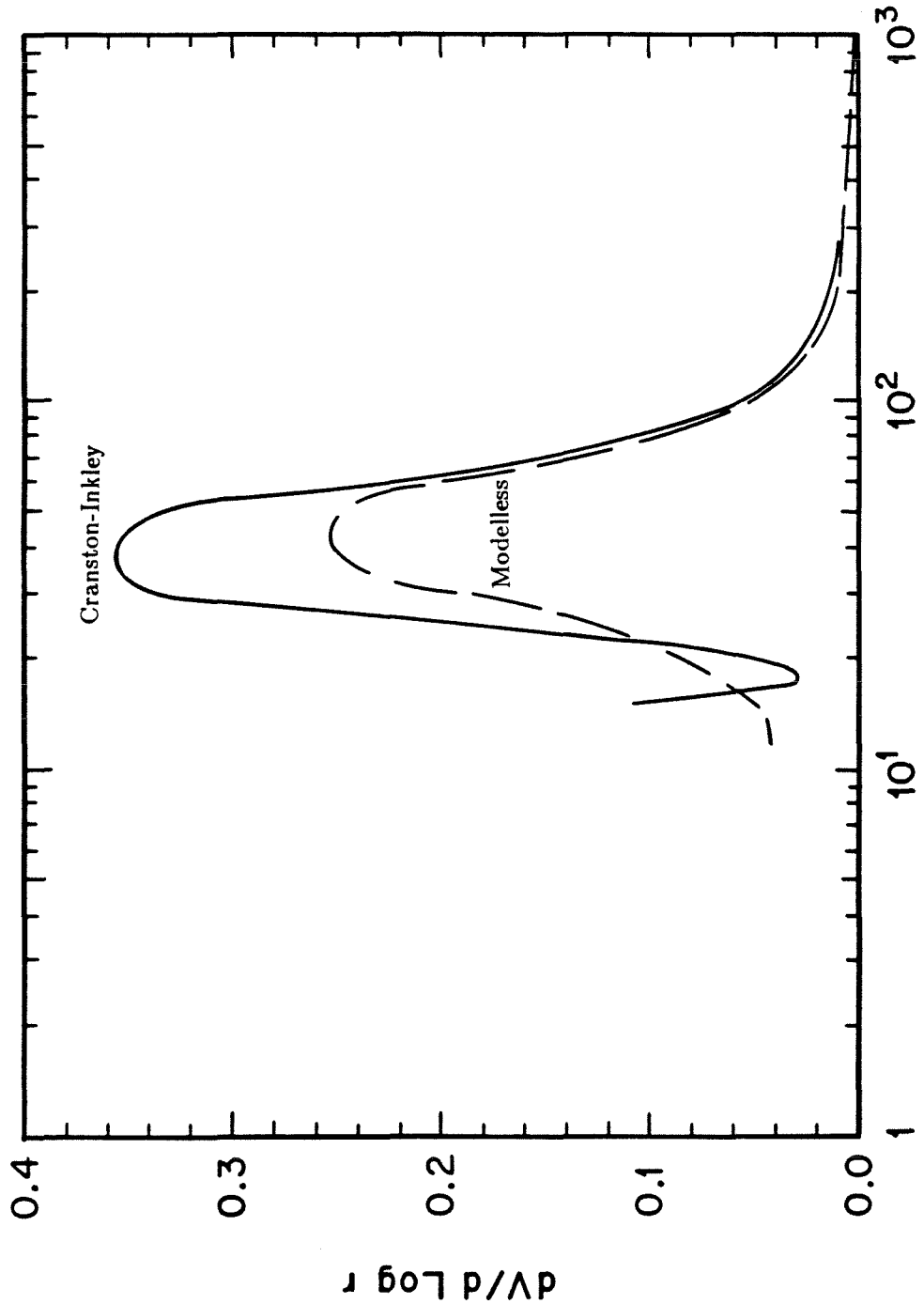

Figure 2.18. Comparision of CI and Modelless pore volume distributions with nitrogen on γ-alumina.

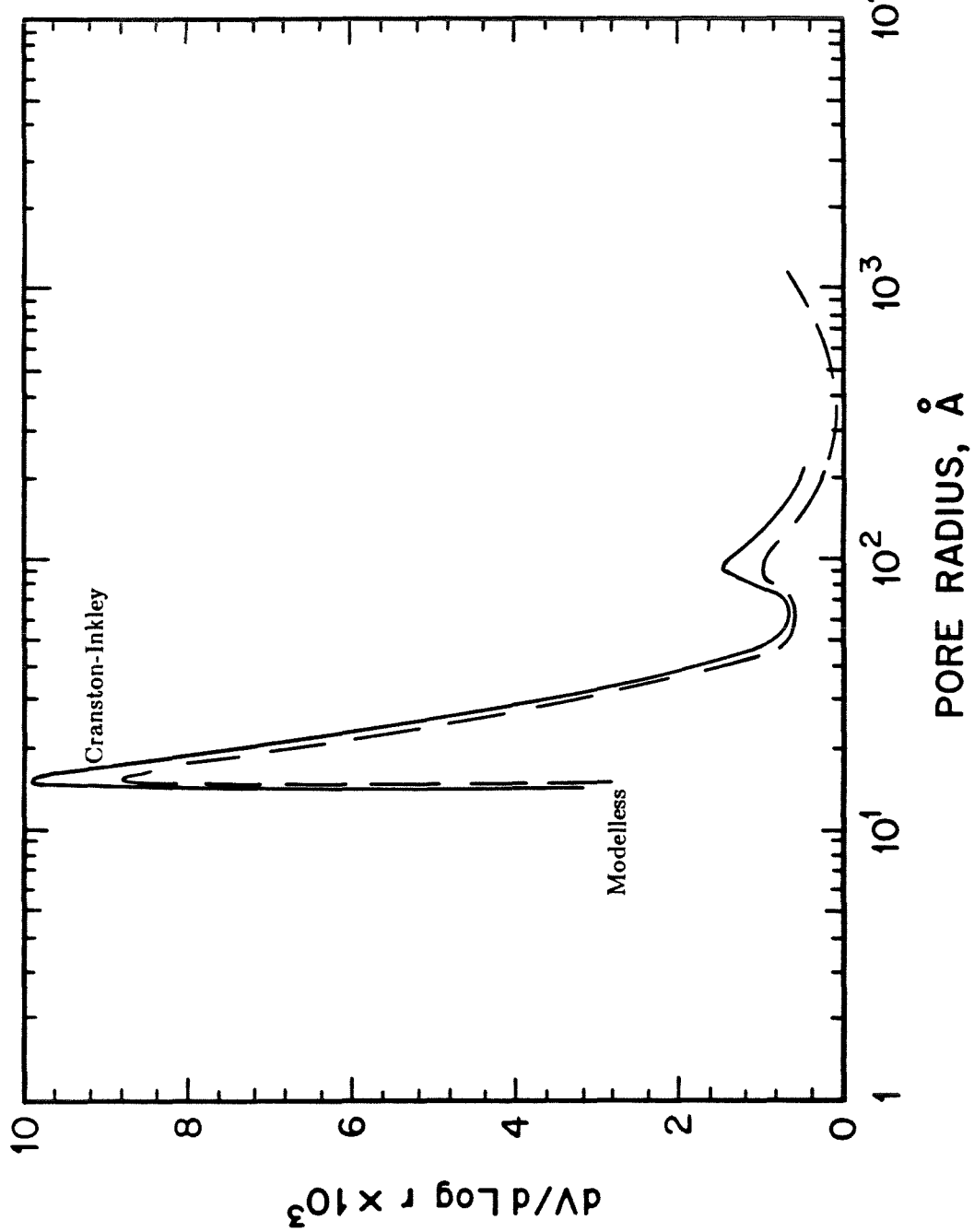

Figure 2.19. Comparision of CI and Modelless pore volume distributions with nitrogen on oxidized char.

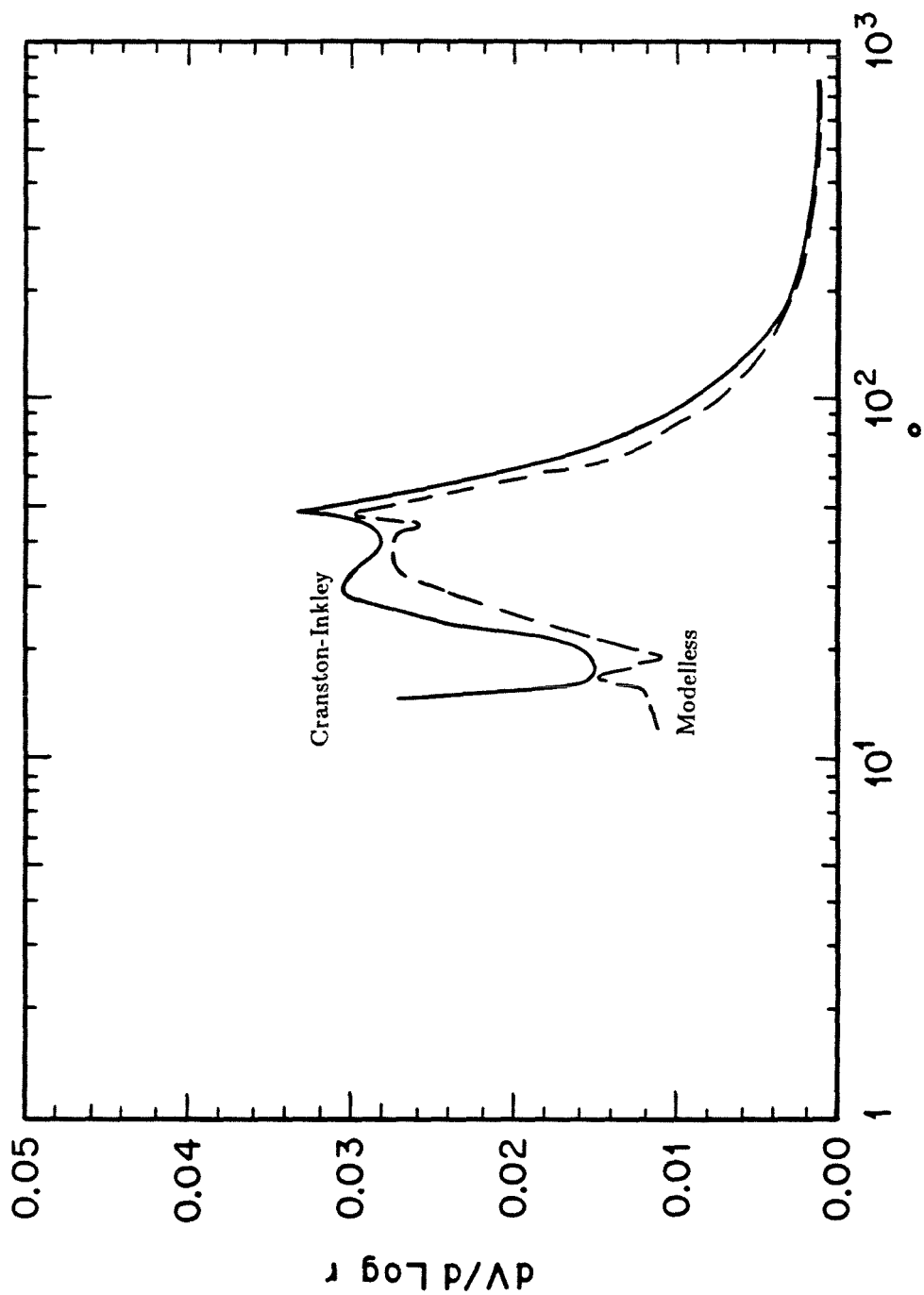

Figure 2.20. Comparision of CI and Modelless pore volume distributions with nitrogen on PSOC-190 coal.

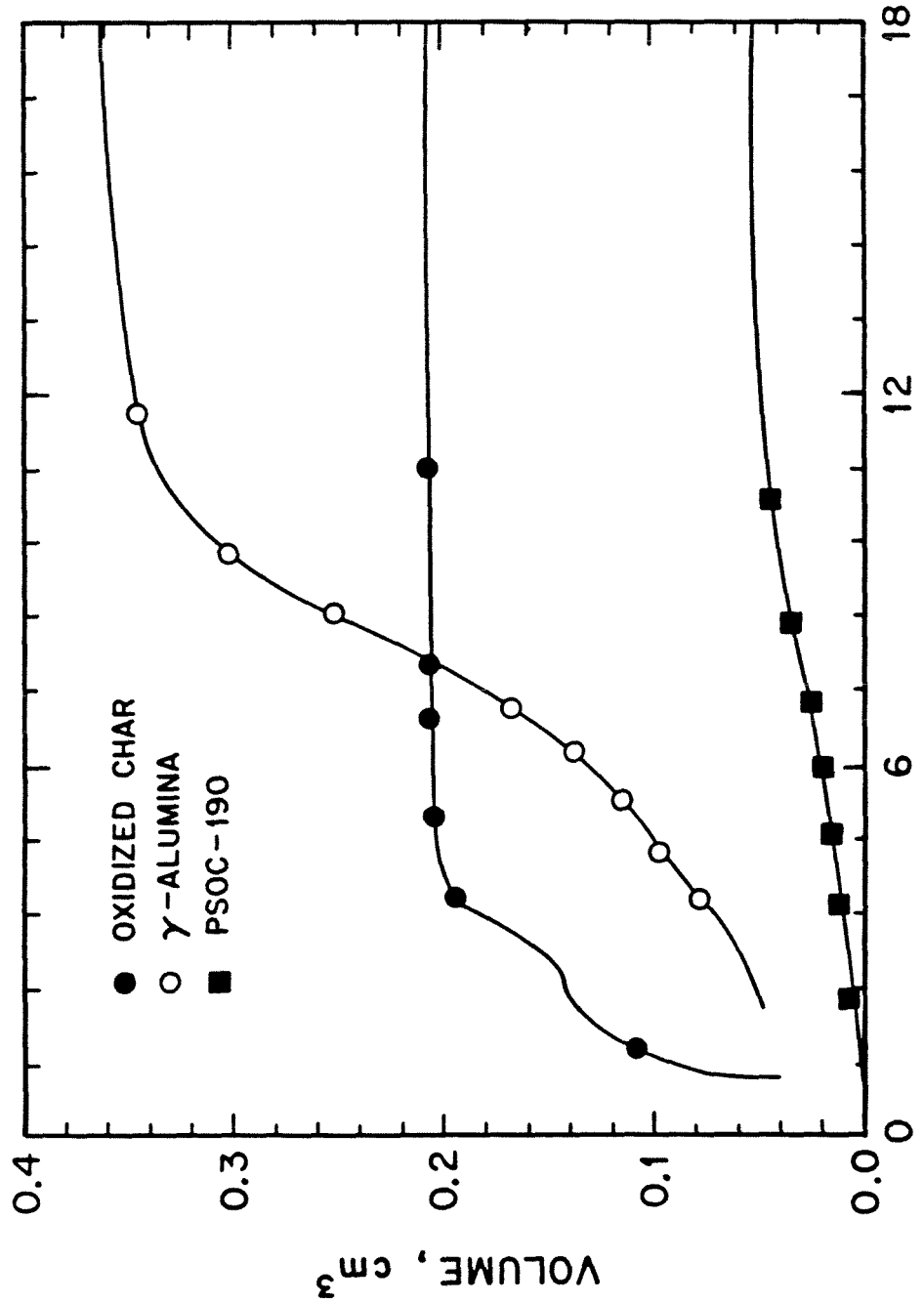

Figure 2.21. V-t plots with nitrogen.

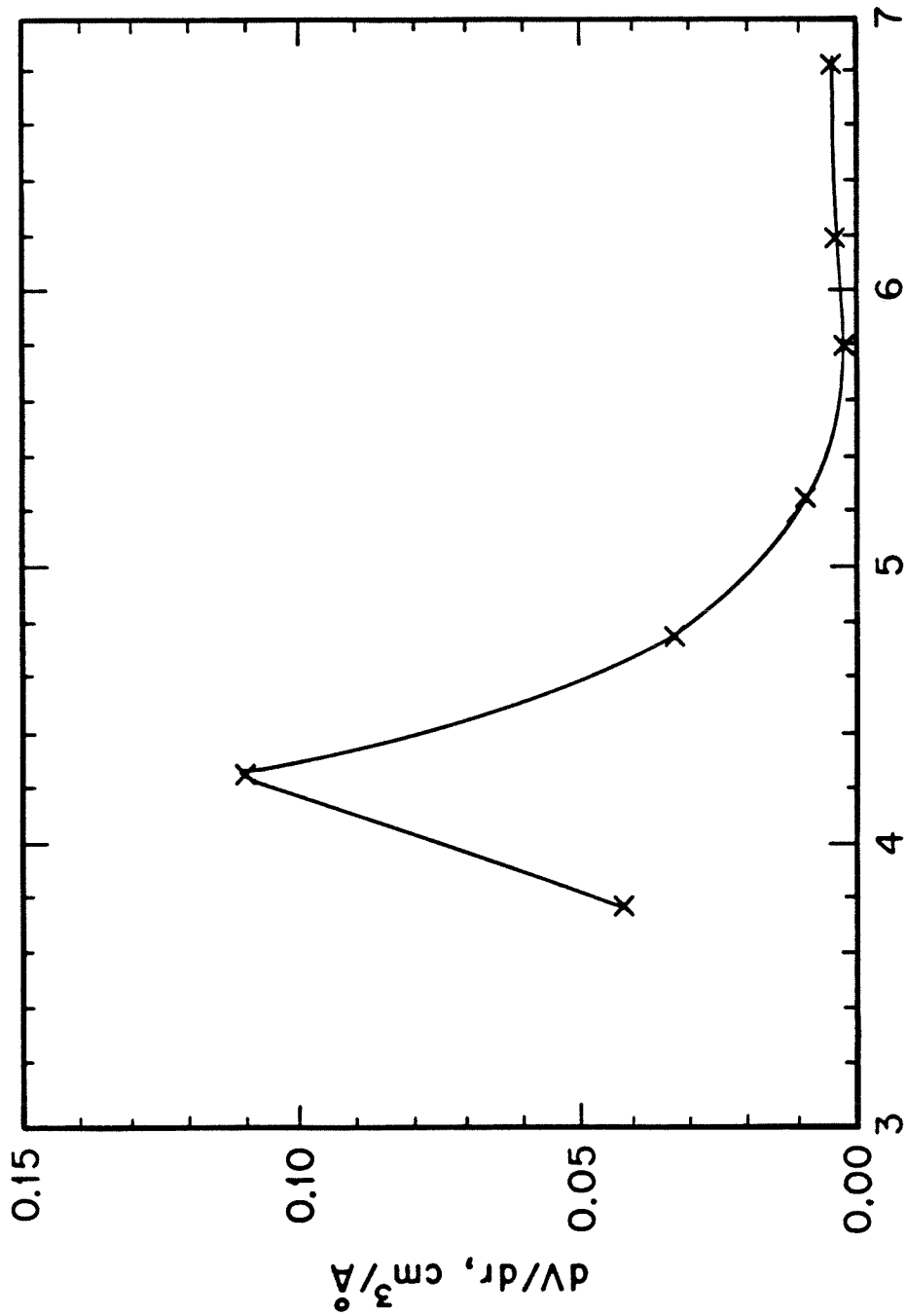

Figure 2.22. MP distribution with nitrogen on oxidized char.

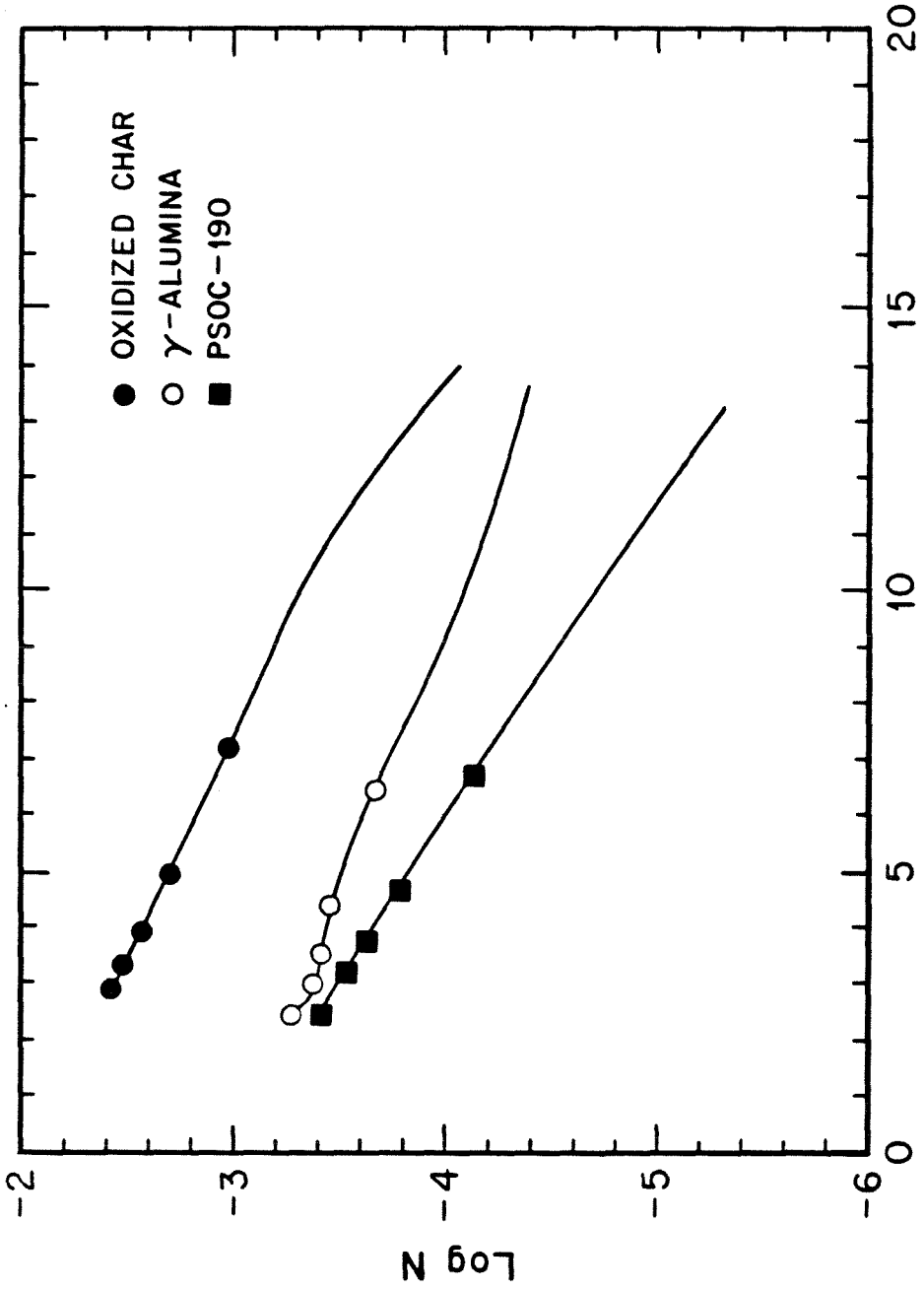

Figure 2.23. DRK plots with carbon dioxide at 298K.

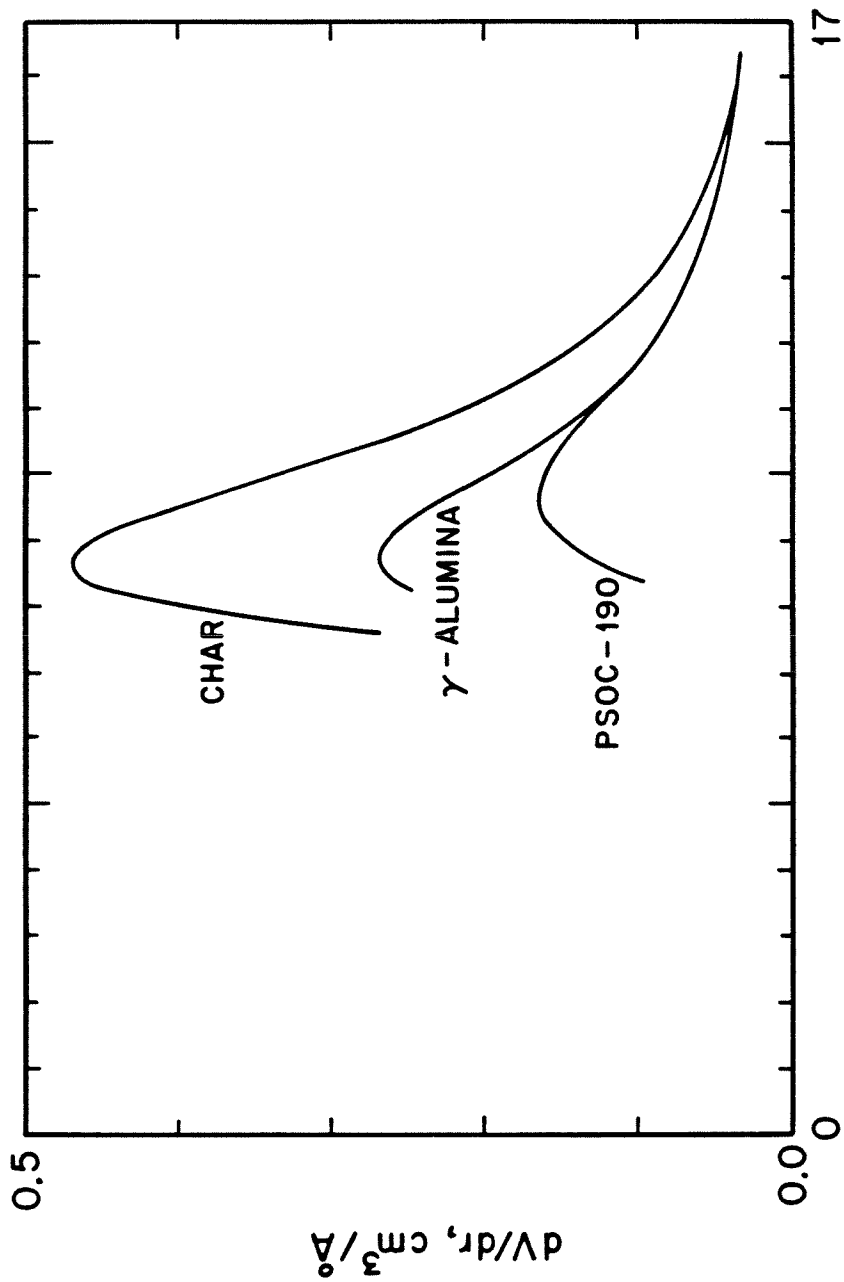

Figure 2.24. Medek plots with carbon dioxide at 298K.

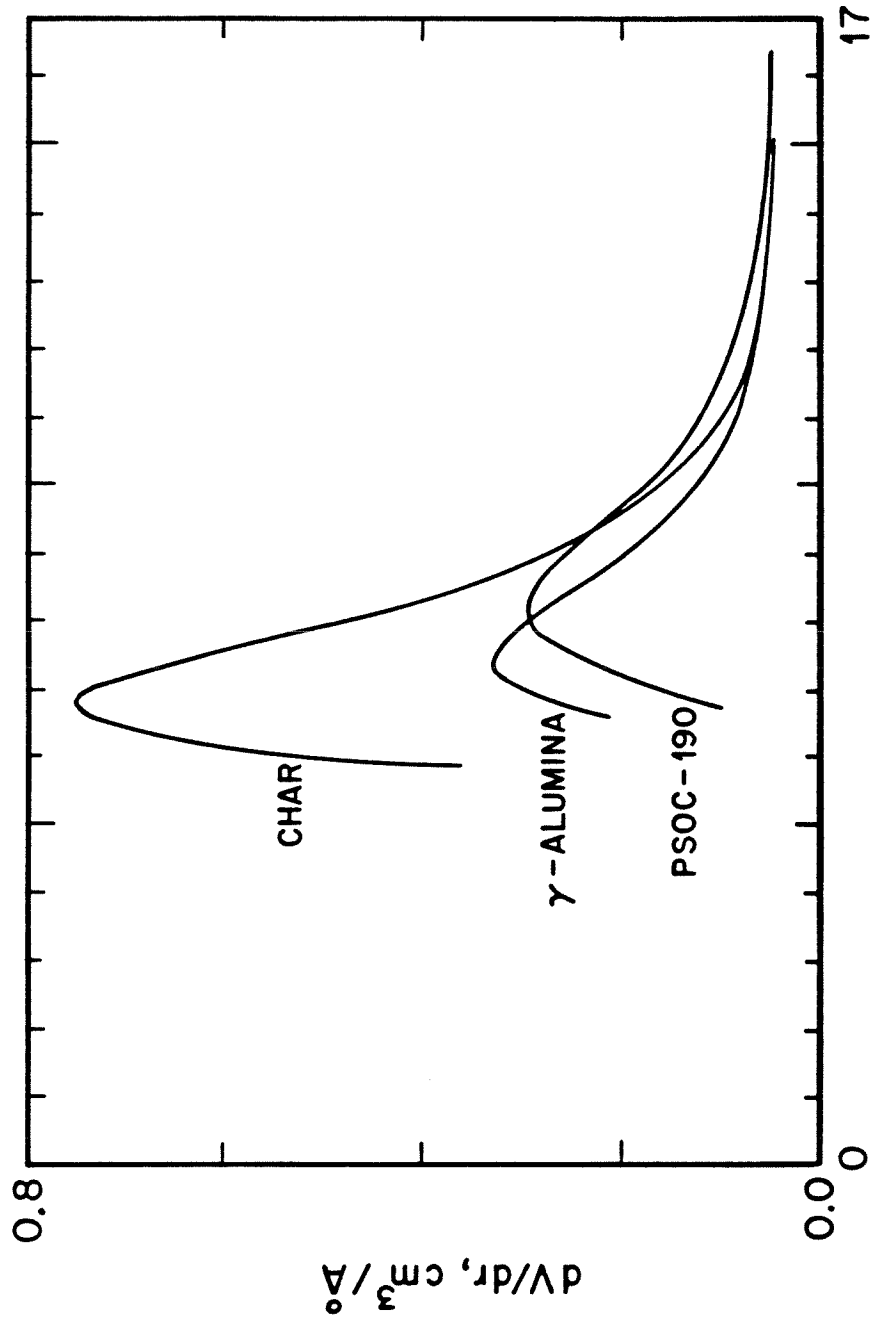

Figure 2.25. Medek plots with Freon.

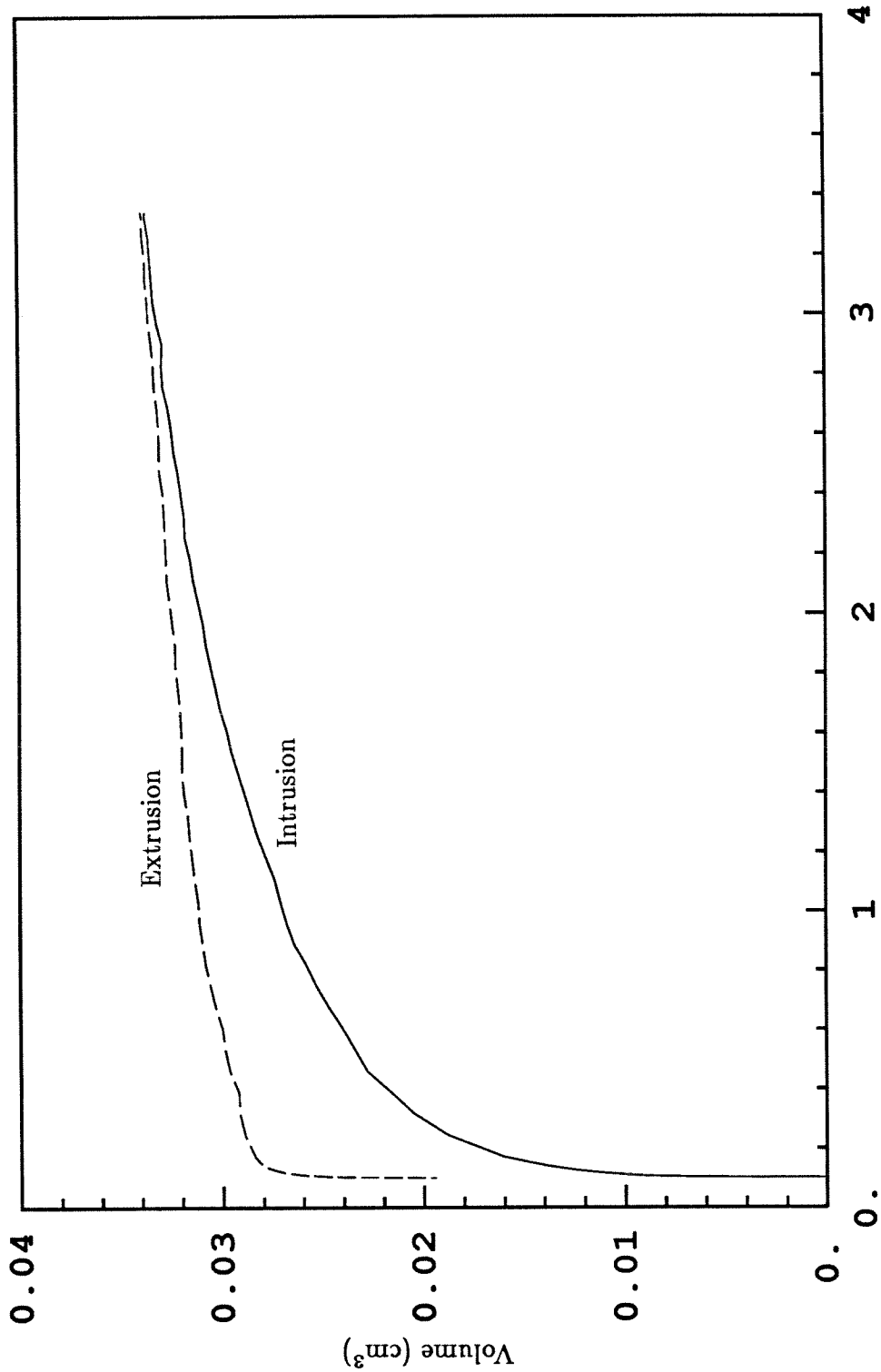

Figure 2.26. Intrusion and extrusion curves for raw PSOC 1443.

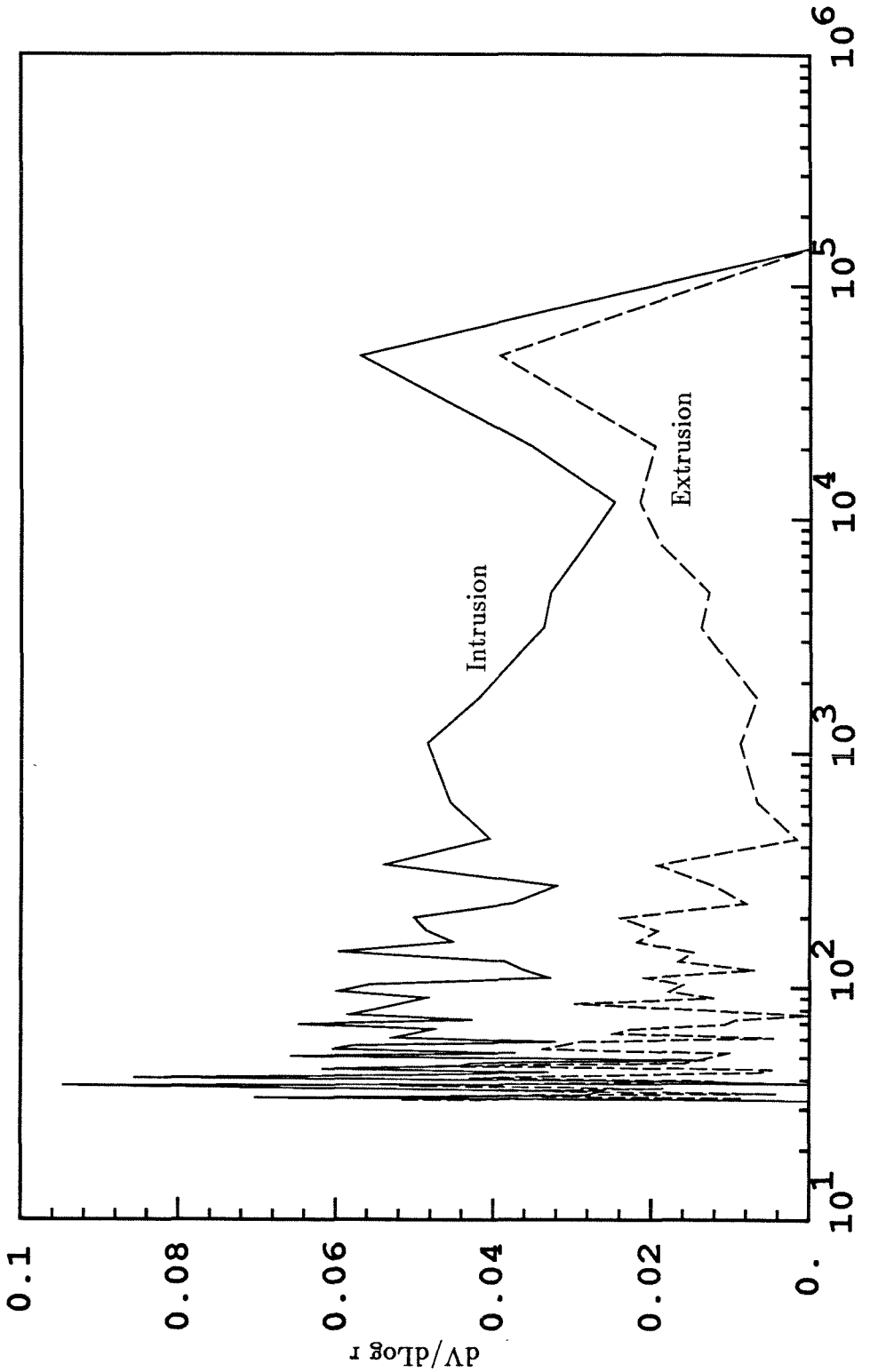

Figure 2.27. Pore volume distributions for traces in Figure 2.26.

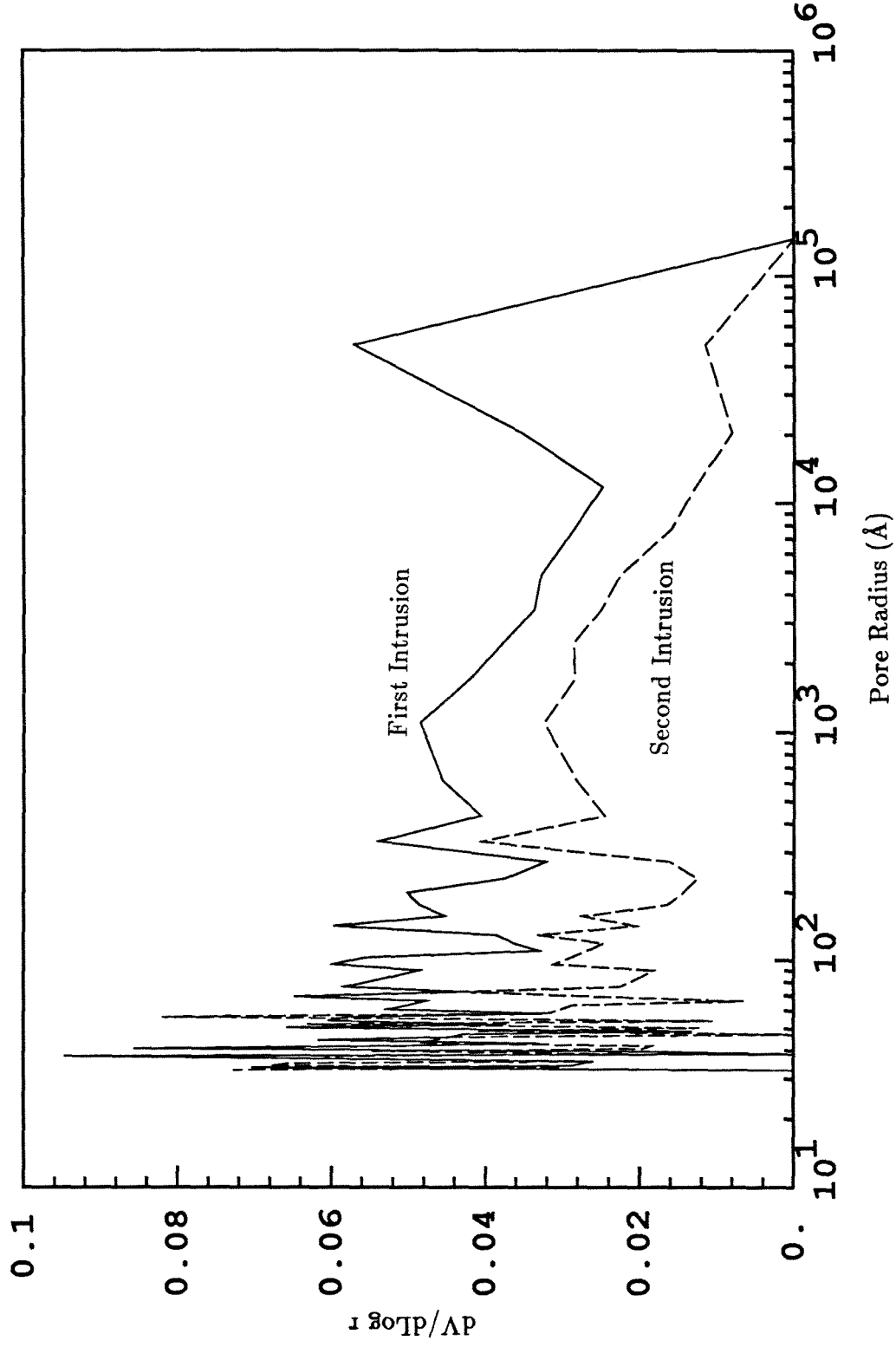

Figure 2.28. Pore volume distributions for first intrusion and second intrusion.

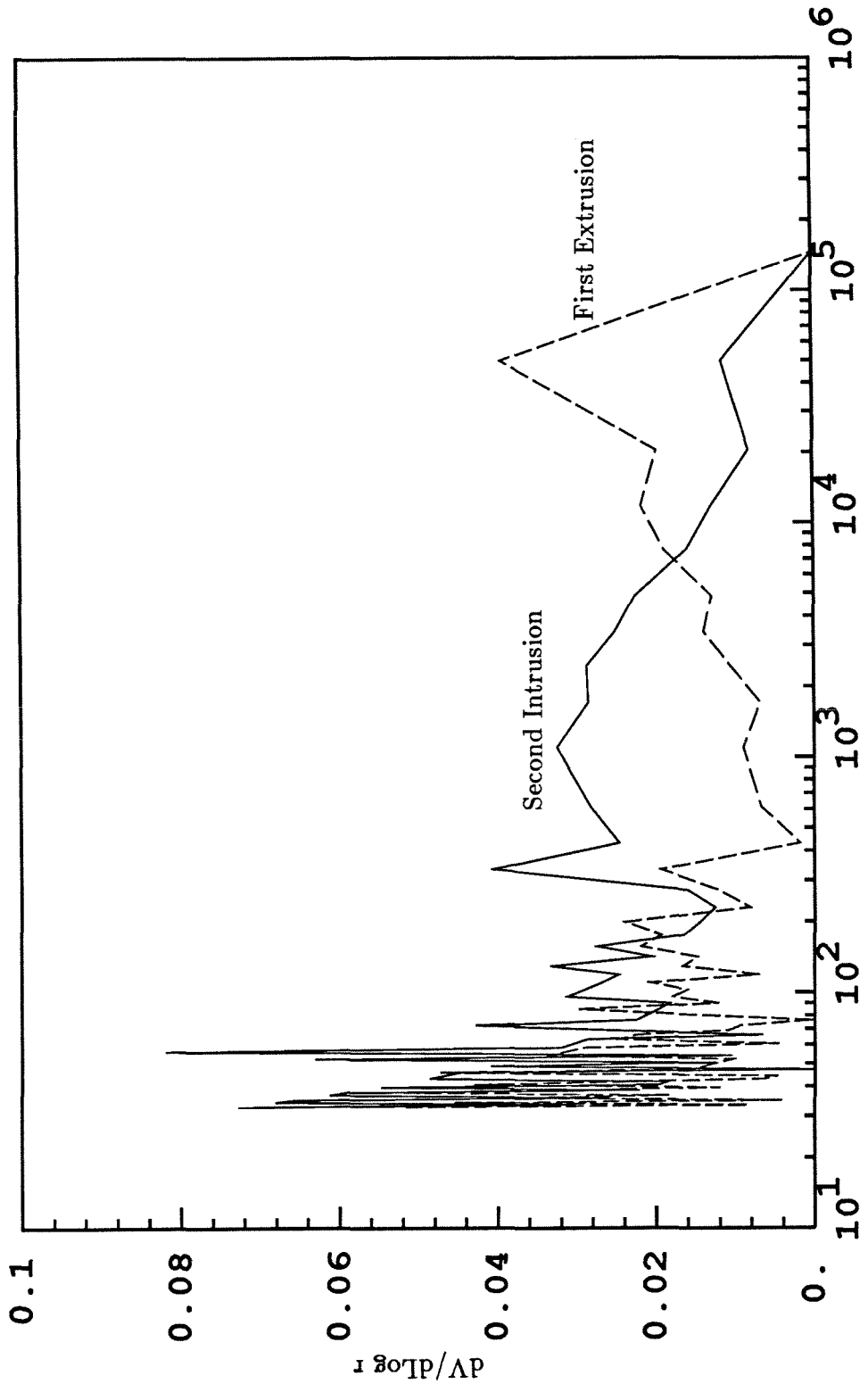

Figure 2.29. Pore volume distributions for first extrusion and second intrusion.

CHAPTER 3

CHARACTERIZATION OF CHARS OXIDIZED AT LOW TEMPERATURE

3.1 Introduction

Raw coals were obtained from the Pennsylvania State University Coal Bank. Pyrolysis, char classification, reactivity studies and char characterization were performed for one HVA bituminous (PSOC 1451), one lignite (PSOC 1443) and one subbituminous (PSOC 1488) coal. The data sheets for these raw coals are given in Appendix A. Scanning electron micrographs of the raw coal particles are shown in Figures A.1-A.3 in the same appendix. Also, results of some of the physical characterization experiments on raw coals are given there.

3.1.1 Coal Preparation

The as-received bituminous coal was below 25 mesh. This coarse graded coal was ground in air for approximately 30-60 seconds on a Retsch mechanical mortar and pestel. The ground material was sieved in air for about 10 minutes on a Ro-Tap mechanical shaker into the following size fractions: 45-53μm, 53-74μm, 74-90μm, 90-104μm, and 104-125μm. The size-classified coals were then stored in glass vials.

Size classified samples of the lignite and subbituminous coals were obtained from the Vortec Corporation. This classification was done with a cyclone. The sizes were 45-63μm, 63-75μm, and 75-106μm.

3.1.2 Char Generation

Chars were generated from the 53-74μm size fraction of bituminous coal, and the 45-63μm fractions of the other coals. The coals were pyrolyzed in an electrically heated, drop-tube reactor. This reactor consists of an alumina tube of 5 cm internal diameter heated by Kanthal heating elements placed in a radiation cavity 20 cm

long. Coal particles were entrained in a flow of nitrogen using a syringe pump feeder. The particle stream was injected into the alumina tube through a wide-bore (1 cm), water-cooled injector. Reactor wall temperatures were measured by thermocouples attached to the outside of the alumina tube. Gas temperatures were measured using a suction pyrometer. The steady-state particle temperature was deduced from a thermal energy balance based on the wall and gas temperatures.

Pyrolysis was carried out in nitrogen at reactor wall temperatures of 1200K, 1400K and 1600K for the bituminous coal, and at a temperature of 1600K for the other two coals. The carrier gas-flow rate was adjusted to achieve a residence time of about 2 seconds in all cases. The coal feed rate was approximately 2 g/hr. The weight loss that was due to devolatilization was estimated to be between 30-50%, depending on the coal type. This could not be measured directly because of loss of particles in the furnace.

The chars were collected on Gelman glass fiber filters. The bituminous chars were washed with tetrahydrofuran to eliminate any tars that might have condensed. This procedure was not necessary for the other chars, since no tar appeared to collect on the filter.

The tar-free chars were sieve-classified into the following size fractions: less than 45 μm, 45-53 μm, 53-90 μm, 90-104 μm, 104-125 μm, 125-147 μm and greater than 147 μm. The sample from each size cut was weighed and subsequently sealed in a glass vial.

3.1.3 Low-Temperature Stagnation Flow Reactor

The oxidation of chars at "low" temperature (675-900K) was studied to de-

termine the influence of key chemical and physical characteristics on the rate of oxidation. A specially designed low-temperature quartz reactor was built to measure the low-temperature reactivity of the chars toward oxygen. It was designed so that oxidation could be stopped at any time, so that gas adsorption experiments on the partially oxidized sample could be performed without contamination by air. A schematic of this reactor is shown in Figure 3.1.

The experimental procedure is as follows: Approximately 50-100 mg of char is weighed out and placed in the reactor. The reactor is then attached to the gas adsorption apparatus (Figure 2.1) in such a way that the lower half is inside a small furnace. This furnace is capable of maintaining temperatures between 450K and 950K.

At the beginning of the run, the system is flushed with helium. Gas flows down the inside tube, impinges on the sample, then flows up through the annular space to an exhaust line, where the flow rate is monitored by a wet test meter. The total flow rate is kept around 1 lpm, which results in a residence time of less than 5 seconds.

The preheater and furnace are then turned on. The system is allowed to come to temperature (typically 650K to 850K), which usually takes about 30 minutes. Oxygen is then introduced into the carrier stream at a prescribed rate. The effluent is monitored for O_2, CO_2 and CO using a Varian Gas Chromatograph. The rate of oxidation is calculated from the mass flow rates of CO_2 and CO leaving the reactor; the conversion is obtained by integrating these rates over time. Thus, reaction rate is measured as a function of conversion.

Oxidation is terminated at a predetermined time by stopping the flow of oxygen into the helium stream. After flushing with helium, the valves are closed, and the reactor is removed from the furnace. Since the sample is not exposed to the air, gas adsorption experiments can be done after evacuation and cooling of the sample.

3.2 Low-Temperature Oxidation of Bituminous Chars

The low-temperature reactivities of the three chars derived from the bituminous coal were measured in the reactor described above. For this series of experiments, temperatures between 725 and 875K were used, while the oxygen mole fraction was varied between 0.01 and 0.1 in the helium carrier. Experiments were confined primarily to the 104-125 μm cut of each char originating from 53-74 μm raw coal.

The conversion calculation described above was checked by comparing the results to those obtained by an ash tracer method. Partially oxidized samples for which conversion was calculated were ashed in a muffle furnace. A simple calculation, assuming that ash mass remained constant throughout reaction, was performed for each sample. The conversion calculated using this method was always slightly higher than that from the former method. This is likely due to the fact that only carbon mass loss is accounted for in the first method, while mass loss that is due to hydrogen, sulfur and oxygen are not. Since the ash-free chars consist of over 90% carbon, this error is not serious except at the highest conversions.

The temperature of the bed was checked by insertion of a thermocouple into the system. For the gas flow rates and oxygen concentrations used, the bed temperature never rose more than a few degrees K above the ambient.

The effect of pyrolysis temperature on the reactivity of the bituminous char in 1

mol% oxygen at 775K is shown in Figure 3.2. The rates are expressed per unit mass of remaining ash-free material. The reactivity of the 1200K char is substantially higher than that of the 1400K char, and that of the 1400K char is somewhat higher than that of the 1600K material. This is consistent with the observation that carbons become less reactive with increasing pyrolysis temperature (Blake *et al.* (1967)). The question is whether this is due solely to morphological changes, or if the chemical structure is also altered. The experiments described in the next section will help to resolve this issue.

Figure 3.3 shows the rate of CO_2 and CO production per unit mass of remaining char for the 1400K char at 775K. The CO_2:CO ratio remains roughly constant at 1.67. The 1200K and 1600K chars exhibited similar behavior; however, the ratio was somewhat lower for the 1200K char (1.35) and slightly higher for the 1600K char (1.80). These values are probably representative of the relative rate of production of these species at the carbon surface. Given the low concentrations of CO and O_2, the relatively low temperature, and short residence time, little CO is expected to be oxidized to CO_2.

The reaction order with respect to oxygen was obtained for 1400K PSOC 1451 char by changing the input oxygen mole fraction in steps of about 0.03 during one experimental run. The data from this run were compared to those from the run at fixed oxygen concentration. The results indicate that the reaction order is about 0.8 for oxygen mole fractions of 0.01 to 0.1 at a temperature of 775K. This is in general agreement with what has been observed for similar chars in this temperature range (Tseng and Edgar (1985)). The observed reaction order appeared to remain

constant over the range of conversion studied.

No clear relationship between CO_2:CO ratio and oxygen concentration could be established. This is unfortunate because such a relationship could be used to differentiate between the mechanisms of formation of these two products.

The rate of reaction of the 1400K material was measured at 725K, 835K, 875K, as well as 775K, all at a fixed oxygen mole fraction of 0.01 . Plotting the natural logarithm of these rates at fixed conversion (20%) versus reciprocal temperature yields the Arrhenius plot in Figure 3.4. From the slope of the line between the points corresponding to 725K and 775K, an activation energy of about 37000 cal/gmol is calculated. This is somewhat higher than the value reported by Tseng and Edgar (1985) for a different bituminous char over a similar temperature range. The slope between the points at 835K and 875K gives an activation energy of 22000 cal/gmol. Interestingly, Tseng and Edgar report a similar value for their bituminous char for temperatures above 875K.

If the rate of reaction is adequately represented by the Arrhenius form, and if the reaction is not pore-diffusion-limited at the lowest temperatures, the rate can be written as:

$$R = 3.9 \times 10^{13} \exp(-37000/RT) c_{O_2}^{0.8} \quad (\text{min}^{-1}). \tag{3.1}$$

where c_{O_2} is the oxygen molar concentration, R is the ideal gas constant and T is the absolute temperature. If this form is accurate at higher temperatures, and if the reaction becomes limited by the diffusion of oxygen in the pores of the solid as the temperature is increased, the apparent activation energy will approach one-half the value of the true activation energy. Also, the apparent reaction order will approach

$(m+1)/2$, where m is the true reaction order. Incipient pore-diffusion limitations are one explanation for the shape of the Arrhenius plot. Examination of the Theile Modulus will determine if pore-diffusion limitations are important.

Alternatively, it is possible that the rate is better expressed by another form, *e.g.*, a Langmuir Hinschelwood expression:

$$r = \frac{A_1 \exp[-E_1/RT] c_{O_2}}{A_2 \exp[Q/RT] c_{O_2} + B}. \tag{3.2}$$

At low temperatures, the observed activation energy will be $E_{\text{obs}} = E_1 + Q$; at high temperatures, $E_{\text{obs}} = E_1$. The observed reaction order will be zero at sufficiently low temperature, and it will approach one as the temperature is increased.

In order to determine the extent of pore-diffusion limitations, the method outlined by Smith (1978) will be followed. When external mass transfer limitations are negligible, the observed rate of reaction per unit external surface area (R_{obs}) can be related to the intrinsic rate (R_i) (per unit total area) by:

$$R_{obs} = \eta\gamma\rho_p S_g R_i c_0^m, \tag{3.3}$$

where η is the effectiveness factor, γ is the ratio of particle volume to external surface area, ρ_p is the particle density, S_g is the specific surface area of the particles, and c_0 is the concentration of oxygen in the ambient. It can be shown that

$$\Omega = \eta\phi^2(m+1)/2 = \gamma r_{obs}(m+1)/(8 D_{eff} c_0), \tag{3.4}$$

where ϕ is the Theile modulus which can be written as:

$$\phi = \gamma/2\sqrt{S_g \rho_p R_i c_0^{(m-1)}/D_{eff}}, \tag{3.5}$$

where D_{eff} is the effective diffusivity of reactant in the porous particle. The quantity on the left side of (3.4) can be calculated from the observable quantities on the right side. Mehta and Aris (1971) present correlations of η versus Ω. Strictly speaking, these correlations apply only to slabs. However, for lack of a better alternative, these correlations will be used for the char particles.

The effective diffusivity in a porous particle is given by the Satterfield expression:

$$D_{eff} = D_P \epsilon / \tau, \tag{3.6}$$

where D_P is the pore-diffusion coefficient, ϵ is the void fraction, and τ is the tortuosity of the pores. Since the pores containing the great majority of surface area are quite narrow, the pore diffusion coefficient will be given by

$$D_p = D_{Knud} = 9300 r_p \sqrt{T/M}, \tag{3.7}$$

where D_{Knud} is the Knudsen diffusion coefficient, r_p is the mean pore radius (cm), T is the absolute temperature (K), and M is the molecular weight of the diffusing species. The mean pore radius can be calculated from (Wheeler (1951)):

$$r_p = 2\epsilon\sqrt{\tau}/(S_g \rho_p). \tag{3.8}$$

The void fraction can be calculated from

$$\epsilon = 1 - \rho_p/\rho_{He}, \tag{3.9}$$

where ρ_{He} is the helium density of the sample. Though ρ_{He} could not be accurately measured for the small samples, it is probably about 1.6 g/cm^3. The particle

density (from mercury displacement) was 1.2 g/cm^3, resulting in a void fraction of 0.25. The surface area was about 400 m^2/g for conversions above 20%. The tortuosity was taken as 2. The mean pore radius is 15 Å, resulting in a pore-diffusion coefficient of oxygen at 775K of 7.0x10^{-3}cm^2/sec. The effective diffusivity is therefore 8.8x10^{-4}cm^2/sec. The observed rate per unit-external-area is about 4x10^{-9} gmoleO_2/ cm^{2}sec. For this cenospheric material, the characteristic length is around 5 μm. At 775K, the molar concentration of 1 mol% O_2 is 1.58x10^{-7} gmole/cm^3.

Inserting these numbers into (3.4) yields a value of 3x10^{-3}. From Figure 12 of Mehta and Aris, η is unity, so no pore-diffusion limitations exist at this temperature. At 875K, the observed rate of reaction is about one order of magnitude higher than it is at 775K. The changes in the other constants are relatively small, so the right side of (3.4) is about 0.03. η is still unity for this value. Thus, pore-diffusion limitations should not exist under these conditions.

In order to study the issue of pore diffusion further, the 104-125μm char paritcles were ground through sieves of two different sizes: 61μm and 90μm. In each case, the entire sample was used for the experiments; *i.e.*, ash was not removed by further sieving. The reactivities of these crushed particles were measured at 775K in 1 mol% oxygen. The rates versus conversion are reported in Figure 3.5, along with the rate for whole char under similar conditions. Crushing significantly increases the observed rates of reaction. This could be explained by the existence of pore-diffusion limitations, contrary to the previous analysis. Alternatively, crushing may have opened some blind porosity; however, no increase in surface area was

observed after crushing. Interestingly, the CO_2:CO ratio was higher for the crushed char than for the whole char.

For the whole char, the CO_2:CO ratio decreased with increasing temperature. This cannot be due to the heterogeneous reaction of CO_2 with carbon to produce carbon monoxide because of the high activation energy of this reaction (Dutta *et al.* (1977)). (This could be verified by carrying out the gasification with CO_2 to determine if detectable amounts of CO are produced.) Thus, the primary mechanism for char oxidation appears to shift gradually from CO_2 production to CO production. Figure 3.6 shows Arrhenius plots for the individual species. Both show a change in slope, which may be indicative of pore-diffusion limitations. The activation energy for the CO_2 reaction is 32000 cal/mol at the lower temperatures, and decreases to 18000 cal/mol at the higher temperatures. The activation energy for the CO reaction is about 40000 cal/mol at the lower temperatures, and decreases to 23000 cal/mol at the higher temperatures. Since oxygen is the limiting reactant in both cases, it is reasonable to expect that both reactions become pore-diffusion-limited to similar extents. Alternatively, it is possible that CO and CO_2 are produced by similar reaction mechanisms.

Since mass transfer limitations appear to exist at 875K, significant oxygen concentration gradients must exist in the pores during reaction. This will cause the pore structure to evolve in a manner that is somewhat different from that which would occur if diffusion limitations were not so severe. In order to observe the influence of pore growth on reactivity, a sample of 1400K char was oxidized at 775K. During the run, the temperature was increased to 875K for a short period, and the

rate was measured. The temperature was then returned to 775K. This procedure was repeated several times throughout the run. Thus, the rate of reaction was measured at 875K for a material that had essentially the evolving pore structure of a material oxidized at 775K. Figure 3.7 shows that the rate of reaction of this "thermopulsed" material at 875K was about 50% higher than that of the material oxidized continually at 875K. It is possible that opening the pores at low temperature facilitates penetration of oxygen at higher temperatures. Alternatively, oxygen which is chemisorbed at 775K may desorb at 875K, leading to enhanced oxidation rates.

Because of the unusual configuration of this reactor, extensive experimental and theoretical examinations were done to ensure that reaction was not limited by mass transfer in the bed. The Weisz criterion (Weisz and Hicks (1962)) for catalyst pellets states that if

$$l^2 R / C_0 D > 1, \tag{3.10}$$

mass transfer effects will be important. Here, l is the length of the particle, R is the observed reaction rate per unit volume, C_0 is the external concentration of reactant, and D is the effective diffusivity of reactant in the particle. Applying this criterion to the bed of char particles in the reactor (assuming an effective bed height of 0.1 cm), it was found that, at the highest rates encountered (875K and 1 mol% oxygen), this quantity was quite close to one. This indicates that mass transfer in the bed could be a problem.

In order to determine more exactly the effect of mass-transfer limitations in the bed, several experiments were done with different initial loadings and gas flow

rates at 875K. Figure 3.8 shows reaction rate for four different flow rates. There is some scatter in the data, but it appears that flow rates less than 600 ml/min may cause reaction rates to be artificially low. Figure 3.9 shows reaction rates for several different initial loadings. The smaller loadings lead to slightly larger observed rates.

It appears from this series of experiments that mass-transfer effects in the bed of the stagnation flow reactor are not completely negligible for rates obtained at 875K for this char. However, the effects are not large, and they are negligible at lower temperatures. Mass-transfer effects in the bed cannot explain the the behavior of the Arrhenius plot. The results of crushing and thermopulsing the char appear to show that pore-diffusion limitations are important. The similar trends of carbon-oxide production with increasing temperature support the conclusion that oxygen transport in the micropores becomes the limiting factor. The results of the Thiele analysis, however, indicate otherwise. This may be due to ignorance of the true effective diffusivity in this microporous material. This quantity was not measured directly; it was inferred from the physical characteristics of the char.

3.3 Characterization of Bituminous Chars

The methods described in Chapter 2 were used to characterize partially oxidized samples of PSOC 1451 chars. Observation via scanning electron microscopy was done for several chars. Carbon dioxide adsorption at 298K was also done for selected samples.

The char particle size distribution was obtained by weighing each sieve cut. The normalized distribution for 53-74 μm PSOC 1451 coal pyrolyzed at 1600K is shown in Figure 3.10. It is clear that many of the the bituminous coal particles

swell significantly under these conditions.

3.3.1 Microscopy

Visual observation using an optical microscope showed that these particles were thin-walled "lacy" cenospheres with a few large blowholes and very large internal voids. Observation of partially oxidized char showed that the thin walls were consumed, leaving the "lacy" material behind.

Electron microscopy was used to observe surface features of the chars. Scanning electron micrographs in Figures 3.11 and 3.14 reveal the cenospheric nature of the 1200K and 1600K chars. The swelling behavior and round appearance of the particles indicate that the coal undergoes plasticization during pyrolysis (Street *et al.* (1969)).

Figure 3.11 shows the smooth surface of the 1200K bituminous char. Interestingly, the 1600K material has a more "wrinkled" appearance, as seen in Figure 3.14. Blowholes are more common on the 1600K char. Close observation of the surface shows that the ash is distributed as very small particles on the surfaces of both chars.

The effects of low-temperature partial oxidation on the 1200K char are shown in Figures 3.12 and 3.13. Thin walls are obliterated, while "lacy" structures remain.

Figures 3.15 and 3.16 show micrographs of 1600K char partially oxidized at low temperature. Again, thin walls are consumed during low-temperature oxidation. The ash appears to remain associated with the original particle, as seen in Figure 3.16.

3.3.2 Gas Adsorption

Surface areas were calculated from the BET theory using the nitrogen adsorption isotherms at 77K for many partially oxidized chars (see Chapter 2 for details). A typical isotherm is shown in Figure 3.17. In this particular case, the sample was 1200K char, partially oxidized to 24% burn-off. The large amount of nitrogen adsorption at pressures under than 10 torr is indicative of a highly microporous material. Once the micropores are filled with adsorbate at low pressure, there is little subsequent adsorption, indicating that the volume of transitional and macropores is quite small. This is confirmed by Figure 3.18, which is a plot of pore-volume distribution derived from the same isotherm using the Yan-Zhang method (see Section 2.2.2). This plot is rather noisy because of numerical differentiation of experimental data. By fitting the isotherm over the appropriate range with a fourth degree polynomial, this problem is eliminated, as shown by the dashed line.

The surface areas (corrected for the presence of ash) are given as a function of conversion for three pyrolysis temperatures in Figure 3.19. It is evident that the 1200K char had a substantially larger surface area than either the 1400K or 1600K char. Clearly, the conditions of pyrolysis had a strong effect on particle morphology.

In all cases, there was a large initial rise in specific surface area with conversion. Such large increases cannot be due to simple removal of carbon atoms from pore surfaces; significant microporosity inaccessible to nitrogen at 77K had to exist in the solid (Walker *et al.* (1953)) prior to oxidation. A relatively small amount of oxidation was able to open this structure to nitrogen. After a certain level of oxidation, the specific area appears to be quite constant for each char.

Capillary condensation of nitrogen was used to monitor pore growth with conversion. Figure 3.20 shows total pore volume (pore radii 16-150 Å) as a function of conversion for the 1200K and 1600K bituminous char. In general, pore volumes in this size range grew with conversion during low-temperature oxidataion.

Carbon dioxide adsorption experiments were done for a series of partially oxidized 1400K chars at 298K. The Dubinin-Polyani theory was used to determine maximum carbon dioxide uptake per unit mass of carbonaceous material. Figure 3.21 shows a typical isotherm, while Figure 3.22 shows carbon dioxide uptake as a function of conversion. The uptake remains relatively constant over a wide range of conversions.

3.3.2.1 Intrinsic Rates of Bituminous Chars

The intrinsic rate of reaction was obtained by dividing the normalized reaction rate by the measured surface area at a given conversion. The resulting curves for the three chars are shown in Figure 3.23. In all cases, the intrinsic rate is highest near 0% conversion and falls to a nearly constant value beyond 15% conversion. The high values at low conversion are likely due to artificially low values of surface area from nitrogen adsorption. The nitrogen may not be able to penetrate effectively the micropores at 77K. Thus, nitrogen surface area is probably not a reliable measure of the surface area available to oxygen at 775K at low conversions.

Once sufficient oxidation has taken place, the pores are large enough for efficient nitrogen penetration. In this case, the surface area measured by nitrogen may be representative of the area available to oxygen. Only then is the intrinsic rate constant.

The intrinsic rate of the 1200K char is somewhat higher than that of the 1600K char, while the intrinsic rate of 1400K char is only slightly higher than that of 1600K char. If nitrogen surface area is a valid measure of the area available to oxygen at 775K, then it can be concluded that the pyrolysis temperature has an effect on the chemical nature, as well as the morphology of, the char.

This result is supported by the elemental carbon and hydrogen analyses done on the three chars, shown in Table 3.1. The 1200K char has the highest hydrogen content, while the 1600K material has the lowest. Since milligram samples are used, there is some doubt as to the absolute values of these quantities, as the amount of ash varies from sample to sample. The carbon:hydrogen ratio is a more reliable indicator. The amount of hydrogen present appears to be correlated with intrinsic reactivity. This is in agreement with the observations of Snow *et al.* (1960), who found that the reactivity of carbon blacks toward oxygen depended on hydrogen content of the carbons. Table 3.1 also shows carbon and hydrogen contents for partially oxidized samples of 1400K char. Hydrogen appears to be depleted at about the same rate as carbon, which is in contrast to the results of Snow *et al.* (1960). Since the hydrogen content of PSOC 1451 char decreases with increasing pyrolysis temperature, and the CO_2:CO ratio during oxidation decreases with increasing pyrolysis temperature, the presence of hydrogen may be responsible for enhanced CO formation.

3.3.3 Oxygen Chemisorption

Oxygen chemisorption was carried out on selected samples of chars in order to determine "active" surface area (ASA). Radovic *et al.* (1983) have shown direct

correlation between observed reactivity and active site concentration; this may be useful for differentiating the chemical and physical effects of pyrolysis.

A variety of procedures have been described to measure oxygen uptake (Tong *et al.* (1982), Radovic *et al.* (1983), Wojtowicz *et al.* (1985)). The primary differences in these methods are i)the temperature at which the surface is "cleaned"; ii) the temperature at which the adsorption takes place; and iii) the pressure of oxygen used. Since no set of conditions is universally used, direct comparisons with other workers are not generally possible. However, qualitative comparisons may be useful.

The following volumetric procedure was used to determine ASA in this laboratory: The sample is placed in a quartz tube and weighed. The tube is attached to the gas adsorption apparatus (Figure 2.1) in such a manner that the lower part of the tube is inside a small furnace.

The sample is initially outgassed in a vacuum of 10^{-3} torr at room temperature. The temperature is ramped to 875K over two hours *in vacuo*, then maintained at 875K for one hour. This is necessary to remove surface oxygen complexes to prevent the desorbed species from reacting with the surface. It is doubtful that significant physical or chemical changes take place in the char at these temperatures.

The sample is then cooled to 575K, which is a typical temperature used for oxygen chemisorption. The sample is isolated (*in vacuo*), and a known volume is filled with a fixed amount of oxygen. This volume is then opened to the sample, and the system is allowed to equilibrate for twelve hours. The pressure of the system is measured, using the Baratron. The system is re-evacuated, and its volume is determined using helium. The oxygen uptake is normalized with respect to the

mass of ash-free char.

The results for several levels of partial oxidation of 1200K and 1400K material are shown in Table 3.2. The higher uptakes for the 1200K char again indicate a different chemical structure for this material. Interestingly, there is a minimum in oxygen uptake between 0 and 20% conversion for both chars.

Based on this data, there appears to be no obvious relation between ASA and reactivity.

3.3.4 Mercury Porosimetry

Mercury porosimetry was done on several partially oxidized samples of both 1200K and 1600K chars. The corresponding pore-volume distributions were obtained from the Washburn equation assuming cylindrical pores, as previously described (Section 2.3). Pore-volume distributions obtained by this method are given in Figures 3.24 and 3.25 for the unburned and a partially oxidized (64%) 1200K char. Pore-volume distributions for unburned and partially oxidized (55%) 1600K char are shown in Figures 3.26 and 3.27. It should be noted here that a significant part of the volume in the range $5x10^4$ to 10^5 Å is due to interparticle voidage, which varies from sample to sample. This is especially true for the round 1200K char particles.

There is not much porosity in the range 32-200 Å for the unburned 1200K char; however, the volume of pores in this range has grown after oxidation to 64% burnoff.

The 1600K material has more porosity in the 32-200 Å range than does the 1200K material. After 55% conversion, pore volumes have increased over this range.

This is in qualitative agreement with the findings of the capillary condensation experiments.

In order to visualize the growth of pores more clearly, the pores were divided into two categories: 32-500 Å and 500-17600 Å. In addition, total intruded volumes for each sample were calculated from the given pore-volume-distribution plots. The volumes of all pore sizes generally tend to grow with burnoff, as shown in Figure 3.28 for the 1200K material and Figure 3.29 for the 1600K char.

3.4 Low-Temperature Oxidation of Lignite Char

The low temperature reactivity of 1600K PSOC 1443 char towards oxygen was studied, using the apparatus described in Section 3.1.3. Since this char was more reactive than the bituminous char, the range of temperatures used was 675K to 825K. The oxygen mole fractions were varied between 1 and 5 mol%. The 45-53 μm cut from 45-63 μm coal, and 61-74 μm cut from 75-106 μm coal were used for this series of experiments.

The reaction rate is shown as a function of conversion in Figure 3.30 for a temperature of 725K in 1.0 mol% oxygen. Again, the rate is expressed per unit mass of remaining ash-free material. The reaction order with respect to oxygen was determined, using the method described in Section 3.2. These measurements showed that reaction order was between 0.55 and 0.65 for this range of oxygen concentration at 725K over the whole range of conversion. This is slightly smaller than the observed order for bituminous char at 775K.

The rates of CO_2 and CO production from this char at 725K are shown in Figure 3.31. The CO_2:CO ratio remains fairly constant at 2.8 over a wide range

of conversion. This is similar to the ratio observed for 1600K PSOC 1451 char at 725K, but is much higher than the ratio for that char at 775K.

As with the bituminous char, no relationship between CO_2:CO ratio and oxygen concentration could be established. This may indicate that these reactions are of similar order in oxygen.

An Arrhenius plot was constructed for this material, using rate data from temperatures of 675K, 725K, 775K and 825K, all normalized to an oxygen concentration of 1 mol%. This plot is shown in Figure 3.32. The slope of the line between the points corresponding to 675K and 725K yields an activation energy of 32500 cal/gmol, which is similar to the value reported by Dutta and Wen (1977). This activation energy is somewhat lower than that of the bituminous char. This is probably due to the catalytic effect of ash, which is present in large amount in the lignite char (35w% at 0% conversion).

The slope of the line between the points of highest temperature yields an activation energy of around 19000 cal/gmol. As discussed in Section 3.2, this trend of decreasing apparent activation energy may be due to pore-diffusion limitations.

Ω was calculated for this material from (3.4). At 725K, the value is about 0.10; at 825K, it is nearly 0.9. From the correlations, η is about 0.8. Thus, pore-diffusion limitations are not negligible at this temperature for this material.

Interestingly, the CO_2:CO ratio did not decrease for temperatures above 725K. This results in the nearly parallel Arrhenius traces shown in Figure 3.33. At the lower temperatures, the activation energy for the CO_2 reaction is 31000 cal/gmol, while for the CO reaction, it is about 36000 cal/gmol. At the higher temperatures,

the activation energies are 17000 cal/gmol and 18000 cal/gmol, respectively. Again, it appears that both reactions are limited to the same extent by diffusion of oxygen in the micropores.

For the bituminous char, the effect of pore structure on reaction was studied using a "thermopulsing" technique. An alternative approach was used to study the effect of pore structure in the lignite char: Approximately 1 gram of the char was partially oxidized in a muffle furnace at 650K in an ambient of air for 45 minutes. The material was found to have a conversion close to 30%. Samples of this material were then oxidized at 675K, 725K, and 775K in the quartz tube reactor. Figure 3.34 compares the rates obtained at 675K for the material preoxidized to a conversion of 30% in the muffle furnace and the fresh char. Initially, the material that was preoxidized in the muffle furnace has a higher rate of reaction. After a small amount of oxidation, the rate of the "preoxidized" material falls to values near that of the fresh char. Similar behavior is observed when these chars are oxidized at 725K, as seen in Figure 3.35. A much greater difference is observed when the materials are oxidized at 775K. Figure 3.36 shows that the rate of the "preoxidized" material starts at nearly three times the rate of the fresh char. It is possible that the "preoxidized char" contained pores that were more accessible to oxygen, particularly at the highest temperatures. An alternative explanation is that partial oxidation of the char at 675K caused oxygen to chemisorb on the surface of the char. This chemisorbed oxygen may have been removed during subsequent oxidation at higher temperature.

As a contrast, another sample of char was oxidized to nearly the same level

of conversion (28.8%) in a high-temperature furnace at 1500K (see Chapter 4 for details). This material was subsequently oxidized at 725K. The observed rate of oxidation is plotted against conversion in Figure 3.37. For comparison, the rate of oxidation for the same cut of char (61-74μm) is shown. Clearly, oxidation at high temperature reduces the apparent reaction rate.

3.5 Characterization of Lignite Char

The methods described in Section 3.3 were used to characterize the partially oxidized samples of PSOC 1443 chars.

Figures 3.38 and 3.39 show particle-size distributions for two different size cuts (45-63 μm and 75-106 μm) of lignite coal. In both cases, the particles shrink on the average. This is likely due to fragmentation or attrition.

3.5.1 Microscopy

Visual observation using an optical microscope showed that these particles were quite irregular in shape. There was no discernible difference from the precursor material.

Electron microscopy has shown that the surface of the lignite char particles are quite rough (Figure 3.40). It is difficult to distinguish the carbon surface from the ash residing on it.

There is little visible change after conversion to 28% at 725K, as seen in Figure 3.41. After oxidation to 55%, a thicker layer of ash appears to be resting on the surface. Interestingly, one of the particles had ash particles that were spherical, indicating that the ash was molten at some time (Figure 3.42). The ash probably

melted during pyrolysis at 1600K. It is not known why other particles did not show round ash particles.

The ash appeared to remain agglomerated even after complete burnout, as shown in Figure 3.43. The individual ash particles are irregular, so they did not pass through a molten state. They can be separated by crushing.

3.5.2 Gas Adsorption

Surface areas for the lignite char were obtained in a manner similar to that outlined above (cf. Section 3.3.2). A typical isotherm is shown in Figure 3.44. The sample was unburned 1600K PSOC 1443 char. There is significant adsorption beyond 350 torr, indicating the presence of pores with diameters greater than 40Å. This is confirmed by Figure 3.45, which is a plot of pore volume distribution derived from the same isotherm. The solid line is the result obtained from the unsmoothed isotherm; the dashed curve is obtained by first fitting the appropriate interval of the isotherm to a fifth-degree polynomial, then performing the pore-volume inversion.

Figure 3.46 shows BET surface area (corrected for ash) versus conversion for this char. Unlike the case of bituminous char, the unburned material has a significant surface area. Also, a shallow maximum in the surface area per carbon mass is apparent at intermediate conversions. These areas are substantially higher than those of the partially oxidized bituminous chars.

Capillary condensation of nitrogen was used to monitor pore growth with conversion. Figure 3.47 shows total pore volume (20-200 Å) as a function of conversion of 1600K lignite char. The volume of pores in this size range grew significantly with conversion.

An interesting study of evolving pore structure was carried out by first oxidizing a sample of char at high temperature. This material was partially oxidized at low temperature to observe the development of surface area. The result is shown in Figure 3.48. The maximum surface area is much smaller than that of the untreated material. This may be due to thermal annealing of the microporous structure during high temperature oxidation (Smith and Tyler (1972)).

Carbon dioxide uptakes were measured for a few chars. The results are given in Table 3.3.

3.5.2.1 Intrinsic Rate of Lignite Char

The areas from Figure 3.46 were used to calculate the intrinsic rate as a function of conversion for the lignite char, as shown in Figure 3.49. There is an initial drop, as in the case of bituminous char. Again, this may be due to the inability of nitrogen to penetrate the micropores at low conversions. Beyond that, the intrinsic rate rises slightly and subsequently falls. This may be due to the presence of large amounts of ash, which catalyzes the reaction but also acts to inhibit mass transfer at high conversion.

The intrinsic rate of the lignite char at 725K is comparable to that of the bituminous char at 775K. This is partly due to the lower rank of the parent coal (Jenkins *et al.* (1973)). It must be noted, however, that the hydrogen content of this char is lower (0.43%) than that of the bituminous char (1.0%). Perhaps the lower hydrogen content is overcome by the catalytic effect of mineral matter.

The intrinsic rate was also calculated for the material partially oxidized at high temperature. On this basis, the rate is higher than that of the original material,

until a conversion of 60% is achieved, as seen in Figure 3.50.

3.5.3 Oxygen Chemisorption

Oxygen chemisorption was carried out on selected samples of the lignite chars in order to determine "active" surface areas. The procedure is described in Section 3.3.3. The results for unburned char and two partially oxidized chars are shown in Table 3.3. The uptakes are generally higher than those of the partially oxidized bituminous chars. They appear to follow the same trend as intrinsic reactivity.

3.5.4 Mercury Porosimetry

Mercury porosimetry was done on several partially oxidized samples of the lignite char. The corresponding pore-volume distributions were obtained from the Washburn equation, assuming cylindrical pores as previously described. Pore-volume distributions obtained by this method are given in Figures 3.51 and 3.52 for unburned char and char partially oxidized (55%) at 725K. There is a significant amount of porosity over the entire range of measurement, including those pores with radii between 30 Å and 1000 Å. This is in contrast to the bituminous chars, which had very few pores of this size. Again, some of the volume in the $5x10^4$ to 10^5Å range is due to interparticle voids.

The volumes of all pores generally tend to grow with burnoff, as shown in Figure 3.53. In order to more clearly visualize the growth of pores, the pore sizes were divided into two ranges: 32-500 Å and 500-17600 Å. Total volumes for each group were also calculated at each level of conversion from the given pore-volume-distribution plots. Figure 3.53 shows that total volume of pores in these size ranges

steadily increase with conversion.

3.6 Low-Temperature Oxidation of Subbituminous Char

Several low temperature oxidation experiments were carried out for the char derived from the subbituminous coal, PSOC 1488. The rate of oxidation of this char was measured at 725K in 2 mol% and in 5 mol% oxygen. The results of these experiments showed that the reaction order with respect to oxygen for this char is 0.5 at 725K. The observed oxidation rates were normalized to an oxygen concentration of 1 mol% and plotted in Figure 3.54. There is an initial drop in observed reaction rate, followed by relatively constant reactivity. At conversions above 40%, the rate per carbon mass slowly falls. The two runs give reproducible results.

An Arrhenius plot was made based on data from three different temperatures: 725K, 775K and 875K. Figure 3.55 shows that the slope of the line corresponding to the lowest temperatures gives an activation energy of 33000 cal/gmol; the slope from the points at highest temperature yields an activation energy of only 14000 cal/gmol.

Ω was calculated for this material from (3.4). At 725K, the value is about 0.08; at 825K, it is around 0.5. From the correlations, η is about 0.9. Thus, pore-diffusion limitations are not completely negligible at this temperature for this material.

The rates of CO_2 and CO production were determined at 725K in 1 mol% oxygen. Again, the ratio of rates remained constant after a small amount of conversion, as seen in Figure 3.56. The ratio was about 2.2, which was smaller than that of the 1600K PSOC 1451 char at 725K, but larger than that of the 1600K PSOC 1451

char at 775K. No trend with oxygen concentration was found.

The Arrhenius plots for the separate reactions are given in Figure 3.57. The reactions appear to become limited to similar extents, as observed with the two other chars.

3.7 Characterization of Subbituminous Char

The methods described in Section 3.3 were used to characterize the partially oxidized samples of PSOC 1488 chars.

The particle size distribution for char derived from the 45-63 μm cut of subbituminous char is given in Figure 3.58. As in the case of the lignite, particles appear to shrink on the average.

3.7.1 Microscopy

Visual observation using an optical microscope showed that both the raw coal and char particles were quite irregular in shape. No outstanding features were discernible.

Electron micrographs in Figure 3.59 show that the char particles have a round, bubbly appearance. This indicates that the particles underwent plasticization during pyrolysis. Interestingly, these particles did not swell significantly, as did the bituminous char particles.

Figures 3.60 and 3.61 show particles from samples that were oxidized to 18% and 40% at 725K. Ash appears to accumulate on the surface.

3.7.2 Gas Adsorption

Nitrogen adsorption isotherms of this char were obtained at several conversions.

The isotherm for unburned char is given in Figure 3.62. There is strong adsorption at pressures less than 10 torr, indicating the presence of a relatively large volume of micropores. This is similar to what was observed for the bituminous chars; this may indicate that chars that go through a plastic state are generally microporous. Unlike the bituminous char, there is significant adsorption at pressures above 400 torr. Figure 3.63 shows the pore-volume distribution derived from capillary condensation information.

The surface area normalized with respect to carbon mass is shown as a function of conversion in Figure 3.64. The area increases quickly at low conversions. This is indicative of a porous network that is initially difficult for nitrogen to penetrate.

Carbon dioxide uptakes were measured according to the procedure outlined above. The uptakes remained quite constant with conversion, as seen in Table 3.4.

3.7.2.1 Intrinsic Rate of Subbituminous Char

The area curve (Figure 3.61) was used to calculate the intrinsic rate of 1600K PSOC 1488 char as a function of conversion, shown in Figure 3.65. The intrinsic rate decreases initially with conversion, but levels off and remains constant for the remaining observed range of conversions. This behavior is strikingly similar to that of the bituminous char.

3.7.3 Oxygen Chemisorption

Oxygen chemisorption was carried out on selected samples of this char in order to determine "active" surface areas. The procedure is described in Section 3.3.3. The results for several experiments are shown in Table 3.4. The uptakes are nearly

constant with conversion.

3.7.4 Mercury Porosimetry

Mercury porosimetry was done on several partially oxidized samples of this char. The corresponding pore-volume distributions were obtained from the Washburn equation, assuming cylindrical pores as previously described. Pore-volume distributions obtained by this method are given in Figures 3.66 and 3.67 for unburned char and char partially oxidized (42%) at 725K. There is a significant amount of porosity over the entire range of measurement, including those pores with radii between 30 Å and 1000Å. This is similar to what is observed in the lignite char. Again, some of the volume in the $5x10^4$ to 10^5Å range is due to interparticle voids.

REFERENCES

Blake, J.H., Bopp, G.R., Jones, J.F., Miller, M.G. and Tambo, W. (1967). *Fuel*, **46**, 115.

Debelak, K.A. and Schrodt, J.T. (1979). Comparison of Pore Structure in Kentucky Coals by Mercury Penetration and CO_2 Adsorption. *Fuel*, **58**, 732.

Dutta, S., Wen, C.Y. and Belt, R.J. (1977). Reactivity of Coal and Char. 1. In Carbon Dioxide Atmosphere. *Ind. Eng. Chem.*, **16**, 20.

Dutta, S. and Wen, C.Y. (1977). Reactivity of Coal and Char. 2. In Oxygen-Nitrogen Atmosphere. *Ind. Eng. Chem.*, **16**, 31.

Field, M.A. (1969). Rate of Combustion of Size-Graded Fractions of Char from a Low-Rank Coal Between 1200K and 2000K. *Combust. Flame*, **13**, 237.

Hamor, R.J., and Smith, I.W. (1973). Kinetics of Combustion of a Pulverized Brown Coal Char Between 830 and 2200K. *Combust. Flame*, **21**, 153.

Hengel, T.D. and Walker, P.L., Jr. (1984). Catalysis of Lignite Char by Exchangeable Calcium and Magnesium. *Fuel*, **63**, 1214.

Jenkins, R.G., Nandi, S.P. and Walker, P.L., Jr. (1973). Reactivity of Heat-Treated Coals in Air at 500oC. *Fuel*, **52**, 288.

Lightman, P. and Street, P.J. (1968). Microscopical Examination of Heat-Treated Pulverized Coal Particles. *Fuel*, **47**, 7.

Mehta, B.N. and Aris, R. (1971). Communications on the Theory of Diffusion and Reaction–VII The Isothermal p-th Order Reaction. *Chem. Eng. Sci.*, **26**, 1699.

Pohl, J.H., Kobayashi, H., and Sarofim, A.F. (1978). The Effects of Temperature and Time on Pulverized Coal Particles. *Combustion Institute Technical Meeting*, Boulder,CO.

Radovic, L., Walker, P.L., Jr. and Jenkins, R.G. (1983). Importance of Carbon Active Sites in The Gasification of Coal Chars. *Fuel*, **62**, 849.

Smith, I.W. and Tyler, R.J. (1972). Internal Burning of Pulverized Semi-Anthracite: The Relation Between Particle Structure and Reactivity. *Fuel*, **51**, 312.

Smith, I.W. and Tyler, R.J. (1974). The Reactivity of a Porous Brown Coal Char to Oxygen Between 630 and 1812K. *Comb. Sci. Tech.*, **9**, 87.

Smith, I.W. (1978). The Intrinsic Reactivity of Carbons to Oxygen. *Fuel*, **57**, 409.

Smith, I.W. (1982). The Combustion Rates of Coal Chars: A Review. *Nineteenth Symposium (International) on Combustion, the Combustion Institute*, 1045.

Snow, C.W., Wallace, D.R., Lyon, L.L. and Crocker, G.R. (1960). *Proc. of the Fourth Conf. on Carbon*, Pergamon Press, New York, p.79.

Street, P.J., Weight, R.P. and Lightman, P. (1969). Further Investigations of Structural Changes Occurring in Pulverized Coal Particles During Heating. *Fuel*, **48**, 343.

Tong, S.B., Pareja, P. and Back, M.H. (1982). Correlation of the Reactivity, the Active Surface Area and Total Surface Area of Thin Films of Pyrolytic Carbon. *Carbon*, **20**, 191.

Tseng, H.P. and Edgar, T.F. (1984). Identification of the Combustion Behavior of Lignite Char Between 350 and 900°. *Fuel*, **63**, 385.

Tseng, H.P. and Edgar, T.F. (1985). Combustion Behavior of Bituminous and Anthracite Coal Char Between 425 and 900°. *Fuel*, **64**, 373.

Walker, P.L.,Jr., Foresti, R.J.,Jr. and Wright, C.C. (1953). Surface Area Studies of Carbon-Carbon Dioxide Reaction. *Ind. Eng. Chem.*, **45**, 1703.

Walker, P.L.,Jr. and Kini, K.A. (1965). Measurement of the Ultrafine Surface Areas of Coals. *Fuel*, **44**, 453.

Weisz, P.B. and Hicks, J.S. (1962). The Behavior of Porous Catalyst Particles in View of Mass and Heat Diffusion Effects. *Chem. Eng. Sci.*, **17**, 265.

Wheeler, A. (1951). Reaction Rates and Selectivity in Catalyst Pores. *Adv. Cat.*, **3**, 249.

Wojtowicz, M., Calo, J.M. and Suuberg, E.M. (1985). The Behavior of Active Sites in a Model Compound Char. *AIChE Ann. Mtg.*, Chicago, Ill.

Pyrolysis Temp.	C(wt%)	H(wt%)	N(wt%)	C:H
1200K	69.94	1.86	1.31	37.6
1400K	76.01	1.03	1.13	73.8
1600K	78.30	0.96	1.10	81.6
Conversion (1400K)				
0%	76.01	1.01	1.38	73.8
2%	72.49	1.03	1.29	70.4
12%	67.16	0.76	1.22	88.4
30%	60.74	0.81	1.14	74.9
65%	50.68	0.66	1.28	76.8

Table 3.1: Elemental analyses of PSOC 1451 chars.

1200K Char		1400K Char	
Conversion %	O_2 Uptake μmoles/g d.m.m.f. char	Conversion %	O_2 Uptake μmoles/g d.m.m.f. char
0	270	0	205
5	105	2	79
19	180	12	107
40	326	30	135
		65	159

Table 3.2: Oxygen uptake of PSOC 1451 chars after 12 hours at 575K.

Conversion %	O_2 Uptake μmoles/g d.m.m.f. char	CO_2 Uptake mmoles/g d.m.m.f. char
0	400	4.5
28.5	250	6.0
55.5	390	7.8

Table 3.3: Oxygen and carbon dioxide uptakes of partially oxidized 1600K PSOC 1443 chars.

Conversion %	O_2 Uptake μmoles/g d.m.m.f. char	CO_2 Uptake mmoles/g d.m.m.f. char
0	250	6.5
18.1	250	6.7
40.3	260	6.7
59.8	280	6.9

Table 3.4: Oxygen and carbon dioxide uptakes of partially oxidized 1600K PSOC 1488 chars.

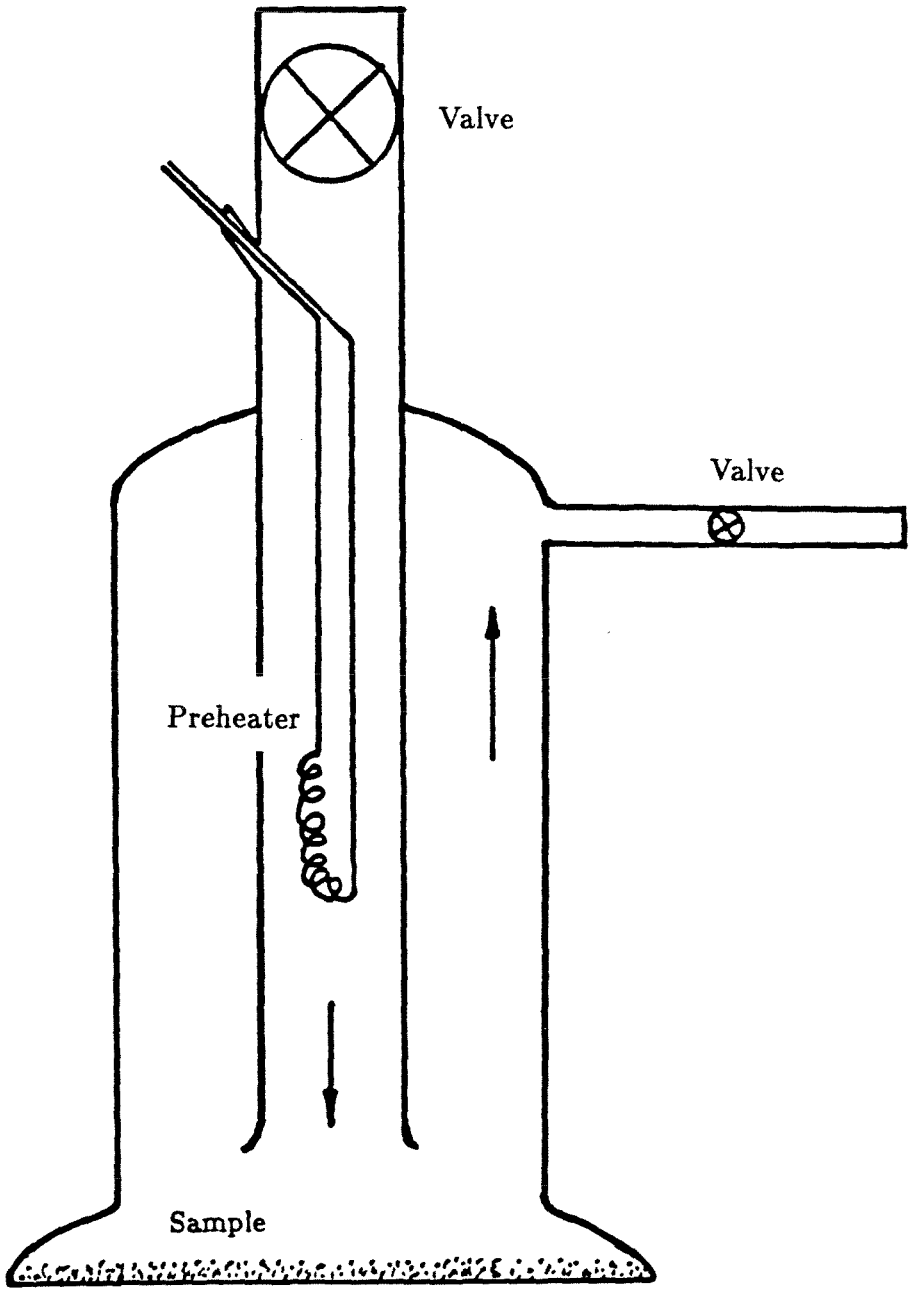

Figure 3.1. Schematic of low temperature quartz reactor.

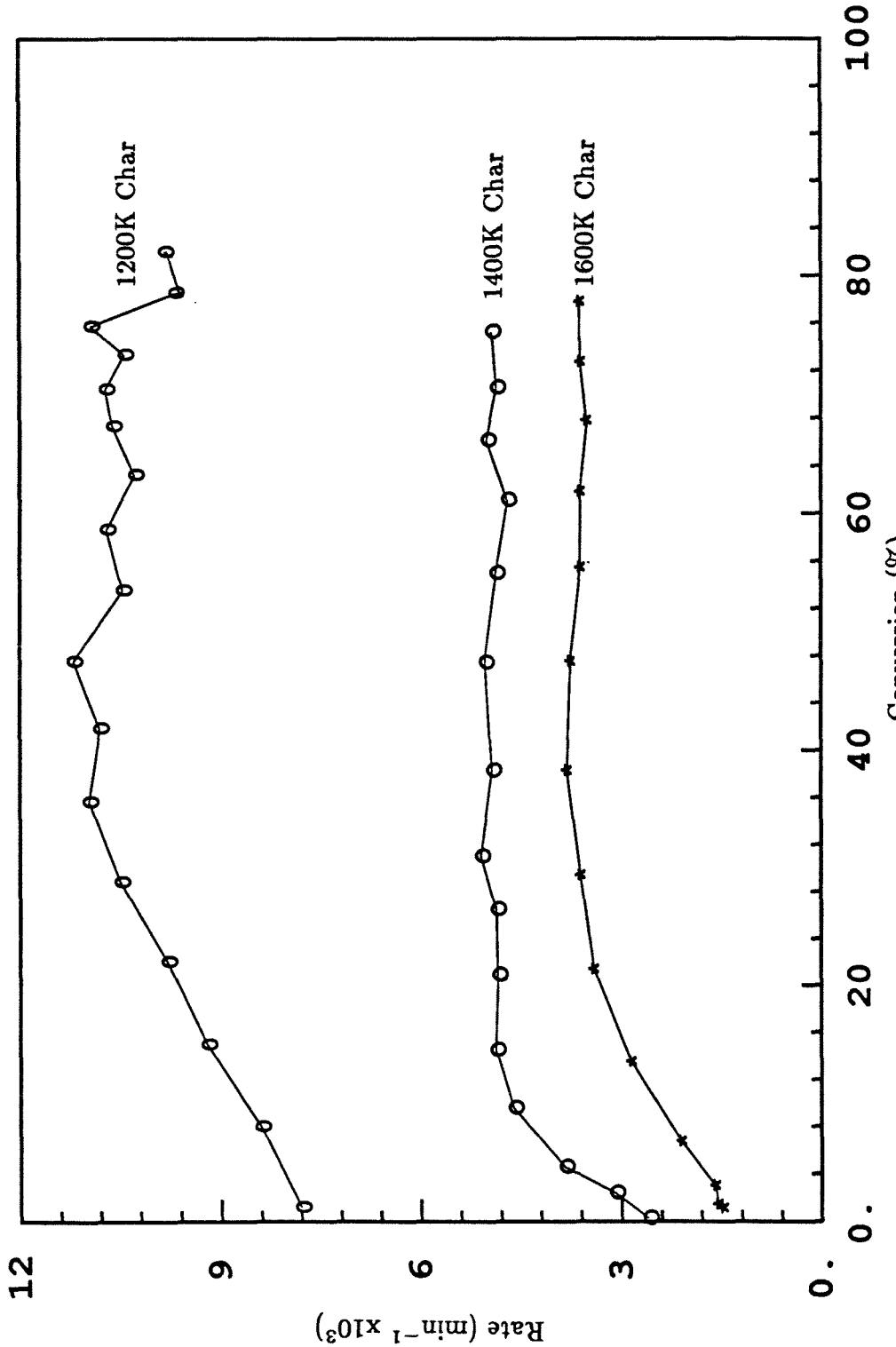

Figure 3.2. Oxidation rates of 104-125μm PSOC 1451 chars at 775K in 1mol% oxygen.

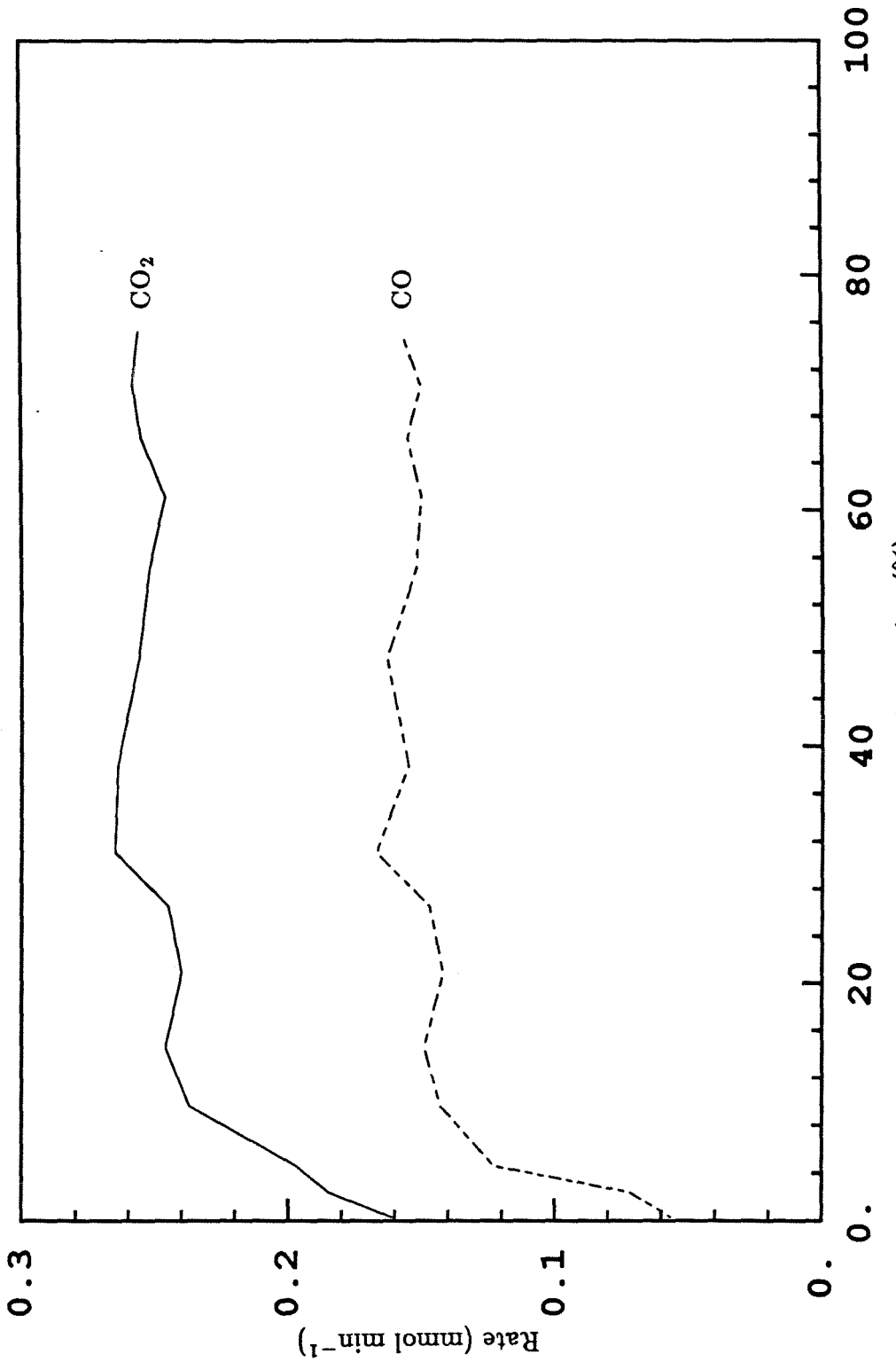

Figure 3.3. Carbon oxide production rates for 1400K PSOC 1451 char at 775K in 1mol% oxygen.

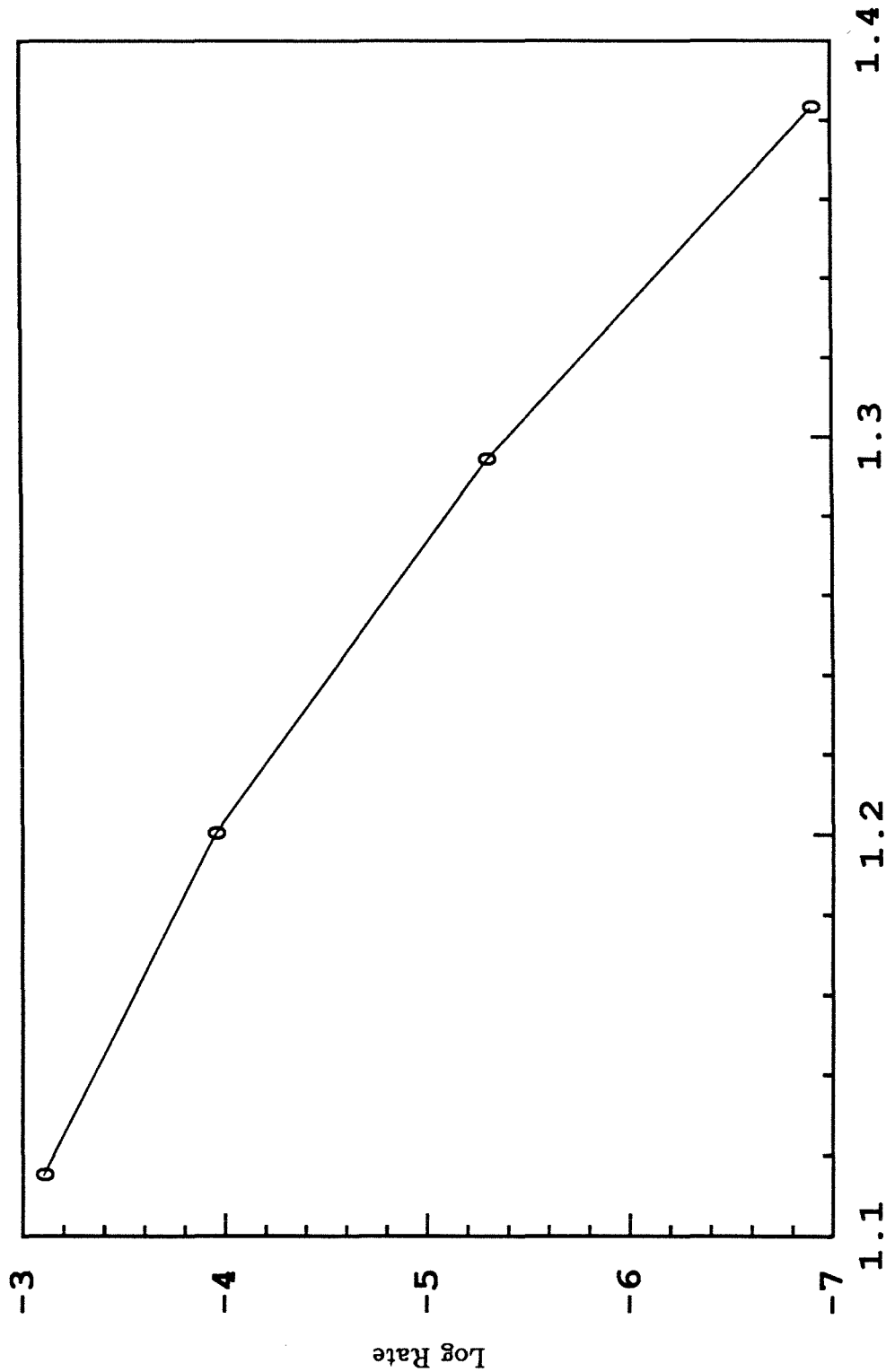

Figure 3.4. Arrhenius plot for 1400K PSOC 1451 char in 1mol% oxygen.

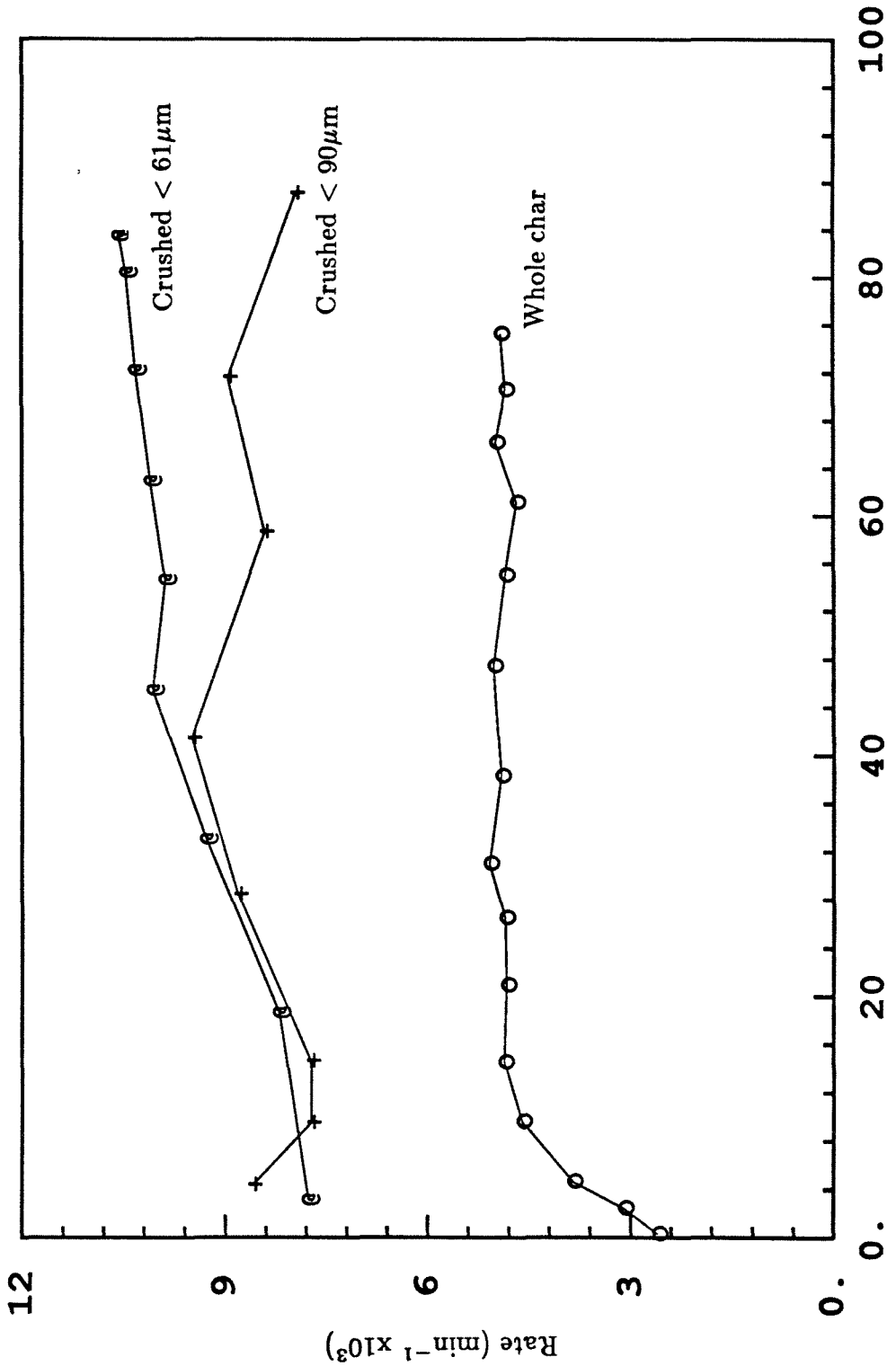

Figure 3.5. Effect of crushing on observed oxidation rate of 104-125μm 1400K PSOC 1451 char.

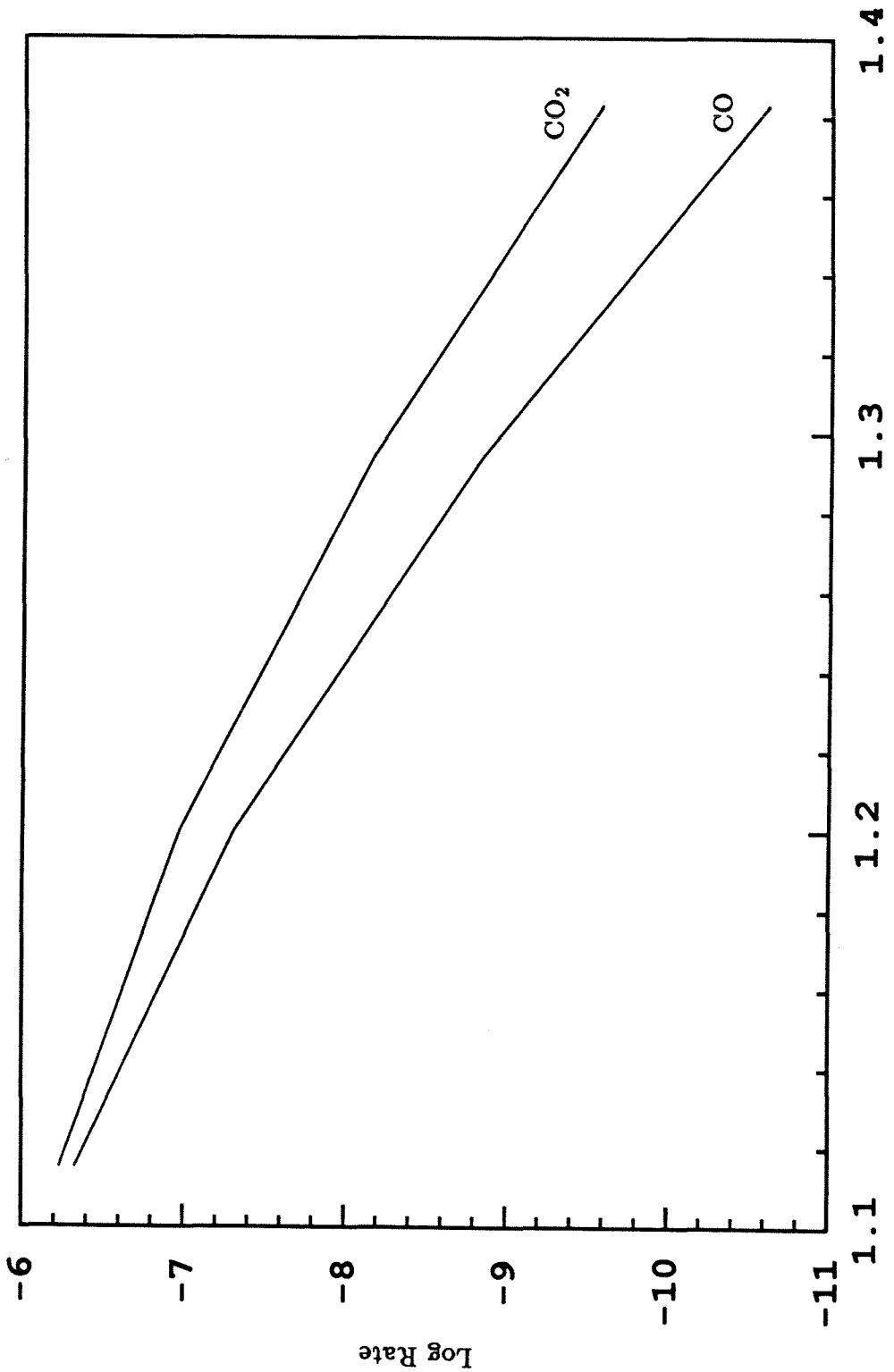

Figure 3.6. Arrhenius plot for carbon oxide production from 1400K PSOC 1451 char in 1mol% oxygen.

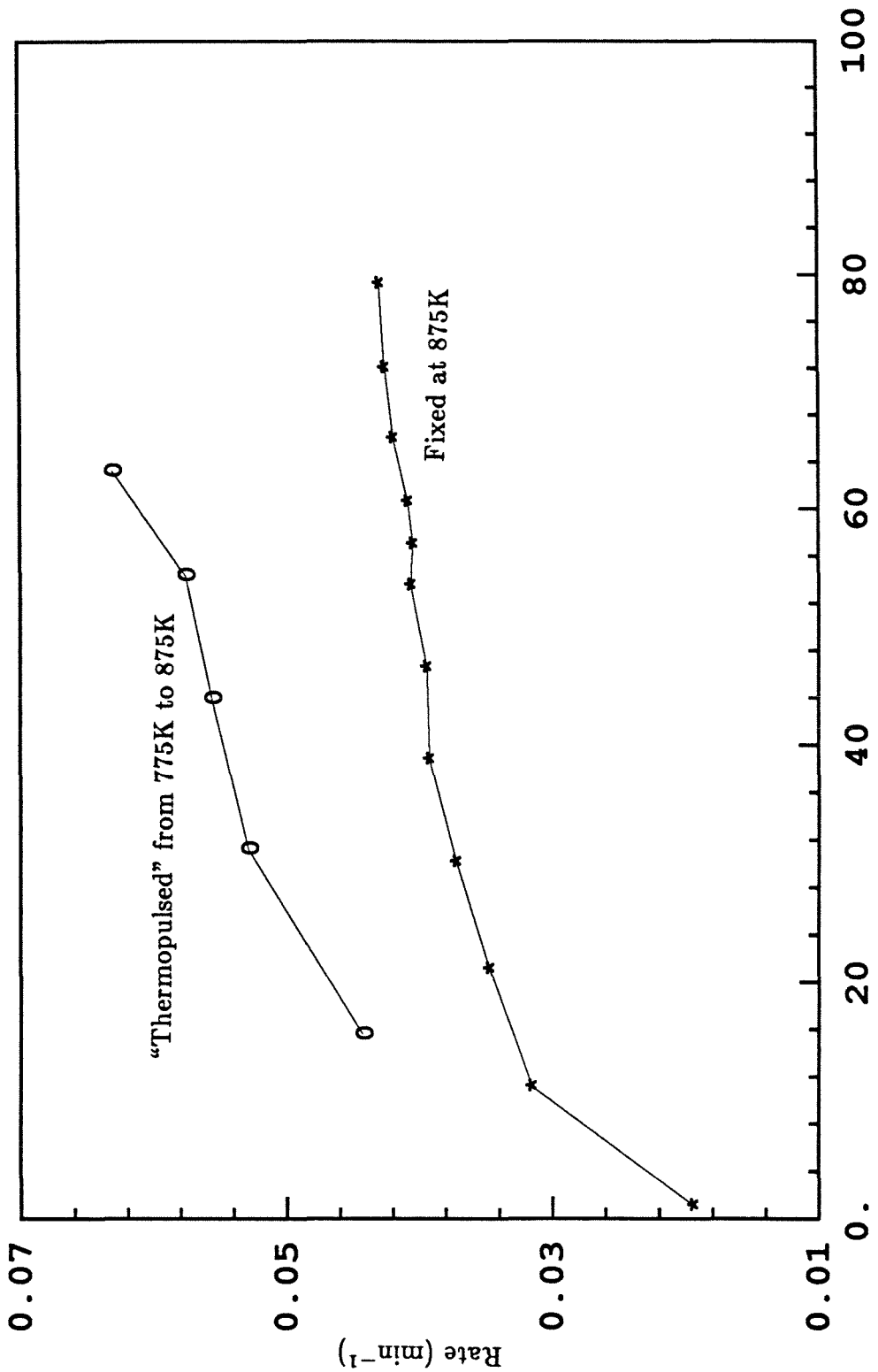

Figure 3.7. Effect of "thermopulsing" 1400K PSOC 1451 char.

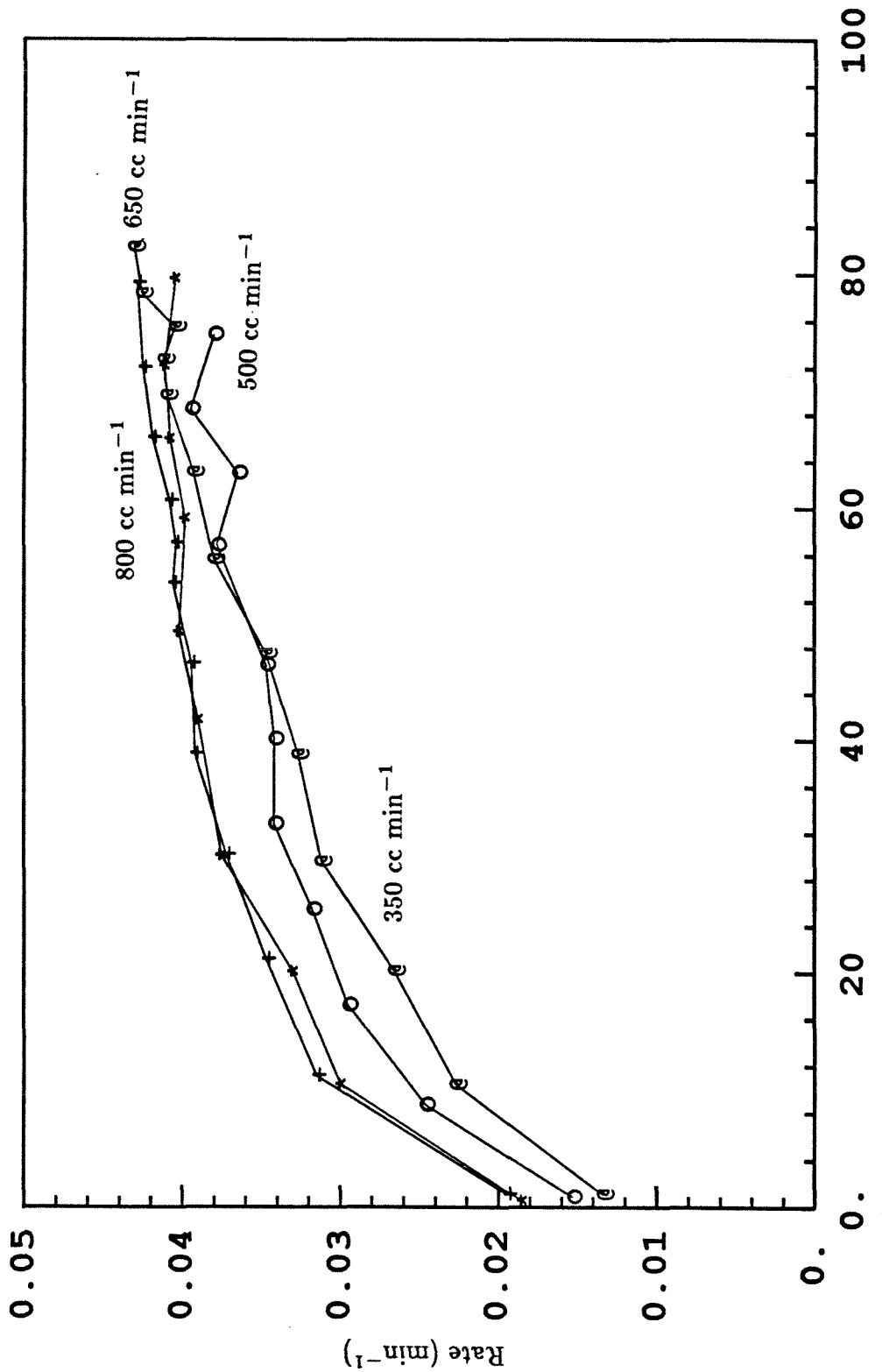

Figure 3.8. Effect of flow rate on observed reaction rate.

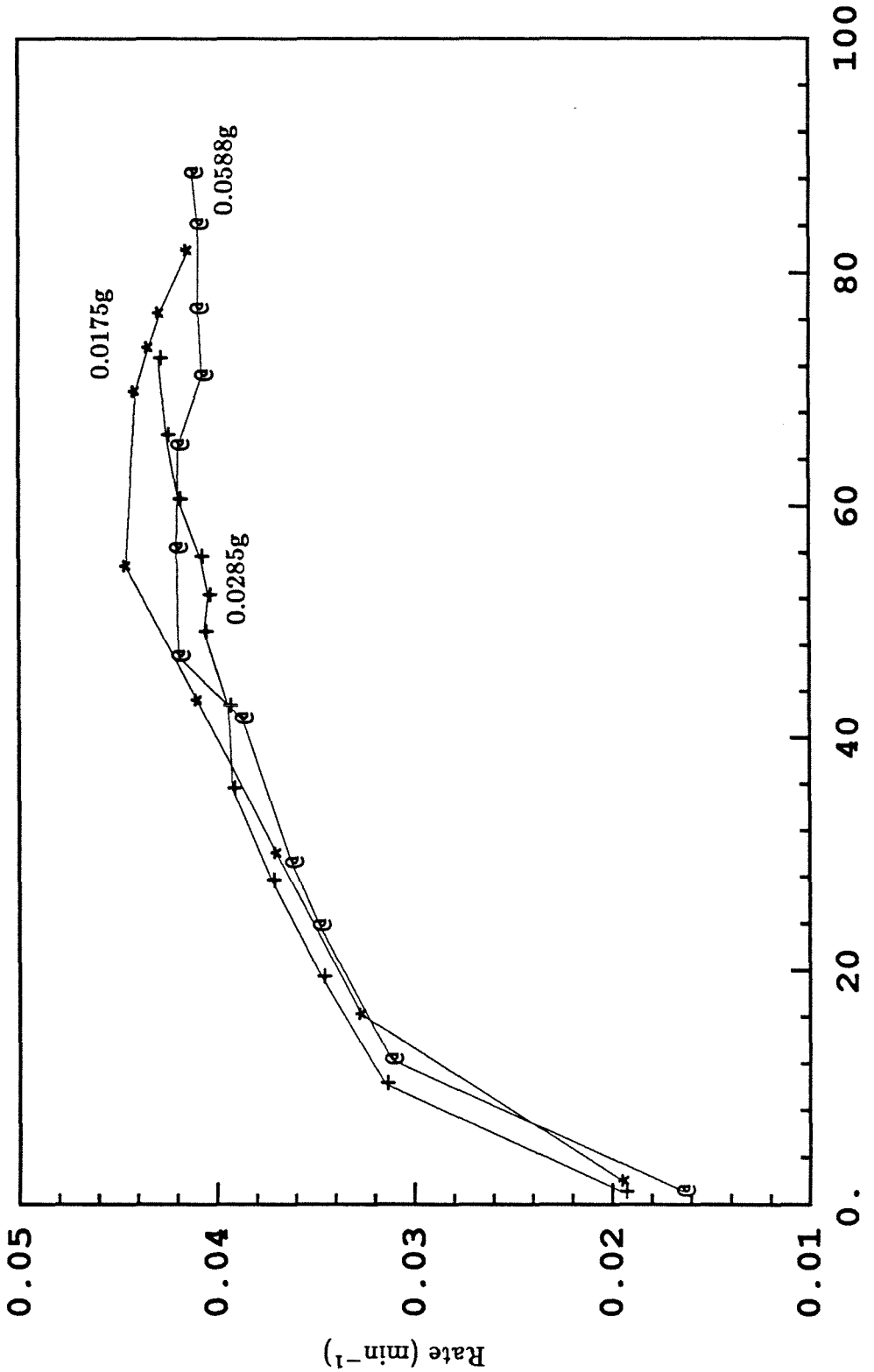

Figure 3.9. Effect of initial loading on observed reaction rate.

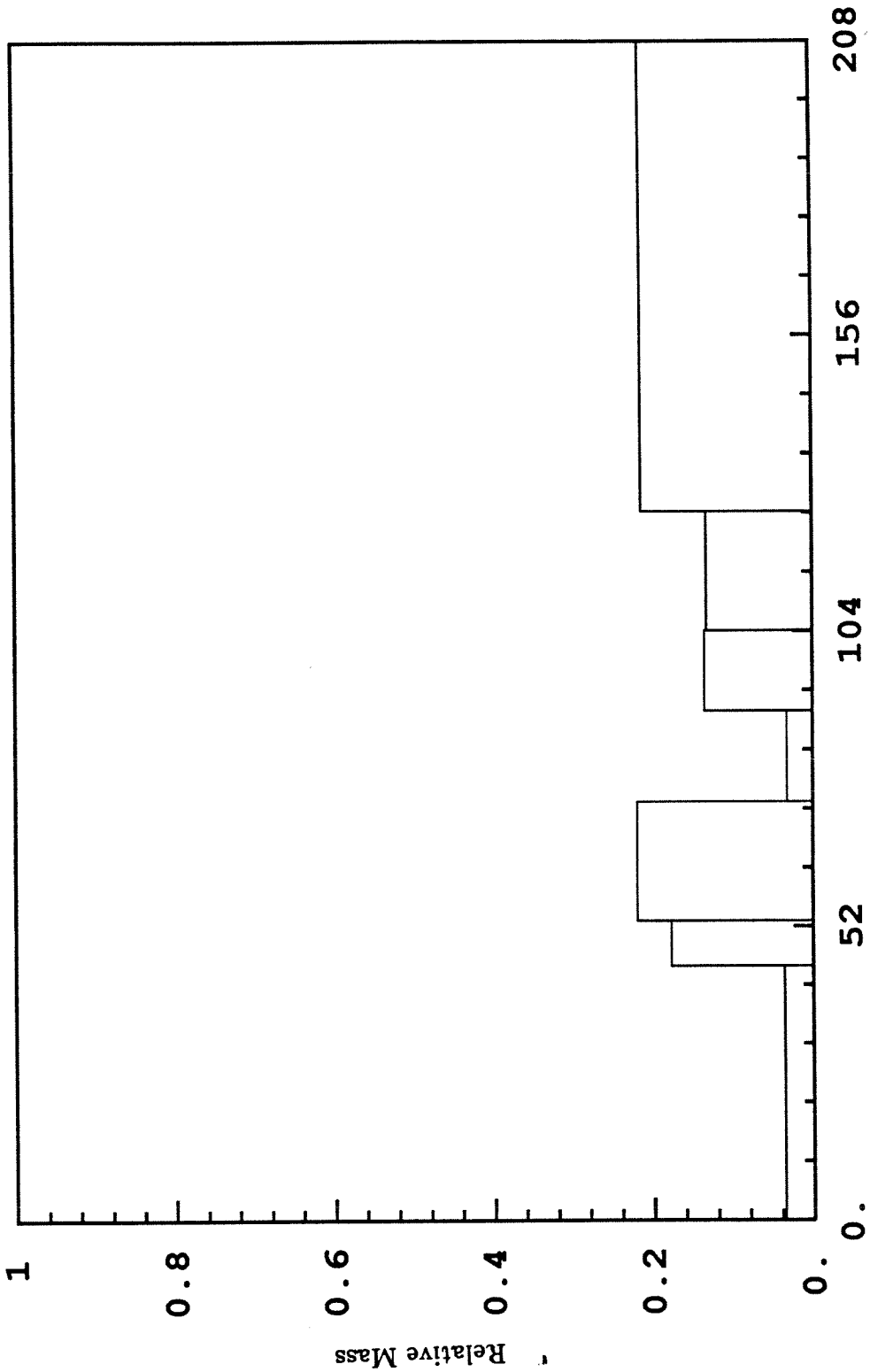

Figure 3.10. Particle size distribution for 1600K char derived from 53-74μm PSOC 1451 coal.

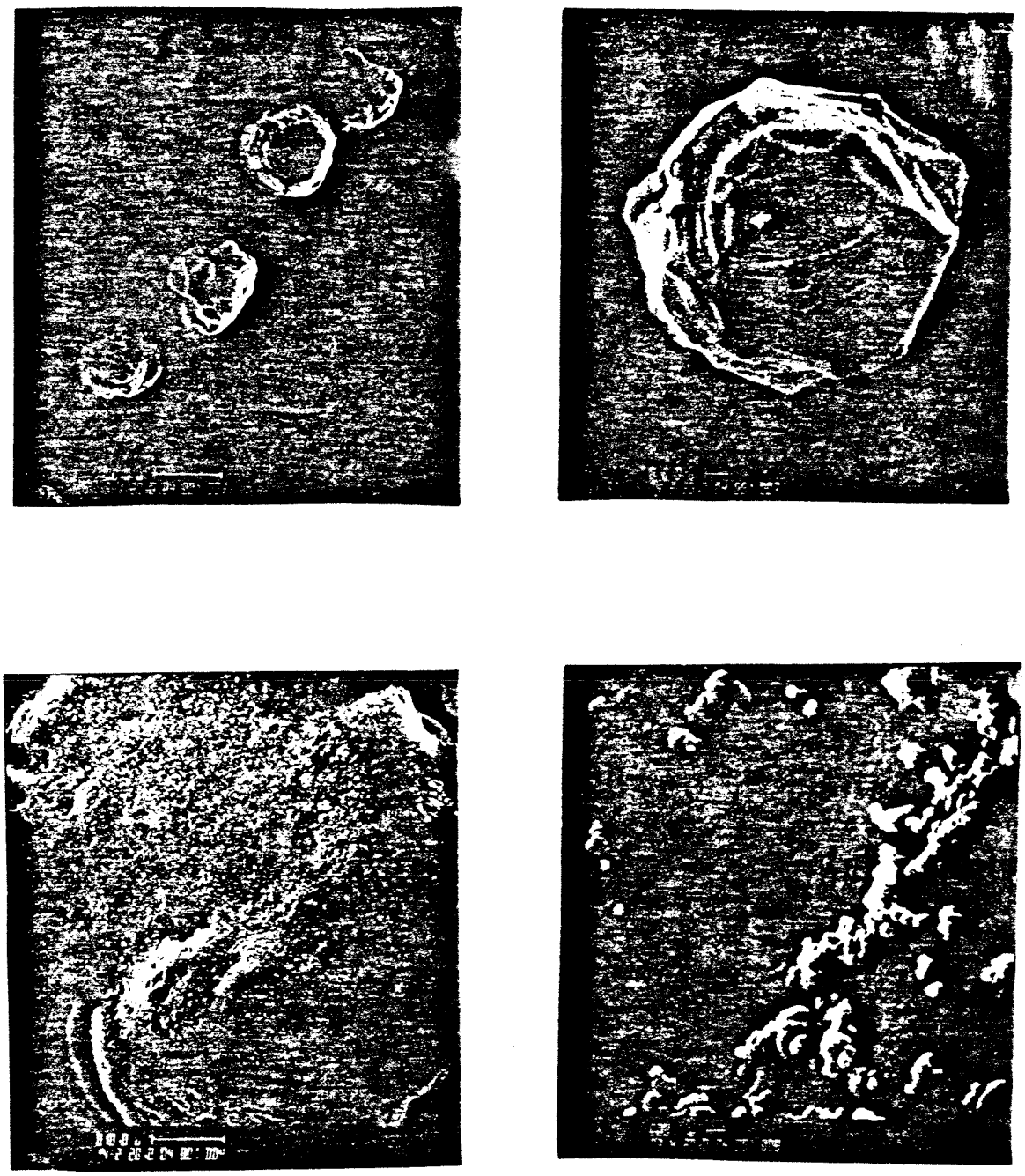

Figure 3.11. Electron micrographs of 1200K char derived from 53-74μm PSOC 1451 coal.

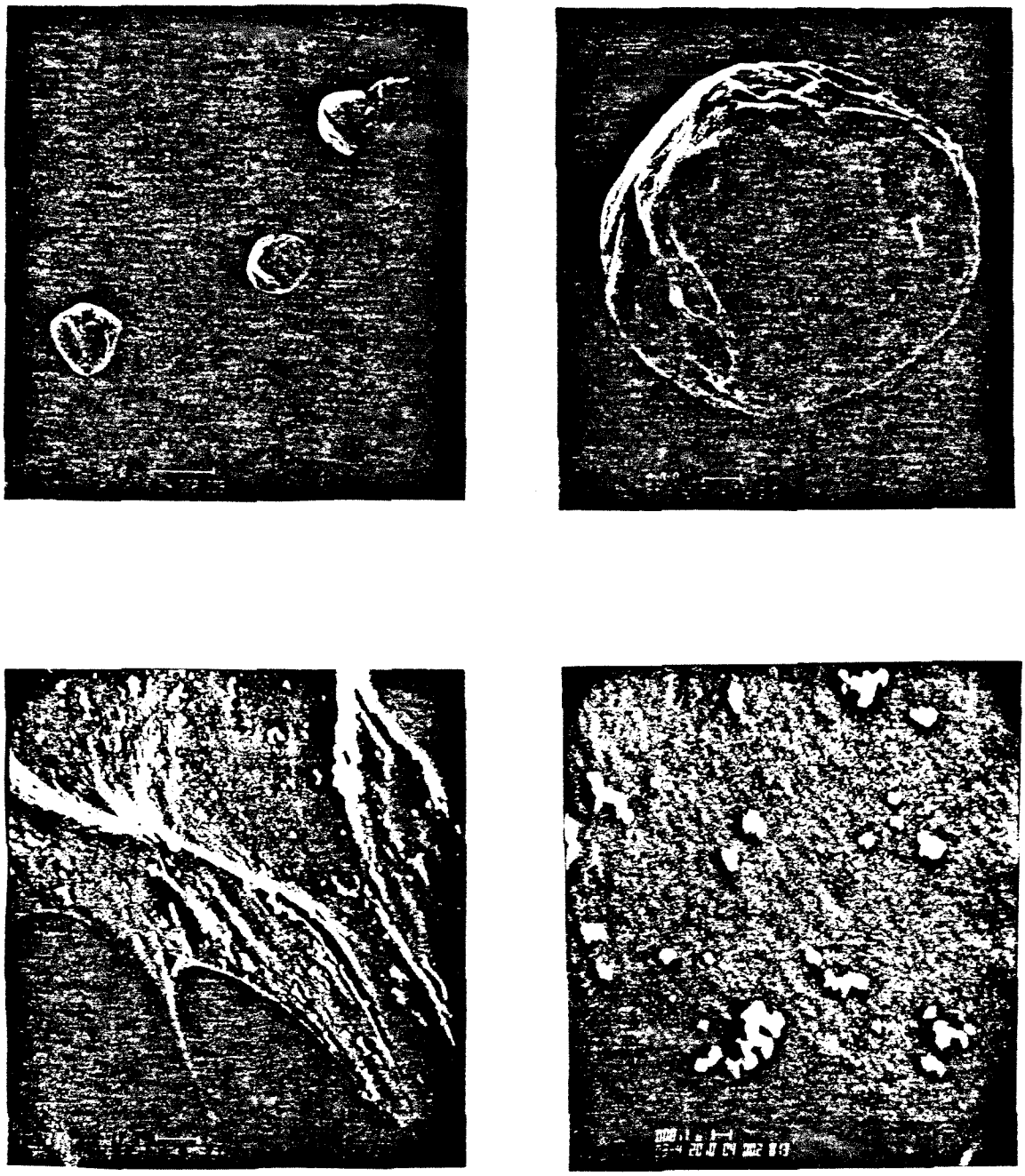

Figure 3.12. Electron micrographs of 1200K PSOC 1451 char after partial oxidation to 26% at 775K.

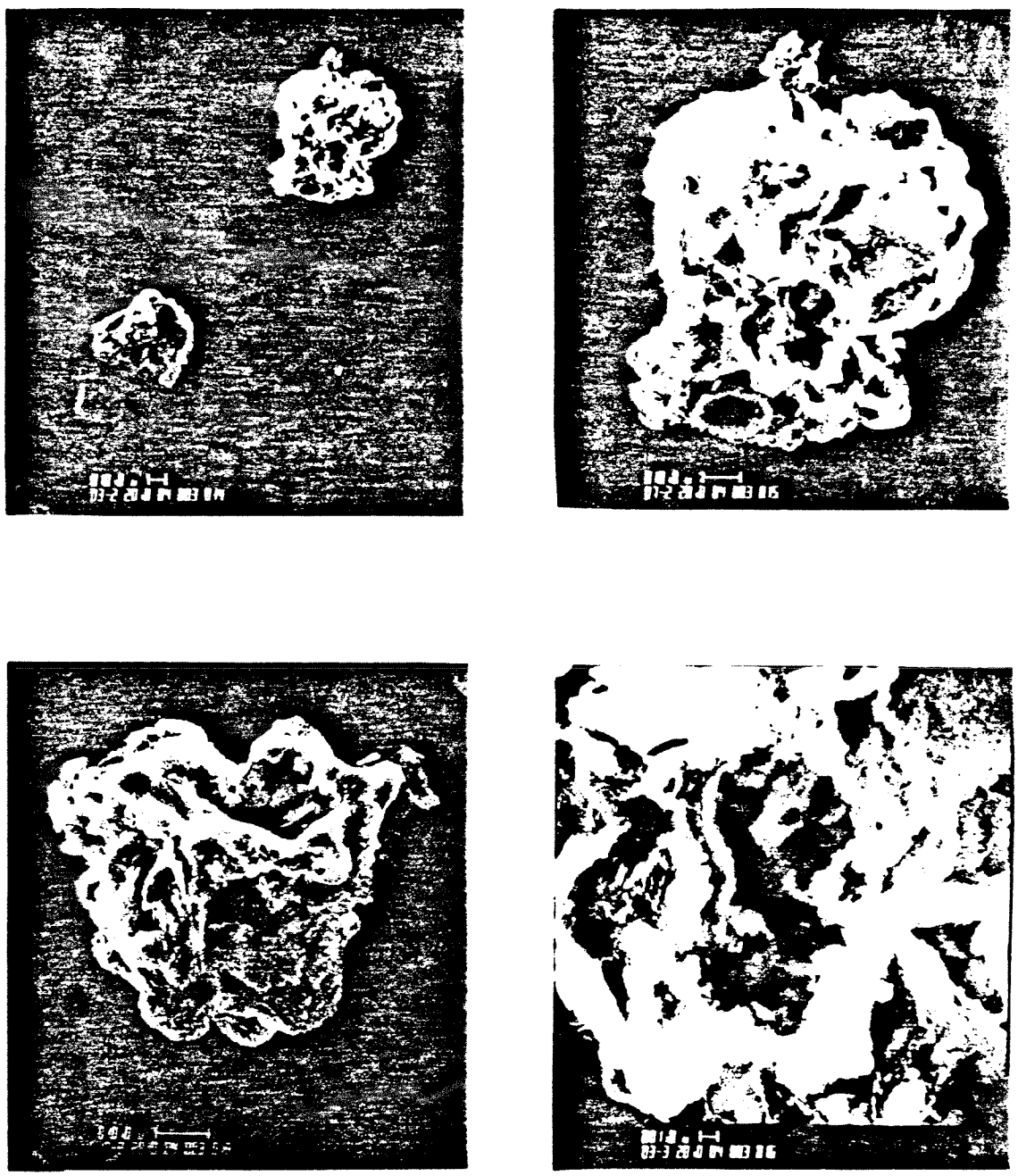

Figure 3.13. Electron micrographs of 1200K PSOC 1451 char after partial oxidation to 64% at 775K.

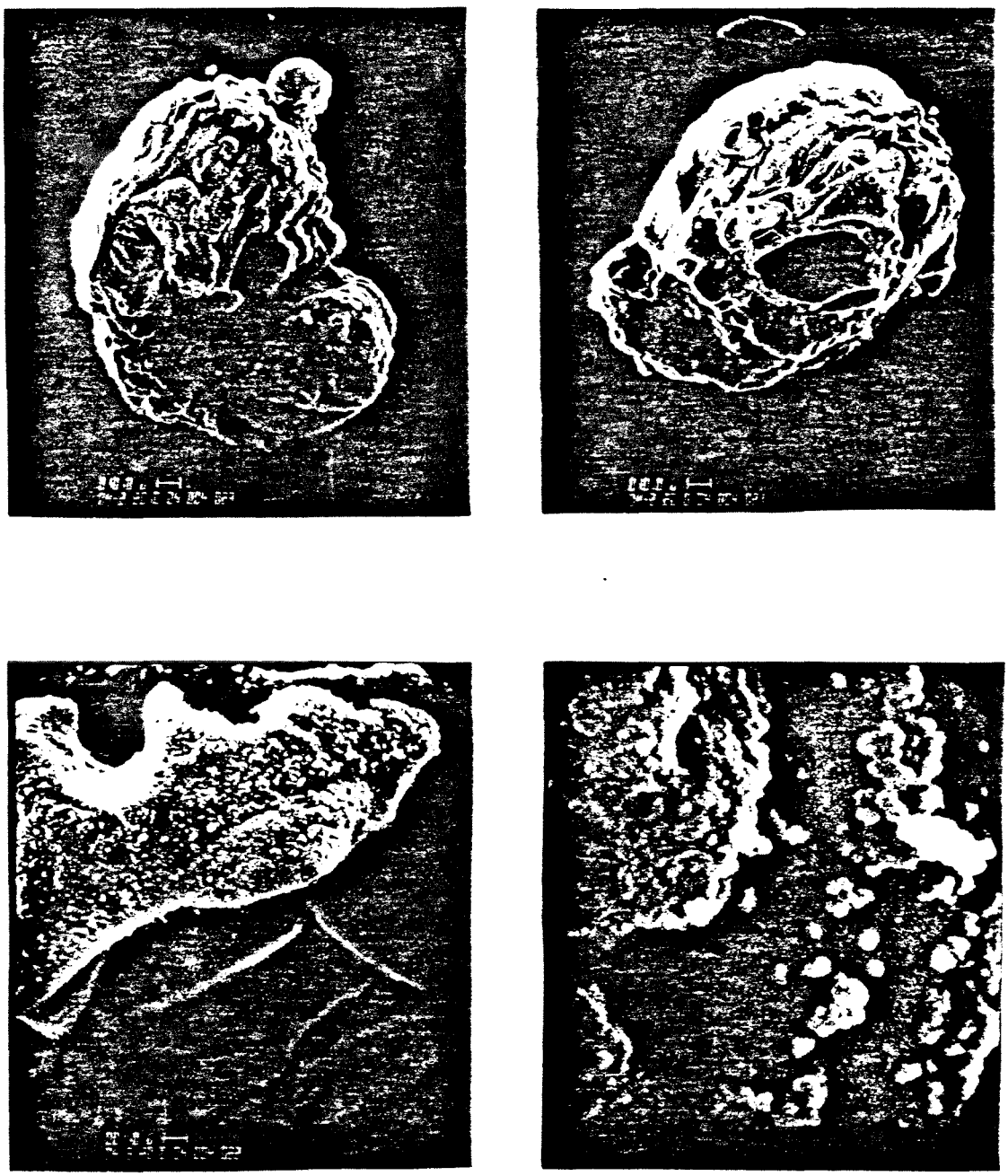

Figure 3.14. Electron micrographs of 1600K char derived from 53-74μm PSOC 1451 coal.

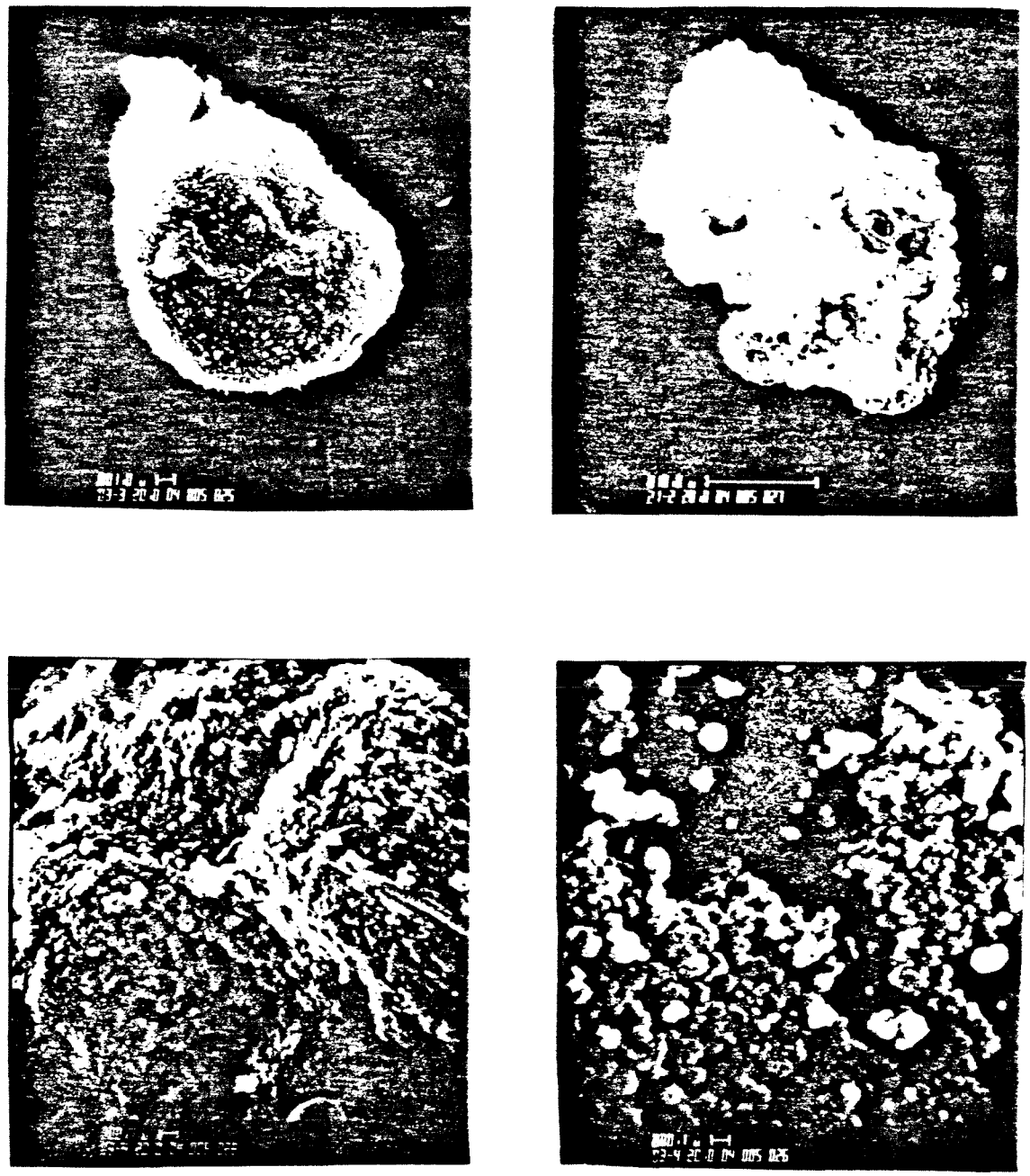

Figure 3.15. Electron micrographs of 1600K PSOC 1451 char after partial oxidation to 30% at 775K.

Figure 3.16. Electron micrograph of 1600K PSOC 1451 char after partial oxidation to 67% at 775K.

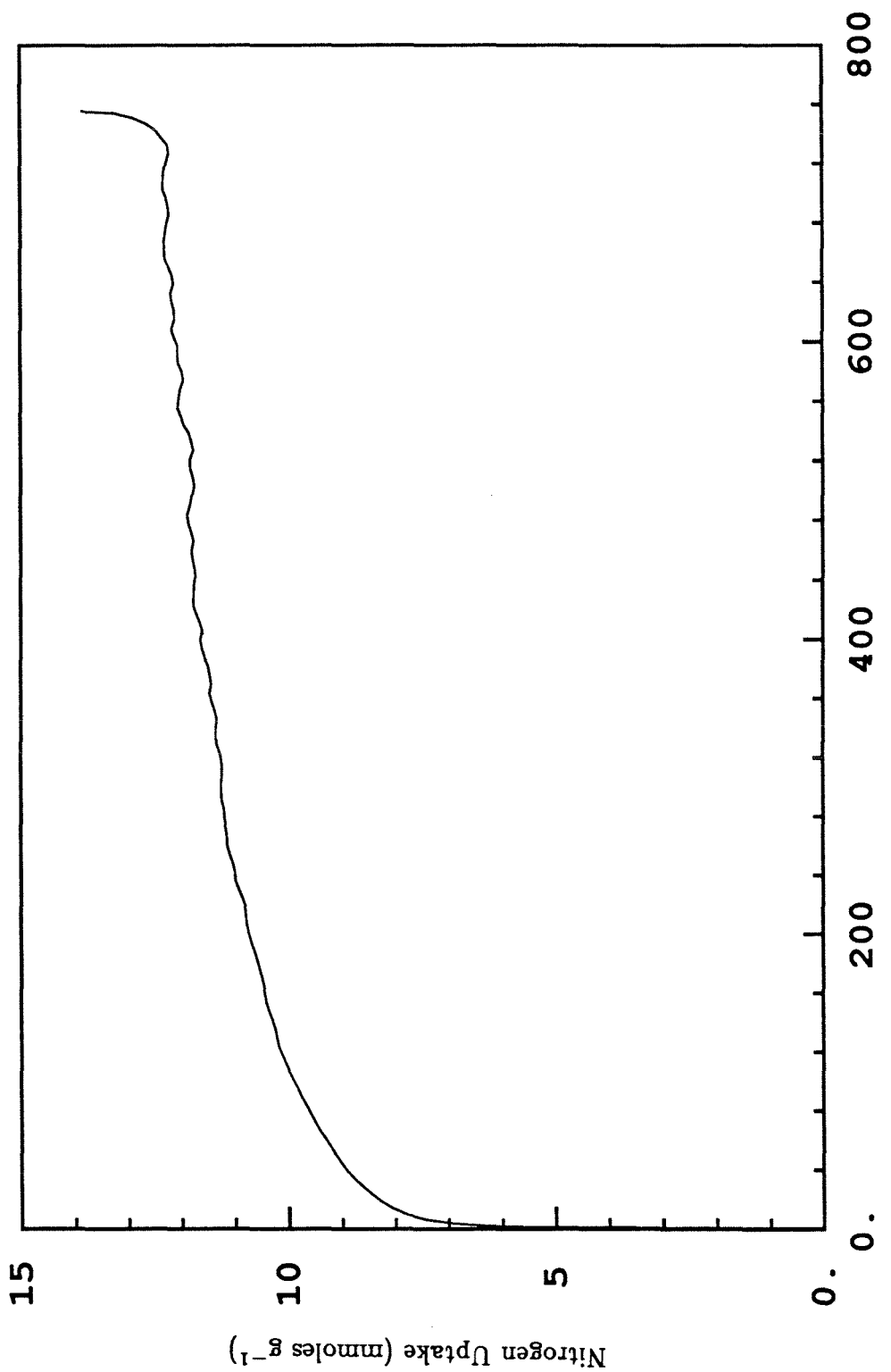

Figure 3.17. Nitrogen isotherm on 45% burnout 1200K PSOC 1451 char.

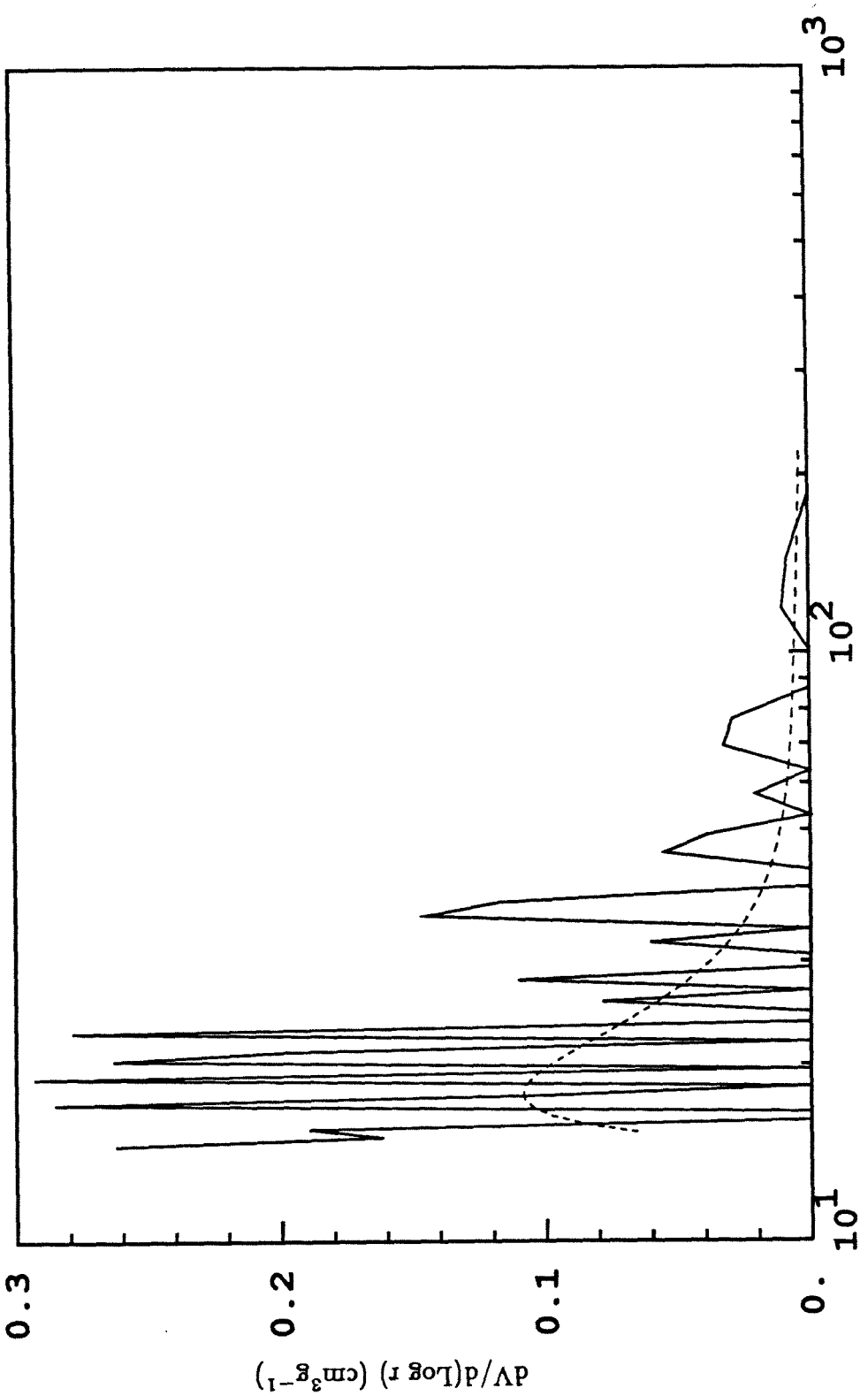

Figure 3.18. Pore volume distribution from capillary condensation in 45% burnout 1200K PSOC 1451 char.

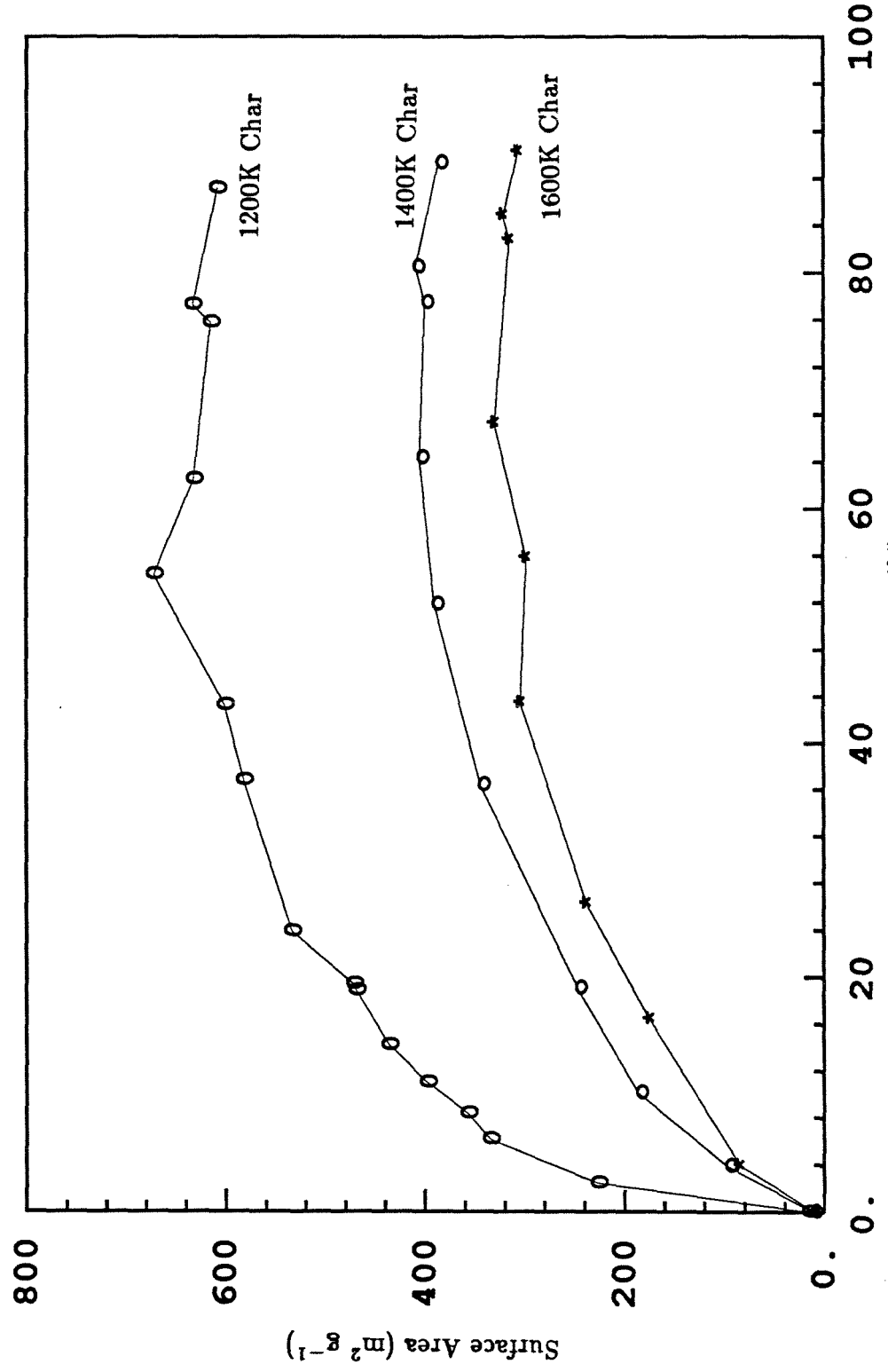

Figure 3.19. Specific surface areas of PSOC 1451 chars versus conversion.

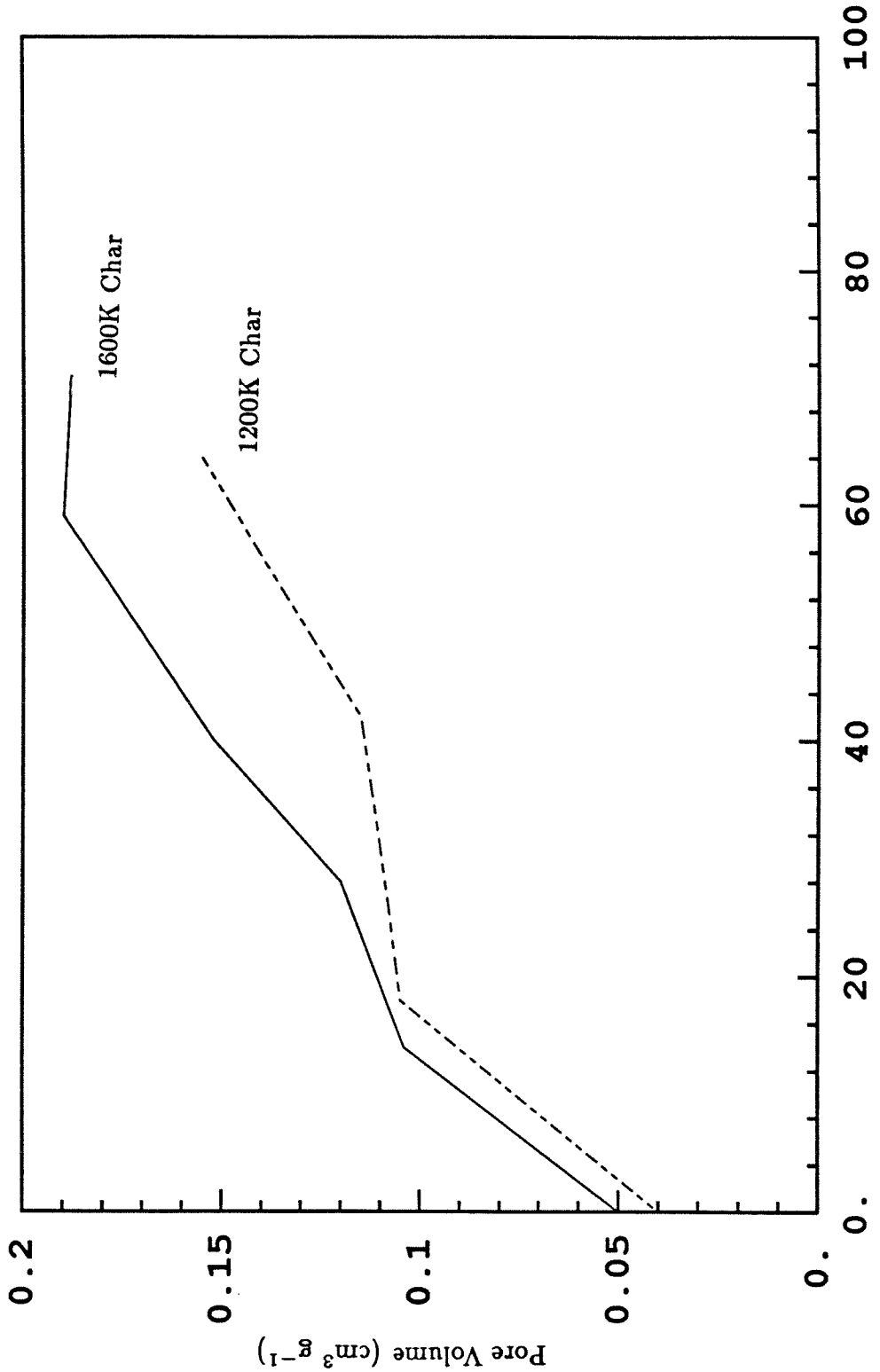

Figure 3.20. Pore volume (radii 16-150Å) as a function of conversion for PSOC 1451 chars.

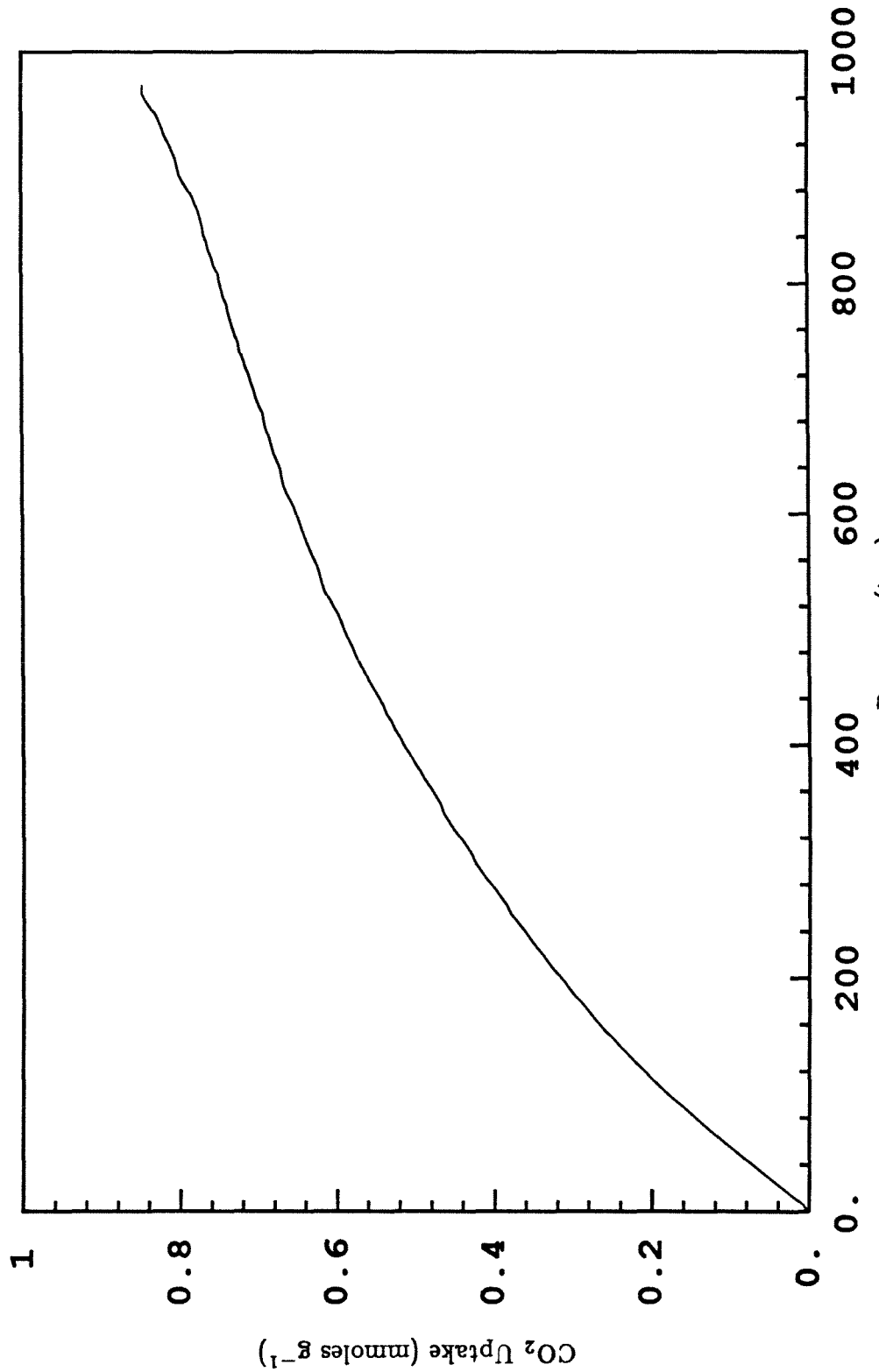

Figure 3.21. Carbon dioxide adsorption on unburned 1400K PSOC 1451 char.

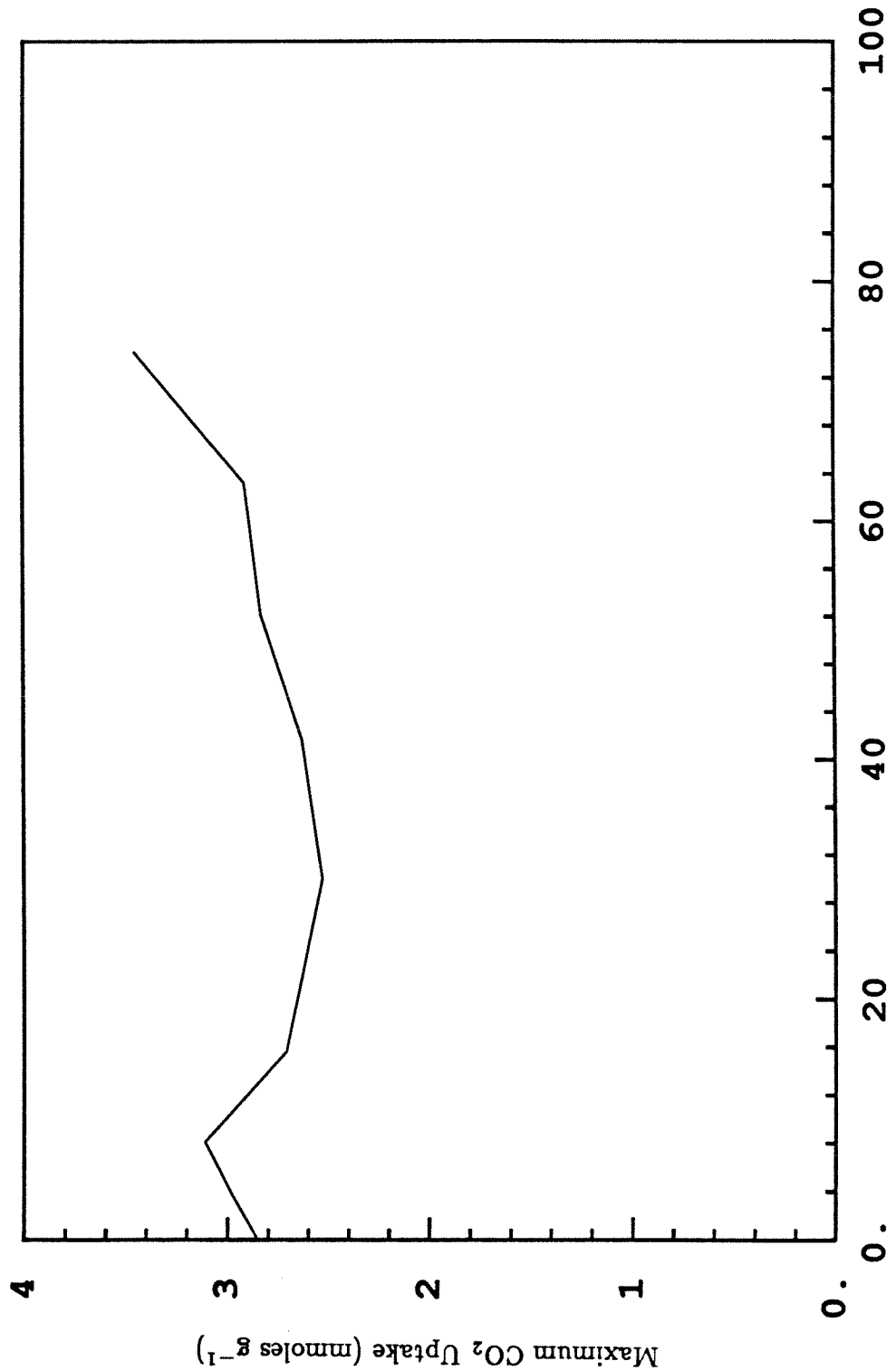

Figure 3.22. Maximum carbon dioxide uptake as a function of conversion 1400K PSOC 1451 char.

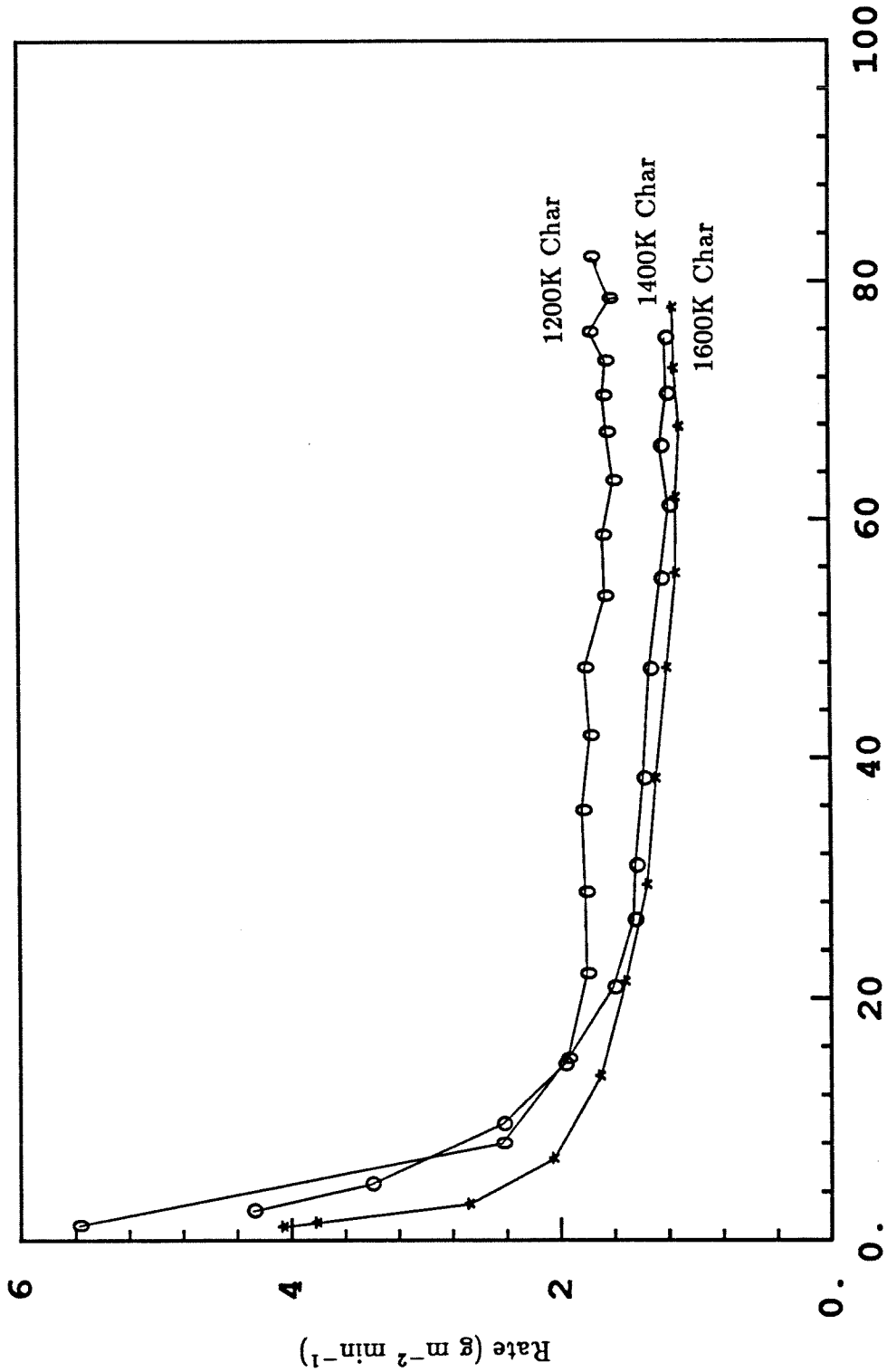

Figure 3.23. Intrinsic rates of PSOC 1451 chars at 775K in 1mol% oxygen.

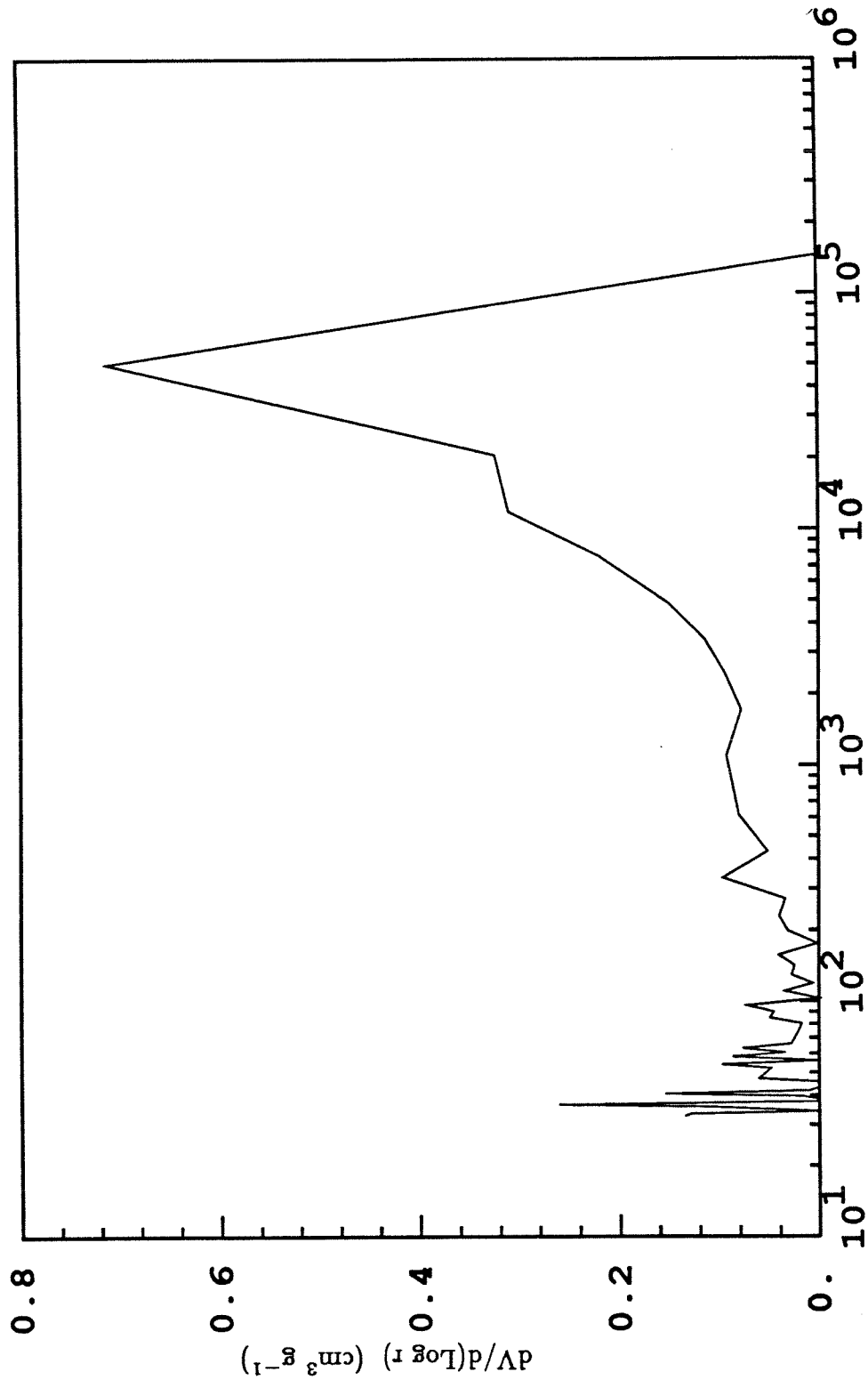

Figure 3.24. Pore volume distribution for 1200K PSOC 1451 char from mercury porosimetry.

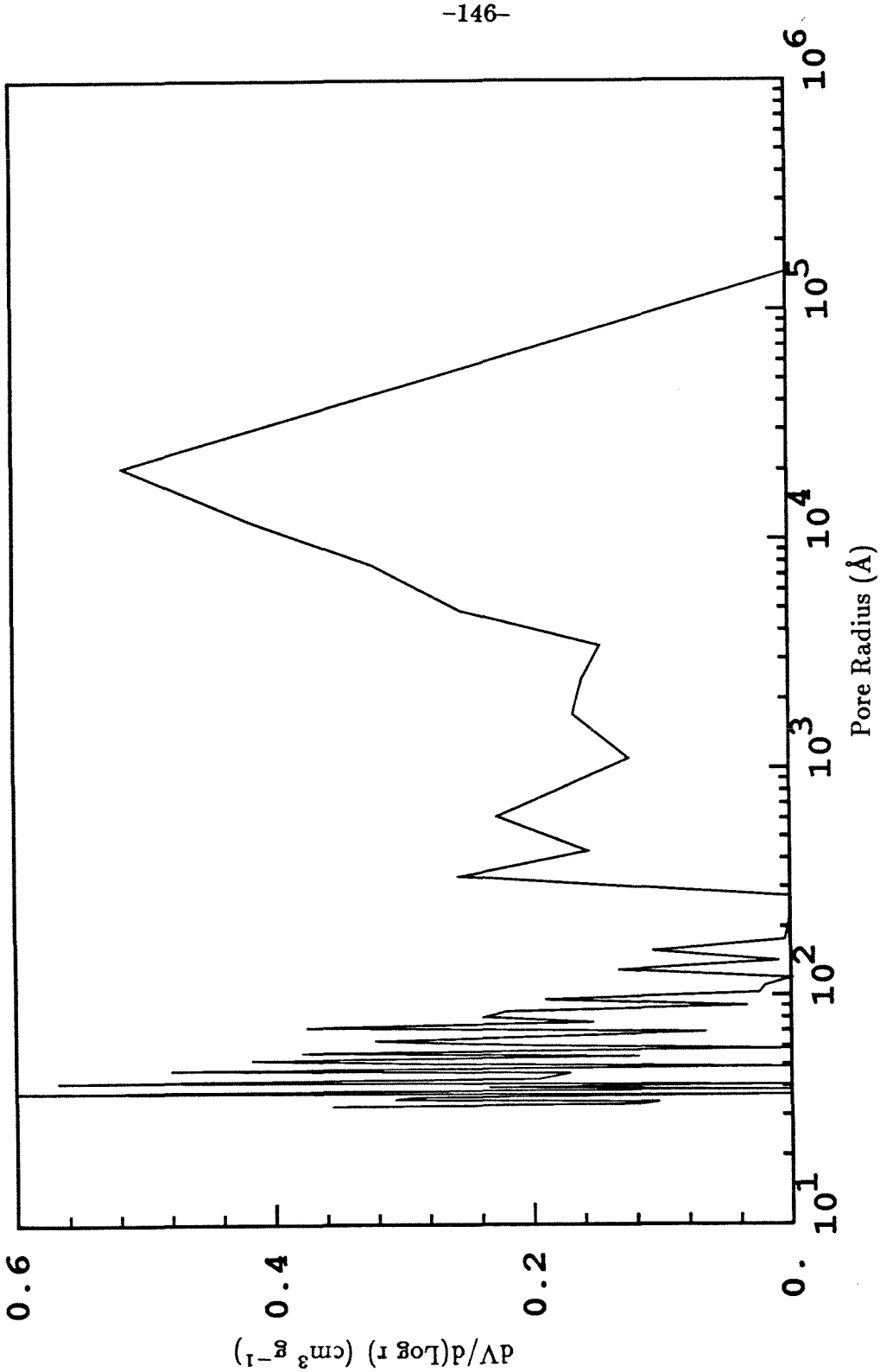

Figure 3.25. Pore volume distribution for 1200K PSOC 1451 char after partial oxidation to 64% at 775K.

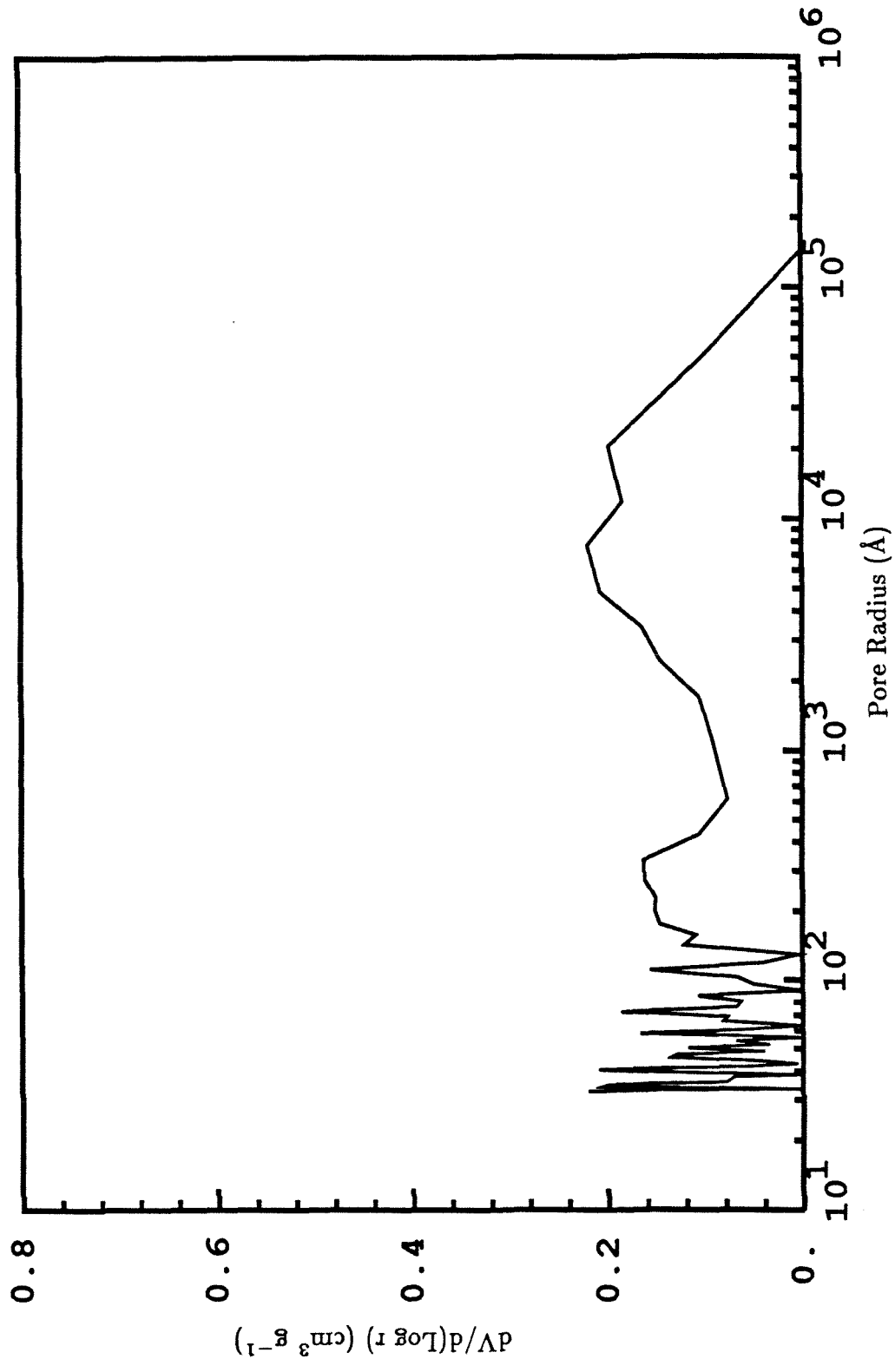

Figure 3.26. Pore volume distribution for 1600K PSOC 1451 char from mercury porosimetry.

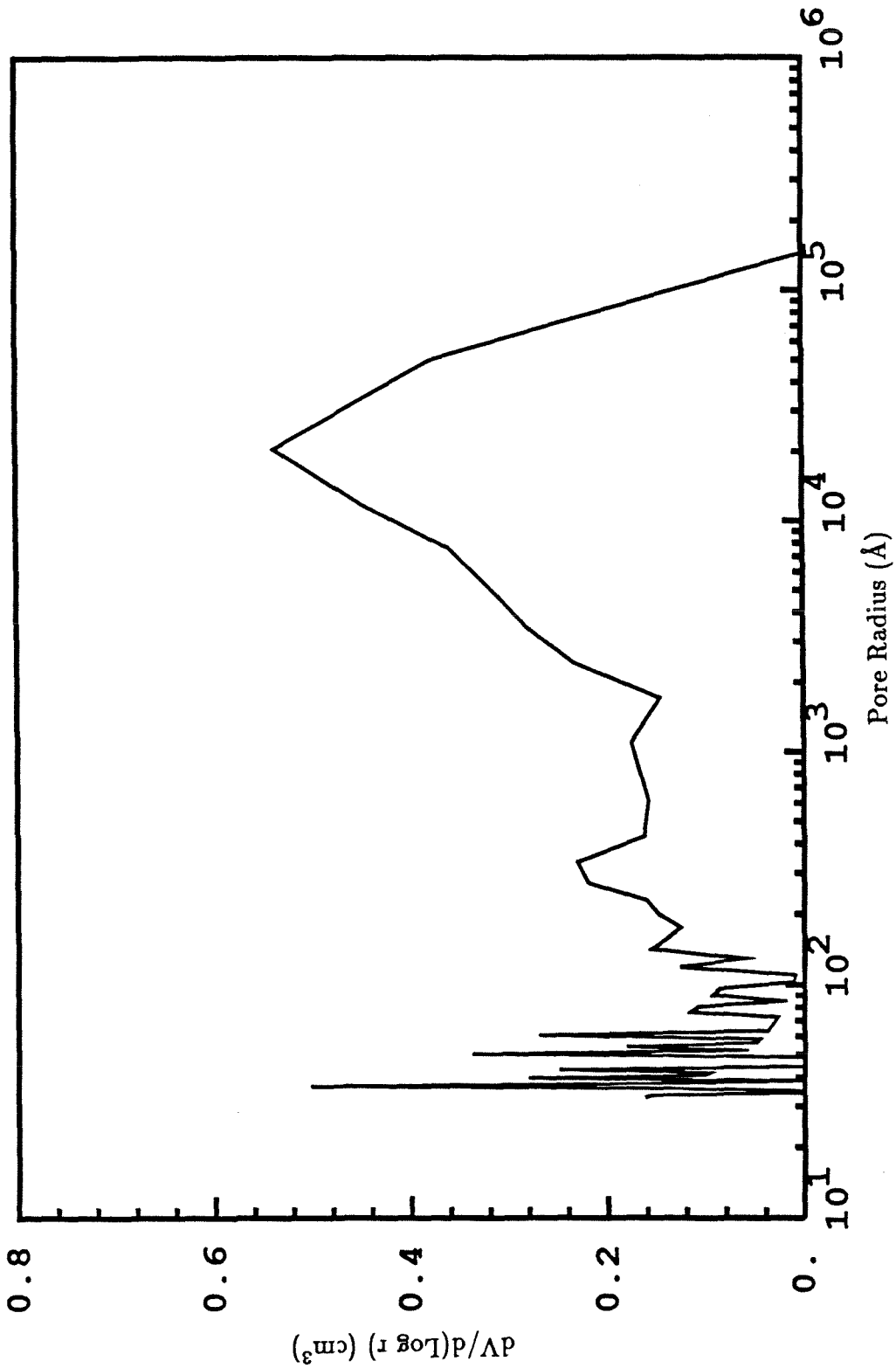

Figure 3.27. Pore volume distribution for 1600K PSOC 1451 char after partial oxidation to 55% at 775K.

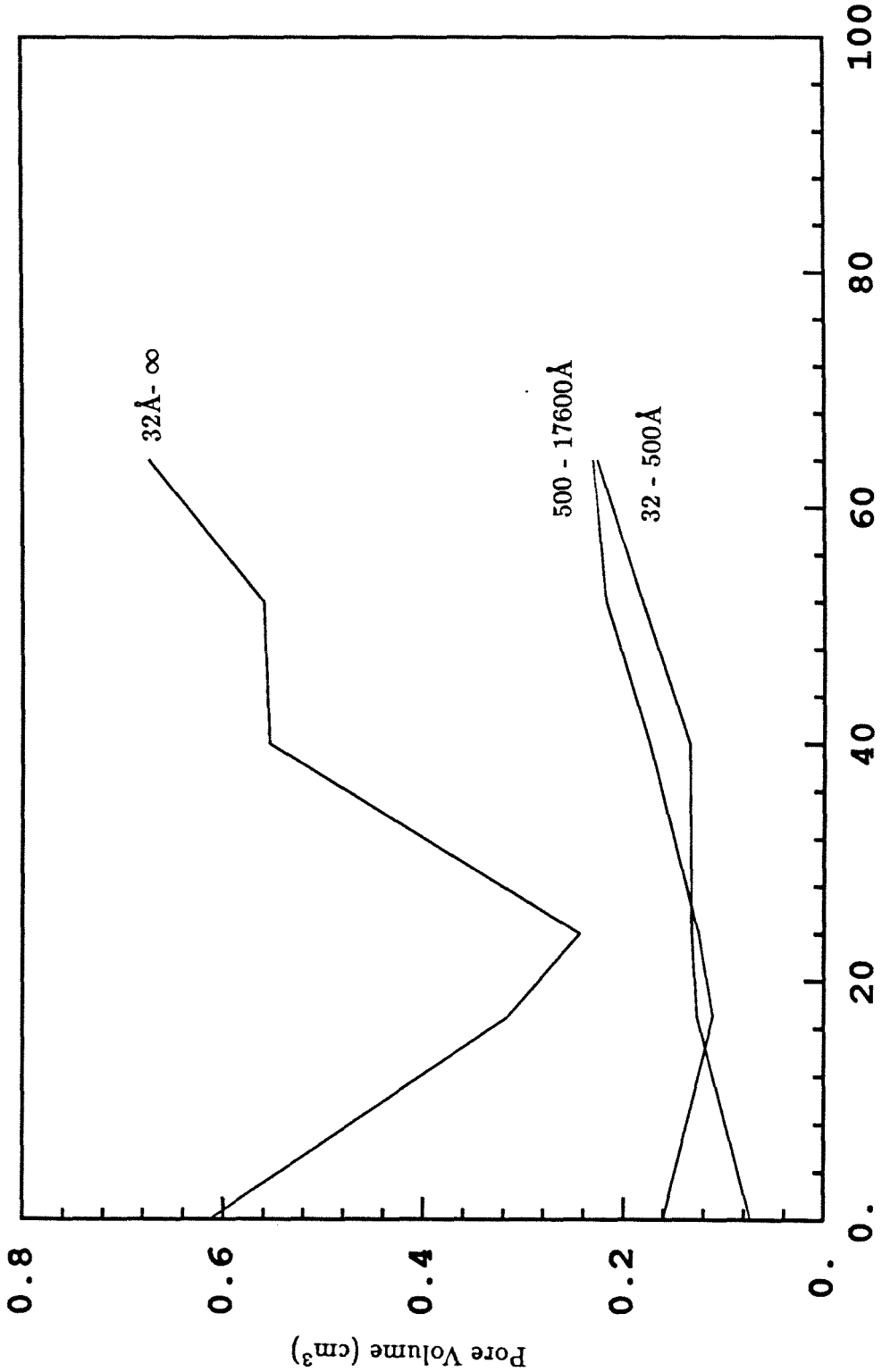

Figure 3.28. Total pore volumes for 1200K PSOC 1451 char as a function of conversion.

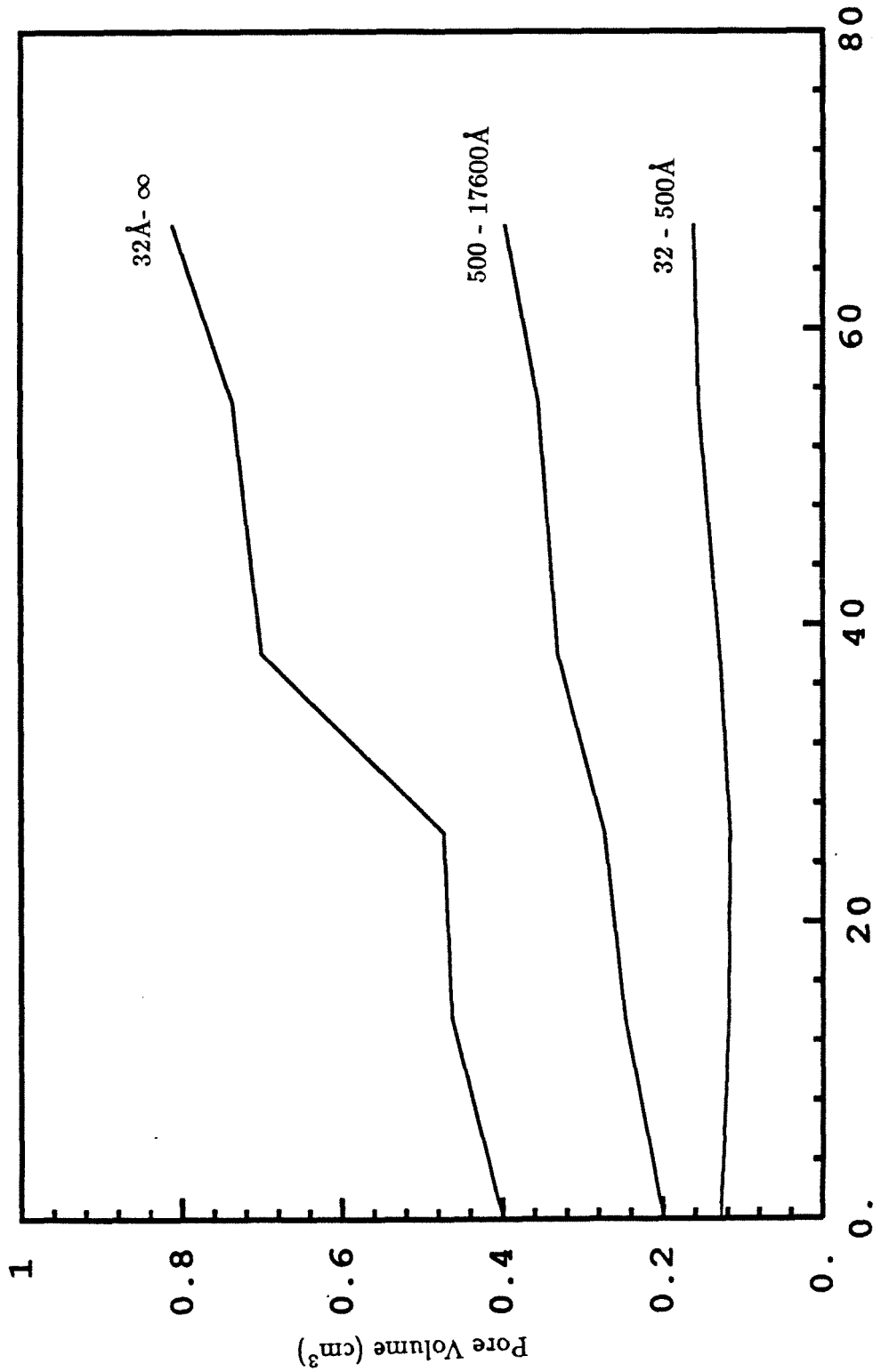

Figure 3.29. Total pore volumes for 1600K PSOC 1451 char as a function of conversion.

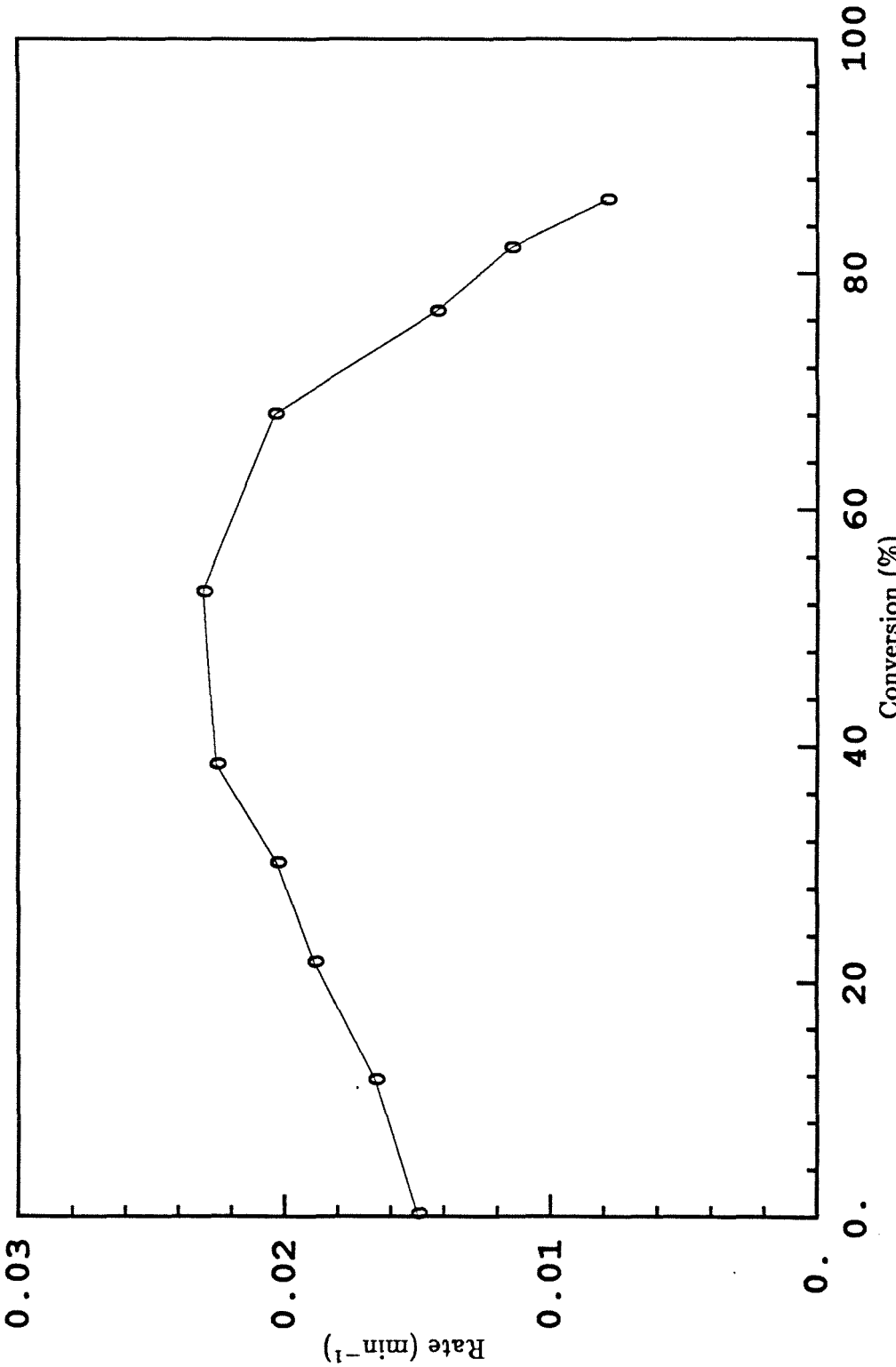

Figure 3.30. Oxidation rate of 45-53μm 1600K PSOC 1443 char at 725K in 1mol% oxygen.

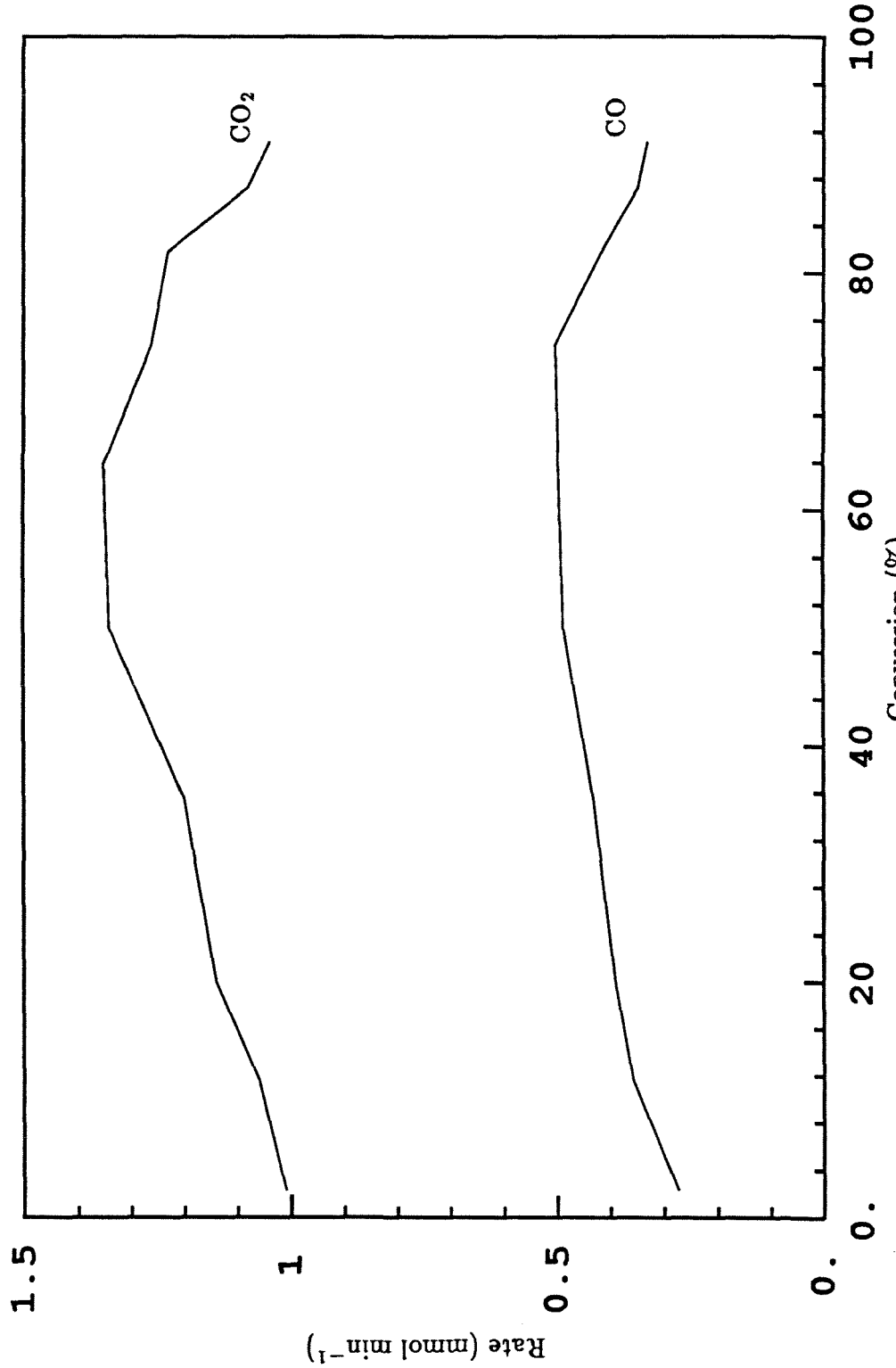

Figure 3.31. Carbon oxide production rates for 1600K PSOC 1443 char at 775K in 1mol% oxygen.

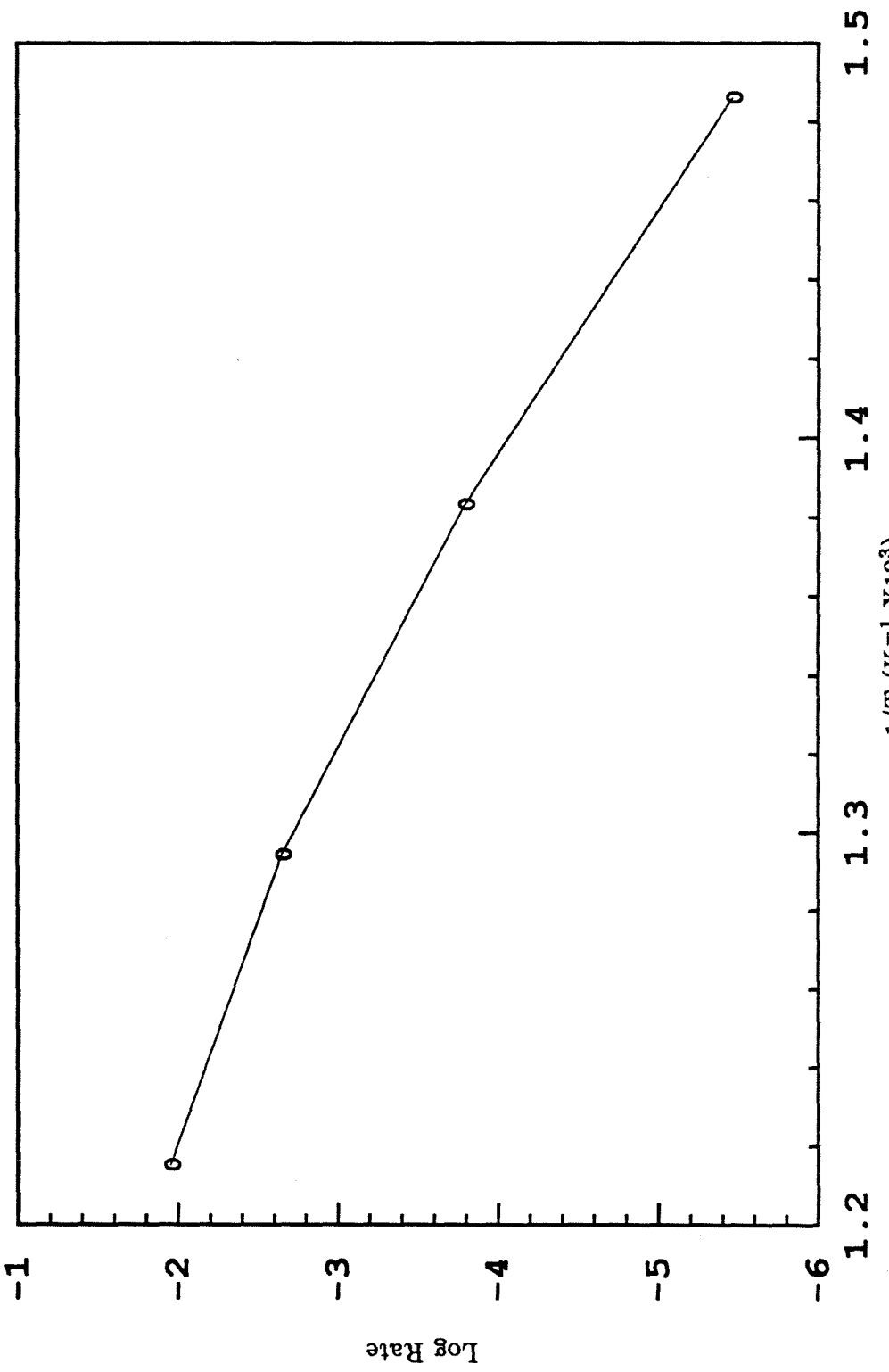

Figure 3.32. Arrhenius plot for 1600K PSOC 1443 char in 1mol% oxygen.

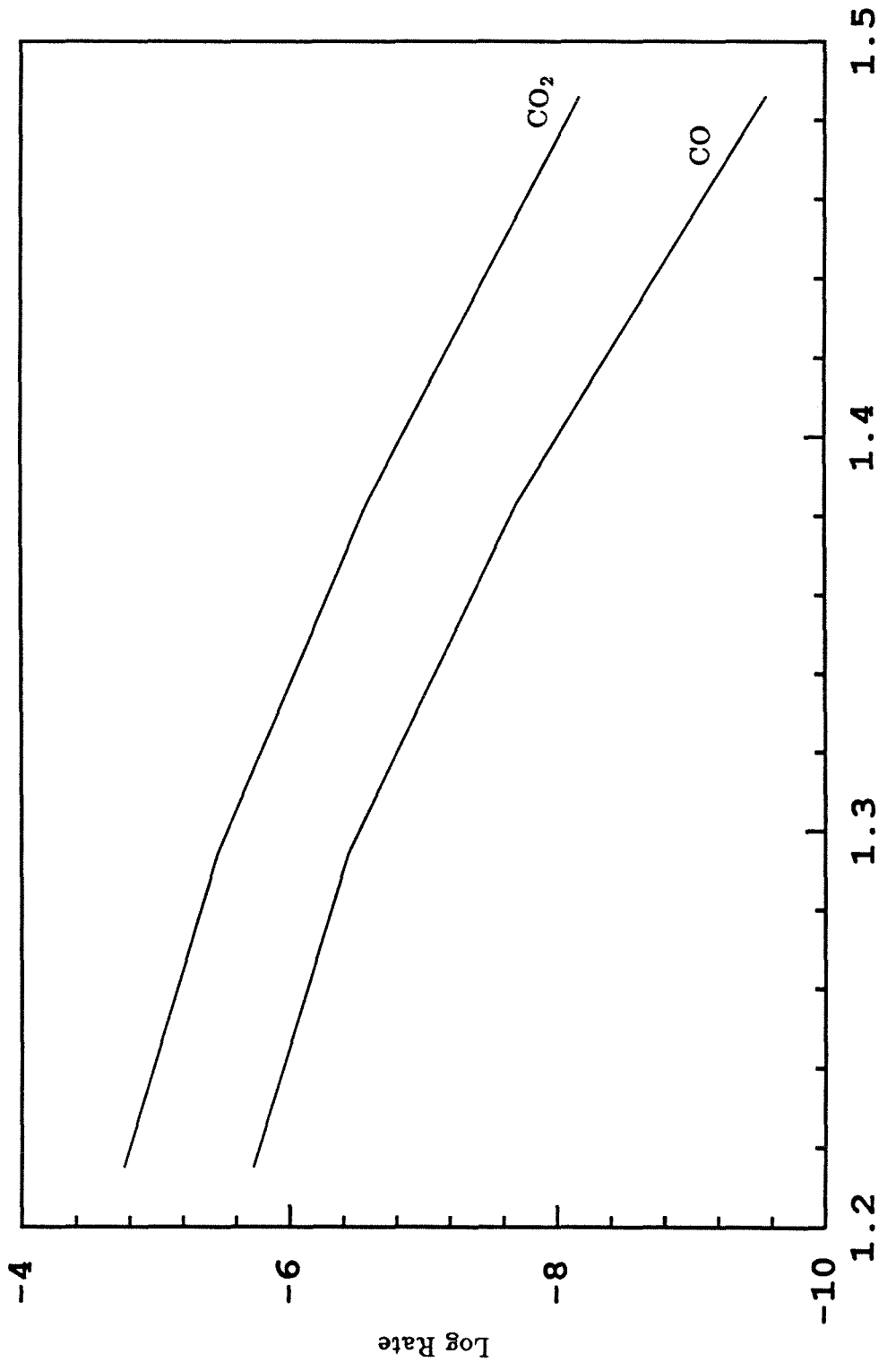

Figure 3.33. Arrhenius plot for carbon oxide production from 1400K PSOC 1451 char in 1mol% oxygen.

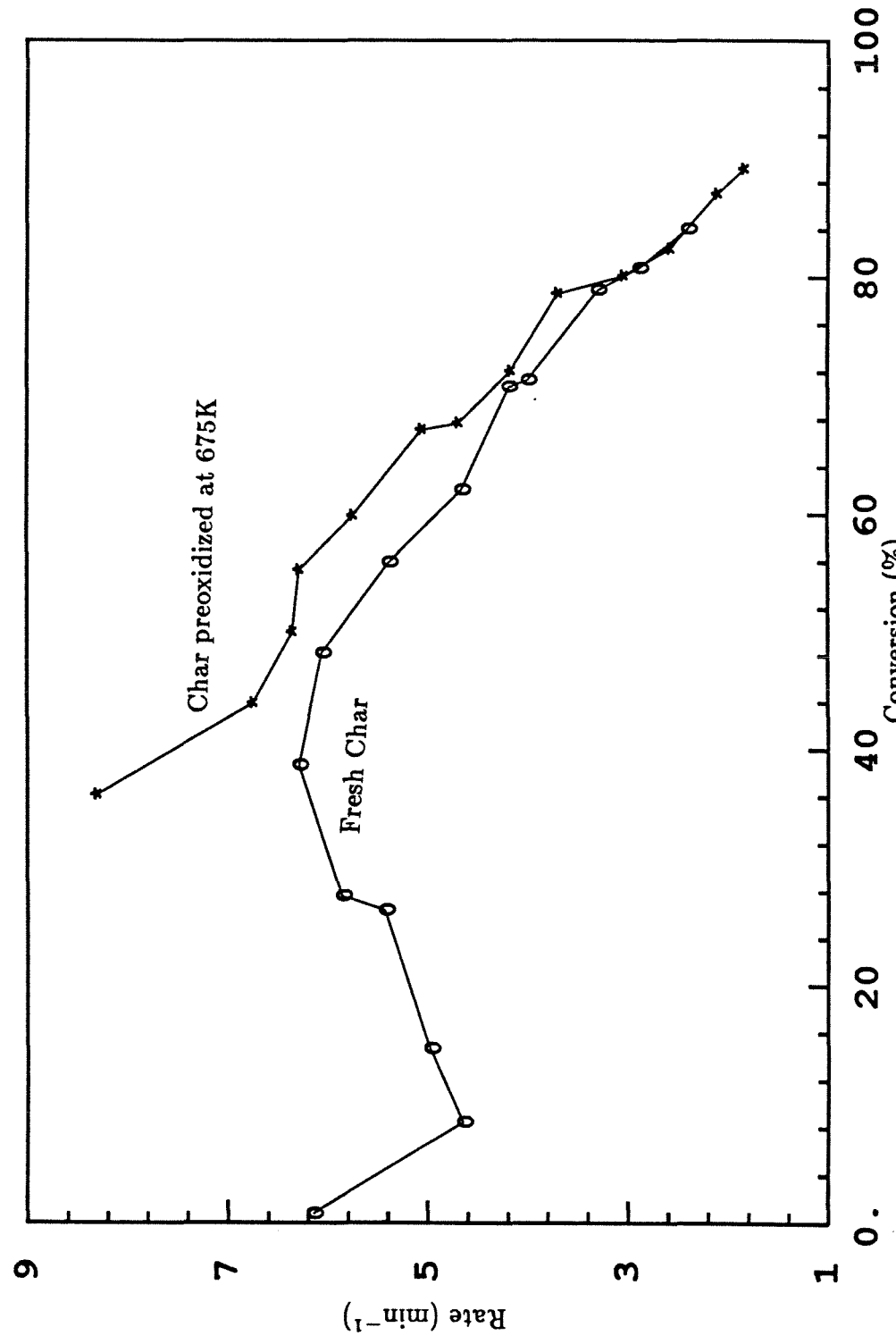

Figure 3.34. Rate of "preoxidized" 1600K PSOC 1443 char at 675K.

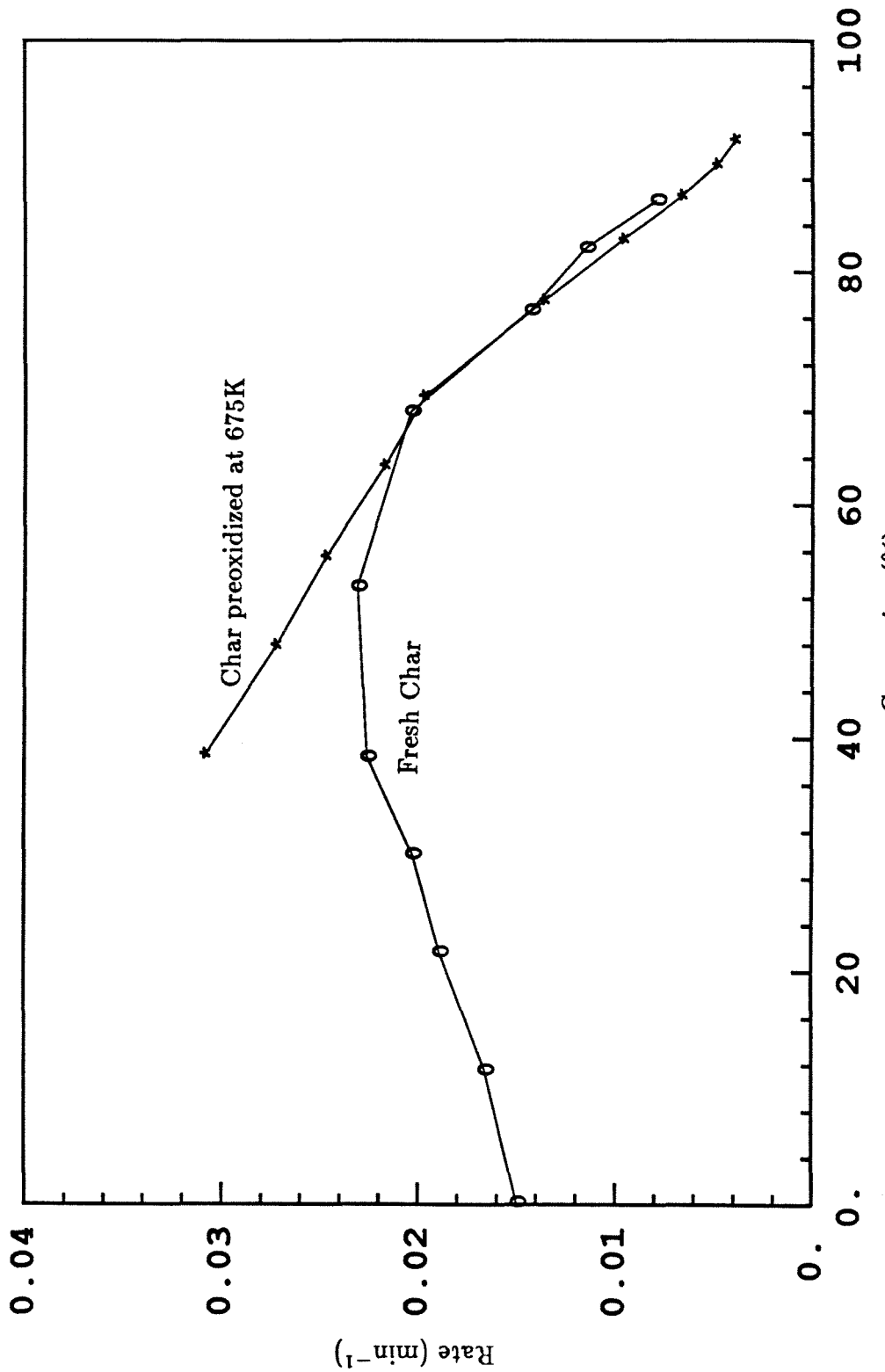

Figure 3.35. Rate of "preoxidized" 1600K PSOC 1443 char at 725K.

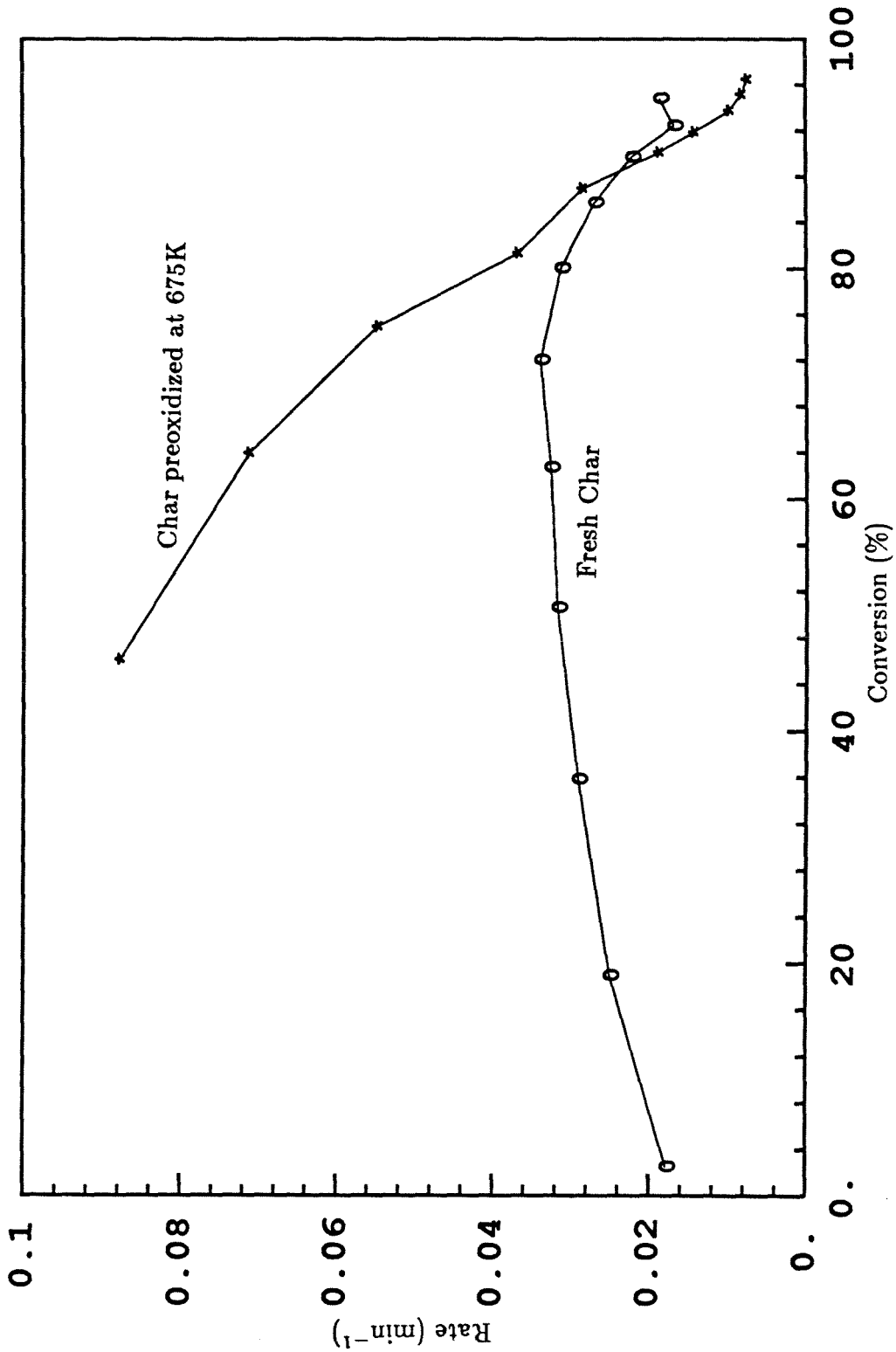

Figure 3.36. Rate of "preoxidized" 1600K PSOC 1443 char at 775K.

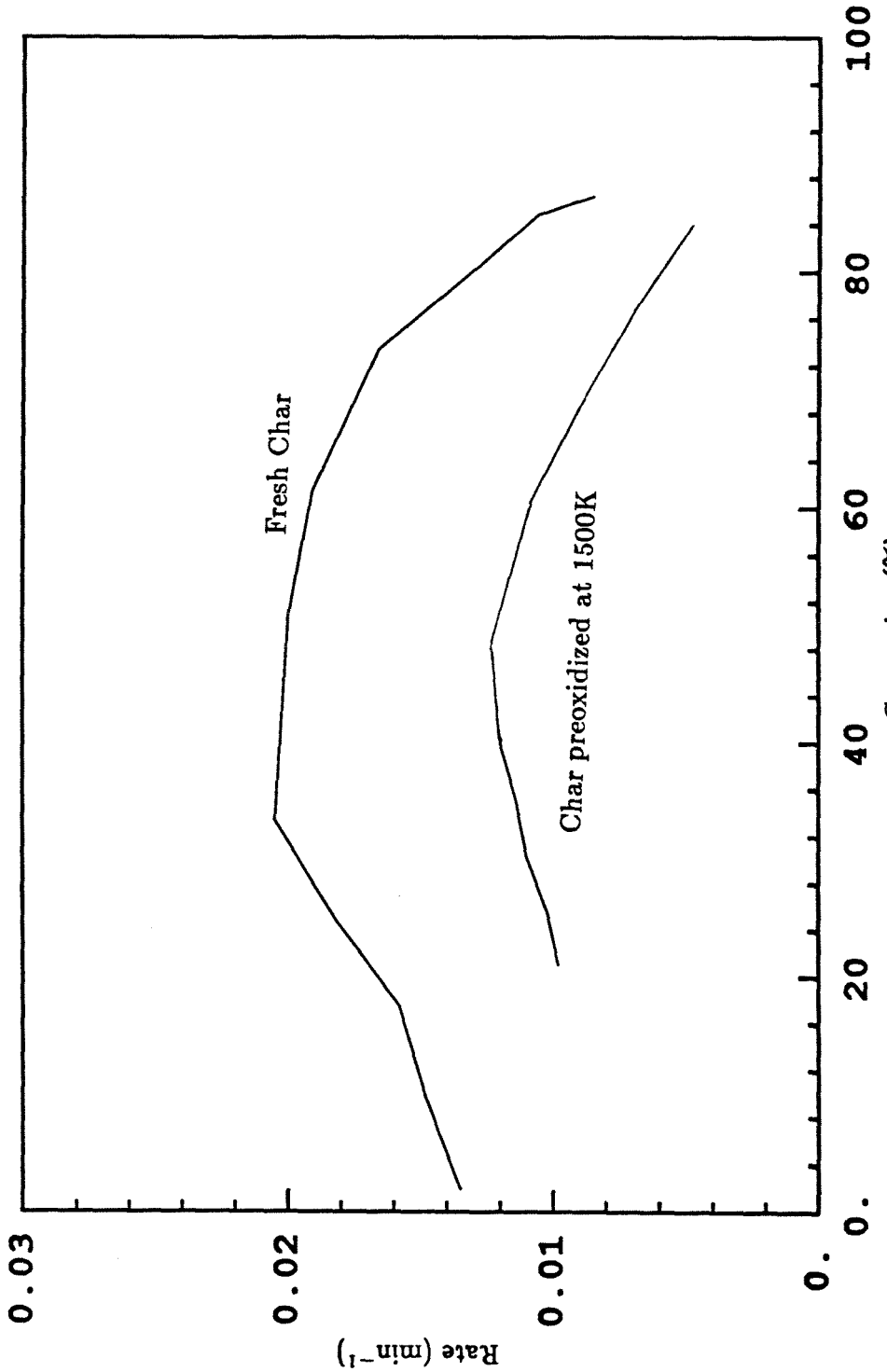

Figure 3.37. Rates of 1600K PSOC 1443 chars in 1mol% oxygen at 725K.

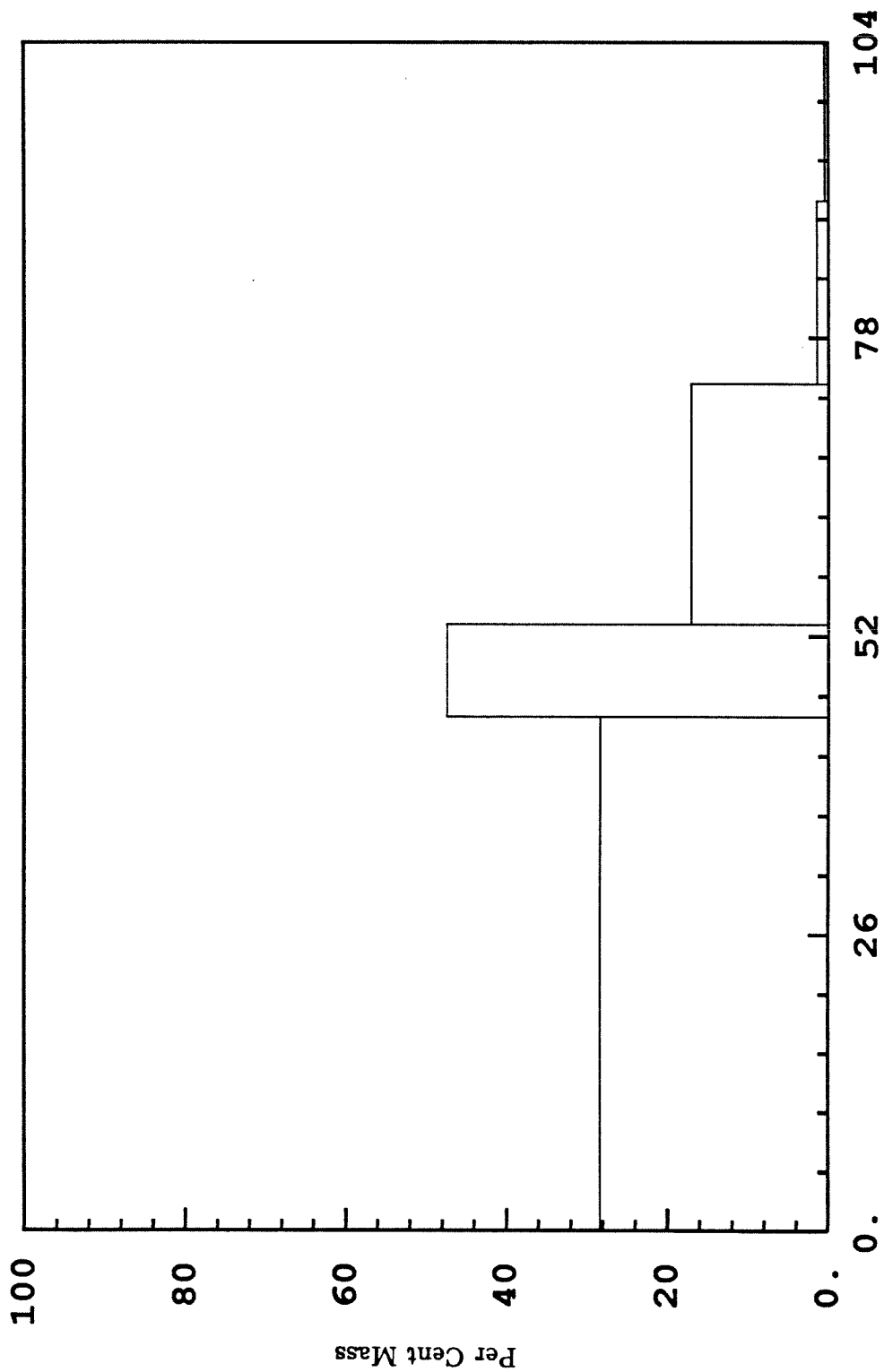

Figure 3.38. Particle size distribution for 1600K char derived from 45-63μm PSOC 1443 coal.

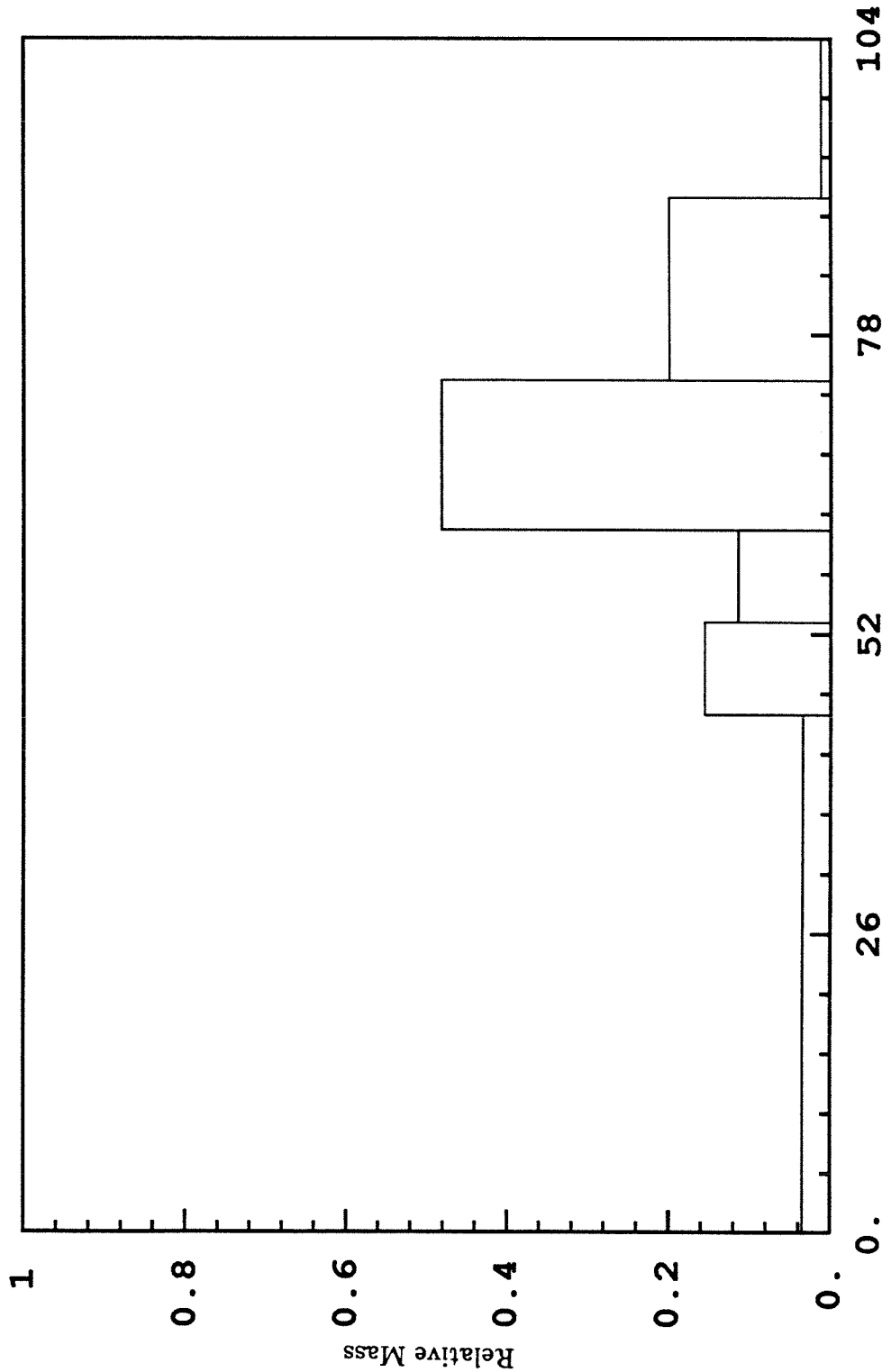

Figure 3.39. Particle size distribution for 1600K char derived from 75-106μm PSOC 1443 coal.

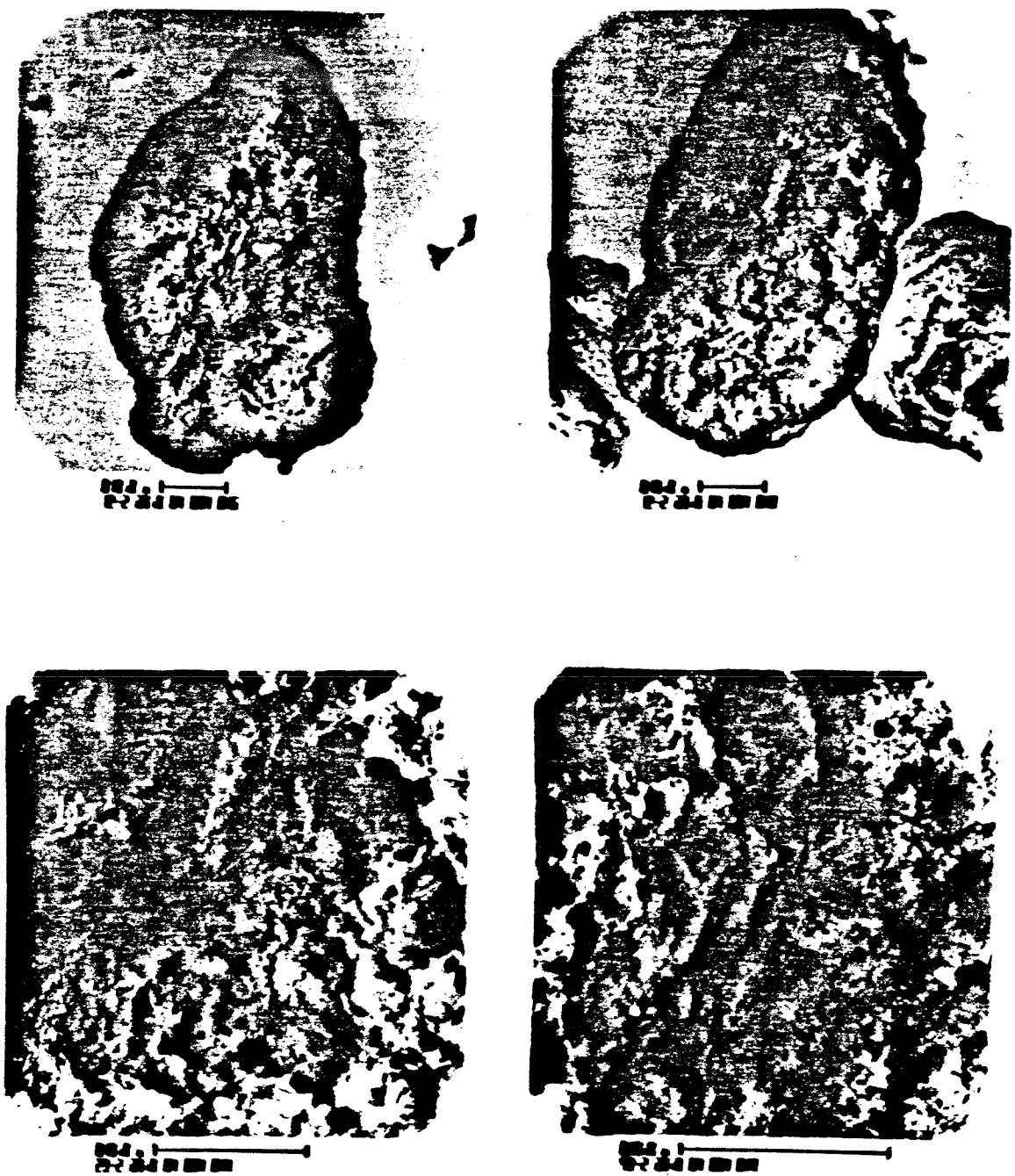

Figure 3.40. Electron micrographs of 1600K char derived from 45-63μm PSOC 1443 coal.

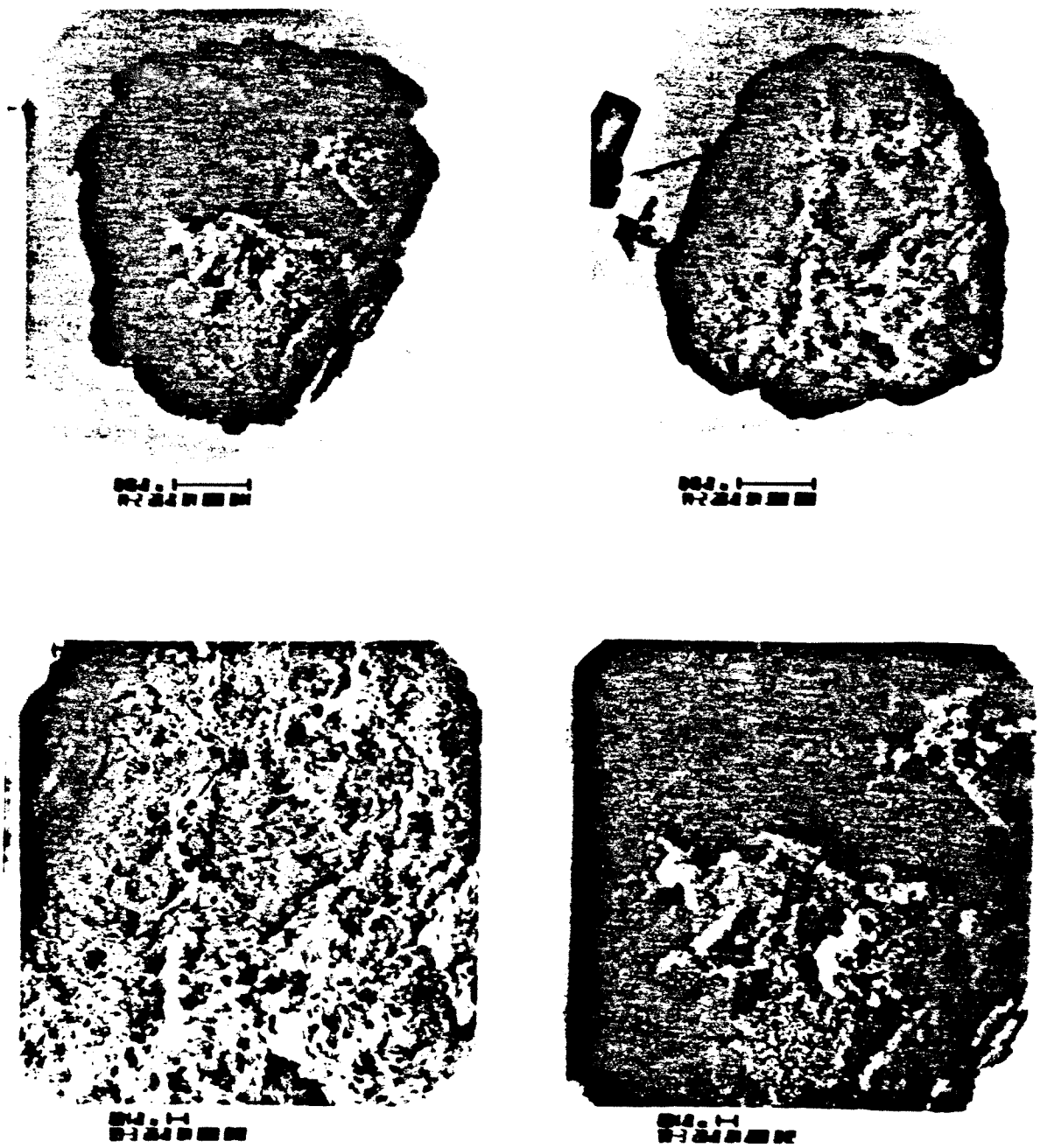

Figure 3.41. Electron micrographs of 1600K PSOC 1443 char after partial oxidation to 28% at 725K.

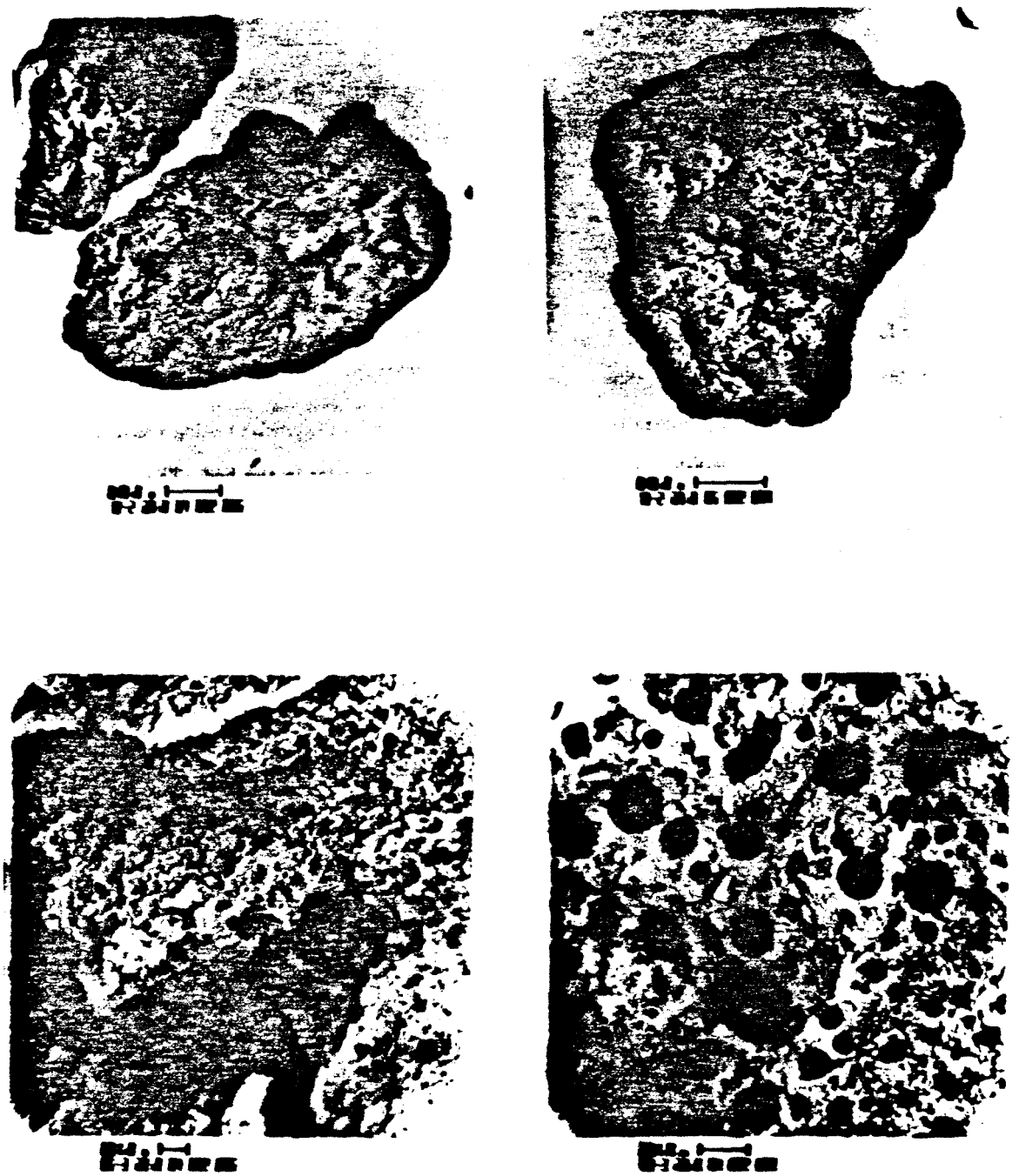

Figure 3.42. Electron micrographs of 1600K PSOC 1443 char after partial oxidation to 55% at 725K.

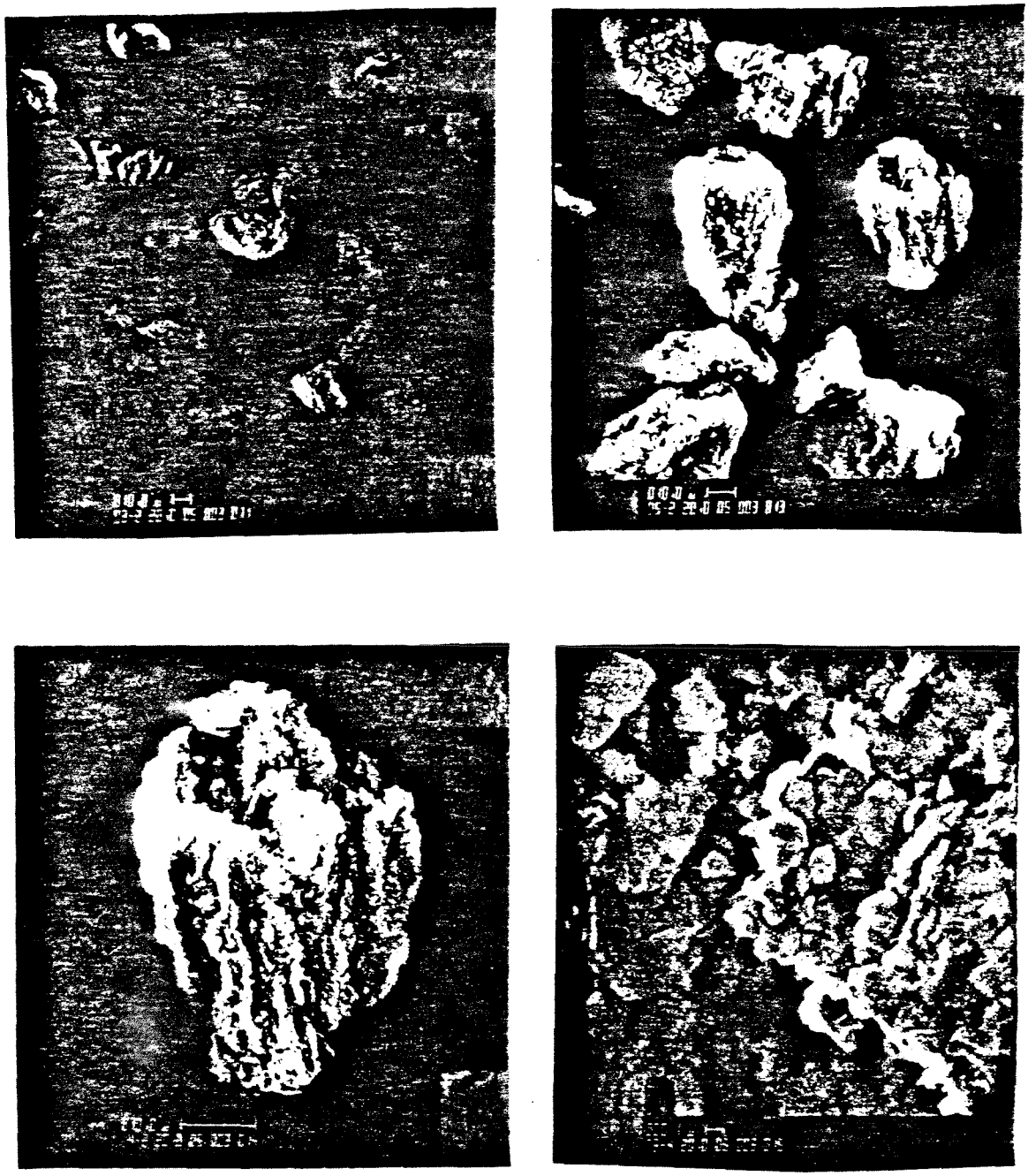

Figure 3.43. Electron micrographs of 1600K PSOC 1443 char after complete oxidation.

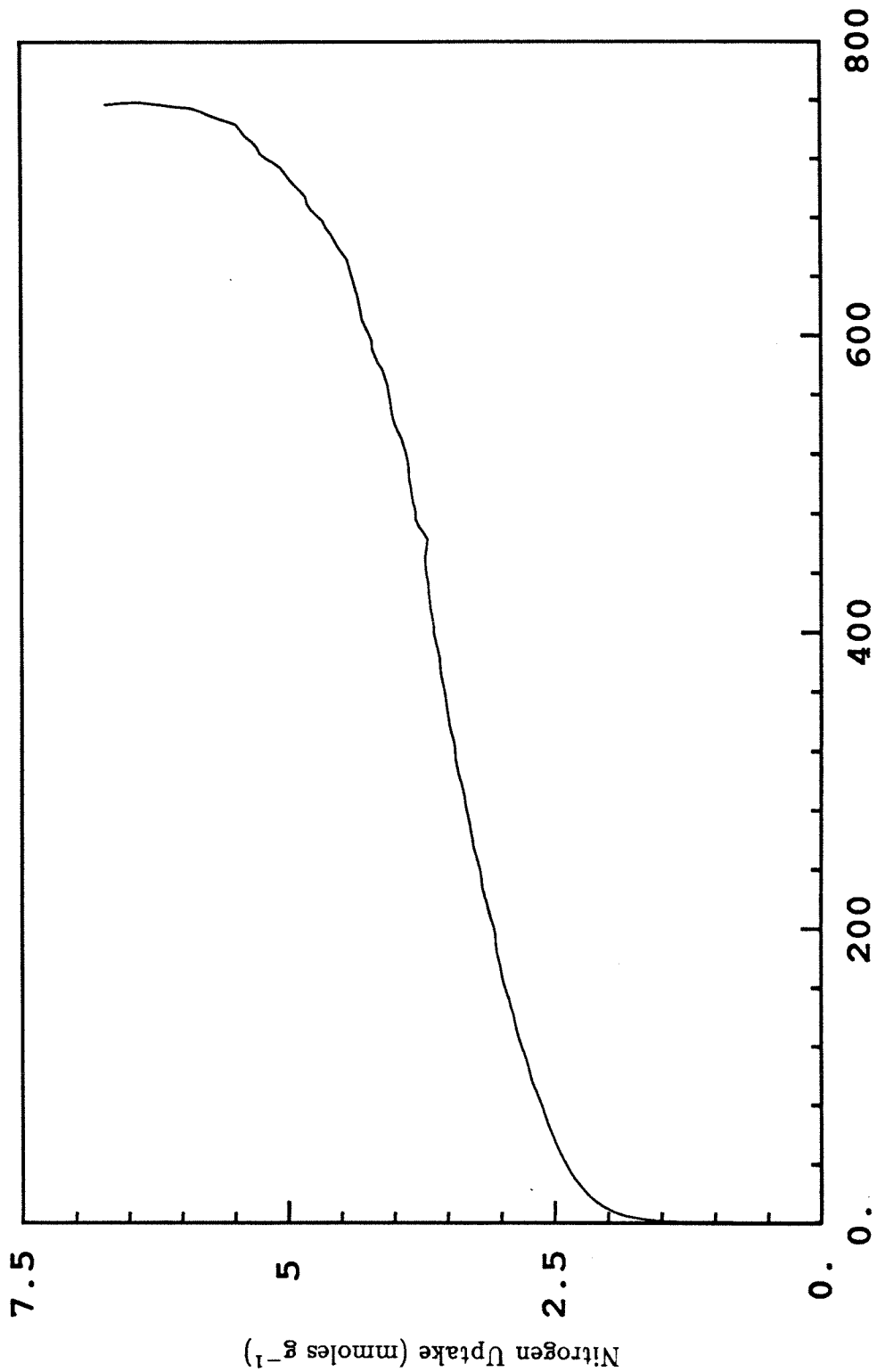

Figure 3.44. Nitrogen isotherm on 1600K PSOC 1443 char.

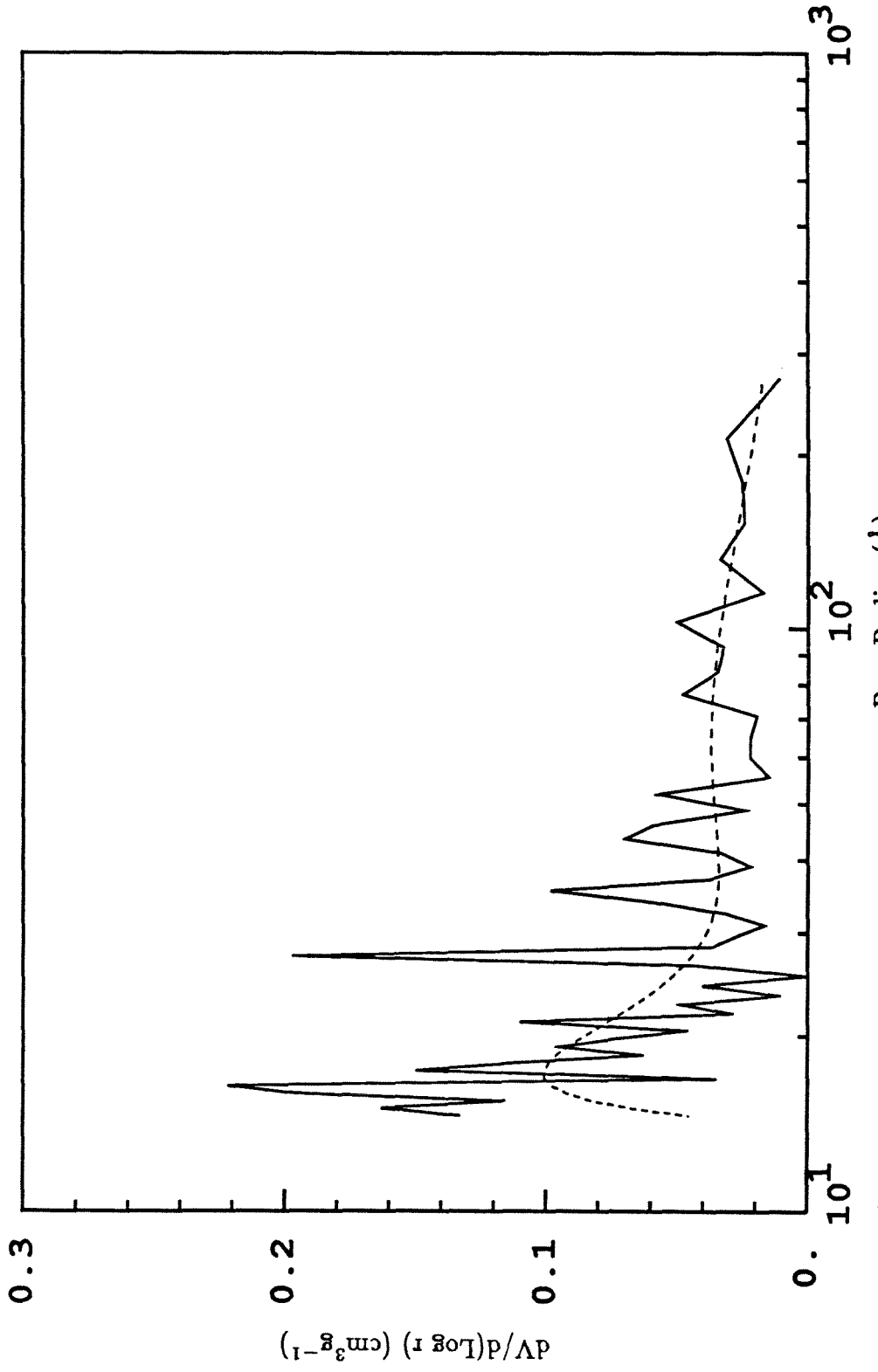

Figure 3.45. Pore volume distribution from capillary condensation in 1600K PSOC 1443 char.
Dashed line is from smoothed isotherm.

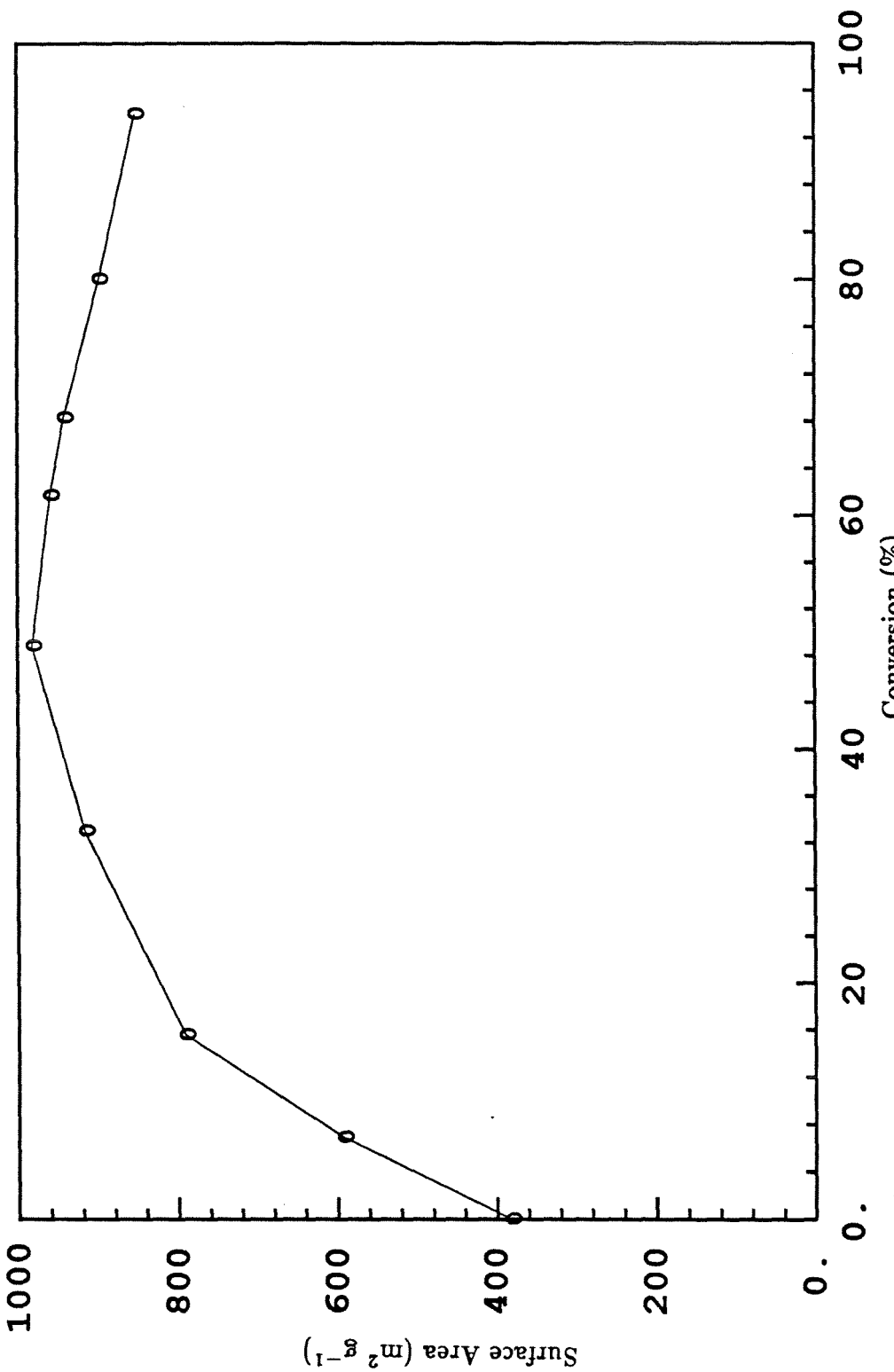

Figure 3.46. Specific surface areas of 1600K PSOC 1443 char as a function of conversion.

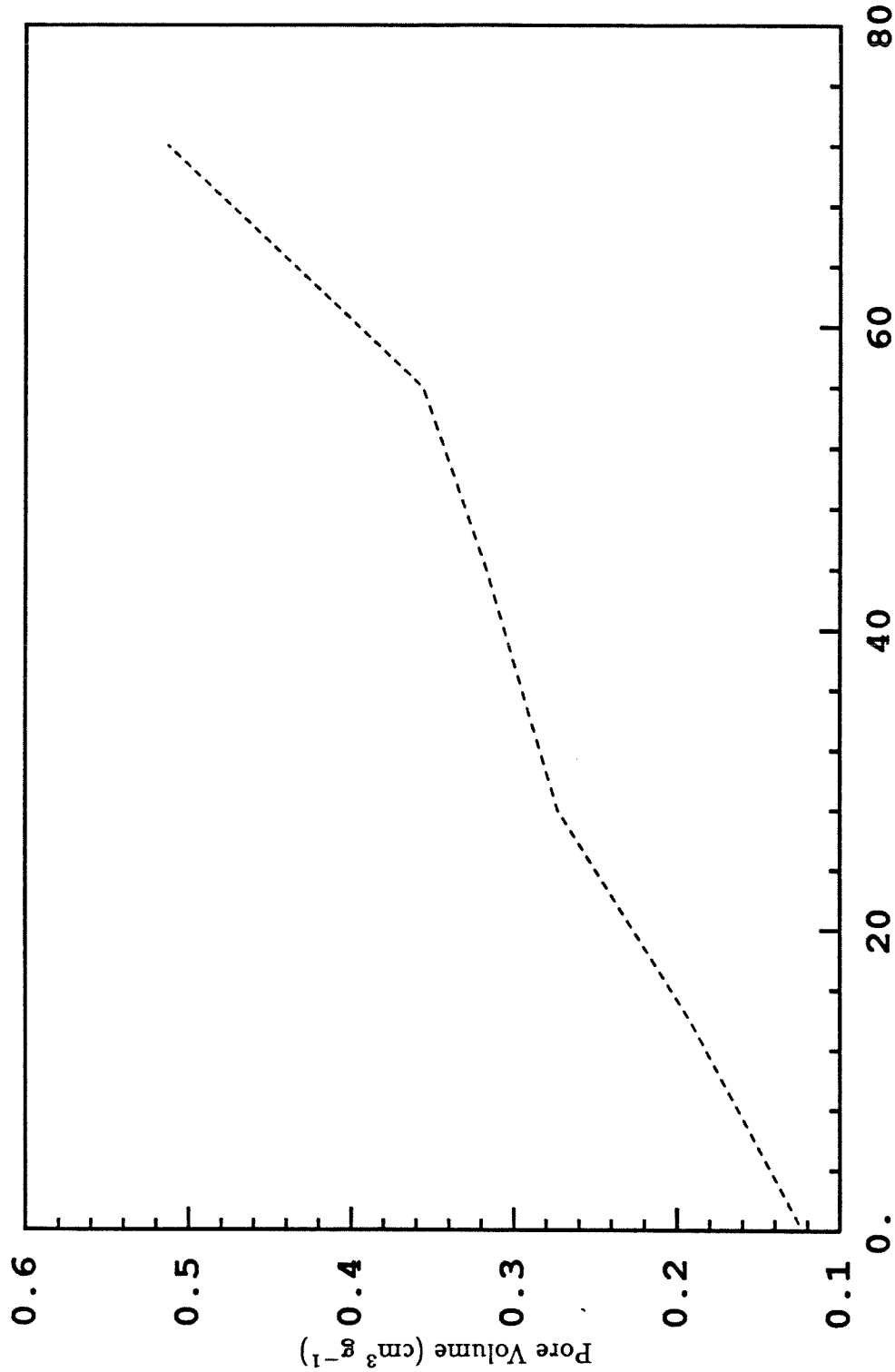

Figure 3.47. Pore volume (radii 16-150Å) as a function of conversion for PSOC 1443 char.

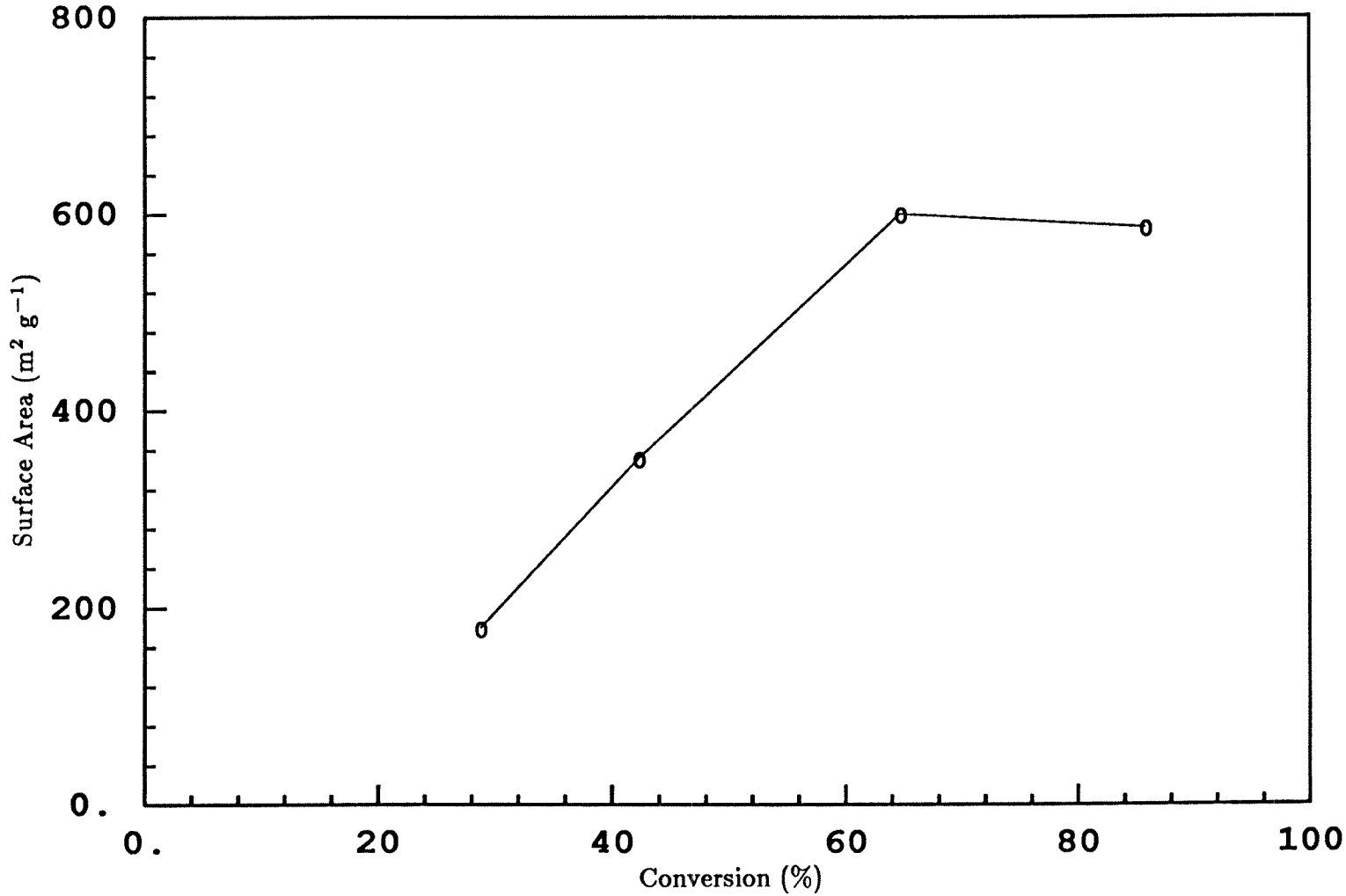

Figure 3.48. Specific surface areas of 1600K PSOC 1443 char preoxidized at 1500K, then oxidized at 725K.

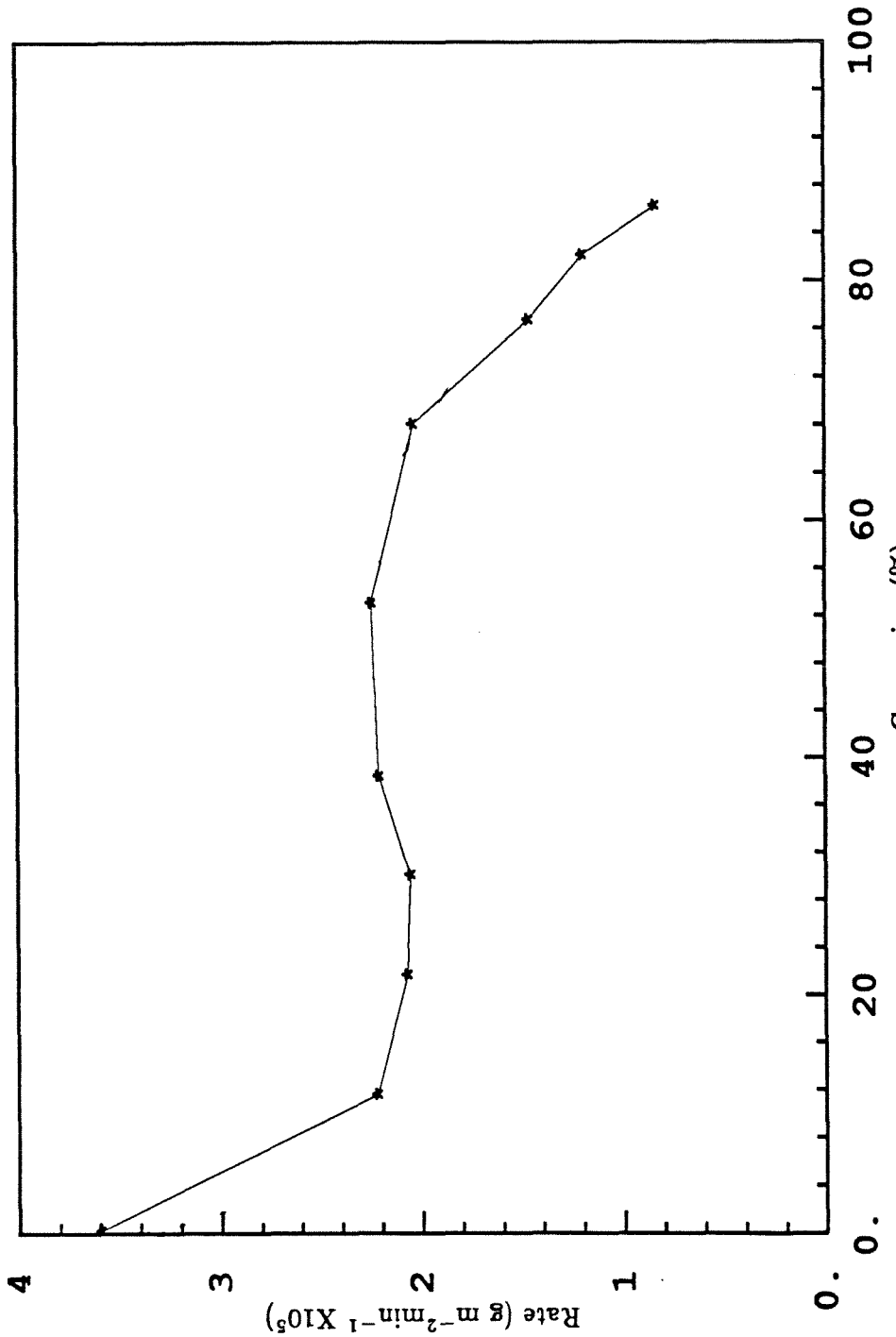

Figure 3.49. Intrinsic rate of 1600K PSOC 1443 char at 725K in 1mol% oxygen.

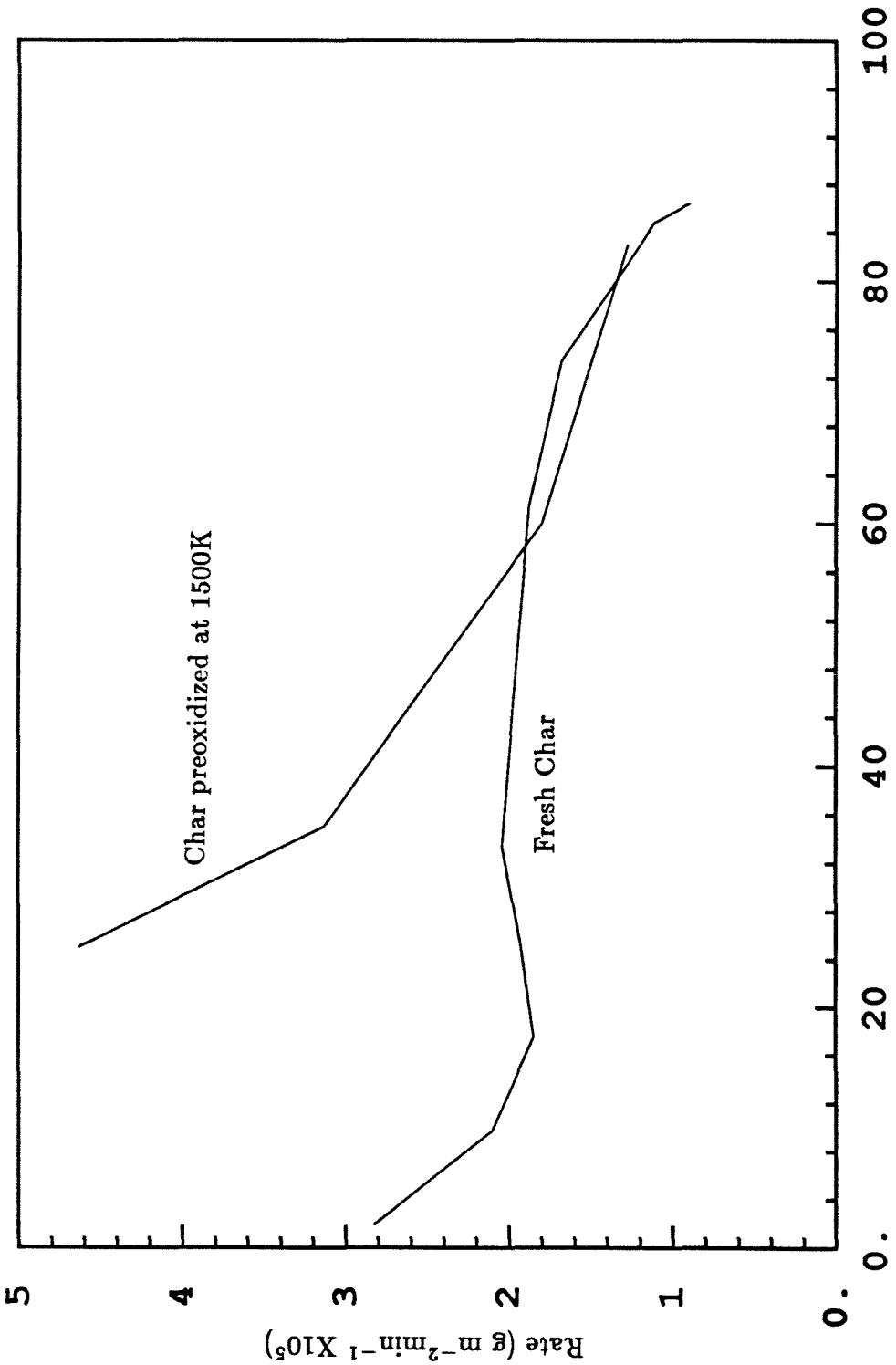

Figure 3.50. Intrinsic rates of 1600K PSOC 1443 chars in 1mol% oxygen at 725K.

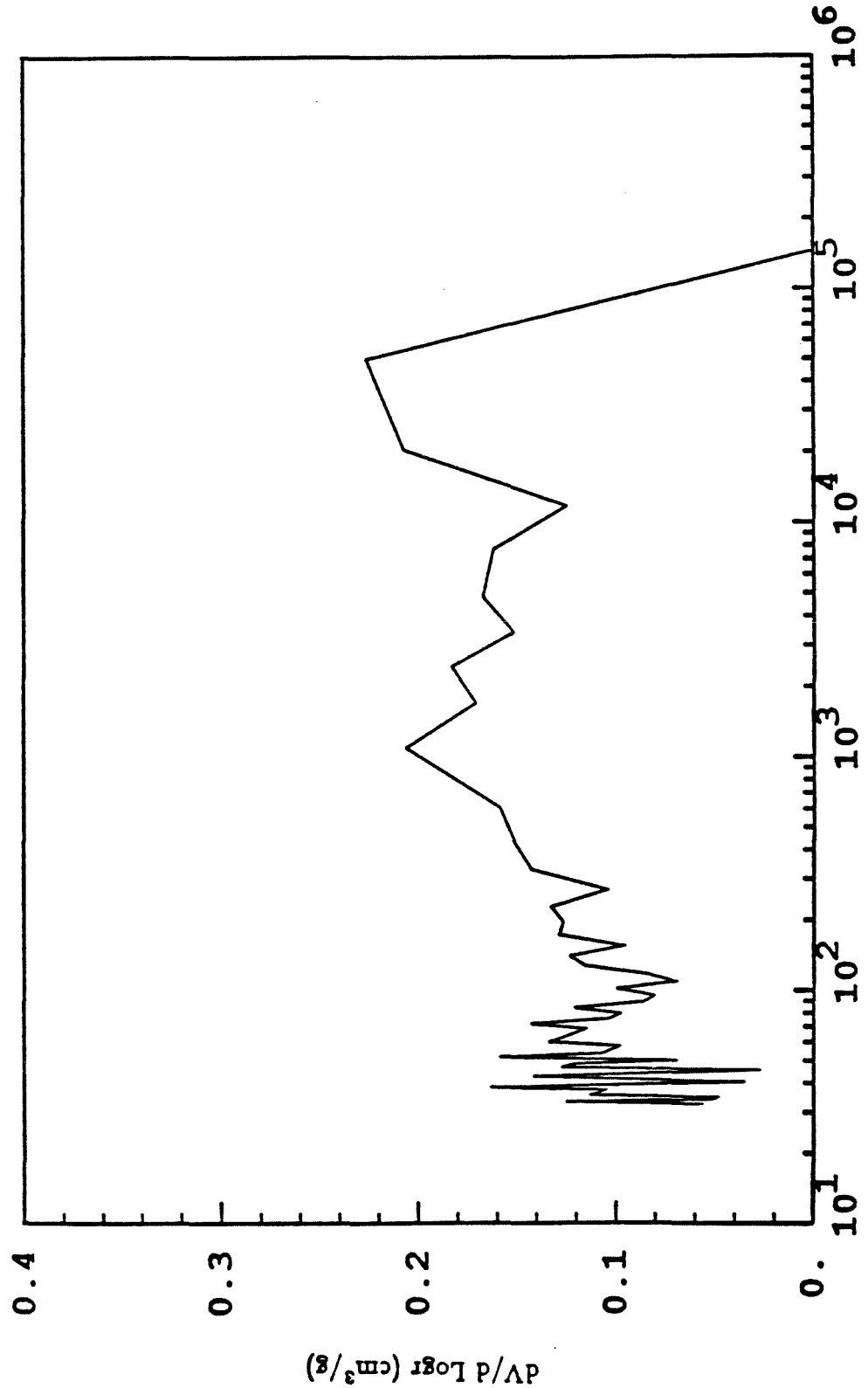

Figure 3.51. Pore volume distribution for 1600K PSOC 1443 char from mercury porosimetry.

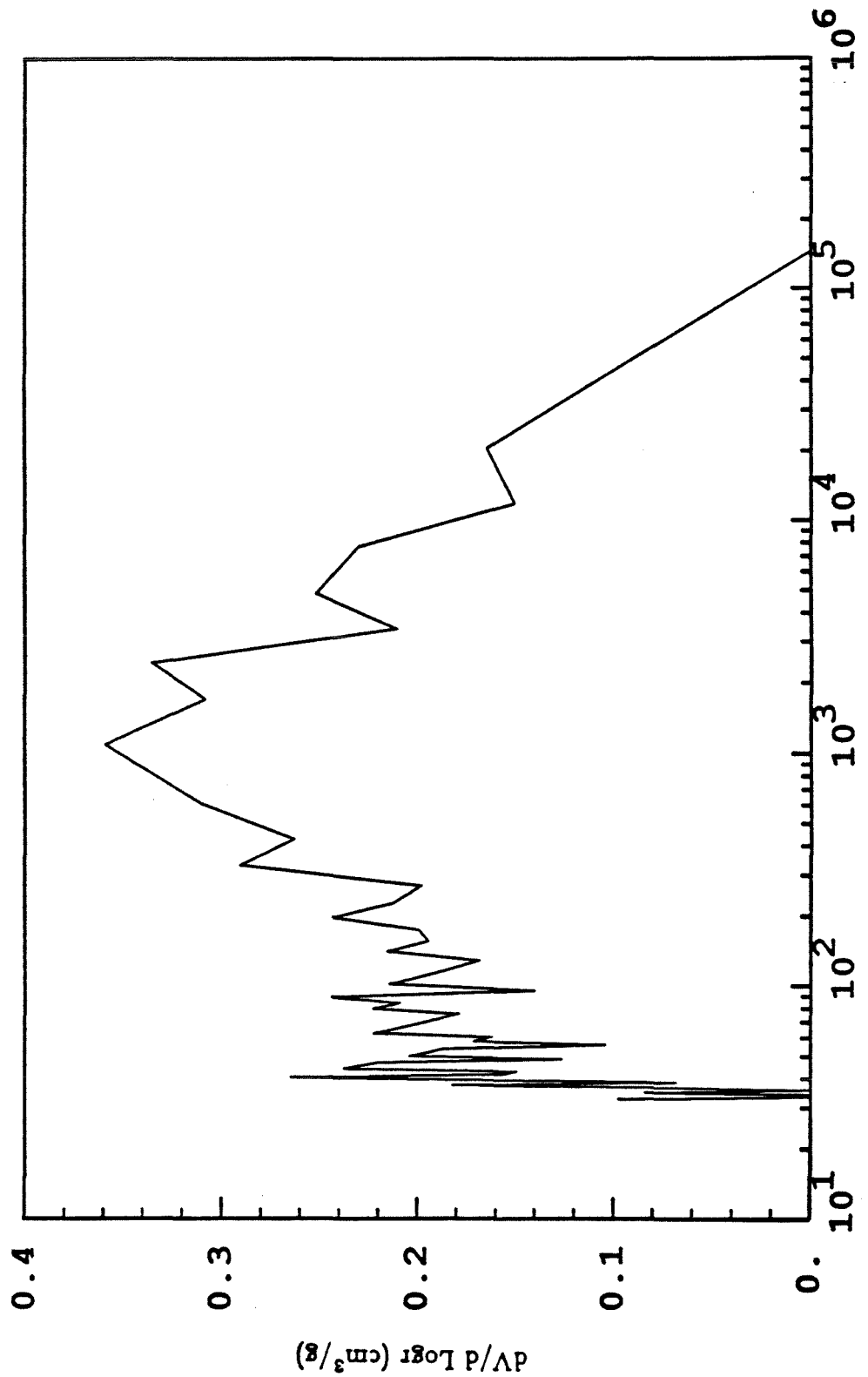

Figure 3.52. Pore volume distribution for 1600K PSOC 1451 char after partial oxidation to 55% at 725K.

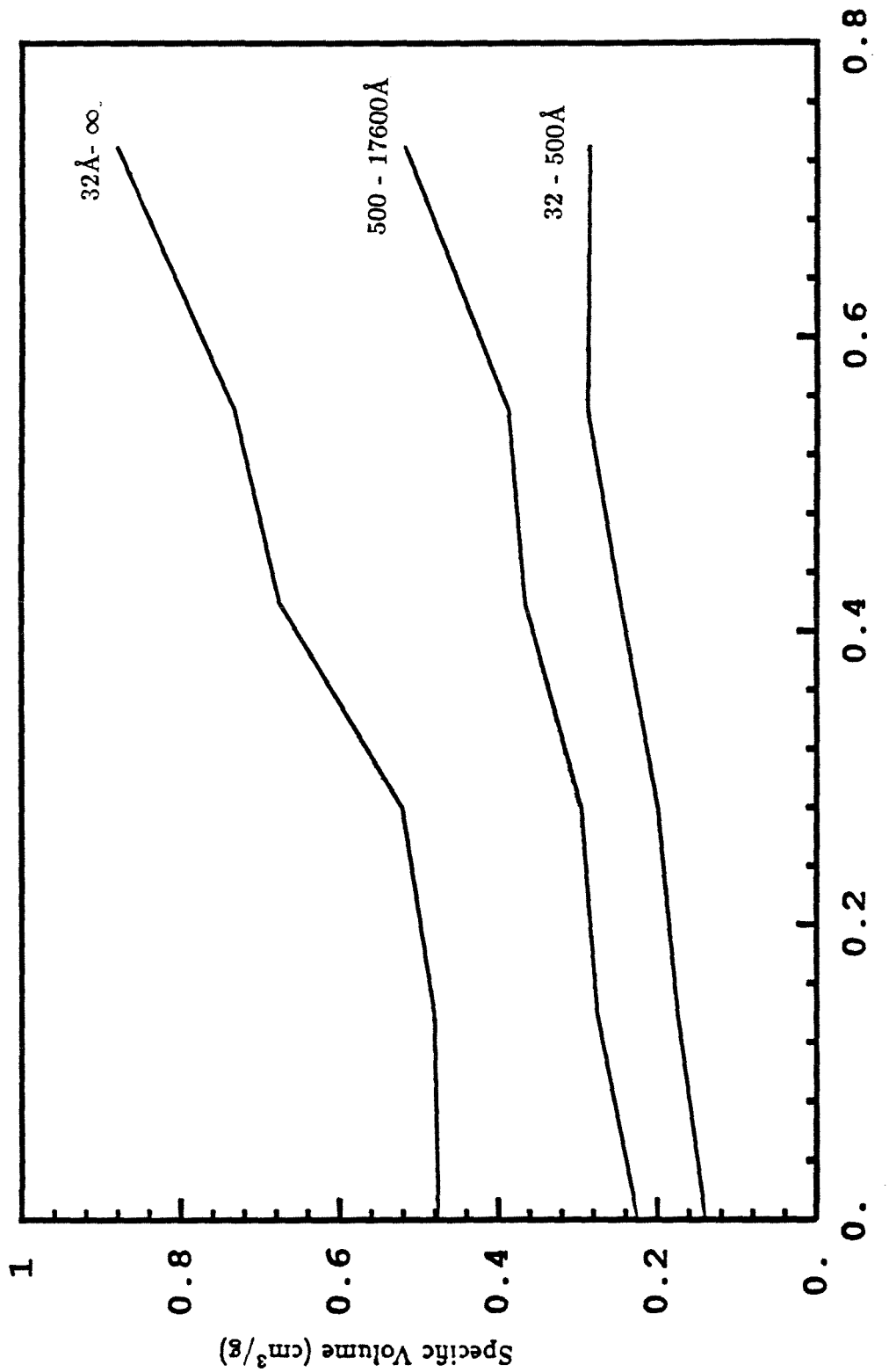

Figure 3.53. Total pore volumes for 1600K PSOC 1443 char as a function of conversion.

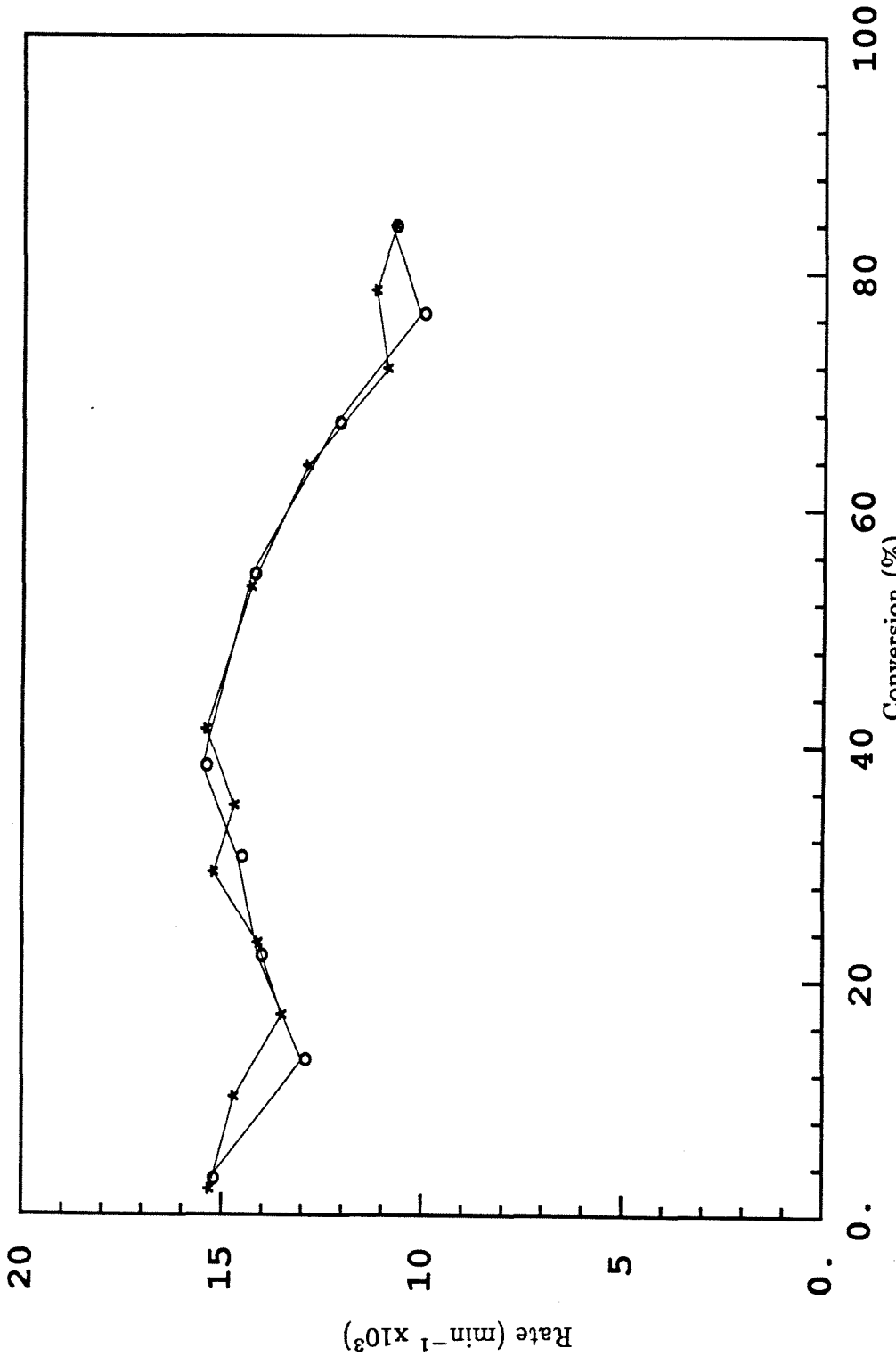

Figure 3.54. Oxidation rate of 45-53μm 1600K PSOC 1488 char at 725K normalized to 1mol% oxygen.

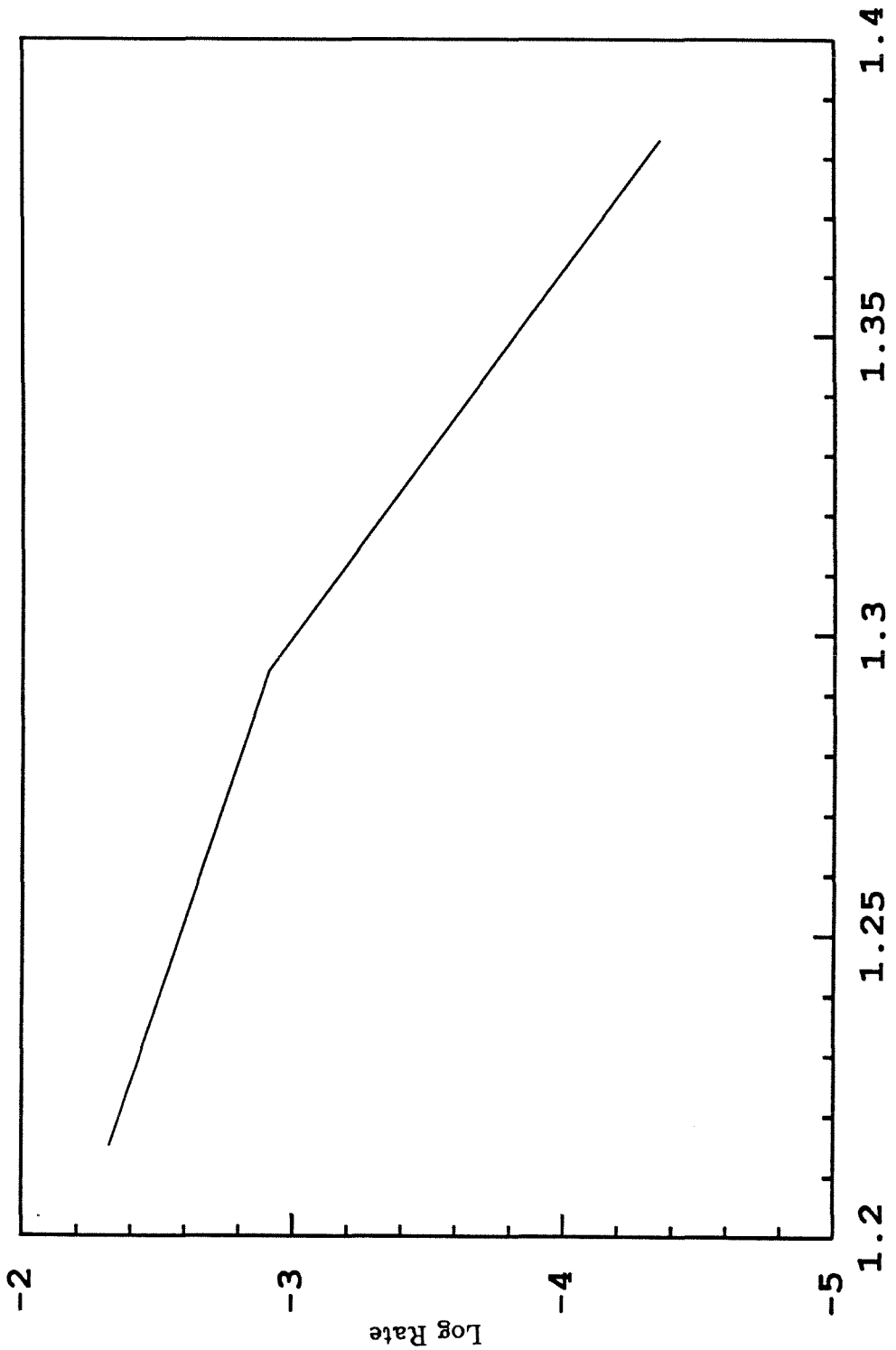

Figure 3.55. Arrhenius plot for 1600K PSOC 1488 char in 1mol% oxygen.

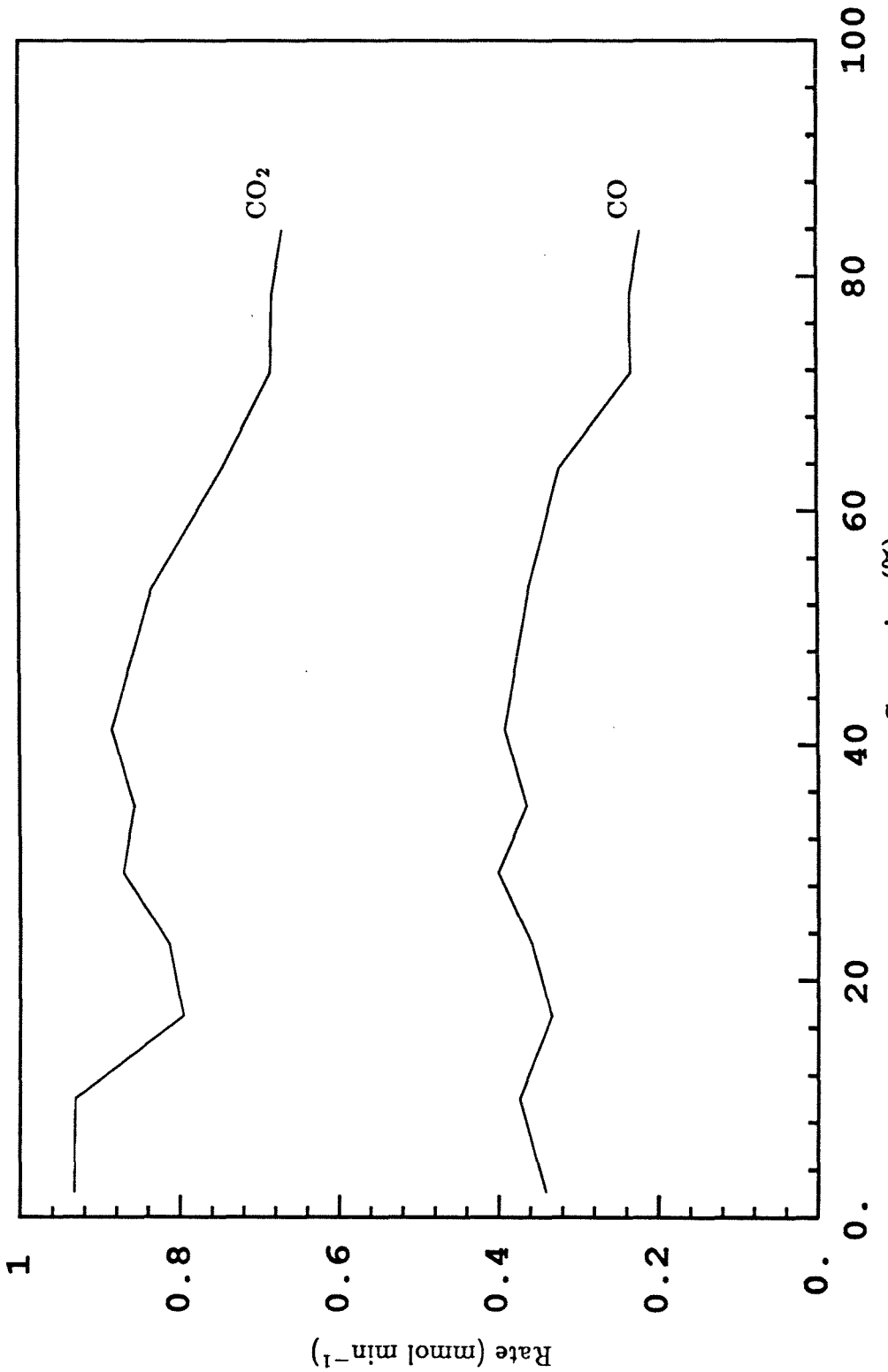

Figure 3.56. Carbon oxide production rates for 1600K PSOC 1488 char at 725K in 1mol% oxygen.

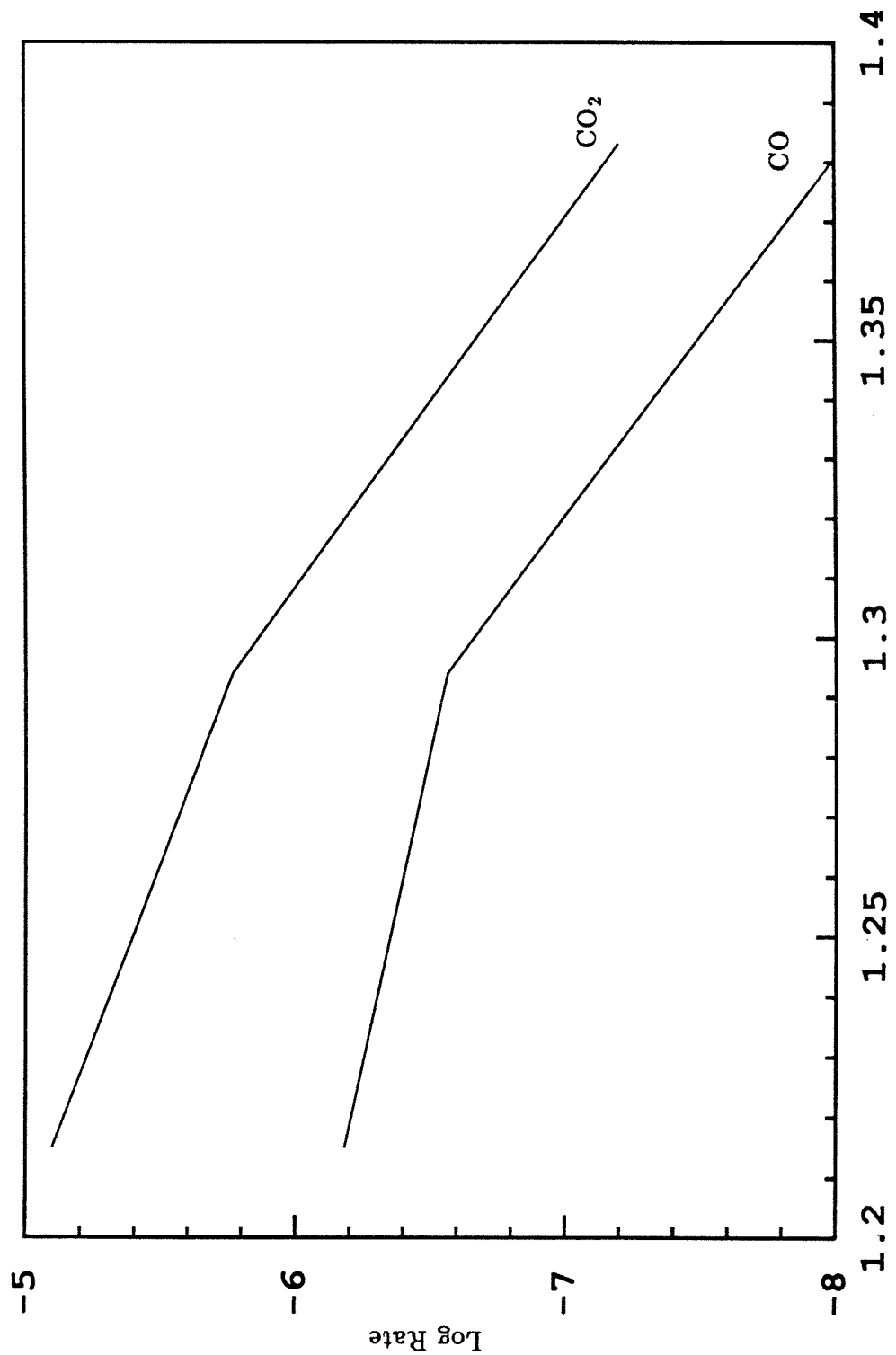

Figure 3.57. Arrhenius plot for carbon oxide production from 1600K PSOC 1488 char in 1mol% oxygen.

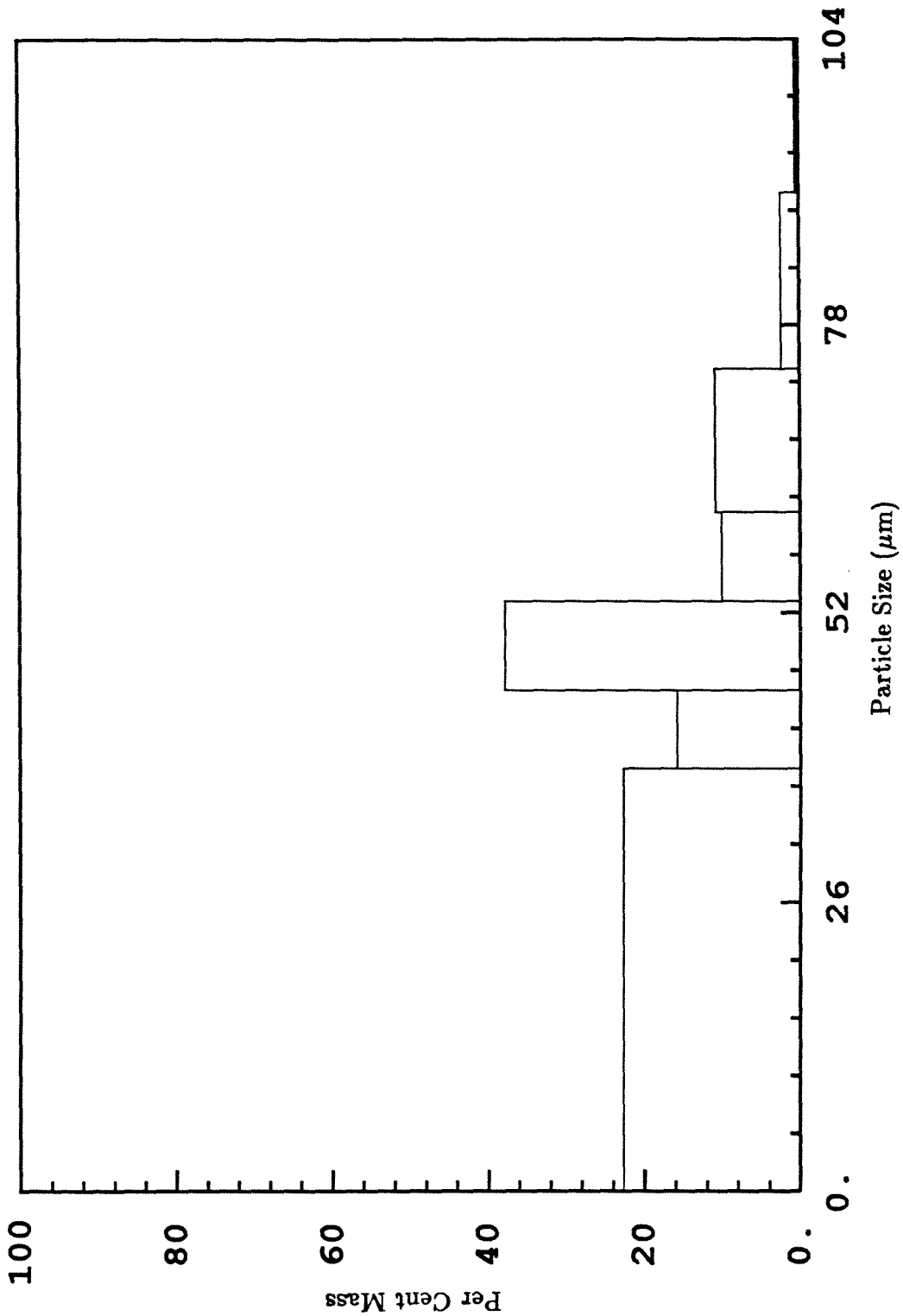

Figure 3.58. Particle size distribution for 1600K char derived from 45-63μm PSOC 1488 coal.

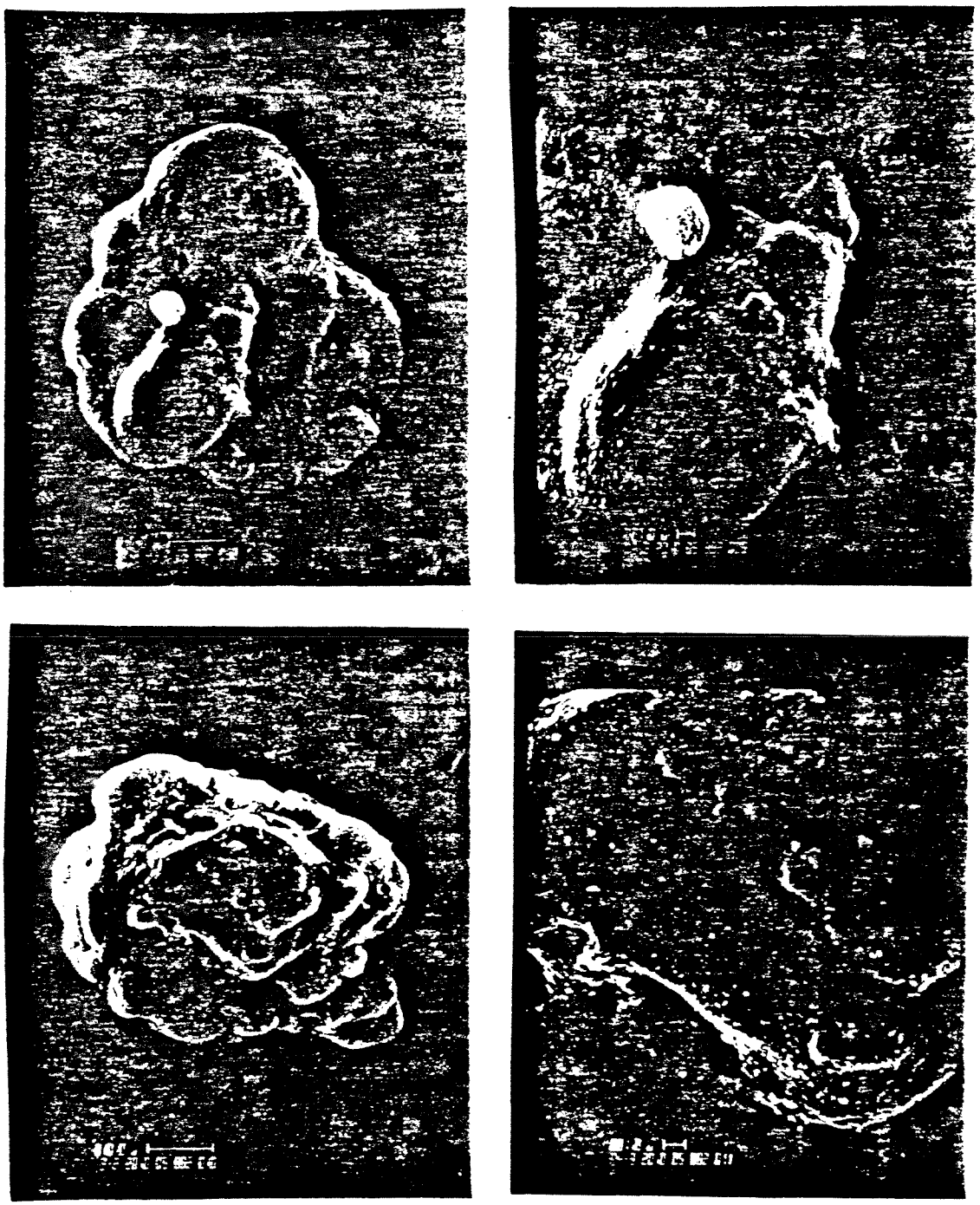

Figure 3.59. Electron micrographs of 1600K char derived from 45-63μm PSOC 1488 coal.

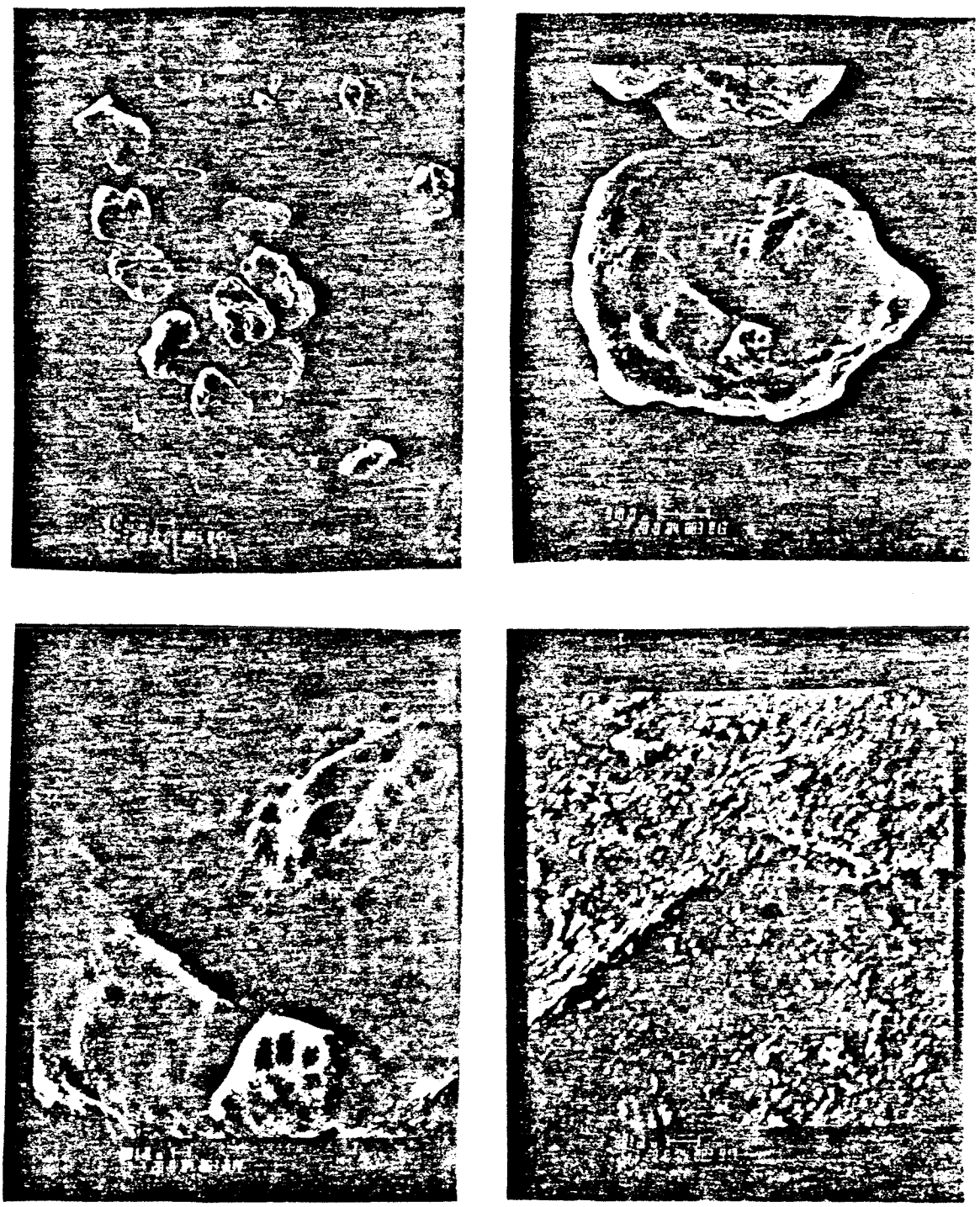

Figure 3.60. Electron micrographs of 1600K PSOC 1488 char after partial oxidation to 20% at 725K.

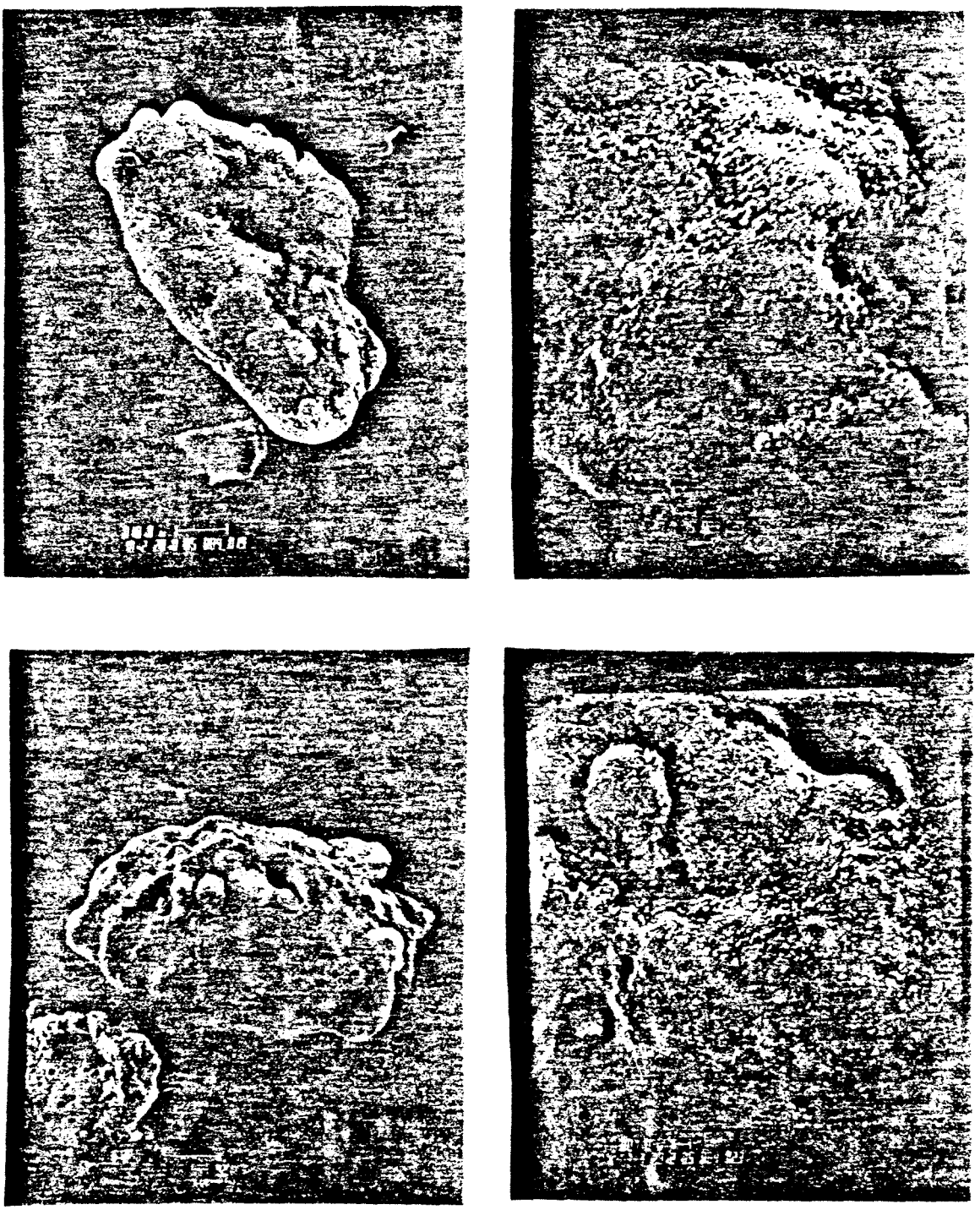

Figure 3.61. Electron micrographs of 1600K PSOC 1488 char after partial oxidation to 40% at 725K.

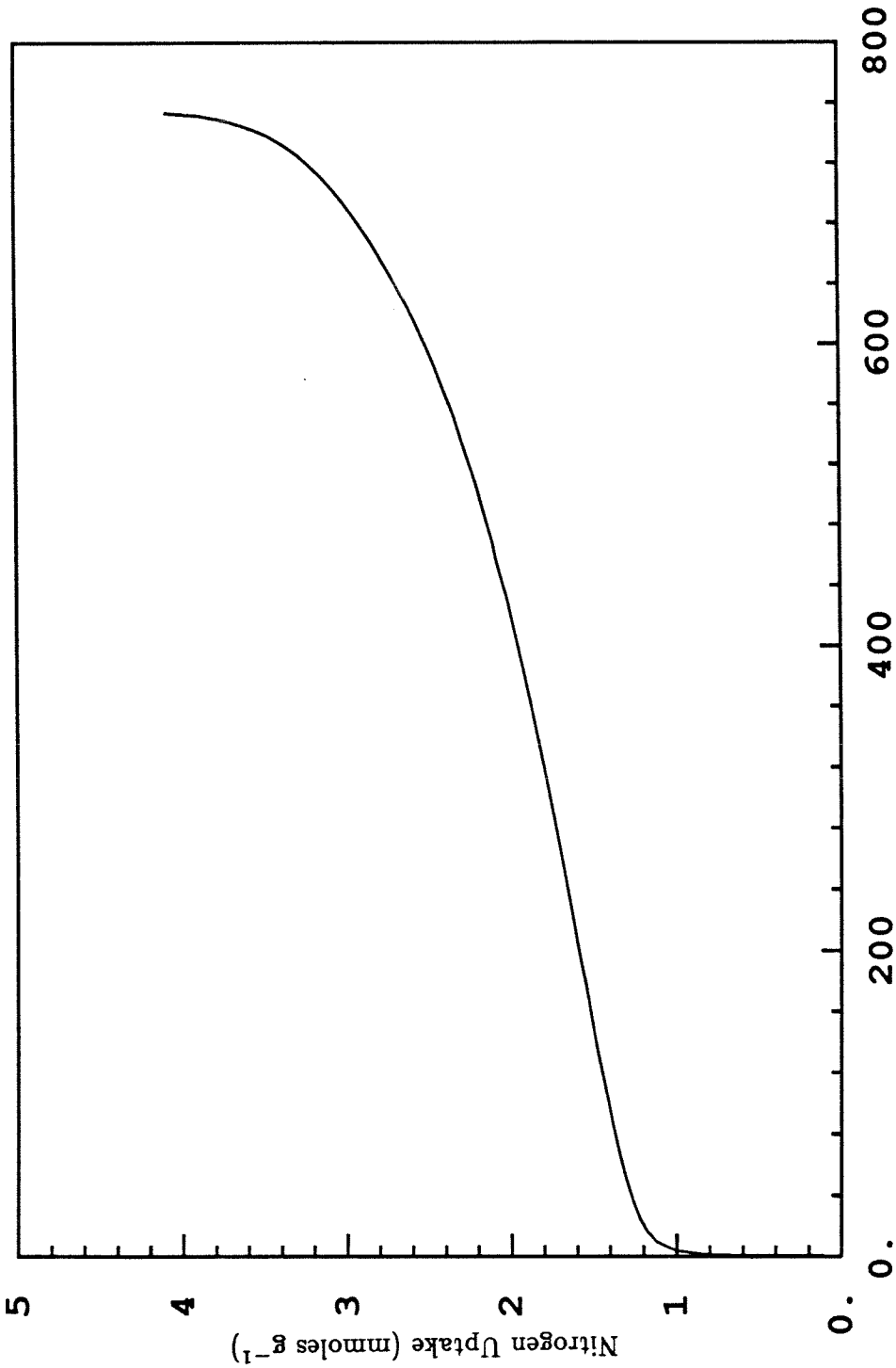

Figure 3.62. Nitrogen isotherm on 1600K PSOC 1488 char.

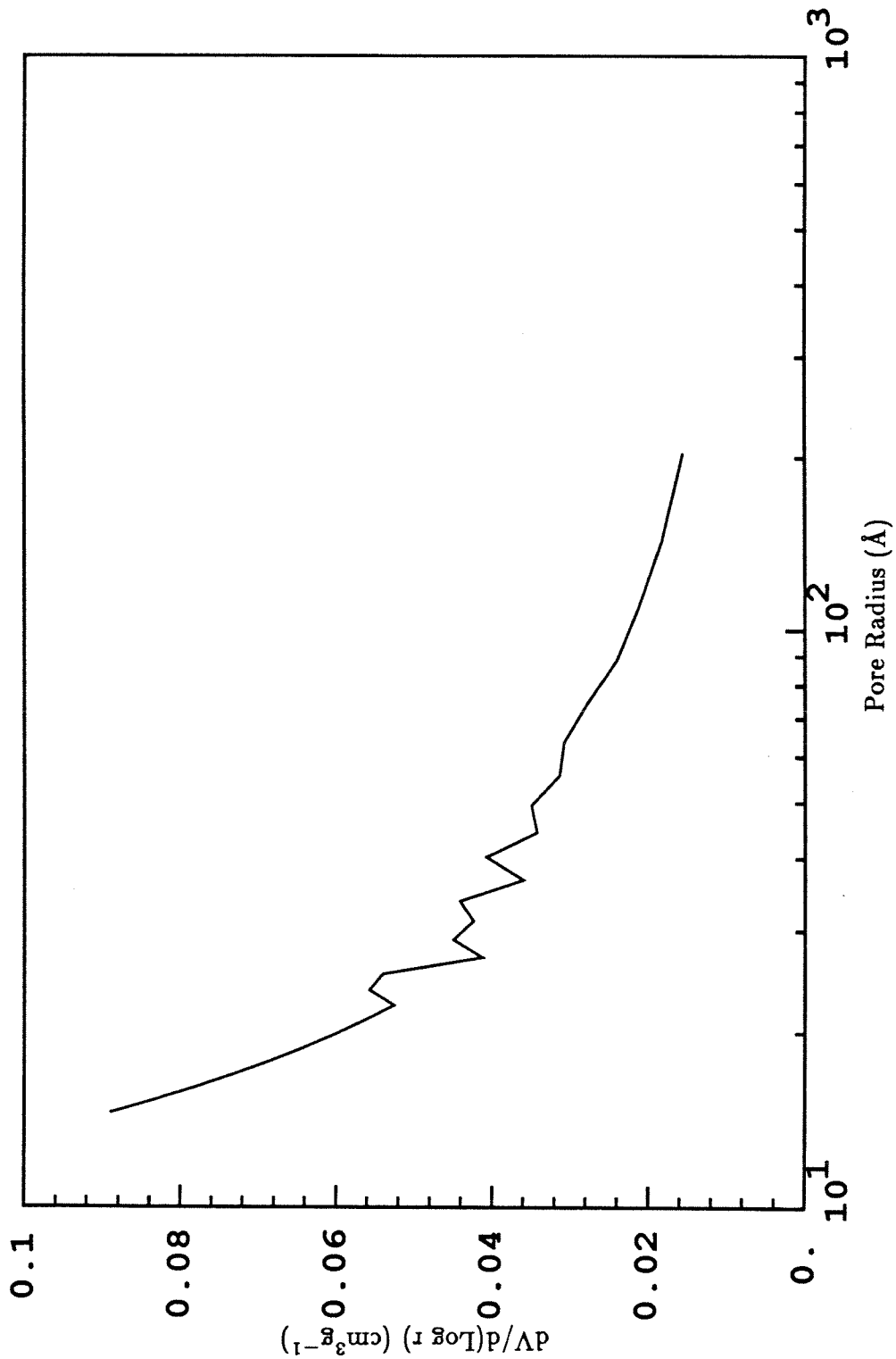

Figure 3.63. Pore volume distribution from capillary condensation in 1600K PSOC 1488 char.

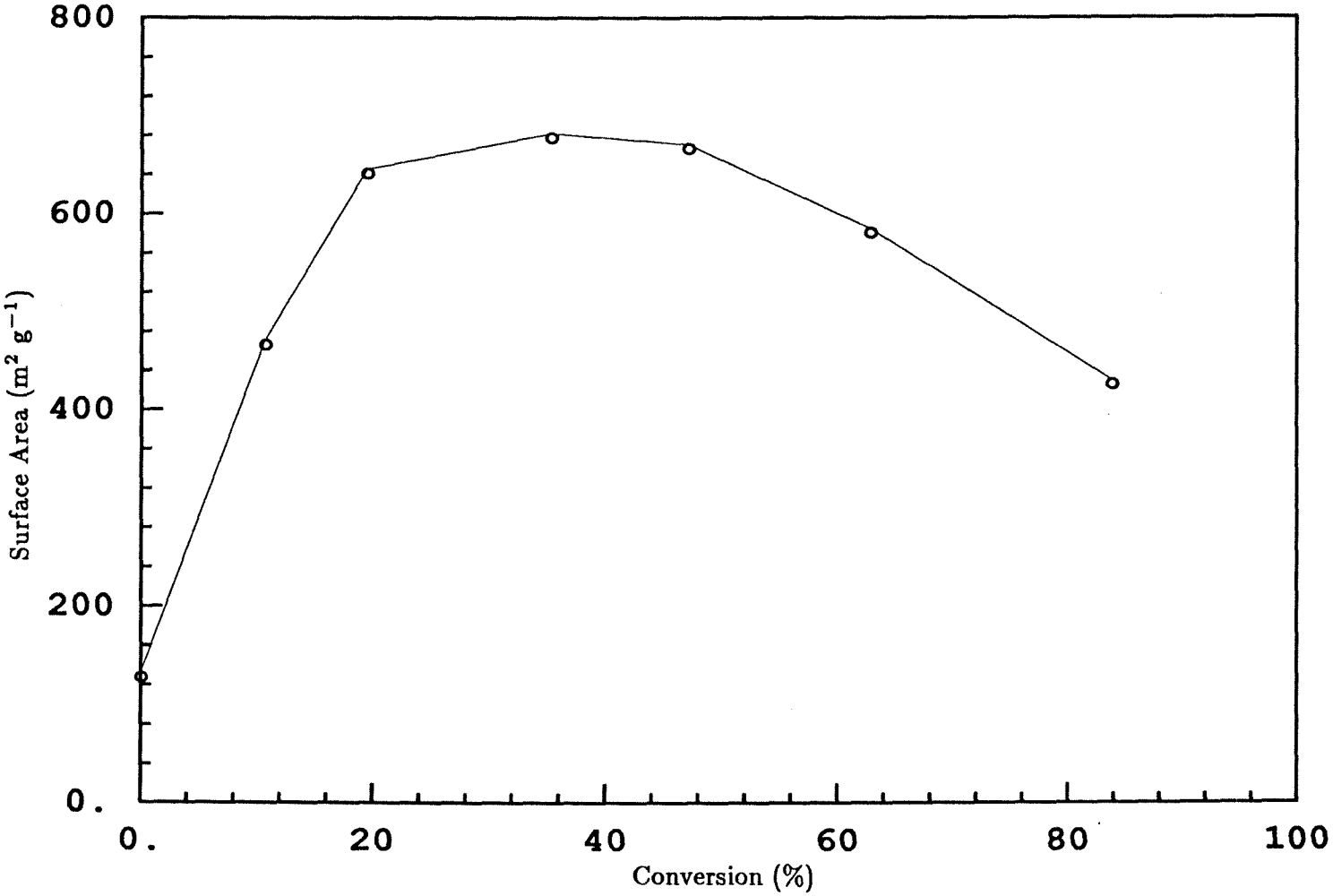

Figure 3.64. Specific surface areas of 1600K PSOC 1488 char as a function of conversion.

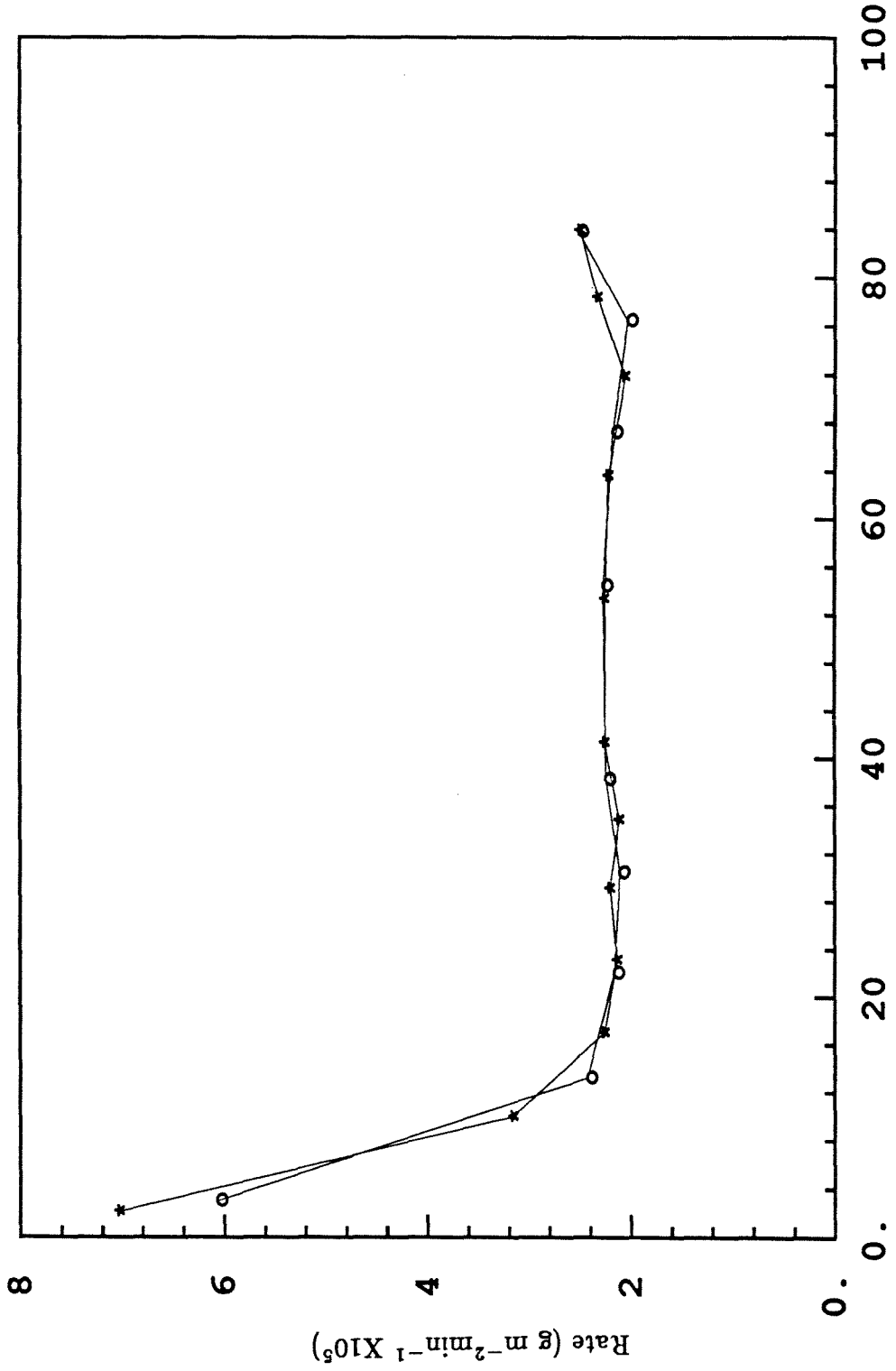

Figure 3.65. Intrinsic rate of 1600K PSOC 1488 char at 725K in 1mol% oxygen.

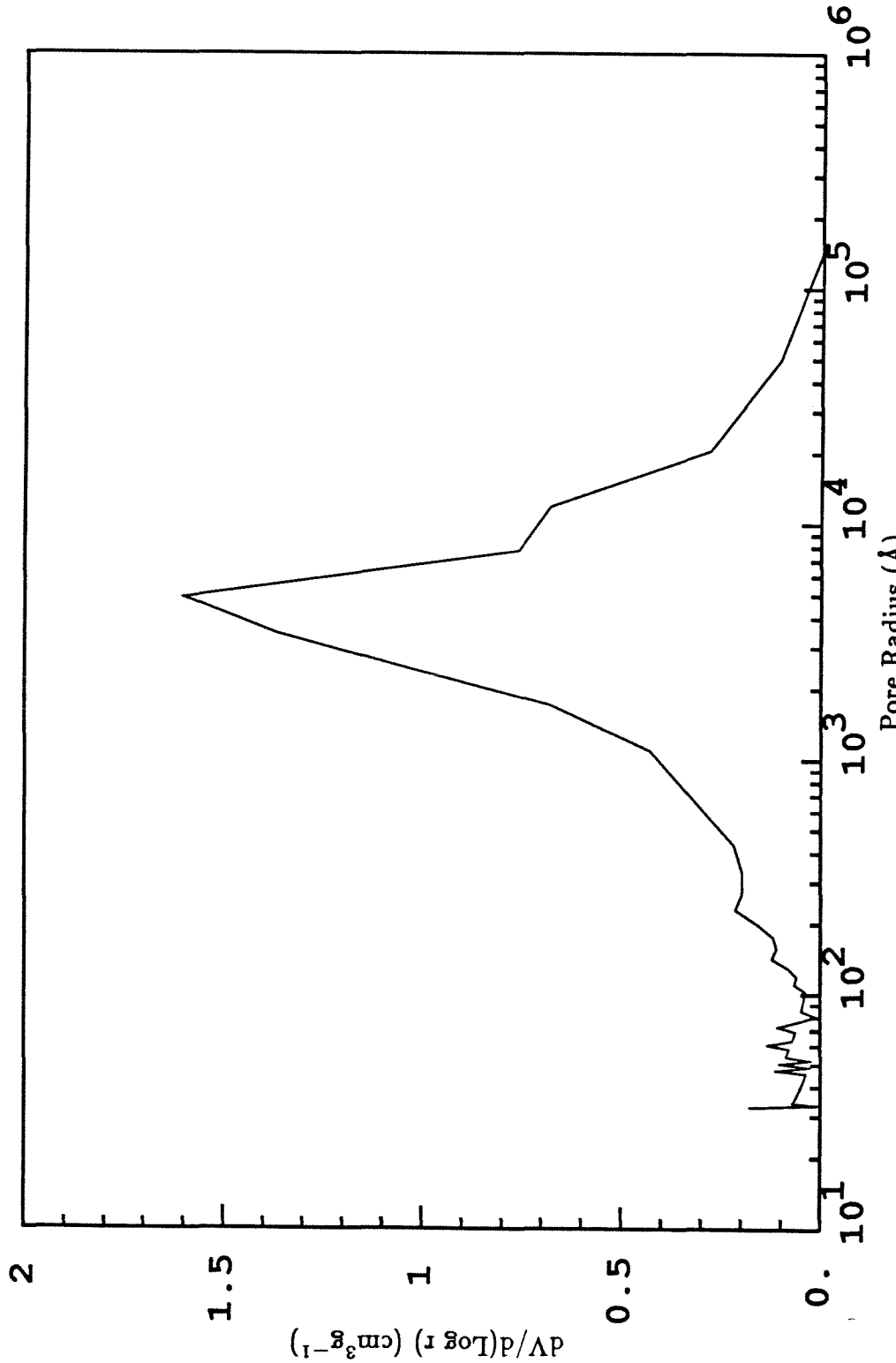

Figure 3.66. Pore volume distribution for 1600K PSOC 1488 char from mercury porosimetry.

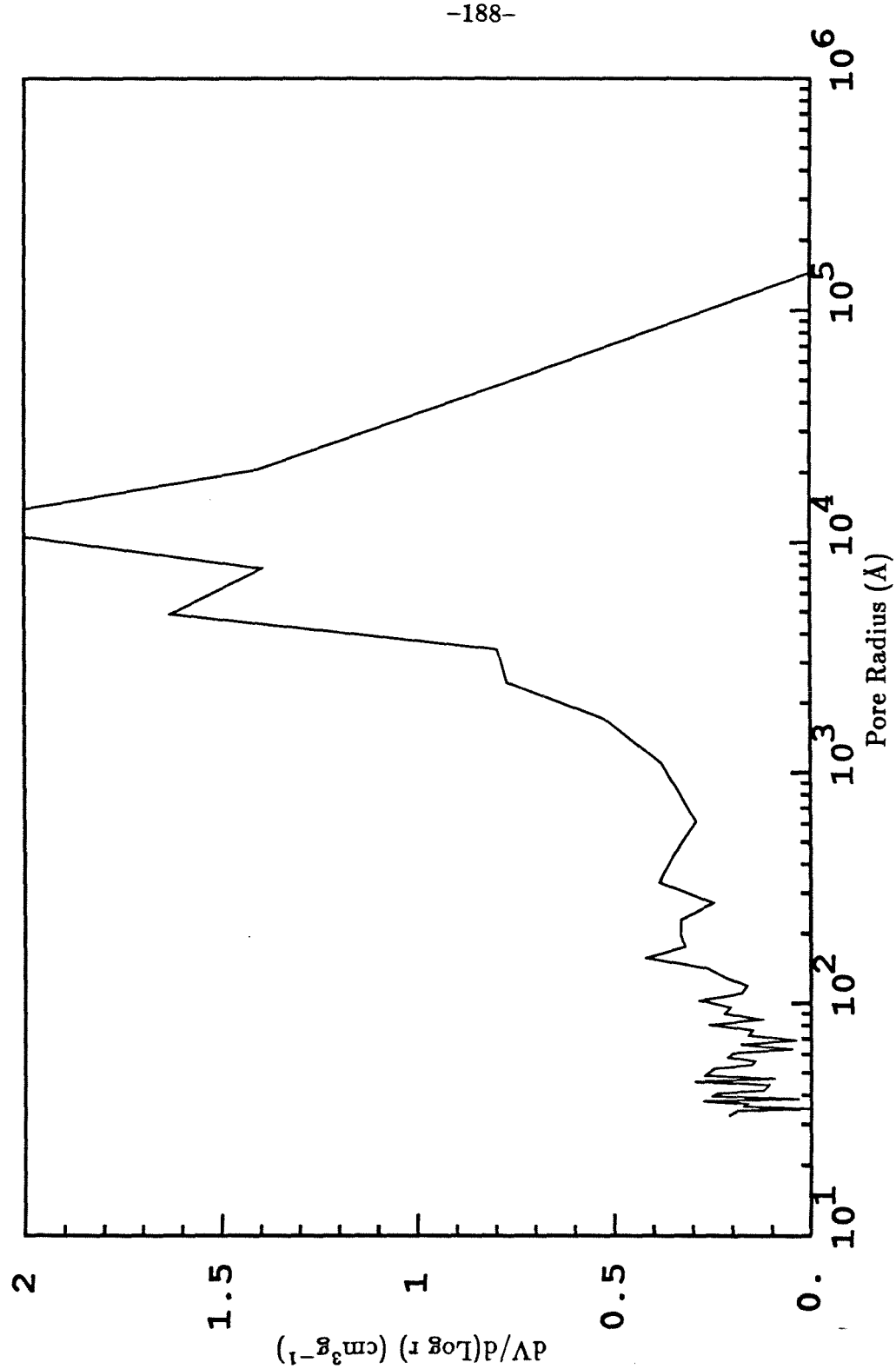

Figure 3.67. Pore volume distribution for 1600K PSOC 1488 char after partial oxidation to 60% at 725K.

CHAPTER 4

CHARACTERIZATION OF CHARS OXIDIZED AT HIGH TEMPERATURE

4.1 Introduction

In Chapter 3 we found that pore-diffusion limitations exist in these chars at temperatures as low as 775K. Thus, we might expect these limitations to be quite severe at higher temperatures. While this is true, evidence of internal burning was found at temperatures as high as 1600K.

4.2 Methods and Analysis

The following paper describes an experimental technique for obtaining characterization information on chars partially combusted at temperatures between 1350K and 1650K.

A STUDY OF THE DEVELOPING MORPHOLOGY OF BURNING CHAR PARTICLES

Paul S. Northrop[§], Ranajit Sahu[†],

Richard C. Flagan[†,‡], George R. Gavalas[§]

Depts. of Mech.(†), Env.(‡) and Chem.(§) Engrng.

California Institute of Technology, Pasadena, CA 91125, USA

ABSTRACT

Combustion experiments were carried out with 50-100μm diameter char particles derived from a lignite, a subbituminous and an HVA bituminous coal. Reactor temperatures in the range 1375 K to 1675 K were used in an ambient of air. Apparent combustion rates were inferred from residence time measurements and using ash as a tracer on partially oxidized material. Gas adsorption (N_2 at 77K and CO_2 at 298K) and mercury porosimetry were used to characterize the partially oxidized samples. The results of the characterization experiments indicate that internal burning takes place even at these relatively high temperatures.

Introduction

The entrained flow reactor is a standard experimental system for the measurement of pulverized char combustion rates. This type of reactor can be used to generate partially oxidized chars under a variety of conditions. Important characterization experiments that reveal information about the combustion process can be performed on this partially oxidized material. Some measurement techniques and procedures for this type of work have been described in the well-known papers of Field (1969) and Smith and coworkers (*e.g.* Hamor and Smith (1973)).

Peak temperatures in large pulverized coal combustion systems are generally greater than 1000K and may be in excess of 2000K. Many published measurements

of coal or char combustion rates were made at temperatures much lower than this (Essenhigh (1981), Tseng and Edgar (1984)). These low-temperature data can be obtained with relative ease by using standard experimental techniques. However, the complex nature of coal and the combustion process makes it difficult to extrapolate low-temperature-combustion data confidently to predict behavior at higher temperatures. Thus, better experiments are needed.

Prior to understanding combustion behavior, it is imperative that the physical and structural changes in the char be well characterized. This paper describes experiments that were carried out to characterize lignite, subbituminous and bituminous chars combusted at high temperatures.

Experimental Procedure

Char Formation

Chars were made from one lignite coal (PSOC 1443), one subbituminous coal (PSOC 1488), and one high-volatile A bituminous coal (PSOC 1451). A few chemical and physical characteristics of these coals are given in Table 4.1. The lignite and subbituminous coals were classified into 45-63 μm and 63-75 μm by Vortec Corporation. The bituminous coal was ground in a mechanized mortar and pestle grinder in air for approximately 30 seconds, then sieved on a mechanical shaker for 10 minutes and classified into the following size fractions: less than 45 μm, 45-53 μm, 53-74 μm, 74-104 μm, 104-125 μm and greater than 125 μm. Chars were then generated from the 53-74 μm size fraction of bituminous coal.

The coals were pyrolyzed in an electrically heated drop tube furnace. The furnace consists of an alumina tube of 5 cm internal diameter heated by Kanthal

heating elements placed in a radiation cavity 20 cm long. Coal particles were entrained in a stream of nitrogen at rates of 2 g/hr, using a syringe pump feeder and were injected into the alumina tube through a wide-bore (1 cm) water-cooled injector. Furnace wall temperatures were measured by thermocouples attached to the outside of the alumina tube. Gas temperatures were measured using a suction pyrometer. Based on wall and gas temperatures, the particle temperature was deduced from a steady-state thermal-energy balance. For this series of experiments, the chars were prepared from the raw coals at 1600K. The carrier gas flow rate was adjusted to achieve residence times of 2 seconds. The devolatilization loss for the coals was estimated to be between 30-50%, depending on the coal type.

The chars were collected on a filter. To eliminate the condensed tars, the bituminous chars were washed repeatedly with tetrahydrofuran, then dried at room temperature for 1 hour. The tar-free chars were sieve-classified into the following size fractions: less than 45 μm, 45-53 μm, 53-90 μm, 90-104 μm, 104-125 μm, 125-147 μm and greater than 147 μm. A few chemical and physical characteristics of the chars are given in Table 4.2.

High-Temperature Combustion

High-temperature combustion experiments were performed in the high-temperature flow reactor shown in Figure 4.1. Wall temperatures of 1375K, 1475K and 1675K were used to heat the primary air stream. Because of heat losses in the section between the preheater and the reactor, the gas temperature at the entrance to the reactor was 100K to 200K less than the preheater wall temperature.

For each value of the preheater wall temperature, partially burned particles

were collected at three or four axial locations by a water-cooled, nitrogen-quenched collection probe. This ensured that no further reaction occurred after particle capture. The axial locations were chosen to obtain a wide range of residence times.

Experimental Conditions

Experiments were carried out with char particles of different sizes in air at reactor temperatures between 1375K and 1675K. For the lignite and subbituminous chars, particle sizes of 45-53 μm and 53-74 μm (derived from 45-63 μm and 63-75 μm fractions of the raw coals, respectively) were used. For the bituminous char, particle sizes of 45-53 and 90-104 μm were used.

The gas velocity in the high-temperature combustor was maintained at roughly 0.7 m/s, so the particles moved several centimeters before burning out. The particle stream was directly observable through the quartz windows in the test section. Measurement of the length of the burning stream was made to estimate the burnout time of the particles. Similar measurements allowed calculation of approximate times required for ignition.

Particle Temperature Determination

The particle temperatures at several axial locations were measured in the dilute stream by a two color pyrometer. The detector optics was mounted on a 3-axis slide, so that a variety of volumes in the reactor could be focussed. Since the particle stream was nearly coaxial with the reactor, the pyrometer was focussed at the center of the reactor. The whole assembly was moved vertically to position it at the desired axial location. The minimum dimension of the view volume of the detector optics was about 0.4 to 0.8 mm. At the flow rates used, the particle residence time in

the view volume was about 1 ms. Since the view volume was so small and the particle stream so dilute, the probability of more than one particle's occupying the view volume at the same time was negligible. Average particle temperatures at a given axial location were determined by observing many particles. This temperature measurement was **not** used to infer kinetic parameters.

Conversion Calculation

The single most important variable in characterizing the partially oxidized samples is the carbon conversion or burnoff. There are several ways to determine the conversion. The most common method is gravimetric, involving mass measurements before and after combustion. Assuming that there are no sampling losses and that only carbon is burned, the extent of conversion is easily estimated. However, in this system, sampling losses are unavoidable, so it is not possible to use this method.

The carbon conversion was deduced by using ash as a tracer to estimate the quantity of carbon lost by a particular sample. The mass of ash is assumed to remain constant during combustion. This assumes negligible loss of ash mass that is due to volatilization. Even at combustion temperatures, volatilization is minimal, amounting to less than a few percent of the ash (Flagan and Friedlander (1978)). Since the chars were formed at 1600K, ash volatilization during subsequent combustion is expected to be quite small. Thus, the ash-tracer technique appears well-suited for measuring carbon conversion in chars made at high temperatures. The drawback of the ash-tracer method is that the char sample must be destroyed to determine its ash content. Furthermore, for the most accurate results, the sample size should be as large as possible. Therefore, all non-destructive char-characterization tests were

performed on the sample before its ash content was determined by incineration and subsequent weighing.

The calculation of conversion based on ash mass is straightforward: Let the mass fractions of ash in the unburned and partially burned chars be x_0 and x, respectively. Let the total masses in the beginning and at the end of partial combustion be m_0 and m, respectively. Since the mass of ash is assumed to remain constant during combustion, we have

$$m_0 x_0 = mx. \tag{4.1}$$

Also, the mass of carbon burnt, m_{loss}, is

$$m_{loss} = m_0 - m. \tag{4.2}$$

The carbon conversion, X, is defined as the mass of carbon burnt divided by the initial mass of carbon. Thus,

$$X_{expt} = \frac{m_{loss}}{m_0(1 - x_0)}. \tag{4.3}$$

Combining (4.1), (4.2) and (4.3), and eliminating m and m_0, we have

$$X_{expt} = \frac{x - x_0}{x(1 - x_0)}. \tag{4.4}$$

Thus, the conversion X_{expt} can be calculated from the ash-mass fractions x and x_0.

Experimental Results

Observation of the Particle Stream

The burning stream of particles was directly observable. Distances along the stream could be measured along the outer wall of the reactor. Knowledge of gas velocity allowed accurate estimation of residence times at various points in the reactor.

For a preheater temperature of 1275K, no visible ignition of 45-53μm lignite char particles was observed. Increasing the temperature by 100K caused some of the particles to ignite at various axial positions within the reactor. The individual particles appeared to burn for less than 50 msec. Apparently, the temperature was too low to sustain ignition.

Increasing the preheater temperature to 1475K caused all of the particles to ignite. Not all of the particles ignited at precisely the same position because of variability in the individuals. However, an average distance from the injector could be measured, and converted into an estimate of the time required for ignition. Values for these times under different conditions are shown in Table 4.3. Not surprisingly, ignition times decrease for increasing preheater temperature and for decreasing particle size.

Table 4.3 also shows estimates of the time required for extinction of most of the particles. Again, there is variability among individuals, so averages that are representative of the group are shown. It is interesting to note that the subbituminous takes the least amount of time to burn out at 1475K, while the bituminous char takes the greatest.

Particle Temperatures

Temperatures were found to vary from particle to particle. This is not surprising, since the individual particles are of different sizes and shapes, and contain different amounts of voids and ash. On the average, particle temperatures were 100-200K above the preheater wall temperature.

Optical Microscopy

Particle size was determined visually under the optical microscope. Since the particles were generally irregular, the following procedure was used: the length along the major axis and the greatest length along its perpendicular were measured. The average particle size was computed as the arithmetic mean of these lengths. This was repeated for 25 particles in each category. Figure 4.2 shows the distributions of the average particle sizes for the unburned lignite and bituminous chars. The subbituminous char showed a spread in particle sizes similar to that of the lignite char.

An indication of the irregularity of shape of a particle is the aspect ratio, which is defined as the ratio of the major to the minor dimension. The average aspect ratio for the unburned 45-53 μm lignite char particles is 1.35. The corresponding value for the 45-53 μm subbituminous is 1.28, while that for the 90-104 μm bituminous char particles is 1.15. This indicates that on the average, the lignite particles are the most irregular, while the bituminous particles are the least irregular. These measurements show that the chars differ in their external geometry.

Observations using the optical and electron microscopes have shown that the bituminous char is cenospheric; *i.e.*, it contains large bubble-like voids (Lightman and Street (1967)). The free swelling index (FSI) for the bituminous coal (7.5) confirms this observation. Neither the lignite nor the subbituminous coal exhibits any sort of swelling (FSI=0). Thus, the chars differ greatly internally as well as externally.

Electron Microscopy

Electron micrographs shown in Figures 4.3 to 4.5 show differences in particle surface

structure for the three chars. The bituminous char has a relatively smooth surface with a few large blow holes. The cenospheric nature of the material is readily apparent.

The ash content of the bituminous char is nearly 20% by weight. The ash is unevenly distributed as small particles (less than 1 μm in diameter) on the surface. Figures 4.3a and 4.3b show two bituminous char particles before combustion. Large pores, which act as reactant feeders into the interior of the particles, are clearly visible. Figure 4.3c shows a particle at higher magnification. The smaller ash particles, present as globules on the surface, are clearly visible.

Figures 4.4a and 4.4b show micrographs of a typical unburned lignite char particle at different magnifications. The ash content of this char is quite high, nearly 38% by weight. The entire particle surface is quite rough. Much of this is due to the presence of ash particles. After complete oxidation at 500°C, the ash from an individual particle remains aggregated, as shown in Figure 4.4c.

Figures 4.5a and 4.5b show that unburned subbituminous char particles have a somewhat bubbly, rounded appearance. In this way, it is similar to the bituminous char. However, it does not swell to a great degree; hence, it resembles the lignite char. Interestingly, the ash content of this char is quite low: only 9.1% by weight.

The presence of ash in the chars is expected to influence combustion behavior chemically via catalysis (Walker and Nichols (1957)) and physically, via blockage of oxygen. The catalytic effects of ash are expected to be more important at lower temperatures than at higher temperatures. However, the physical effects of ash are important at higher conversions at all temperatures, particularly for chars with

high ash contents. It appears from examination of the micrographs that ash does remain associated with its parent carbon matrix. Figure 4.3d shows a bituminous char particle oxidized to 67% conversion at low temperature. Significant amounts of ash are still present along with the remaining carbon.

During high temperature combustion, some ash may be lost from the particles because of fragmentation or attrition. This will not affect the conversion calculation as long as the entire sample is used for the ashing experiments. The ash does appear to remain associated with the subbituminous char particles, as seen in Figure 4.5d. The unusual appearance of this particle may be indiciative of the blocking effect of the ash, as described above.

At sufficiently high temperatures, the ash may melt, depending on its composition (Raask (1985)). Ash did not melt on any of the bituminous particles observed; however, melting of ash did occur at the highest temperature used for the lignite char, as seen in Figure 4.4d. Thus, there are pronounced differences in ash distribution and behavior of ash in these materials.

For all chars, average particle size decreases monotonically with the extent of conversion for each nominal wall temperature used. This is shown in Figure 4.6 for the lignite and bituminous chars. No clear trend for aspect ratio with conversion was observed for any char.

Surface Area Measurements

Nitrogen at 77K was used to obtain isotherms for all samples. The BET theory (Brunauer *et al.*(1938)) was used to infer specific surface areas of unburned and partially oxidized samples from these isotherms.

Specific surface areas versus conversion are shown in Figures 4.7 and 4.8 for the lignite and bituminous chars, respectively. Surface areas for the subbituminous chars are reported in Table 4.6. All surface areas are reported on a per-gram carbon basis after accounting for the small area of the ash. Figures 4.7a and 4.8a show surface areas after oxidation at low temperature, while Figures 4.7b and 4.8b show surface areas after oxidation at high temperature. Fewer data points were obtained at the high temperature. However, it is clear that for all chars, surface areas were substantially higher during low temperature oxidation, indicating better oxygen penetration into the porous microstructure.

The surface area for the lignite oxidized at low temperature shows a broad maximum of the order 1000 m^2/g, starting at a conversion of around 25%. When it is oxidized at high temperature, however, it shows a much smaller maximum ($300m^2/g$) at a conversion of about 20%. The surface area decreases significantly after the maximum. The initial rise in the specific area of the material oxidized at high temperature indicates that there is penetration of oxygen into the pores in the early stages of combustion. The subsequent drop in surface area may be due to thermal annealing and closing of the micropores (Smith (1972)).

For the bituminous char, areas obtained after high-temperature conversion are at least one order of magnitude smaller than those obtained after low-temperature conversion. This is due to diffusion-limited burning and a consequent lack of micropore opening at higher temperatures. Maxima in the areas are also moved to lower conversions as seen in Figure 4.8b. Conclusions regarding thermal annealing cannot be drawn because of insufficient data.

During low temperature oxidation, the subbituminous char showed a maximum surface area of 675 m^2/g (see Table 4.6). During high-temperature oxidation, the surface area remained nearly constant at 110 m^2/g. Note that the conversion values are estimated here. Apparently, there was a significant amount of ash that was not removed from the filter, resulting in conversion values that were too low. The conversions were estimated, based on particle shrinkage and void growth.

Carbon Dioxide Adsorption

Carbon dioxide adsorption at 298K was used to obtain an indication of the amount of microporosity associated with the unburned and partially oxidized chars. The Dubinin-Polyani theory was used to esitmate maximum uptake of carbon dioxide, which is proportional to the total micropore volume. Tables 4.4 and 4.6 show the results for chars oxidized at both low and high temperatures.

For the lignite, maximum carbon dioxide capacity increases during both low- and high-temperature oxidation. Evidently, micropores are opened during oxidation over a wide range of temperatures. For the bituminous char, the carbon dioxide uptake remains constant during low-temperature oxidation, but increases during high-temperature combustion. It is not clear how microporosity could be increased during high-temperature combustion, but not during low-temperature oxidation. For the subbituminous char, the uptake remained constant during low temperature oxidation. At high temperatures, the uptake remained constant, but at a value somewhat below the initial. This may be due to some initial pore closing mechanism.

Oxygen Chemisorption

Oxygen uptake was measured on selected samples at 575K after 12 hours' exposure

to oxygen at a pressure of 10 torr. Prior to this, the samples were cleaned in a vacuum of 10^{-3} torr at 875K. Tables 4.4 to 4.6 show the results for the chars after partial oxidation at both low and high temperature. The chemisorption capacities for the bituminous and subbituminous chars remain relatively constant during partial oxidation at both temperatures. It appears that active site concentration of these chars is not greatly affected by oxidation. The chemisorption capacity for the lignite char dropped after a small amount of oxidation, then increased with increasing conversion at both temperatures. Interestingly, the lignite char has the largest capacity for oxygen, while bituminous char has the lowest.

Capillary Condensation

Pore-volume distributions for pores with radii between 16 and 150 Å were obtained from measurement of capillary condensation of nitrogen in the pores of the chars. This corresponds to relative pressures of 0.35 to 0.975 of the isotherm at 77K. Since multilayer adsorption occurs over the entire range of pressures, pore radii and volumes had to be adjusted accordingly. The algorithm given by Yan and Zhang (1986) was used for these calculations. Resulting pore-volume distributions for the unburned chars are given in Figures 4.9 to 4.11, respectively. These experiments show that lignite char contains the greatest amount of porosity in this range of pore sizes, while bituminous char contains the least.

Total pore volume over this range of pore sizes is given for the partially oxidized samples listed in Tables 4.7 to 4.10.

Mercury porosimetry

Mercury porosimetry experiments were performed on an Autoscan-33 apparatus

capable of applying pressures of 33000 psig. The raw data were in the form of cumulative volume versus applied pressure. The pore radius penetrated by a given pressure was calculated from the Washburn equation; pore-volume distributions were obtained by numerical differentiation of the cumulative volume curve. Figures 4.12 to 4.14 show the pore-volume distributions for the unburned chars. The lignite char contains pores over a wide range of sizes. The bituminous char has very few pores with diameters between 32 and 200 Å. The subbituminous char possesses a great number of pores with radii of 1000-10000 Å.

Figures 4.15 to 4.17 show the pore-volume distributions for chars oxidized at high temperature. In each case, there was little change in measured total pore-volume after combustion at high temperature. However, there appeared to be some increase in the macropore volume at the expense of the transition pores. Mercury porosimetry was also performed on lignite and subbituminous chars oxidized at 725K, and on bituminous char oxidized at 775K. These experiments showed that pore volumes increase significantly after oxidation at these low temperatures, as seen in Figures 4.18 to 4.20. These results indicate that oxygen effectively penetrated the porous microstructure of the chars at these low temperatures. Figure 4.21 shows the growth of pores in the ranges 20-500 Å and >500 Å as a function of low-temperature conversion for the lignite char. The total pore volume is also shown. This total pore volume includes the contributions of the micropores and pores larger than 1.76 μm in diameter. Voids larger than this are assumed to be due to interparticle voidage. As seen from the figure, pores in all sizes seem to increase with conversion, confirming the earlier hypothesis. Figure 4.22 shows similar behavior in case of the bituminous

char.

The results of these characterization experiments are tabulated in Tables 4.7 to 4.10. A comparision of the results obtained for the materials oxidized at low temperature to those oxidized at high temperature support the idea that the exterior of the solid is the primary zone of reaction, with some internal burning occurring (as seen by the growth of the macropores). The internal burning most likely takes place in the feeder pores, leaving the smaller transitional and micropores unaffected.

Model Description: Bituminous Char

A simple model of the bituminous char particle will be proposed in this section. Values of carbon conversion obtained experimentally will be compared to theoretical predictions.

As previously mentioned, the bituminous char particles contain large internal voids. In this model, a single particle of this char is assumed to be spherical and to consist of a single concentric spherical void, as shown in Figure 4.23. The external radius of the particle is r, and the radius of the internal void is r_v. The shell is assumed to be composed of carbon, containing micro- and transition pores. The size of the void is chosen such that it accounts for the total macroporosity. In addition, the shell contains feeder pores that allow access of oxygen to the inside, so that reaction can take place on the internal surface. Thus, as combustion proceeds, the external radius shrinks and the internal void radius grows.

Assuming a constant carbon density, ρ_C, the initial mass of such a particle is

$$m_0 = \frac{4}{3}\pi(r_0^3 - r_{v0}^3)(1 - \epsilon_{t0})\rho_C, \tag{4.5}$$

where ϵ_{t0} is the initial porosity that is due to the transition and micropores. The mass, after conversion X, is given by

$$m_1 = \frac{4}{3}\pi(r_1^3 - r_{v1}^3)(1 - \epsilon_{t1})\rho_C. \tag{4.6}$$

Since reaction takes place at both surfaces, it is assumed that the changes in the radii can be related by

$$r_{v1} - r_{v0} = \mathcal{F}(r_0 - r_1), \tag{4.7}$$

where $\mathcal{F}$ is a factor whose value is less than or equal to one. Neglecting curvature effects, if $\mathcal{F}$ is equal to one, the rates of burning are the same at both surfaces. This will be true if there is no diffusion resistance offered by the feeder pores. In reality, $\mathcal{F}$ will most likely be less than one at high temperatures.

The relation between the external radius and the void radius is given by

$$r_{v0} = r_0\left(\frac{\epsilon_m}{1 - \epsilon_t}\right)^{\frac{1}{3}}, \tag{4.8}$$

where ϵ_m is the porosity that is due to the macropores. The conversion X is given by

$$X = \frac{m_0 - m_1}{m_0}. \tag{4.9}$$

Combining (4.5)-(4.9), we get

$$X = 1 - \frac{\left[r_1^3 - \left[r_0\left\{\left(\frac{\epsilon_{m0}}{1-\epsilon_{t0}}\right)^{\frac{1}{3}} + \mathcal{F}\right\} - \mathcal{F}r_1\right]^3\right](1 - \epsilon_{t1})}{r_0^3(1 - \epsilon_{t0} - \epsilon_{m0})}. \tag{4.10}$$

Equation (4.10) is used to calculate values of the conversion from the known quantities. For the char combusted at 1400°C, the average initial radius, r_0, was

57 μm; the average final radius, r_1, was 50.5 μm (after 66% conversion, measured experimentally); the initial macroporosity, ϵ_{m0}, was 0.289; the initial transitional and microporosity, ϵ_{t0}, was 0.161; and the final transitional and microporosity, ϵ_{t1}, was 0.082. Assuming no diffusion resistance ($\mathcal{F}$=1), and using the values quoted above, the conversion is estimated at 74.5%. If $\mathcal{F}$ is lowered to a value of 0.8, the calculated conversion becomes 67.1%, which is close to the experimentally determined value of 66%. According to the model, a certain amount of internal burning must take place. Table 4.11 shows the comparison of the experimental and theoretical conversion values for the samples combusted at 1400°C. The value of $\mathcal{F}$ was assumed to be zero in these calculations. It is clear that external burning alone is not able to account for the carbon mass loss.

The presence of ash was not considered in this model. The effect of ash cannot be neglected in the case of the lignite char. A simple model for lignite char combustion is described in the next section.

Model Description: Lignite Char

Because of the different physical nature of the lignite char, a different model had to be developed. This model assumes that ash particles and voids are randomly distributed throughout the particle. The initial ash volume fraction (ϵ_{ash}) and void fraction (ϵ_{lig}) can be calculated from the mass fraction of ash and the apparent density of the particle (ρ_{app}). The mass fraction of ash is related to the volume fraction of ash by

$$\chi_{ash} = \frac{\epsilon_{ash}\rho_{ash}}{\epsilon_{ash}\rho_{ash} + (1 - \epsilon_{ash} - \epsilon_{lig})\rho_C}, \tag{4.11}$$

where ρ_{ash} is the density of ash and ρ_C is defined as before. The apparent density can be expressed as

$$\rho_{app} = \epsilon_{ash}\rho_{ash} + (1 - \epsilon_{ash} - \epsilon_{lig})\rho_C. \tag{4.12}$$

Given an ash mass fraction of 0.36, an ash density of 2.0 g/cc, an apparent density of 1.1 g/cc and, assuming the carbon density to be 1.5 g/cc, we find an initial ash volume fraction of 0.2 and an initial void fraction of 0.33.

As the carbon is oxidized, the exposed ash is assumed to accumulate on the surface with an interparticle voidage of ϵ_{int}. Thus, the observed particle radius will be the sum of the radius of unburned material plus the thickness of the ash layer. The radius of unburned material (r_C) can be related to the observed radius (r_{obs}) by

$$r_{obs}^3 - r_C^3 = \frac{\epsilon_{ash}}{(1 - \epsilon_{int})}(r_0^3 - r_C^3). \tag{4.13}$$

The conversion (X) is given by

$$X = 1 - \frac{r_C^3(1 - \epsilon_{ash,X} - \epsilon_{lig,X})}{(1 - \epsilon_{ash} - \epsilon_{lig})}, \tag{4.14}$$

where X in the subscript denotes quantities after a conversion X. Assuming that the quantities ϵ_{ash} and ϵ_{lig} do not change significantly during high-temperature combustion, we can combine (4.13) and (4.14) to get

$$X = 1 - \frac{r_{obs}^3 - vr_0^3}{(1 - v)r_0^3}, \tag{4.15}$$

where v is $\frac{\epsilon_{ash}}{(1-\epsilon_{int})}$. So, for an initial particle radius of 24.9 μm, an observed particle radius of 21.0 μm yields a conversion of 57%. This is significantly lower than the

measured conversion of 51.1%. Other values are shown in Table 4.11. In all cases, the predicted conversion was lower than the measured conversion. Since the model accounts only for carbon lost from the external surface, the results indicate that oxidation occurs in the pores of the particles.

The model could not be applied to the subbituminous char, as no reliable measure of conversion was obtained.

Model Description: Area Calculation

The model used to simulate combustion of a single particle is an extension of the model by Loewenberg *et al.*(1987). The voidage of the solid is described by a random capillary model (Gavalas (1981)), using a local burn-off variable, q. The model can be used to predict temperature-time histories of individual particles. In addition, specific surface area can be calculated as a function of overall conversion.

Figure 4.24 shows the model prediction for surface area versus conversion for a particle with an initially trimodal pore-size distribution. There is an increase in surface area at low conversions. This is due to oxygen penetration of the porous structure at relatively low temperatures, and is in qualitative agreement with what is observed experimentally. The surface area then drops as locally high-surface area material is shed from the outer edge of the particle. At intermediate conversions, the surface area remains rather constant. This is in contrast to what was observed for the lignite char. As previously mentioned, the drop in observed surface area may be due to annealing of the micropore structure, which is not accounted for in the model.

A version of the model that lumped the reaction at the external surface of the

particle was used to examine the effect of initial particle size on time-temperature evolution. The results were used to estimate the spread of conversions of particles at fixed residence time, based on the spread of initial radii. Table 4.12 shows model predictions of conversion for different sizes of particles at different times. The results show that the captured samples are likely to contain particles with a wide range of conversions.

Conclusions

Chars derived from lignite, subbituminous and bituminous coals have been burned at high (1200-1400K) and low (725K-775K) temperatures. Partially oxidized samples have been characterized by measuring nitrogen specific surface areas, carbon dioxide uptakes, active site concentration (via oxygen chemisorption), and pore-volume distributions and porosimetry. These measurements, along with direct observations of particles, show that high-temperature combustion is strongly pore-diffusion limited. However, there is evidence of internal burning at these relatively high temperatures.

There is also evidence to support the idea that pore annealing is a significant factor at temperatures below 2000K for the lignite char.

Acknowledgements

This work was supported by the U.S. Department of Energy under contract DE-AC2284FC70915.

REFERENCES

Brunauer, S., Emmett, P. H. and Teller, E., J. (1938). J. Am. Chem. Soc., **60**, 309-319.

Essenhigh, R. H. (1981). in *Chemistry of Coal Utilization*, 2^{nd} Supp. Vol., M. A. Elliot, Ed. John Wiley and Sons, New York, pp. 1153-1312.

Field, M.A. (1969). *Combust. Flame*, **13**, 237.

Flagan, R.C. and Friedlander, S.K. (1978). in *Recent Developments in Aerosol Science*, D.T.Shaw, Ed., John Wiley and Sons, New York, pp. 25-59.

Gavalas, G. R. (1981). *Comb. Sci. Tech.*, **24**, 197-210.

Hamor, R.J. and Smith, I.W. (1973). *Combust. Flame*, **21**, 153.

Lightman, P. and Street, P. J. (1968). *Fuel*, **47**, 7-28.

Loewenberg, M., Bellan, J. and Gavalas, G. R. (1987). *Chem. Eng. Comm.* **58**, 89.

Raask, E. (1985). **Mineral Impurities in Coal Combustion**, Hemisphere Publishing, New York.

Smith, I. W. (1972). *Fuel*, **51**, 312-321.

Tseng, H. P. and Edgar, T. F. (1984). *Fuel*, **63**, 386-393.

Walker P. L., Jr. and Nichols, J. R. (1957). Ind. Carbon and Graphite Conf., London, pp. 334-347.

Yan, J. and Zhang, Q. (1986). *Part. Charact.*, **3**, 20-25.

PSOC #	1451	1443	1488
Rank	HVAB	Lignite	Sub-bit
Location	Pennsylvania	Texas	Montana
Seam	Pittsburg	Wilcox	Dietz
Proximate Analysis%			
Moisture	2.54	28.54	23.66
Ash	13.32	15.31	4.08
Volatiles	33.56	44.17	31.95
Fixed Carbon	50.58	11.98	40.31
Ultimate Analysis%			
Ash	13.32	15.31	4.08
Carbon	70.05	40.62	54.91
Hydrogen*	4.55	2.92	3.78
Nitrogen	1.33	0.76	0.68
Sulfur	1.33	0.53	0.38
Chlorine	0.07	–	0.03
Oxygen*	6.81	11.32	12.47
FSI	7.5	0.0	0.0

Table 4.1. Properties of raw coals.*-excludes moisture.

PSOC #	1451	1443	1488
C(wt%)	78.30	59.62	NA
H(wt%)	0.96	0.43	NA
Ash(wt%)	19.85	38.1	9.1
Apparent Density (g/cm^3)	0.5	1.1	0.45
Void Fraction	0.47	0.33	0.55
Sieve Cuts Used (μm)	45-53,90-104	45-53,61-74	45-53

Table 4.2. Properties of the 1600K chars.

Char Type	Wall Temp. K	Part. Size μm	τ_{ign} msec	τ_{out} msec
Lignite	1475	45-53	~60	~215
	1475	61-74	~75	~275
	1675	45-53	~30	~135
	1675	61-74	~45	~200
Bituminous	1475	45-53	~100	
	1475	90-104	~150	
	1675	90-104	~80	~300
Sub-Bit.	1475	45-53	~60	~160

Table 4.3. Observed ignition and extinction times for chars.

Conversion %	O_2 Uptake mmoles/g d.m.m.f. char	CO_2 Uptake mmoles/g d.m.m.f. char
Low Temperature		
0	0.40	4.5
28.5	0.25	6.0
55.5	0.39	7.8
High Temperature		
9.8	0.29	5.5
50.6	0.41	6.3

Table 4.4. Oxygen and carbon dioxide uptakes of partially oxidized lignite char.

Conversion %	O_2 Uptake mmoles/g d.m.m.f. char	CO_2 Uptake mmoles/g d.m.m.f. char
Low Temperature		
0	0.15	2.9
15.6	0.09	2.7
41.7	0.11	2.6
63.2	0.13	2.9
High Temperature		
46.7	0.10	8.5
65.9	0.11	13.1

Table 4.5. Oxygen and carbon dioxide uptakes of partially oxidized bituminous char.

Conversion %	O_2 Uptake mmoles/g d.m.m.f. char	CO_2 Uptake mmoles/g d.m.m.f. char	Surface Area m^2/g
Low Temperature			
0	0.25	6.4	131
18.1	0.25	6.7	640
40.3	0.26	6.7	675
59.8	0.28	6.8	590
High Temperature			
10*	0.21	4.7	100
30*	0.18	4.0	120
60*	0.29	4.8	115

Table 4.6. Oxygen uptake, carbon dioxide uptake, and nitrogen surface area of partially oxidized subbituminous char. *-estimated values.

Char Size	Conv.	Total Mass	Ash	N_2 BET Areas		Pore Volume (20-200 Å radius)	
(μm)	(%)	(g)	(%)	(m^2/gtot)	(m^2/gC)	(cm^3/gtot)	(cm^3/gC)
45-53	0	0.1698	38.0	185	285	0.1231	0.1985
	14.3	0.1092	41.7	443	744	0.1923	0.3298
	28.5	0.0945	46.1	481	874	0.2730	0.5065
	44.1	0.1014	52.3	476	971	0.3170	0.6646
	55.5	0.0870	57.8	401	922	0.3563	0.8436
	72.0	0.0757	68.6	276	831	0.5130	1.6340

Table 4.7. Characterization results for lignite chars oxidized at 725K.

Char Size	Conv.	Ash	N_2 BET Areas		Vol. (N_2) 20-200 Å radius	
μm	%	%	m^2/gtot	m^2/gC	cc/gtot	cc/gC
104-125	0	19.0	12.4	15.3	0.0405	0.050
	14.2	21.5	146.1	186.0	0.0817	0.1042
	27.3	24.4	190.2	251.5	0.0907	0.1204
	39.9	28.1	148.5	206.4	0.1093	0.1521
	57.7	35.7	181.1	281.5	0.1222	0.1899
	70.6	44.4	200.0	359.7	0.1045	0.1887
90-104	0	19.5	12.6	22.7	0.0400	0.0497
	4.6	20.2	21.7	27.2	0.0473	0.0593
	7.0	20.5	87.2	110.0	0.0774	0.0973
	32.4	26.4	150.3	204.0	0.0597	0.0810
	41.2	37.0	189.2	267.0	0.0812	0.1289
	65.7	41.4	201.5	344.0	0.1041	0.1776
	72.5	44.6	163.0	306	0.1127	0.2034
45-53	0	25.5	11.3	15.1	0.0619	0.0831

Table 4.8. Characterization results for bituminous chars oxidized at 775K.

Reactor Temp.	Sieve Cut	Burn Time	Total Mass	Ash	Conv.	Average Size	Aspect Ratio	N_2 BET Area	Pore Vols. (Hg)			Pore Vol. (N_2)
									32-500Å	500-17600Å	32Å -∞	20-200Å
K	μm	msec	g	%	%	μm		m^2/gtot	cm^3/gtot	cm^3/gtot	cm^3/gtot	cm^3/gtot
1475	45-53	0	0.0850	38.0	0	49.8	1.45	285	0.1402	0.2255	0.476	0.132
		38	0.2329	40.5	9.8	49.4	1.32	354				
		69	0.1401	55.6	51.1	43.6	1.35	250	0.1123	0.2142	0.4470	
		100	0.1587	75.4	80.0	42.1	1.31	203	0.0432	0.1502	0.3158	
1475	61-75	0	0.1052	33.7	0	81.3	1.23	190				0.111
		42	0.1225	36.7	12.3	80.5	1.38	225				0.108
		81	0.1172	45.0	38.0	76.0	1.18	180				0.070
		120	0.0869	70.2	78.4	70.4	1.27	120				0.050
1675	61-75	0	0.1698	36.1	0	46.0	1.48	235	0.1469	0.2384	0.4888	0.135
		33	0.1125	39.8	15.0	45.9	1.36	270	0.1301	0.2086	0.4309	0.119
		62	0.0602	47.7	38.3	45.3	1.43	160	0.1158	0.1939	0.3798	0.077
		82	0.0424	61.8	65.2	43.2	1.29	50				0.092

Table 4.9. Physical characterization of lignite chars oxidized at high temperatures.

Wall Temp.	Sieve Cut	Burn Time	N_2 Mass	Hg Mass	Ash	Conv.	Avg. Size	Aspect Ratio	N_2 BET Area	Vol. (Hg)			Vol. (N_2)
										32-500Å	500-17600Å	32Å -∞	20-200Å
K	μm	msec	g	g	%	%	μm		m^2/gtot	cc/gtot	cc/gtot	cc/gtot	cc/gtot
1475	45-53	0	0.1031		25.5	0			11.3				0.062
		36	0.1400		28.7	5.6			7.8				0.018
		95	0.0716		34.3	46.6			5.2				0.016
		154	0.0829	0.1027	37.4	63.1			8.7	0.0994	0.1931	0.3112	0.024
1475	90-104	0	0.0747	0.1800	19.5	0			12.6	0.1279	0.1991	0.3988	0.040
		45	0.0836		21.3	10.3			4.7				0.018
		104	0.0778		22.7	17.4			5.5				0.014
		153	0.0550	0.1063	25.9	30.4			12.4	0.0851	0.2218	0.3222	0.034
1675	90-104	0	0.0747	0.1880	19.5	0	114.0	1.177	12.6	0.1279	0.1991	0.3988	0.040
		37	0.0693		21.6	11.7	111.7	1.140	6.4				0.026
		115	0.0520		31.3	46.7	109.3	1.186	10.2				0.028
		183	0.0506	0.0639	41.6	65.9	100.9	1.166	5.3	0.0905	0.2845	0.4405	0.027

Table 4.10. Physical characterization of bituminous chars oxidized at high temperatures.

Bituminous		Lignite	
X_{expt}, %	X_{theo}, %	X_{expt}, %	X_{theo}, %
11.7	7.0	9.8	3.4
46.7	22.7	51.1	47.0
65.9	53.7	80.0	56.6

Table 4.11. Comparision of experimental and theoretical conversion values.

Initial Radius	Residence Time		
μm	20 msec	40 msec	60 msec
50	38.4	74.8	97.7
55	31.4	64.0	88.1
60	25.9	54.8	78.0
65	21.5	47.2	68.6

Table 4.12. Predicted conversions at fixed times for different initial radii.

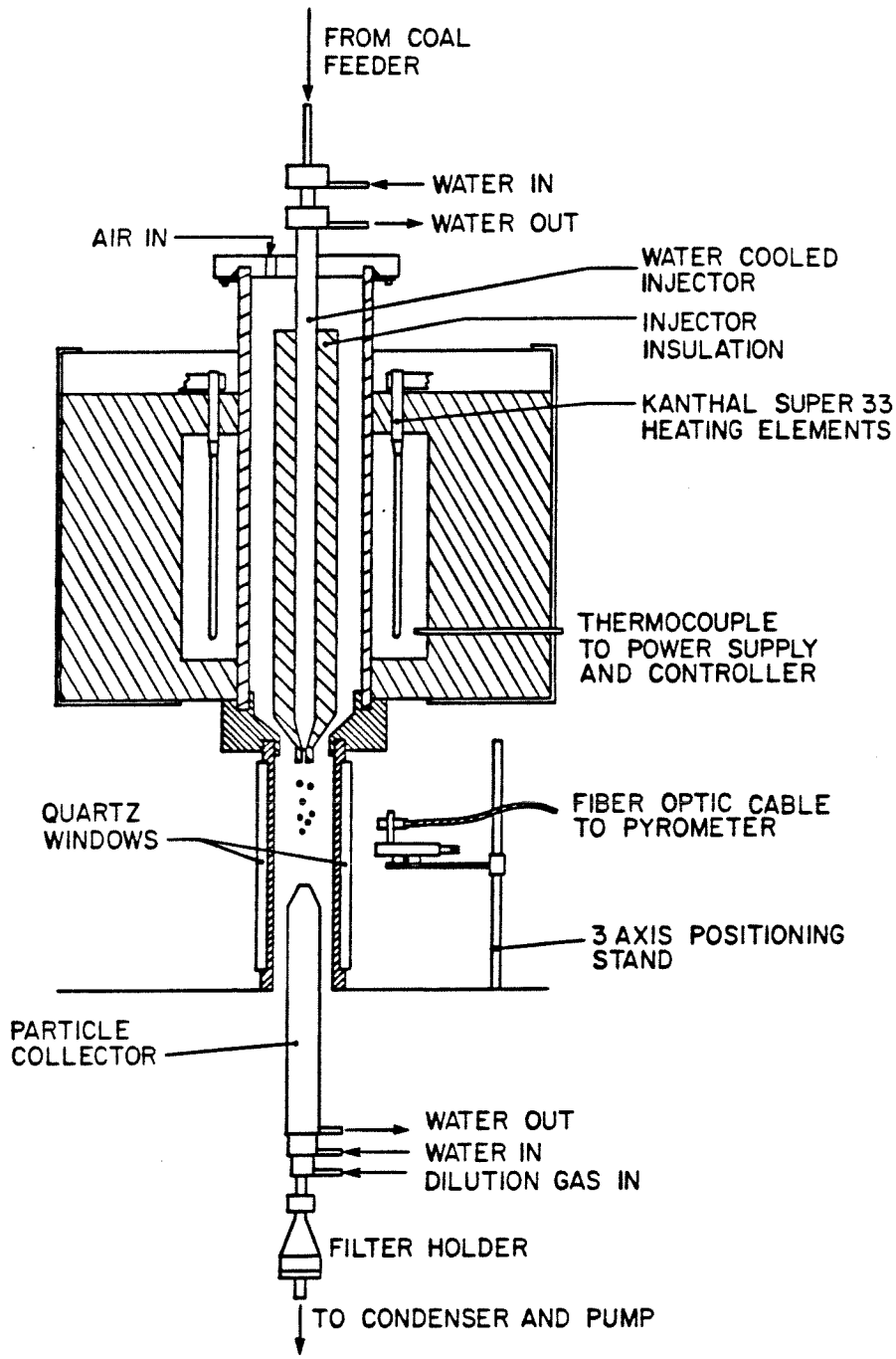

Figure 4.1. Schematic of high-temperature furnace.

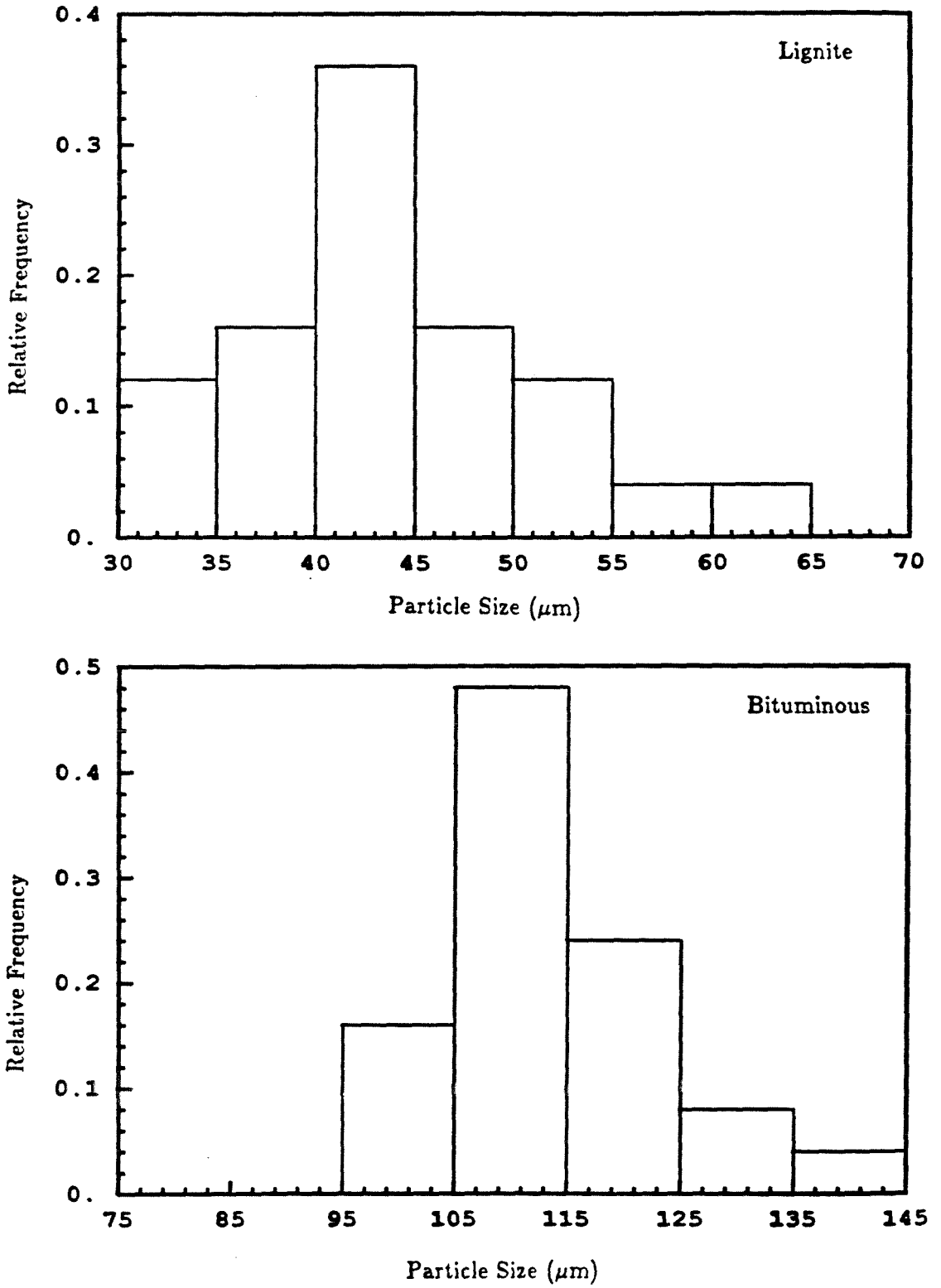

Figure 4.2. Particle size distributions of a) lignite and b) bituminous char .

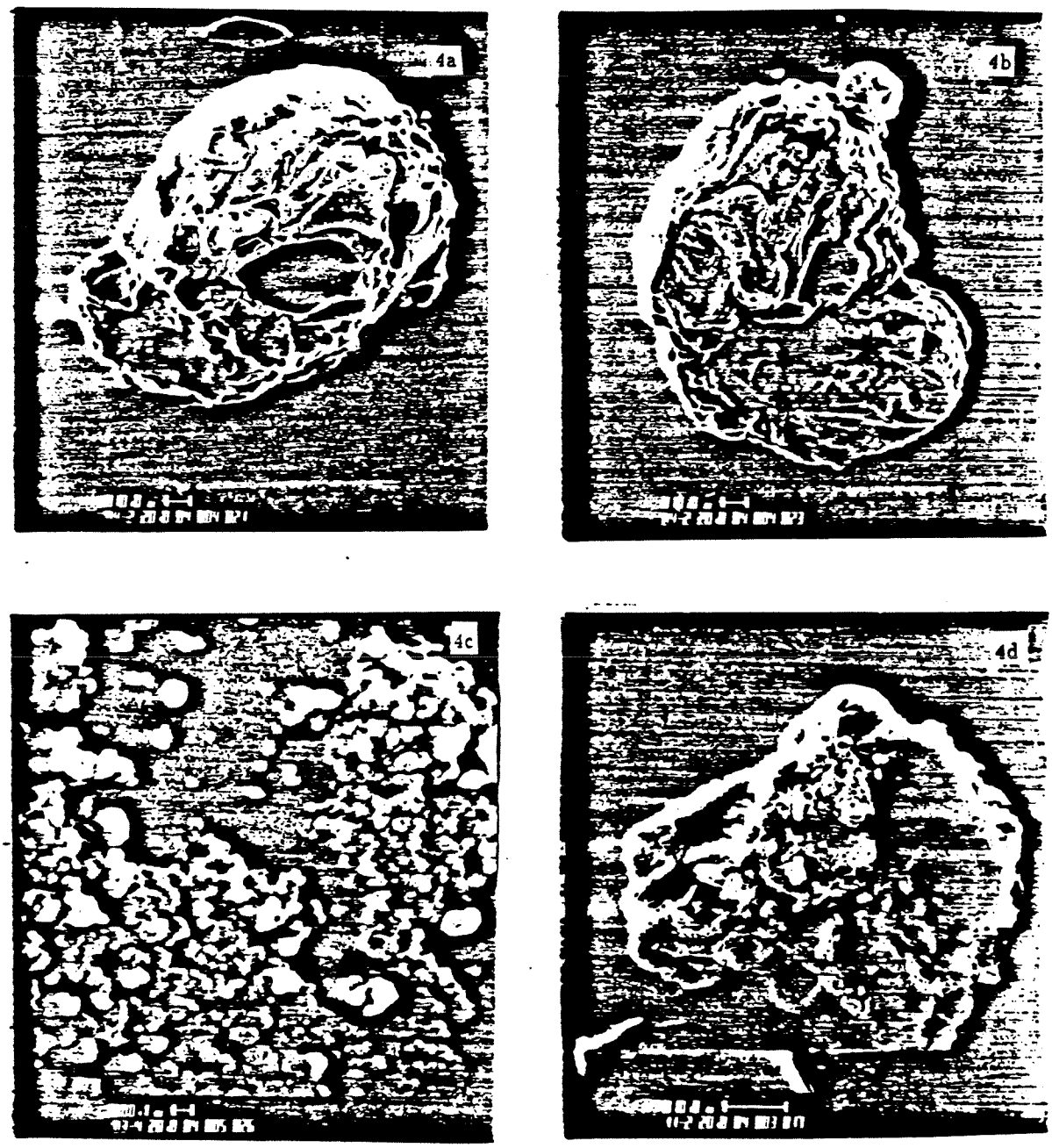

Figure 4.3. Electron micrographs of bituminous char: a) and b) single, unburned particles, c) close-up of ash, d) after 67% conversion at 775K.

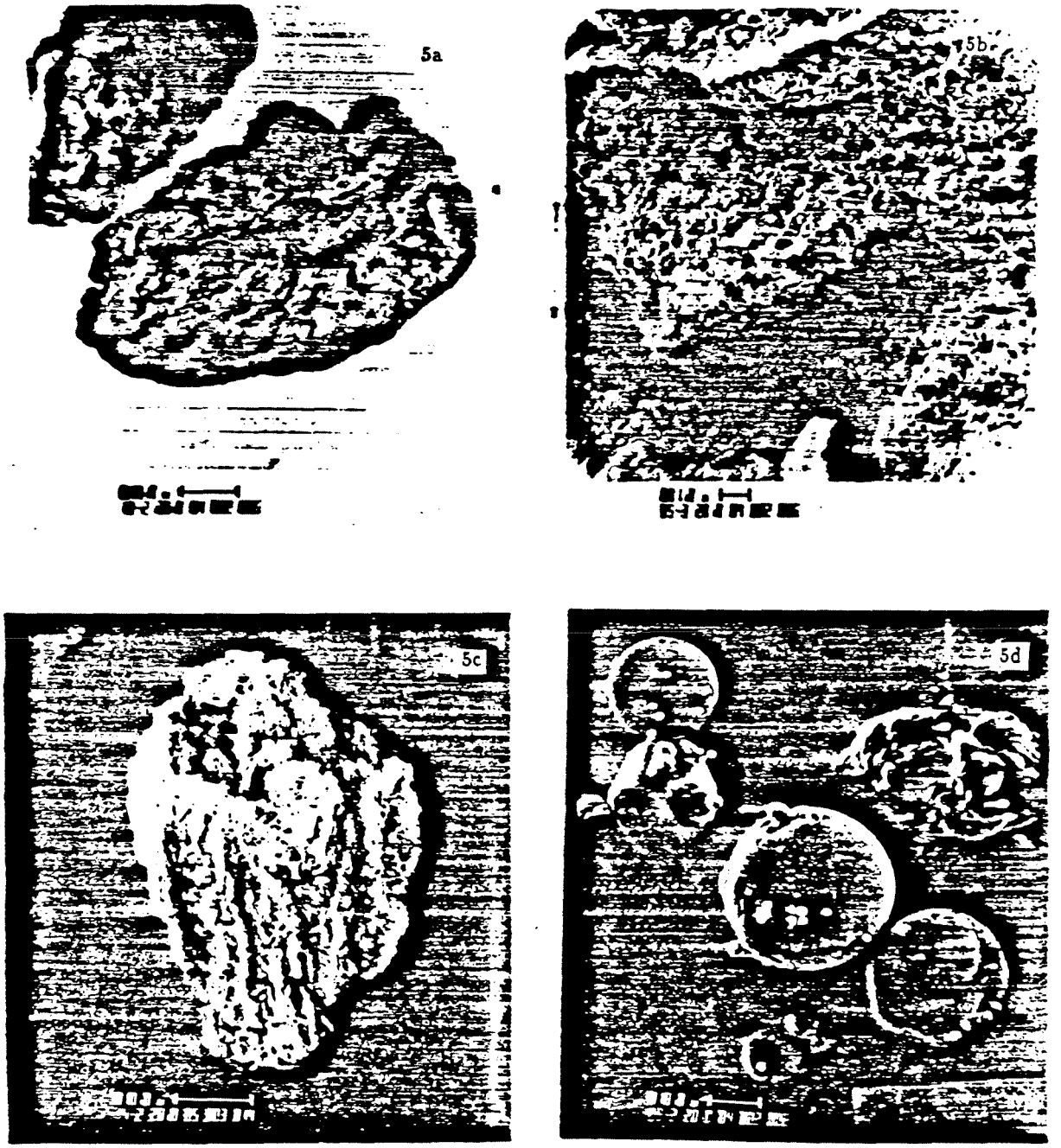

Figure 4.4. Electron micrographs of lignite char: a) typical unburned particle, b) close-up of surface, c) after complete conversion at 775K, d) after combustion at 1675K.

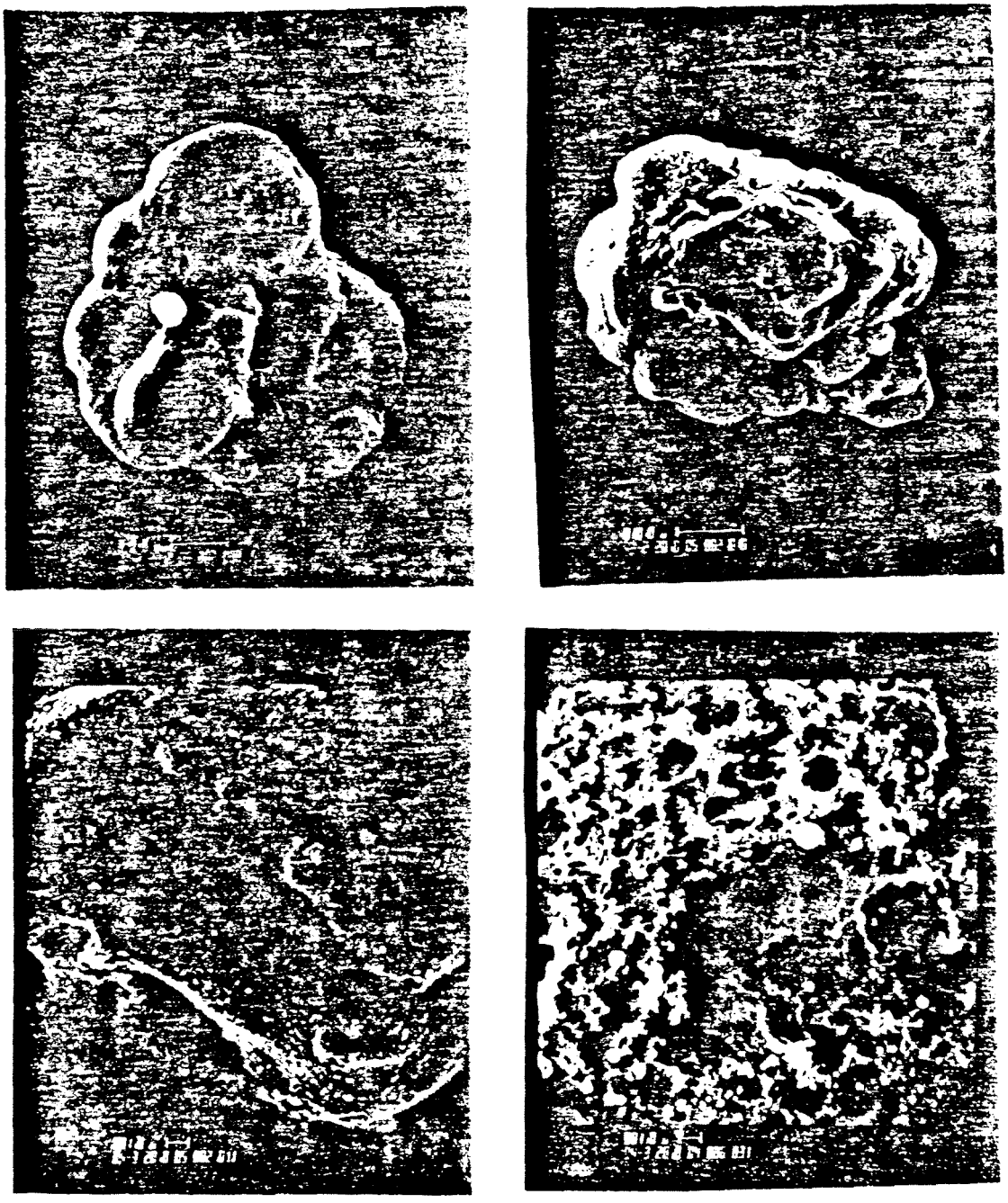

Figure 4.5. Electron micrographs of subbituminous char: a), b) single unburned particle, c) close-up of surface, d) after combustion at 1675K.

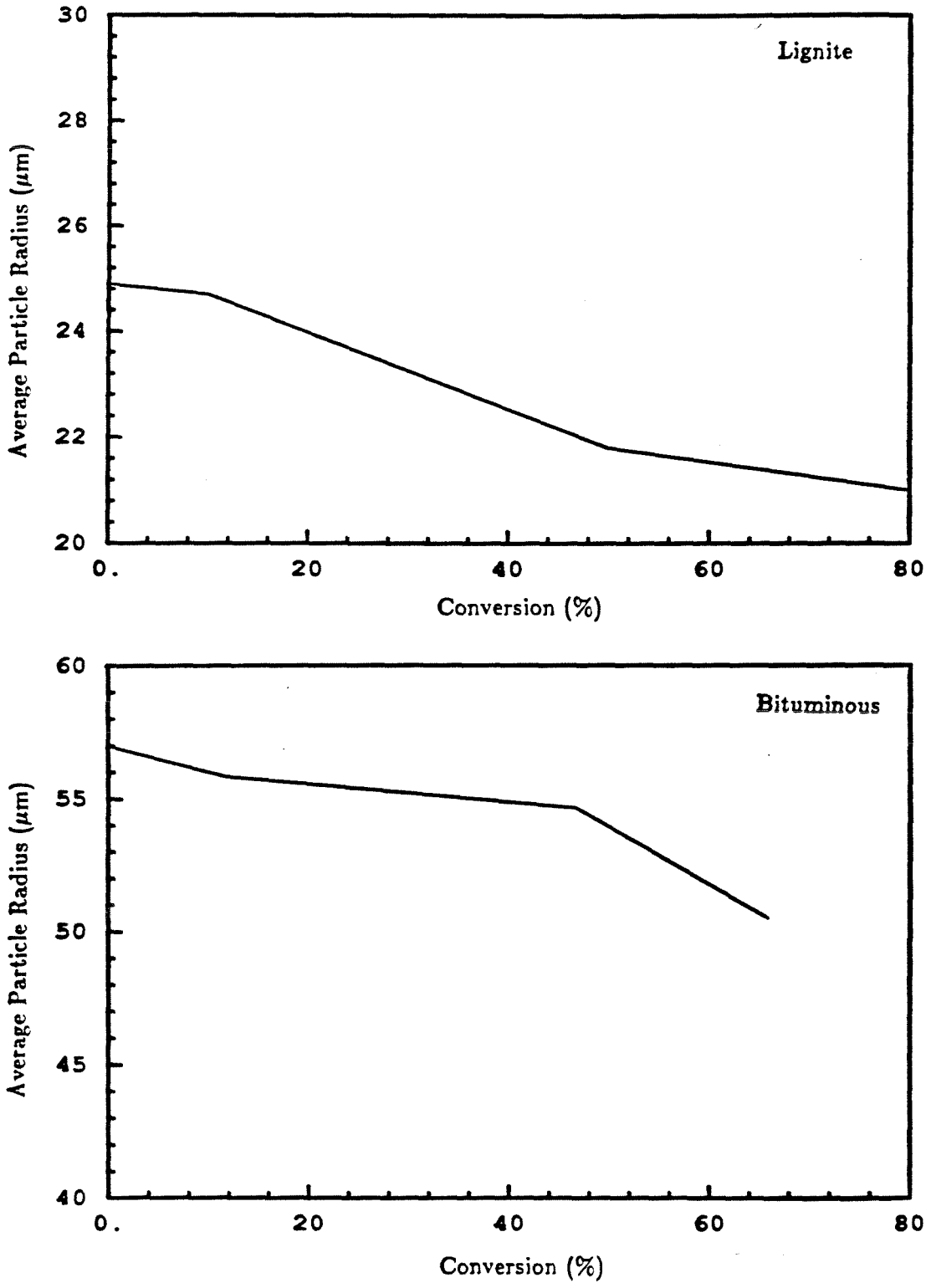

Figure 4.6. Average particle radius versus conversion for a) lignite char at 1475K and b) bituminous char at 1675K.

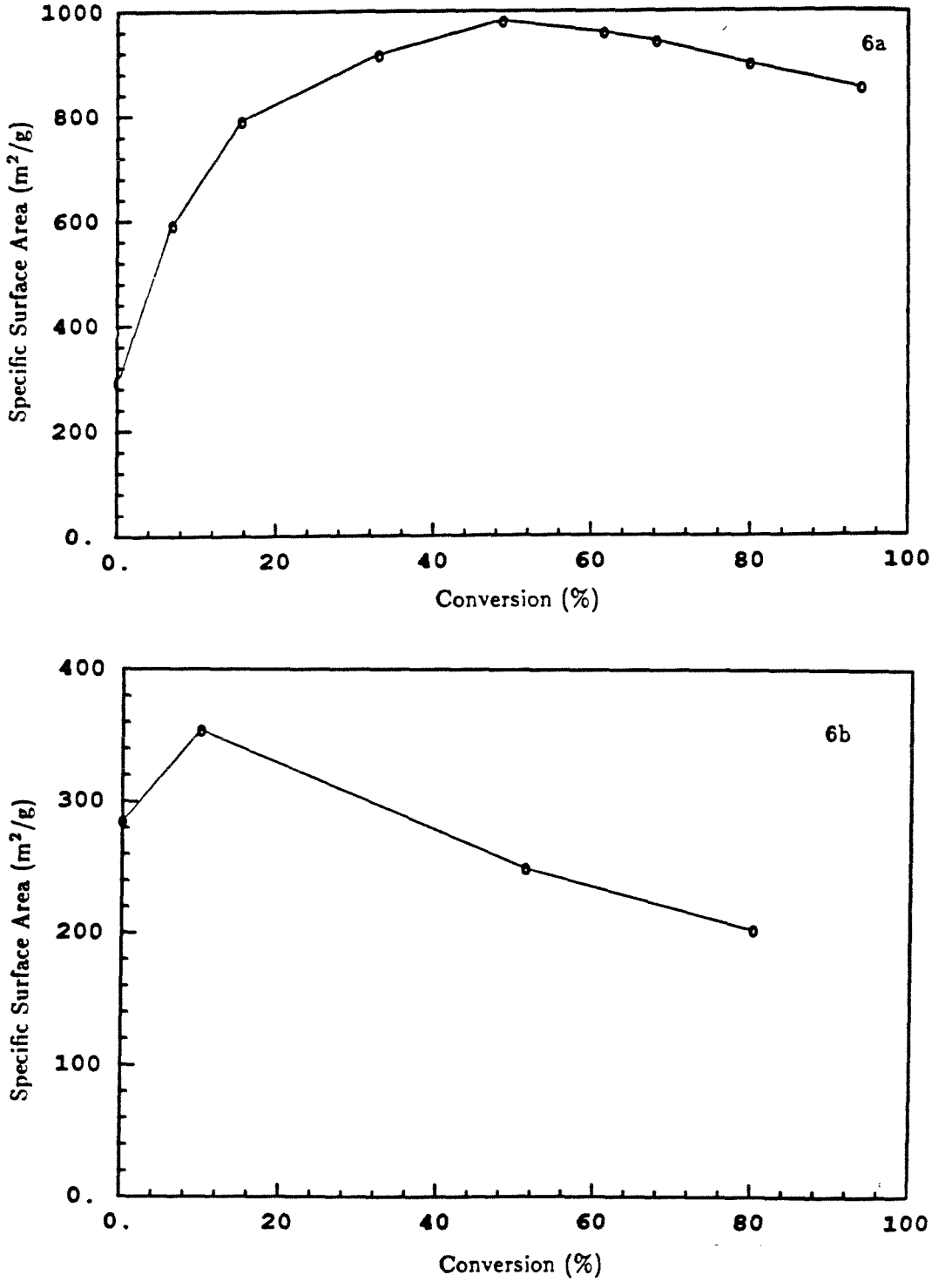

Figure 4.7. Specific surface area versus conversion for lignite char (ash-free basis) a) oxidation at 725K, b) oxidation at 1475 K.

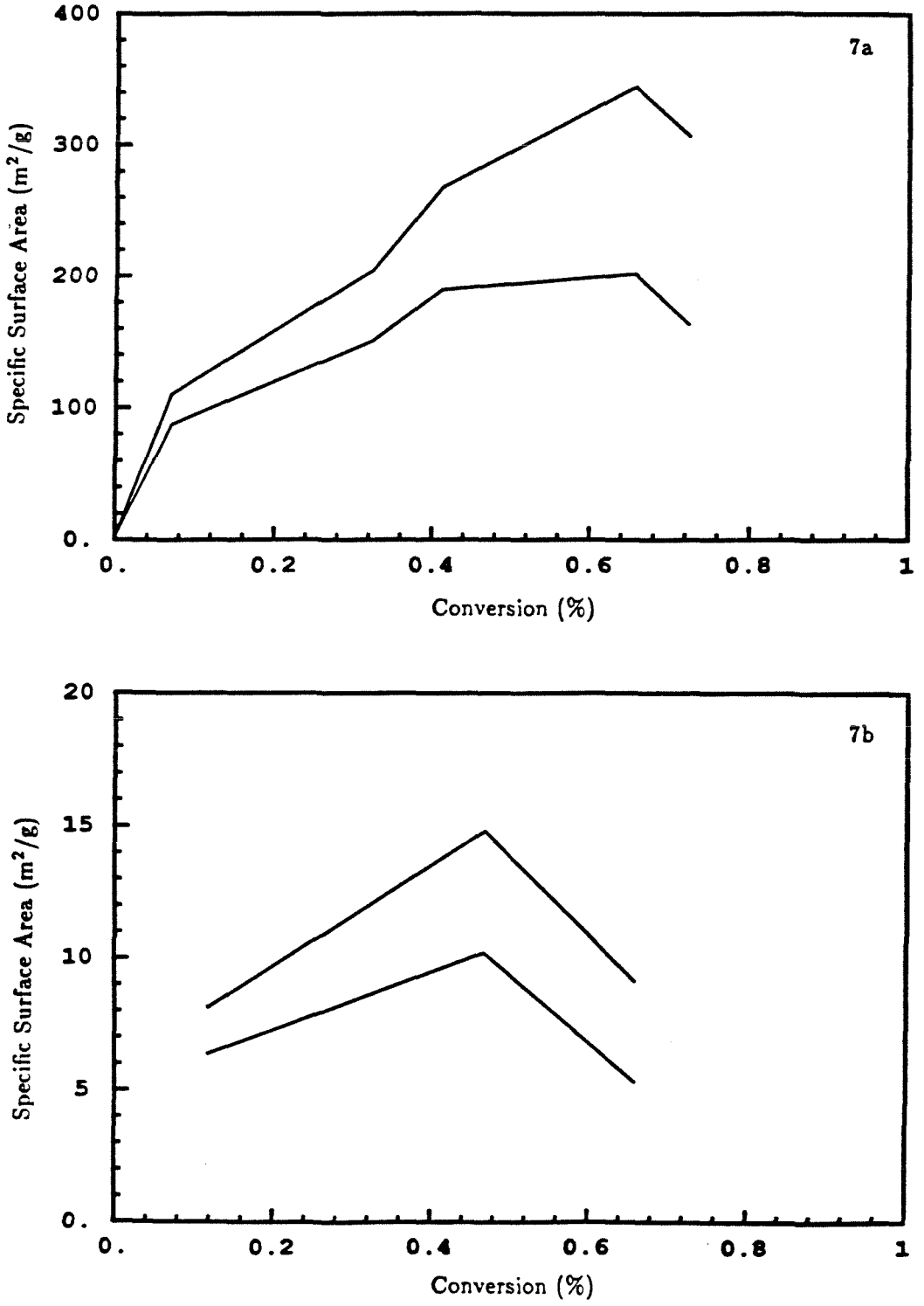

Figure 4.8. Specific surface area versus conversion for bituminous char (ash-free basis) a) oxidation at 775K, b) oxidation at 1675 K.

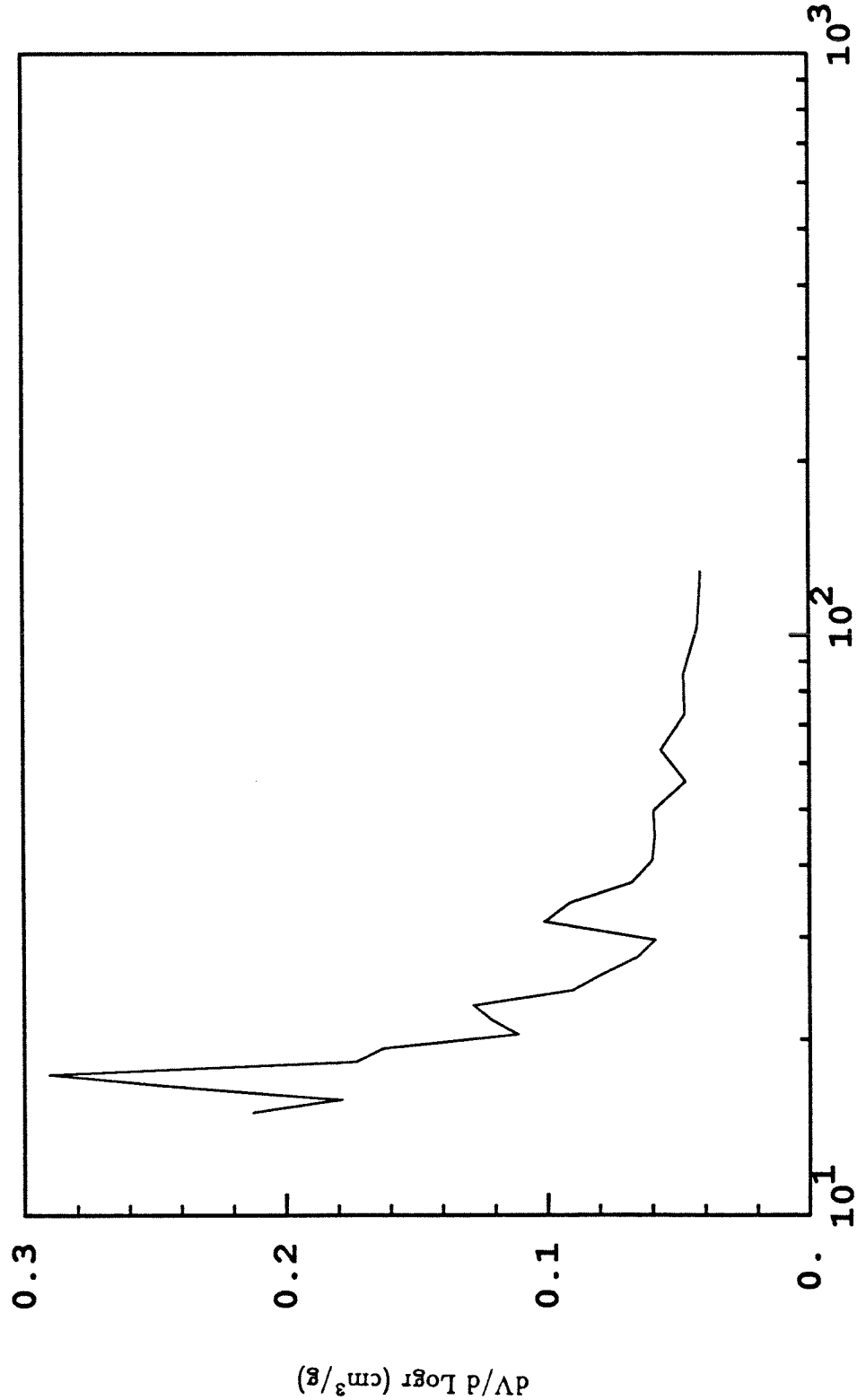

Figure 4.9. Pore volume distribution of unburned lignite char from capillary condensation of nitrogen.

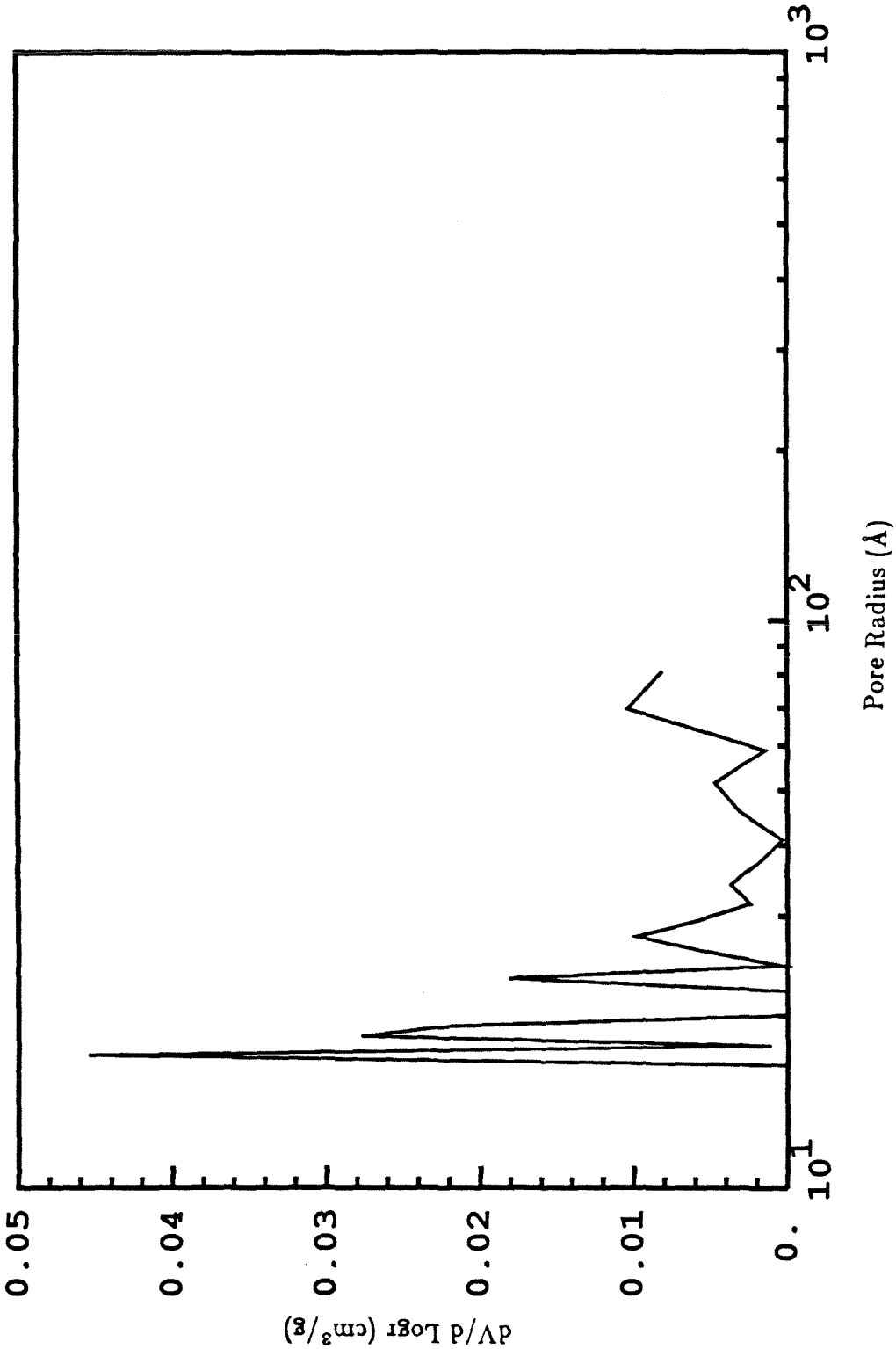

Figure 4.10. Pore volume distribution of unburned bituminous char from capillary condensation of nitrogen.

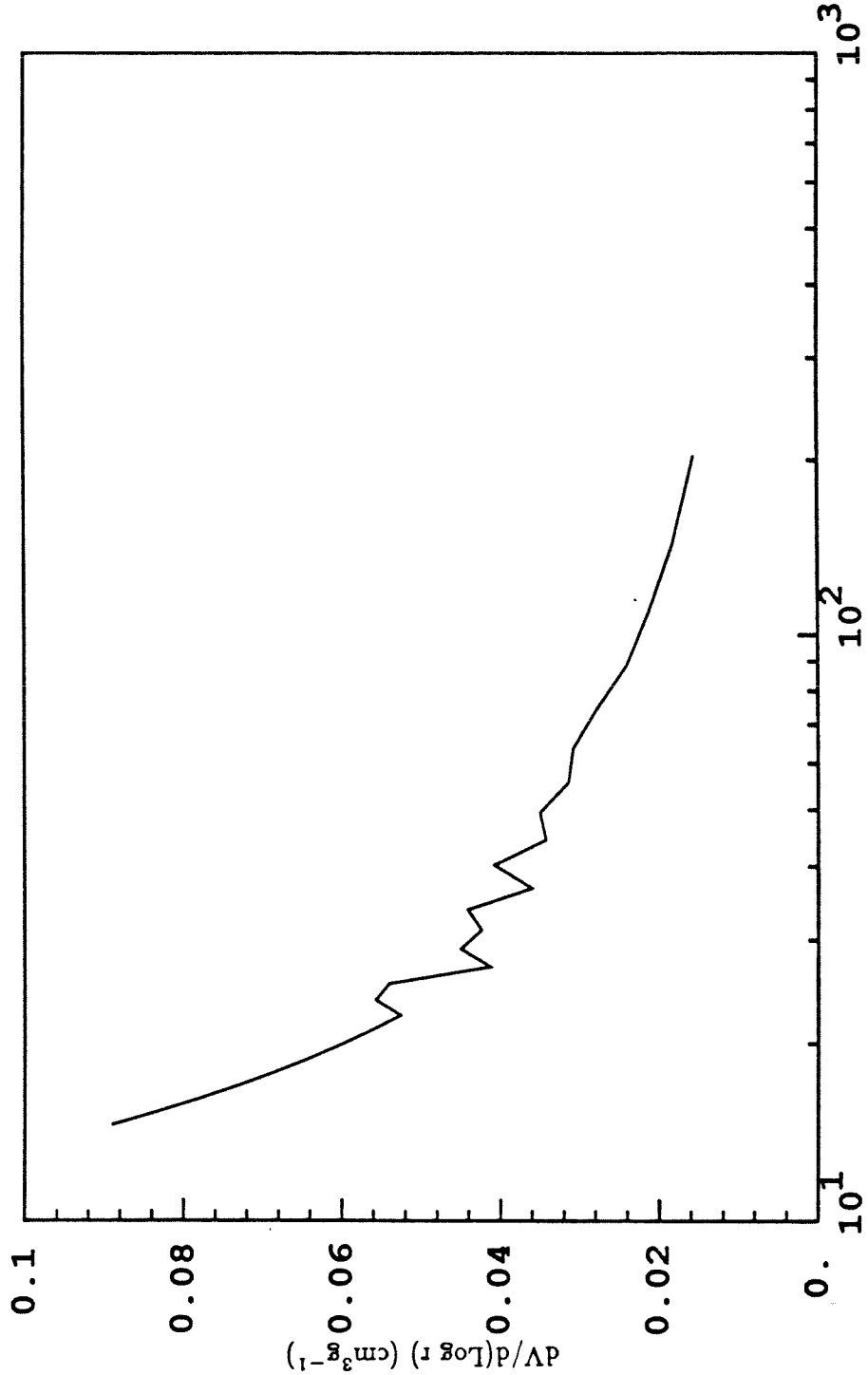

Figure 4.11. Pore volume distribution of unburned subbituminous char from capillary condensation of nitrogen.

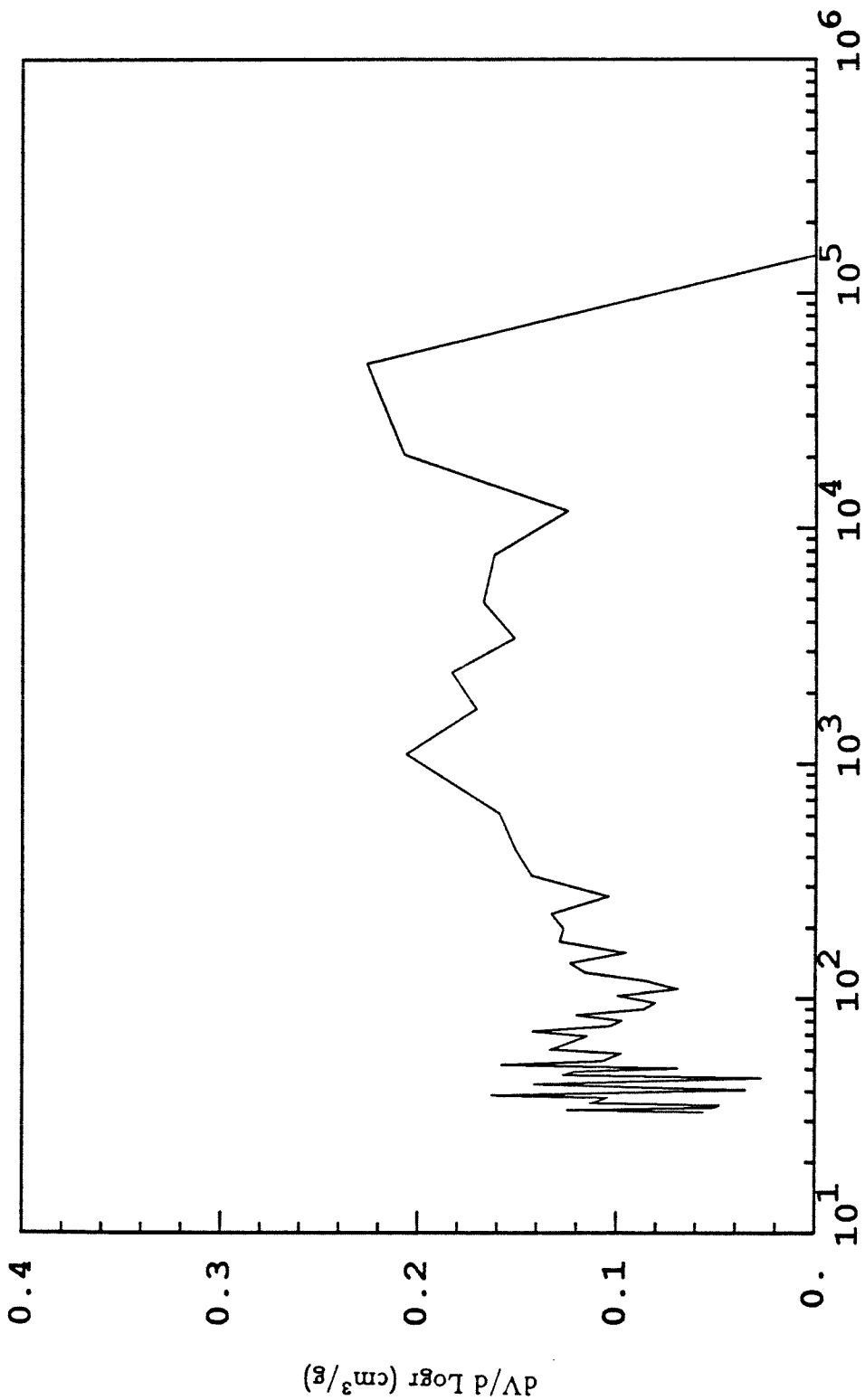

Figure 4.12. Pore volume distribution of unburned lignite char from mercury porosimetry.

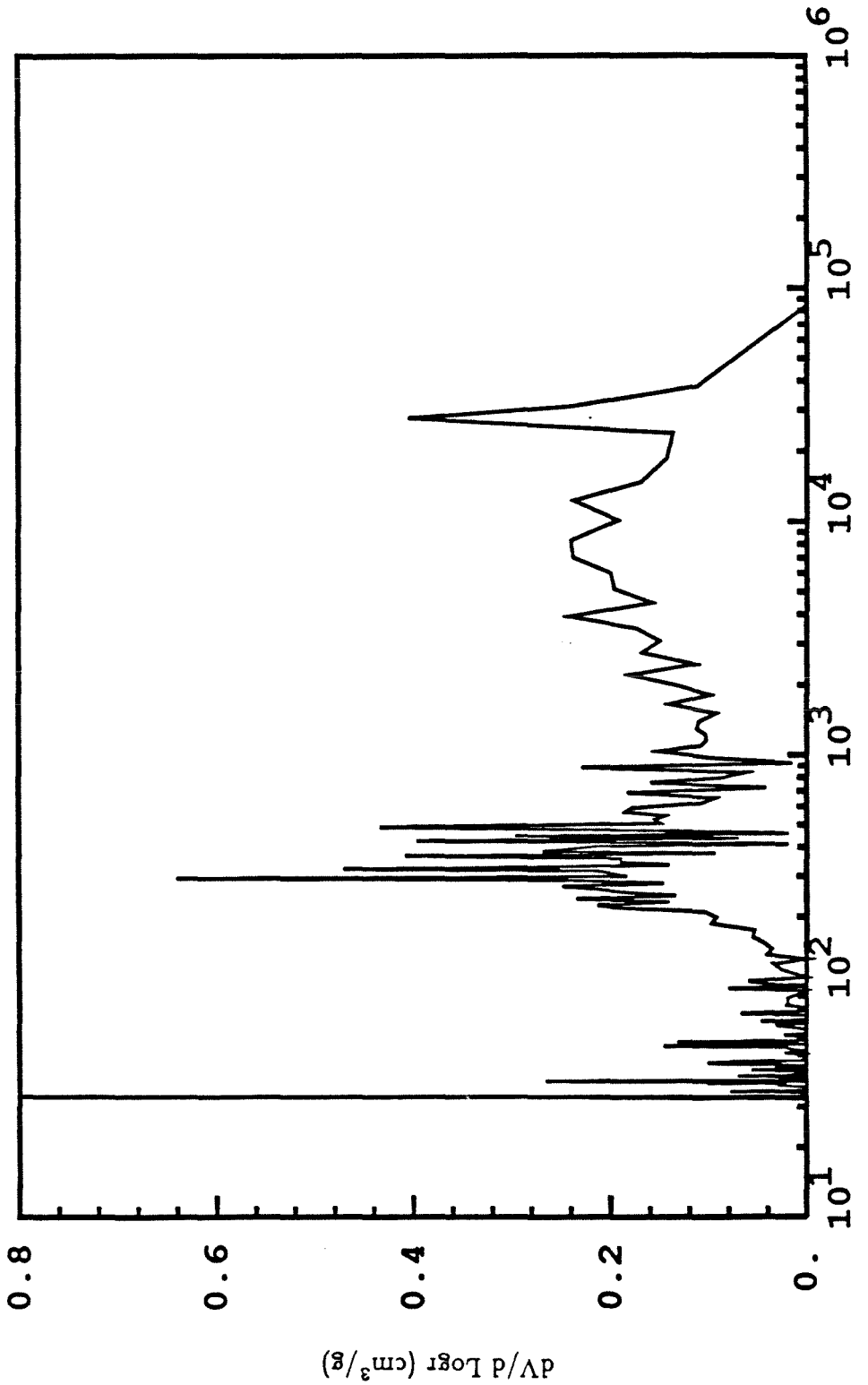

Figure 4.13. Pore volume distribution of unburned bituminous char from mercury porosime try.

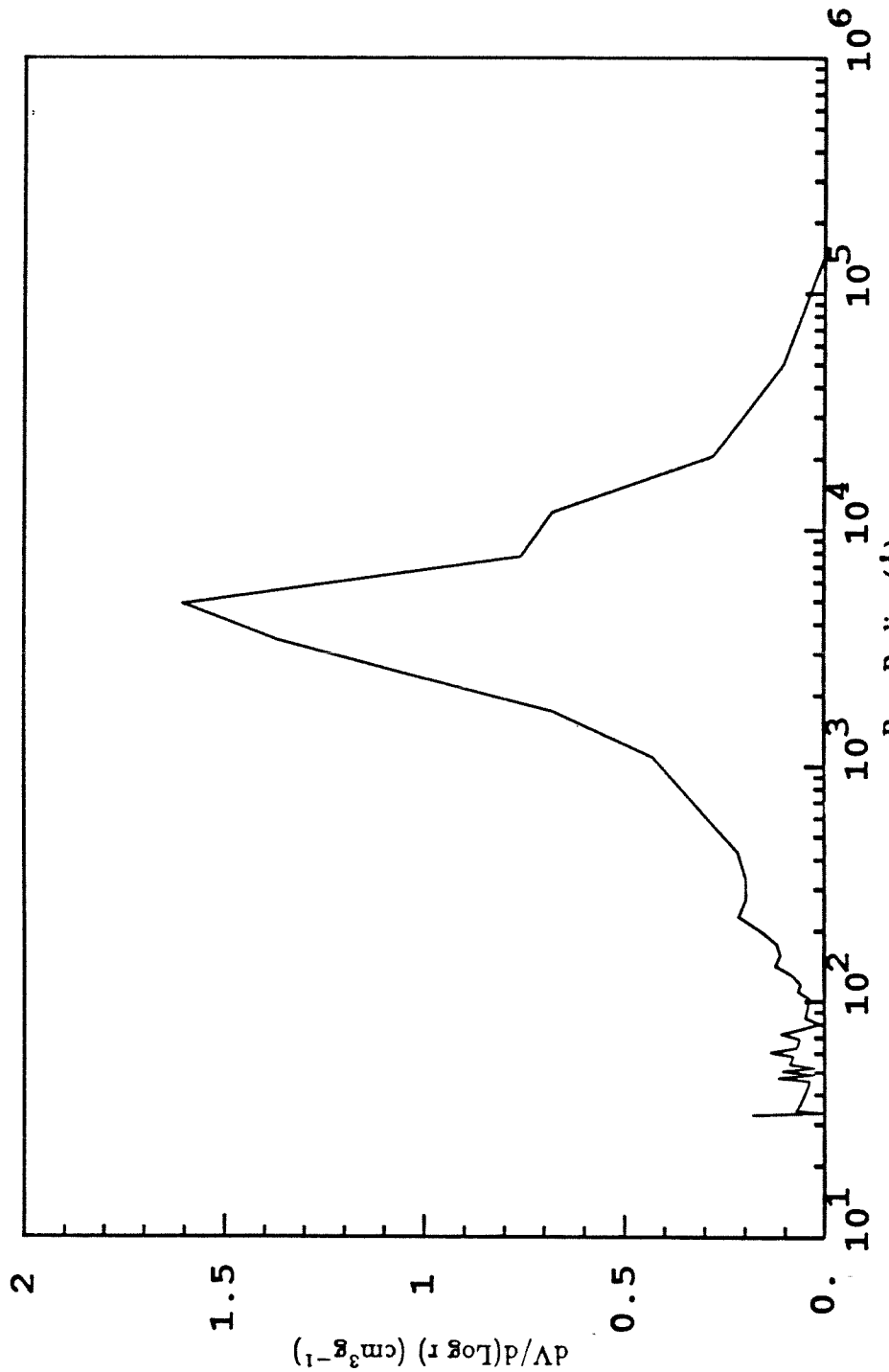

Figure 4.14. Pore volume distribution of unburned subbituminous char from mercury porosimetry.

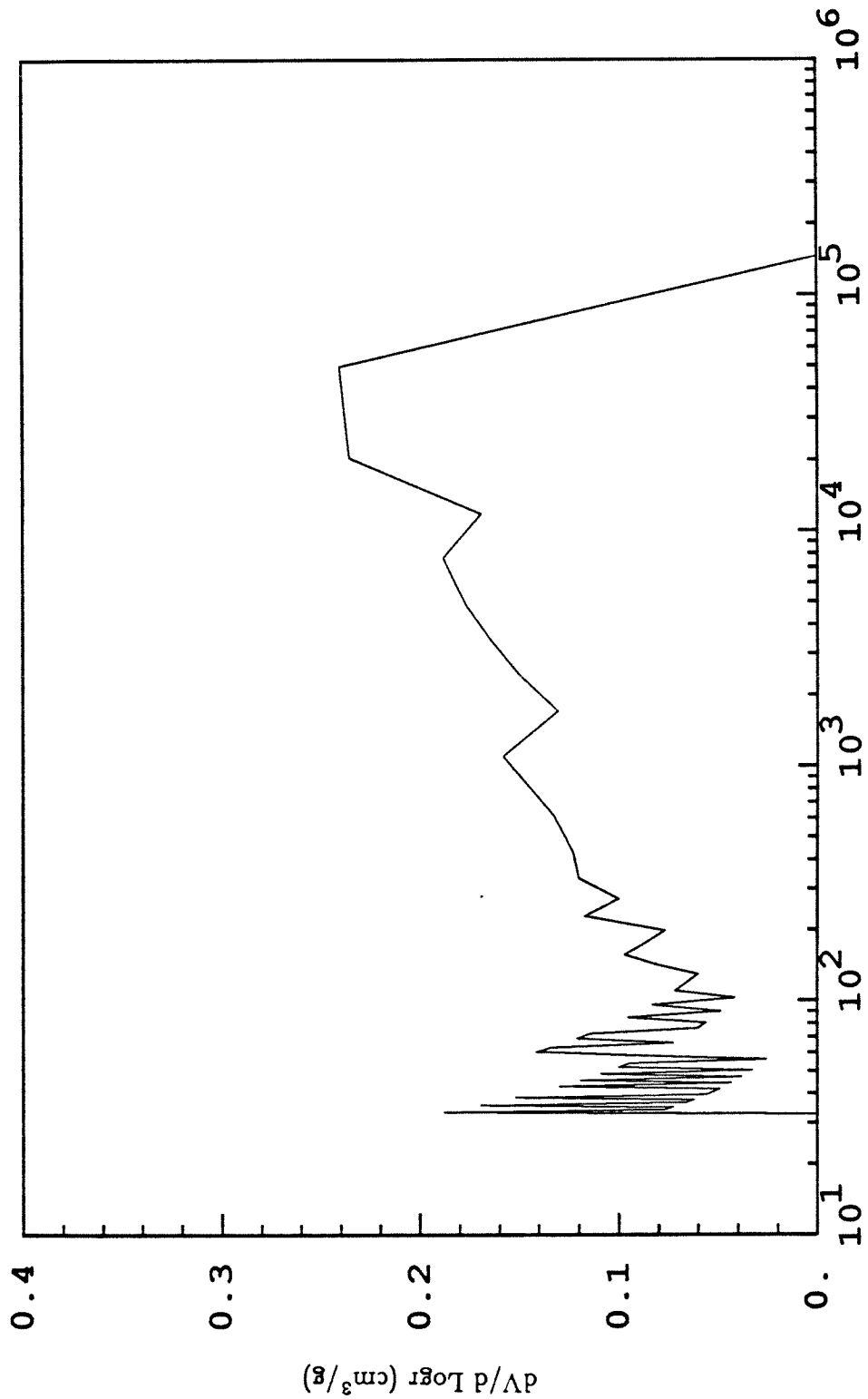

Figure 4.15. Pore volume distribution of lignite char partially oxidized at 1475 K from mercury porosimetry.

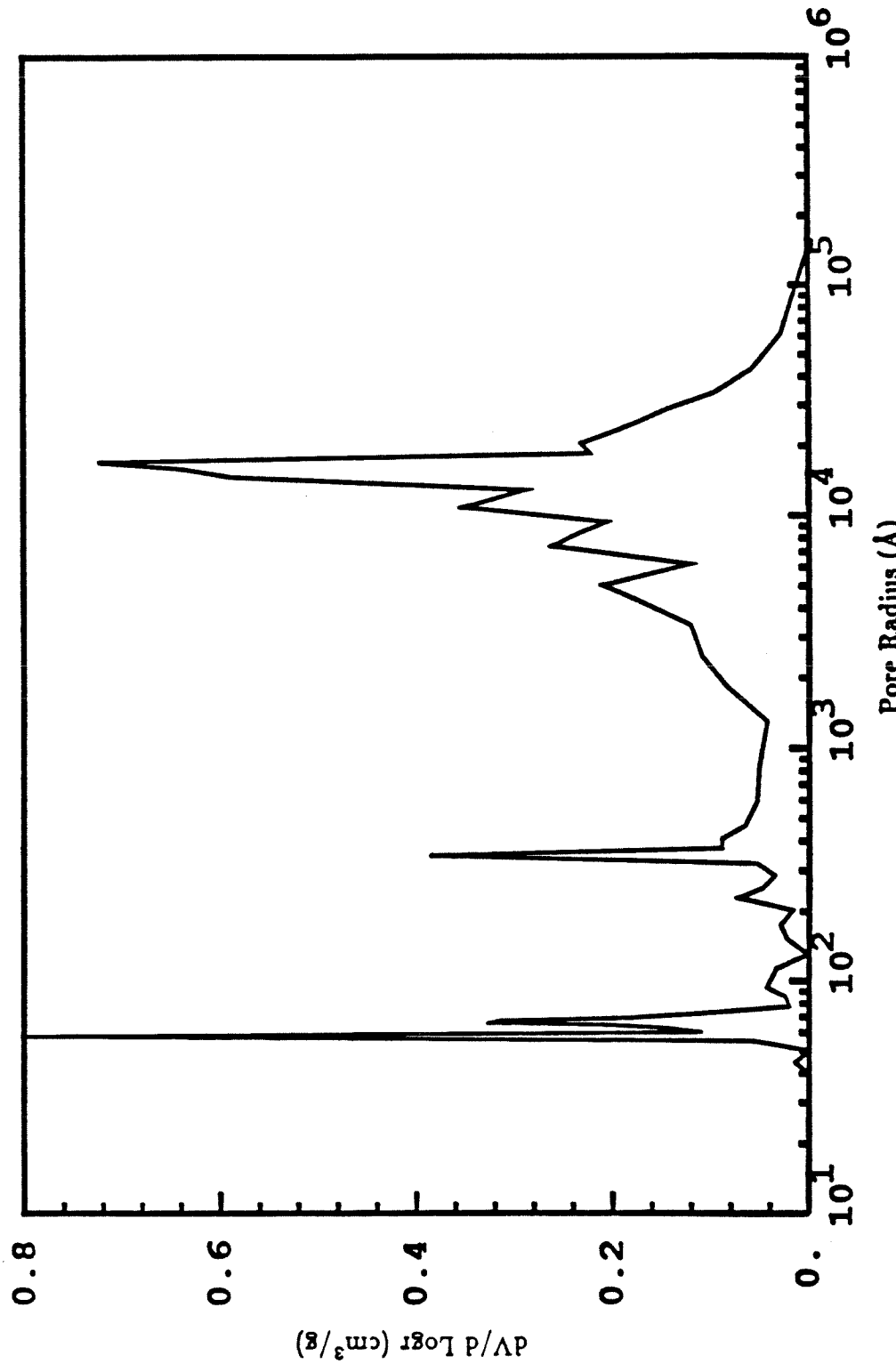

Figure 4.16. Pore volume distribution of bituminous char partially oxidized at 1675 K from mercury porosimetry.

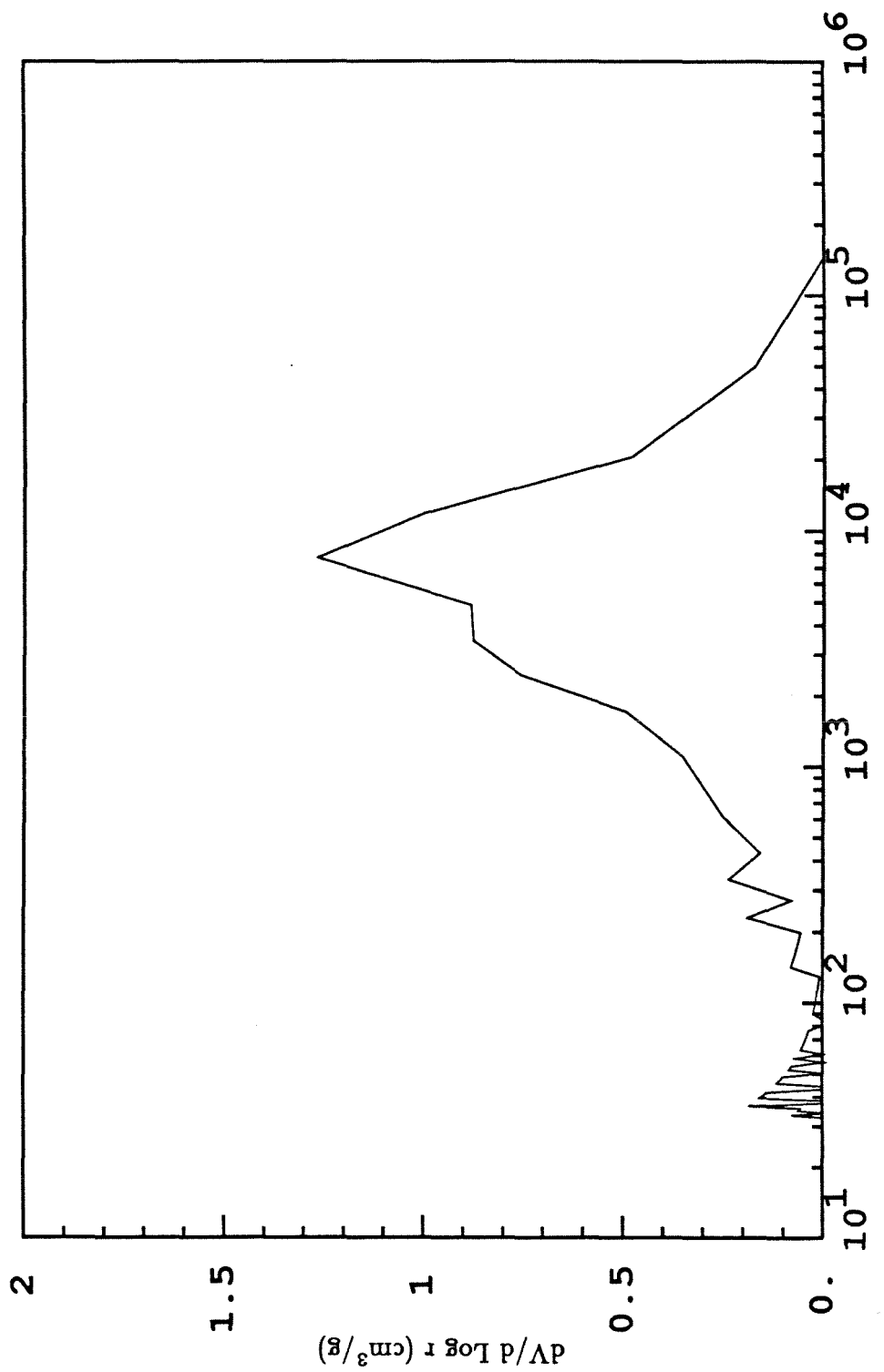

Figure 4.17. Pore volume distribution of sub-bituminous char partially oxidized at 1475K from mercury porosimetry.

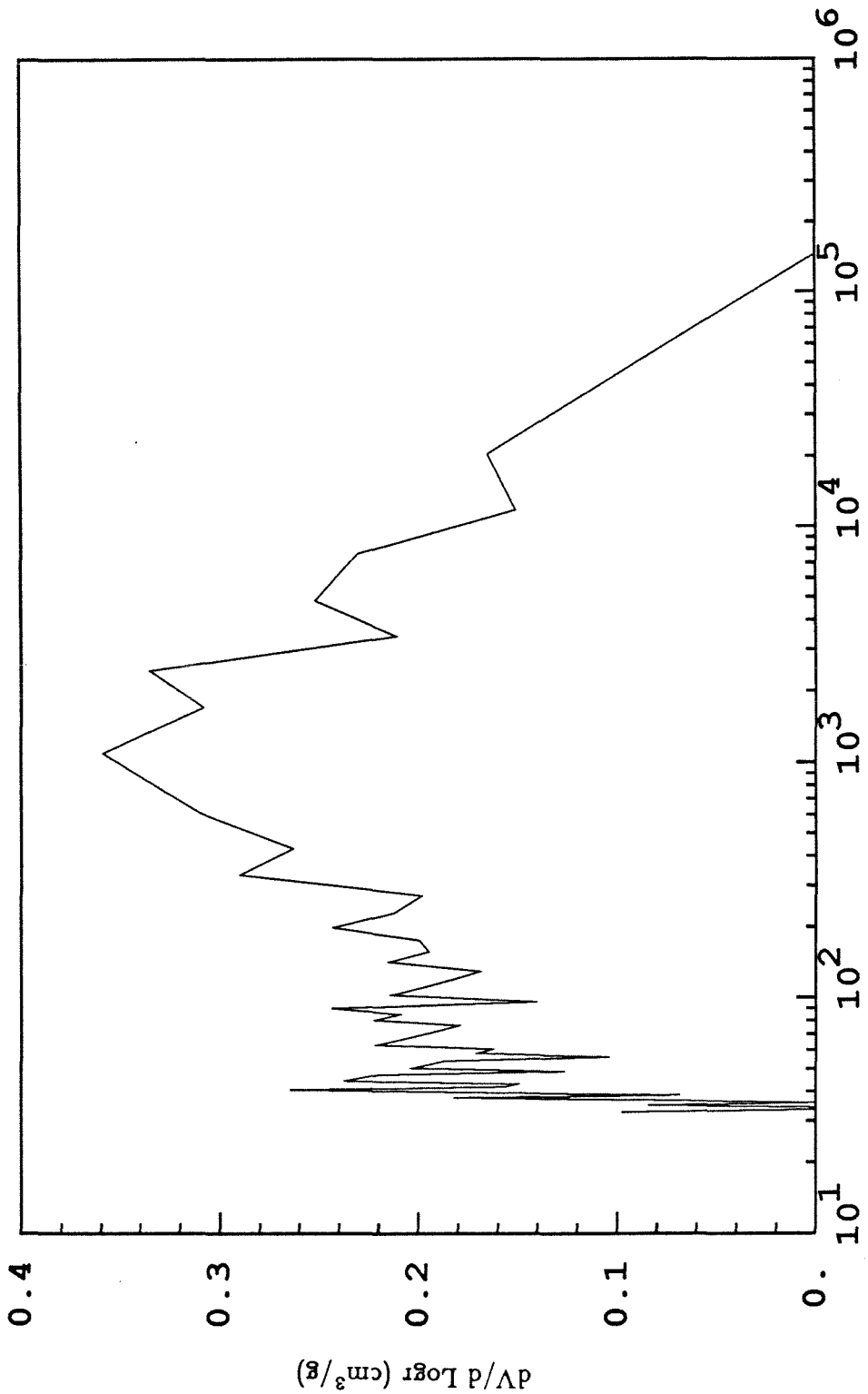

Figure 4.18. Pore volume distribution of lignite char partially oxidized at 725 K.

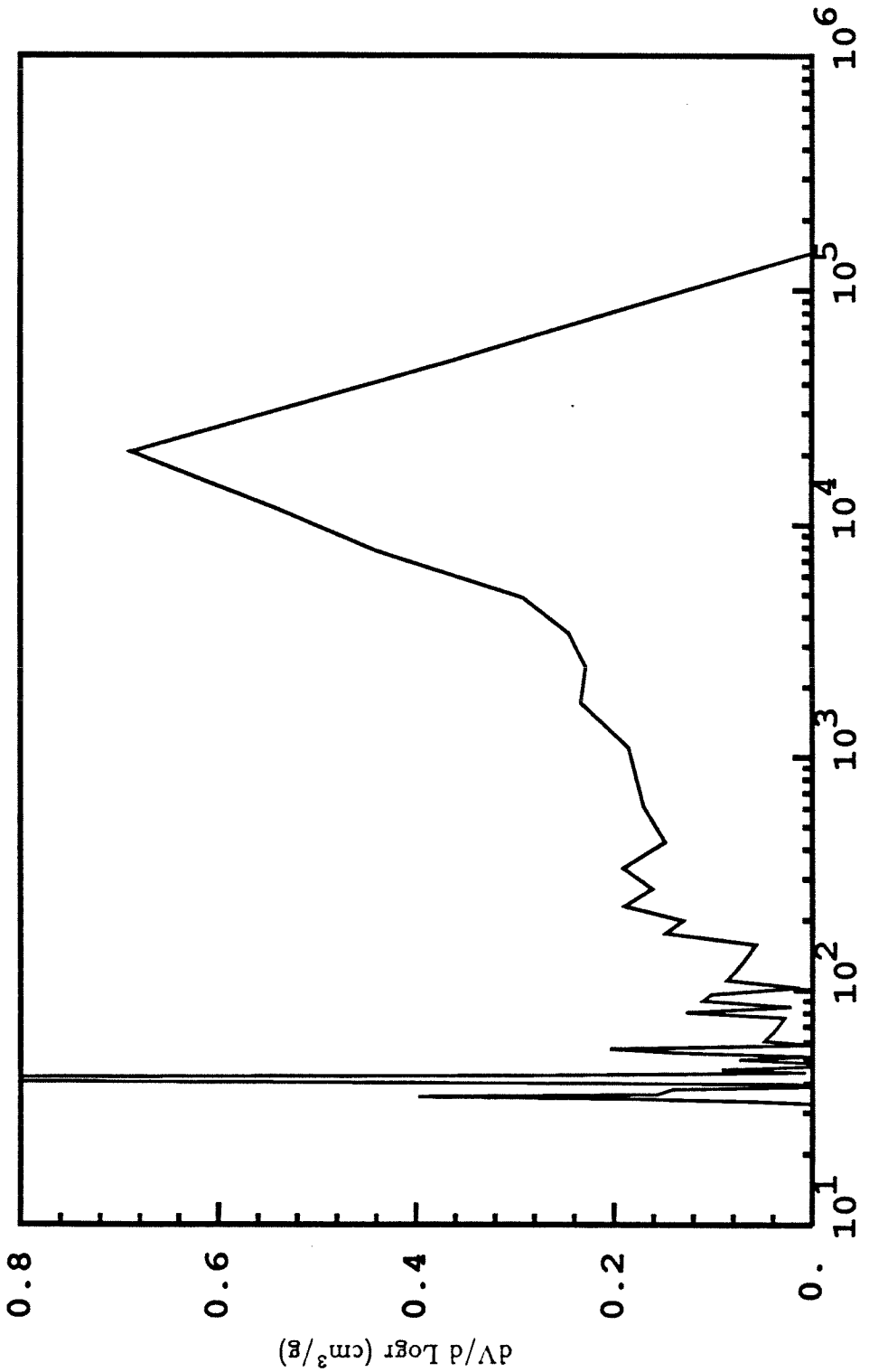

Figure 4.19. Pore volume distribution of bituminous char partially oxidized at 775 K from mercury porosimetry.

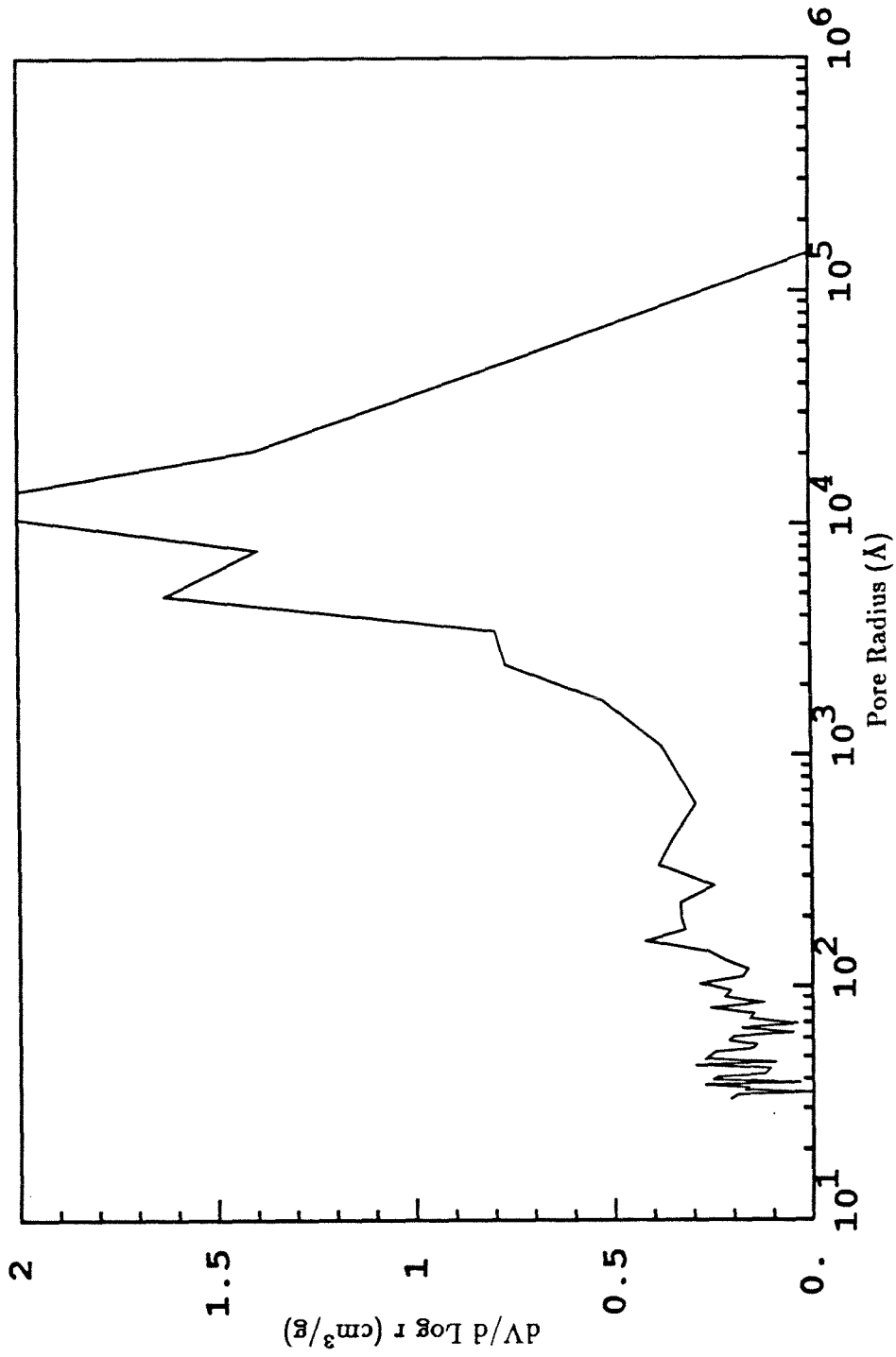

Figure 4.20. Pore volume distribution of subbituminous char partially oxidized at 725K from mercury porosimetry.

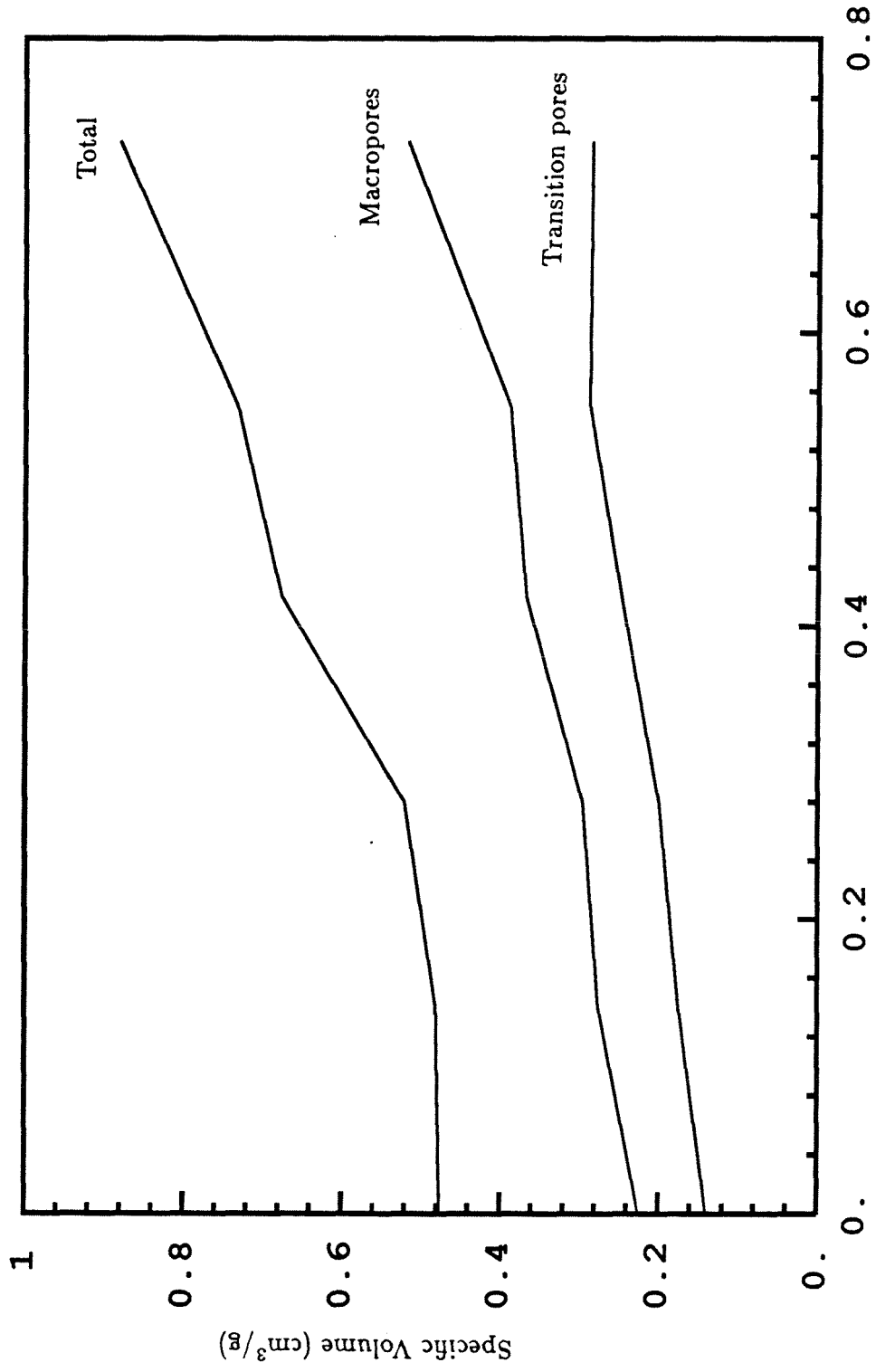

Figure 4.21. Pore volume growth of lignite char oxidized at 725 K.

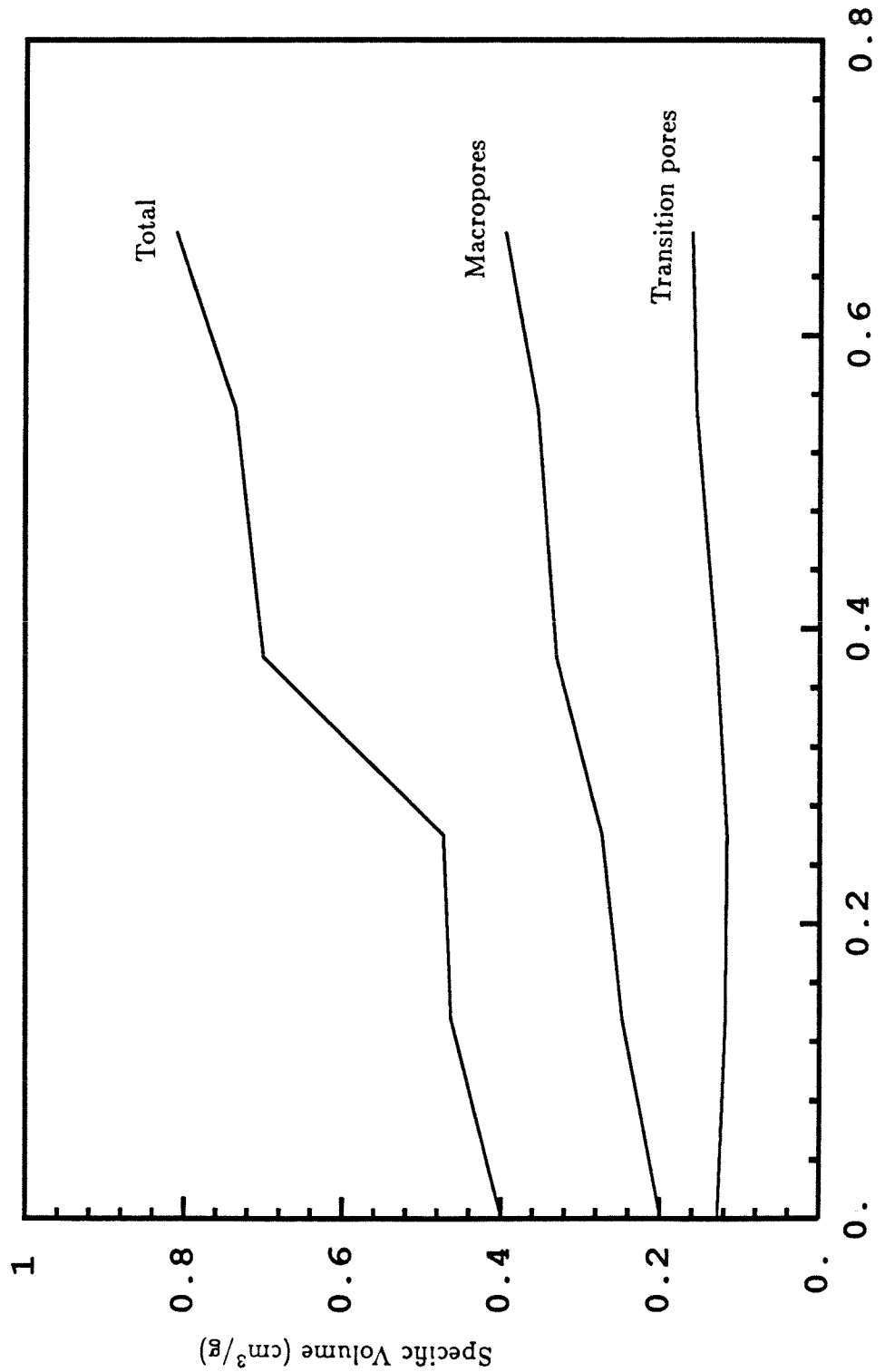

Figure 4.22. Pore volume growth of bituminous char oxidized at 775 K.

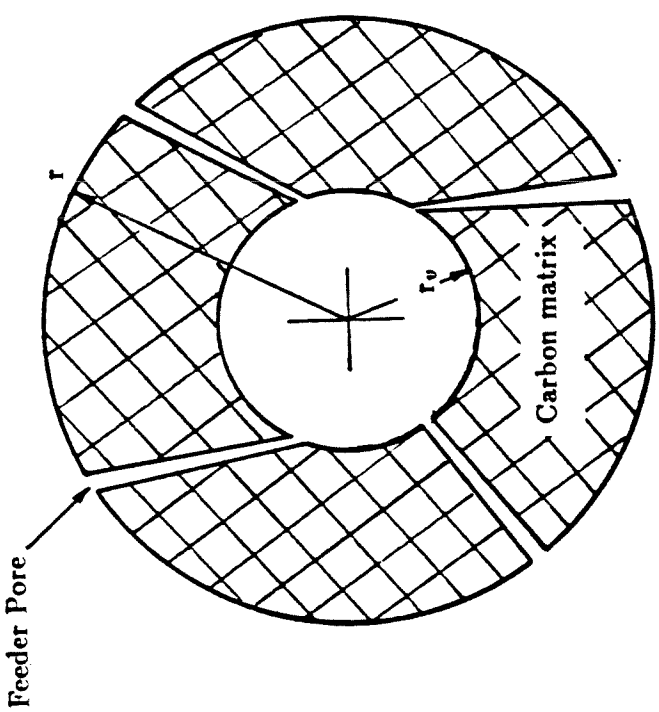

Figure 4.23. Schematic of a bituminous char particle.

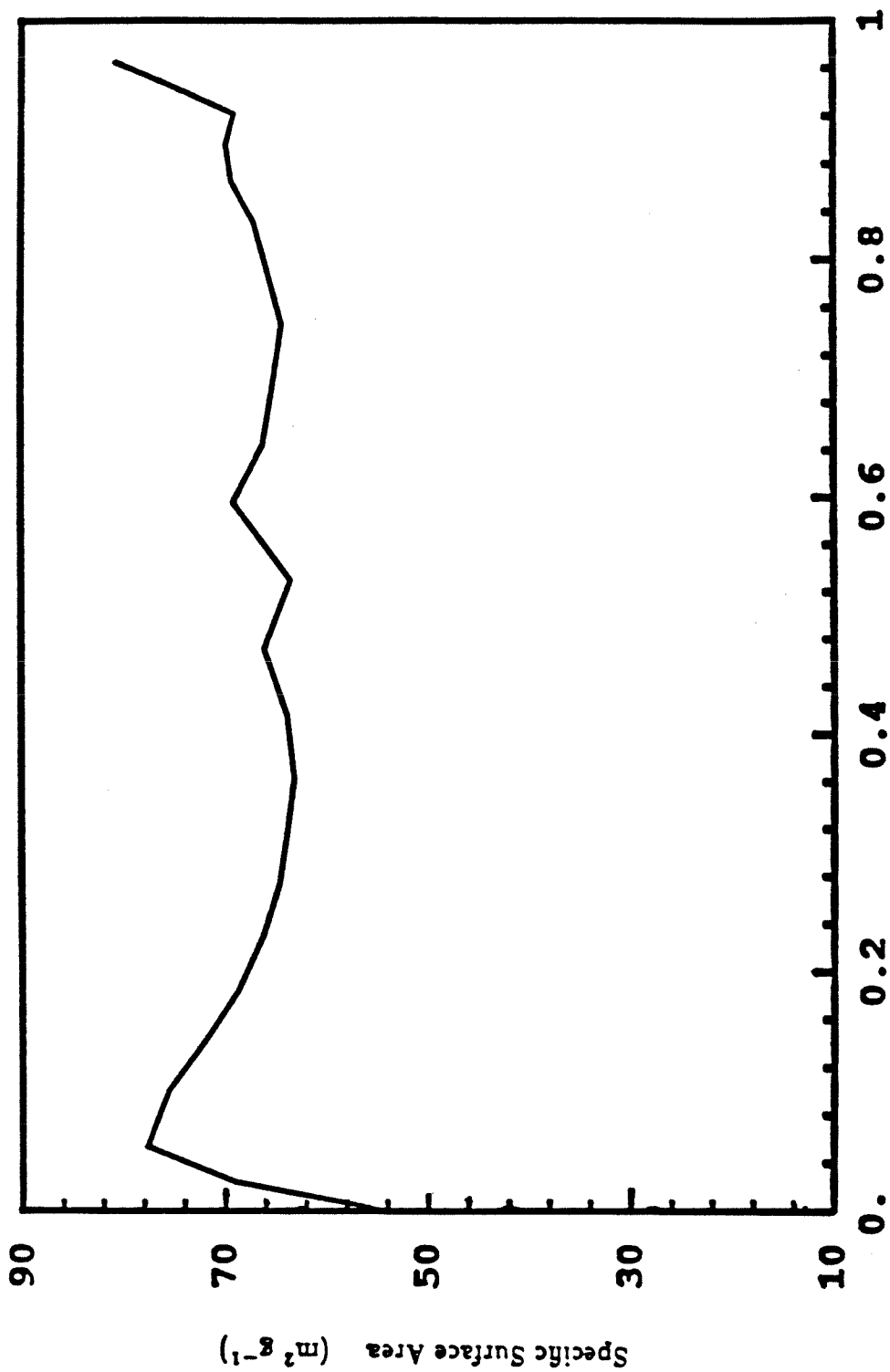

Figure 4.24. Surface area versus conversion as predicted by the model.

CHAPTER 5

SINGLE PARTICLE PYROMETRY

5.1 Introduction

As discussed in Chapter 4, the entrained flow reactor can be used to measure combustion rates of pulverized char. Measurements that can be carried out in this system include (*i*) carbon conversion and characterization of physical properties (size, density, etc.) of partially burned char withdrawn at the reactor outlet or at intermediate axial positions using a cooled probe; (*ii*) reactor wall temperature and gas temperature at various axial locations. The measurement techniques and procedures for data analysis have been described in the well known papers of Field (1969) and Hamor and Smith (1973). In analyzing their data, these authors estimated particle temperatures by a steady-state energy balance, using the measurements of reaction rates and gas and wall temperatures. Ayling and Smith (1972) used two-color pyrometry to determine directly the temperature of a stream of burning particles and found fair agreement between measured and calculated temperatures. Such measurements and calculations involve averages over many particles which, even when carefully sized, can differ considerably in shape, density, mineral content and other properties. This averaging is quite reasonable from the engineering point of view, but it introduces an as yet unexplored uncertainity in the reported apparent or intrinsic reaction rate parameters.

More recently, various workers have been able to measure the temperature of individual burning particles by two-color pyrometry (McLean *et al.* (1981); Mitchell and McLean (1982); Timothy *et al.* (1982); Jorgensen and Zuiderwyk (1985)). The key element in this technique is the introduction of an extremely dilute stream of particles into the reactor, so that the optical volume sampled by a pyrometer,

equipped with a very sensitive detector, contains a single particle. The measurements involve either a particle at a particular location along the furnace, *i.e.*, at a particular instant during its burning history (McLean *et al.* (1981); Mitchell and McLean (1982)); or the complete temperature-time history of the particle (Timothy *et al.* (1982); Jorgensen and Zuiderwyk (1985)). The interpretation of single particle temperature-time traces using a suitable particle combustion model requires specification of particle properties. As mentioned earlier, these properties vary considerably from particle to particle, and this variation poses a major problem in the analysis of the data. The experimental technique of Mitchell and McLean (1982) provides simultaneous information about particle size and particle temperature at a fixed location, but is not applicable in its present form to the measurement of a complete temperature-time trace.

In this chapter we report measurements of temperature-time traces of 45-54μm char particles derived from 45-63μm lignite coal. The coal was pyrolyzed at 1600K for two seconds in nitrogen to produce the char (see Chapter 3).

A particle combustion model was used to analyze the temperature traces and estimate the apparent combustion-rate parameters. The analysis uses a simple approach to account for the random particle-to-particle property variation.

5.2 Experimental Procedure

The temperature of the burning char particles was measured by two-color optical pyrometry in the near infrared. The radiation from the burning particles was focussed onto a bifurcated optical fiber and transmitted to two silicon photodetectors via medium band (70nm) filters centered at 800 and 1000nm. The voltage

signals from each channel were read by a high-speed, computerized, data-acquisition system. Details of the pyrometer construction are given elsewhere (Levendis and Flagan (1987)). By using Planck's law of radiation, the temperature of each particle can be deduced from the ratio of the two signals as a function of time. The system was calibrated at the melting point of pure platinum (2045 K). The pyrometer was aligned along the direction of flow of the particles and thus was able to "see" each particle for its entire burning history.

5.2.1 Experimental Conditions

Experiments were carried out with 45-53 μm lignite char particles derived from 63-75 μm raw-coal particles. Wall temperature was varied from 1200 K to 1500 K; the ambient was air in all cases. The gas velocity in the reactor was roughly 0.1 m/s. Since the particles burned in less than 50 msec, the particles travelled only a few millimeters after igniting. The distance between the point of injection and the detector was 0.3 m, so the detector effectively saw "stationary" particles.

In an attempt to observe the effect of particle morphology on the temperature histories, a sample of lignite char was oxidized at 725K to a conversion of 28.5%. This treatment caused the surface area of the char to increase from 385 m^2/g to nearly 900 m^2/g, as measured by nitrogen adsorption at 77K. Pore volumes increased over the whole range of sizes (see Chapter 3). The temperature-time traces were obtained under the same conditions as those of the untreated char.

5.3 Experimental Results

Intensity-time traces were measured for at least twenty particles for each set of experimental conditions. Figures 5.1 and 5.2 show the the experimemtal

temperature-time traces for two different particles in air with a wall temperature of 1500K. Total burnout time and maximum temperature vary significantly from particle to particle. In all cases, the traces showed maxima at intermediate times.

5.3.1 Data Analysis

The observed variability of the temperature-time traces is due partly to experimental error and partly to the variability in the initial properties of individual particles: size, shape, density, pore structure, maceral and mineral content. Pyrometry measurements on uniform spherical particles of synthetic char (Levendis and Flagan (1987)), using the same reactor and pyrometer, have yielded much more uniform traces of intensity and temperature. Most of the observed variation in the traces of lignite chars must, therefore, be due to differences in the properties of individual particles.

The obvious approach to estimating combustion-rate parameters from a set of temperature traces is to postulate a spherical particle having average size, density, etc., and to assign to that particle a single temperature-time trace obtained by averaging the measured individual traces. This straightforward approach would entail loss of the detailed information contained in the individual traces. Moreover, calculating an "average" trace is not very meaningful because of the different burnout times of the individual traces. In this study we have followed a different approach, whereby the rate parameters are estimated from the individual temperature traces, treating the properties of individual particles as random variables. While the particle-to-particle variation involves several properties, the level of experimental accuracy and the need for mathematical tractability suggests a highly

simplified approach. We assume that the properties of the i^{th} particle are characterized by two random variables: the initial radius, r_{0i} (assuming spherical shape), and the apparent Arrhenius pre-exponential factor A_{ai}. The apparent reaction rate is assumed to be of the form

$$R_a = A_a e^{-E_a/RT} p_s^m. \tag{5.1}$$

This is based on the external surface area of the particle. The reaction order, m, is assumed to be one, but other types of kinetics can be treated without difficulty.

Using an effective radius (*i.e.*, assuming spherical particles) is a clear necessity in view of the impracticability of carrying out mathematical calculations for particles of irregular and unknown shape. The second random variable A_a is assumed to account for particle-to-particle variations in reactivity and porosity, the latter affecting A_a (and not E_a) as discussed by Gavalas (1980). Variations in mineral and maceral content affect E_a as well as A_a. Nevertheless, the accuracy of the data does not warrant using more than one or two parameters that vary from trace to trace. Therefore, we have treated E_a as an unknown parameter common to all traces. The other properties of the particle, namely, density, heat capacity, and mineral content are treated as known constants. With these assumptions, the temperature of the i^{th} particle may be expressed as

$$T_i(t) = f(t; E_a, A_{ai}, r_{0i}) + \epsilon_i(t), \tag{5.2}$$

where $\epsilon_i(t)$ is the error in the measurement of the temperature. The dependence on the known properties (*e.g.*, particle density and heat capacity) is not shown explicitly. The function f is defined by a suitable combustion model. The model that has been used in the present study is discussed briefly in the following section.

The analysis of the data proceeds as follows. For each trace we define a quantity

$$J_i = \sum_{j=1}^{n} [f(t_j; E_a, A_{ai}, r_{0i}) - T_i^{exp}(t_j)]^2 + w(\bar{r}_0 - r_{0i})^2, \tag{5.3}$$

where the first term represents the deviation of experimental and calculated temperatures over a suitable discrete set of times and the second term represents the deviation of the random radius from the known mean radius (the mean of the appropriate sieve size cut). The weighting coefficient w must be chosen in accordance with the expected error in the temperature measurement ($\epsilon_i(t)$) and the spread in particle size. w is given by $\sigma_T^2/\sigma_{r_0}^2$, where σ_T is the standard deviation in the particle temperature measurement and σ_{r_0} is the standard deviation in the initial radius measurement. The error in the temperature measurement can be calculated from the spread observed over many calibrations at the melting point of pure platinum. The error was taken as $\sigma_T \sim 50$K. The experimental error in the radius measurement was calculated by two independent means: (i) from optical size measurements over many particles (ii) from ASTM sieve standards for wire mesh sieves. Both methods give similar results, $\sigma_{r_0} \sim 12\mu m$. The values of A_{ai} and r_{0i} that minimize J_i are denoted by A_{ai}^* and r_{0i}^*. We also denote by J_i^*, the minimum value of J_i. The three quantities, A_{ai}^*, r_{0i}^*, and J_i^* are clearly functions of E_a.

We now calculate the minimum with respect to E_a of the quantity

$$Q = \sum_{i=1}^{N} J_i^*(E_a), \tag{5.4}$$

obtained by summing over all N traces. If we denote by $\hat{E}_a$, the minimizing value of E_a, then the quantities

$$\hat{r}_{0i} = r_{0i}(\hat{E}_a), \tag{5.5}$$

$$\hat{A}_{ai} = A_{ai}(\hat{E}_a), \tag{5.6}$$

are the best estimates of radius and pre-exponential factor for the i^{th} particle. A mean pre-exponential factor can then be defined by the arithmetic mean

$$\bar{A}_a = \frac{1}{N}\sum_{i=1}^{N} \hat{A}_{ai}. \tag{5.7}$$

A mean particle size is not needed since this can be directly determined by simple observation. However, comparision of the range of $\hat{r}_{0i}$ values with the directly observed range of particle sizes provides a general consistency check.

The cumulative sum Q of the J_i's over all particles versus activation energy is shown in Figure 5.3. The estimated apparent rate for this char is given by

$$R_a = 20.8 \exp\left(-14000/RT\right) \qquad \mathrm{gcm^{-2}s^{-1}atm^{-1}}. \tag{5.8}$$

This apparent activation energy is somewhat lower than the value of 16250 cal/gmole that is obtained by halving the "true" activation energy found from the low temperature experiments (see Chapter 3). This difference is not disturbing in view of the very different methods used to obtain these values.

The value for pre-exponential factor reported here is an arithmetic mean over many traces. The spread of this factors was rather large, as shown in the histogram given in Figure 5.4. A similar, though smaller, spread of values was obtained for the estimated particle diameters. The average of the diameter estimates was 45μm. Taking into account the irregular shape of the particles, the estimated equivalent sphere diameters are in fair agreement with the sieve sizes and the sizes observed by microscopy.

The resulting apparent activation energy for the pretreated char was 16000 cal/gmol, while the mean pre-exponential factor was 12.5. The relatively small difference in apparent activation energies for the pretreated and untreated material is not significant, given the uncertainties inherent in the method of determination. However, the fact that the observed rate of reaction for the treated material is so much lower than that of the untreated material is significant. Since the pretreatment opened up porosity over a wide range of sizes, one would expect that mass transfer within the particle would be facilitated. It is clear that any augmentation in observed rate by this phenomenon is overwhelmed by some other factor(s).

It was shown in Chapter 3 that the intrinsic rate of this char at 725K dropped significantly during oxidation from 0% to about 25% conversion. Also, the oxygen chemisorption capacity at 0% conversion was 0.4 mmole/g carbonaceous material, while at 28.5% it dropped to 0.25 mmole/g carbonaceous material. It is possible that reactivity at high temperature depends on the initial concentration of active sites in the char.

5.4 Model Description and Comparision with Experimental Data

The particle combustion model described by Loewenberg *et al.* (1987) (see Chapter 6 for further details) was employed for the calculations after being extended to include the effects of ash. The ash is initially uniformly distributed throughout the particle, but as the carbonaceous material is oxidized, the exposed ash particles accumulate on the surface as a porous layer of increasing thickness. Scanning electron microscopy of individual particles at various conversions has shown that ash does accumulate on the particle surface (see Chapter 4). This does not preclude

the possibility of some ash loss to the gas phase. This loss is expected to be negligible (Flagan and Friedlander (1978)), particularly since the char was pyrolyzed at 1600K.

The ash layer is assumed to add a mass transfer resistance in series with the resistance across the film or boundary layer around the particle. However, it does not create an additional thermal resistance. To calculate the resistance to mass transfer, the ash layer is regarded as a stagnant packed bed with effective diffusivity equal to the bulk gas phase diffusivity multiplied by the ash layer void fraction (~0.4) and divided by a tortuosity factor (~2).

The complete particle combustion model includes a detailed description of intraparticle diffusion and pore growth (see Chapter 6). However, the calculations reported here used a limiting form of the model wherein the reaction takes place in a thin outer shell (Gavalas (1980); Loewenberg *et al.* (1987)). Simulations have shown that this limiting form of the model is adequate for the range of particle temperatures encountered in the experiments. For this limiting form, the mass and energy balances can be written as

$$\frac{d}{dt}\left[m_c + m_{ash}\right] = -4\pi r^2 R_a, \tag{5.9}$$

$$\frac{d}{dt}[\{m_c C_{pc} + m_{ash} C_{p_{ash}}\}T] = 4\pi r^2 \{R_a \Delta H - \Psi_c - Psi_r\}, \tag{5.10}$$

where r is the radius of the particle, including the ash layer; m_c, C_{pc} and m_{ash}, $C_{p_{ash}}$ are mass and heat capacity of the total carbon and the total ash within the particle; R_a is the apparent rate; ΔH is the heat of the combustion reaction; and Ψ_c, Psi_r are heat fluxes from the particle by conduction and radiation, respectively. The radiative term was based on a constant overall emissivity, without provision for

any effects of the accumulating ash. The reason that an overall emissivity is used is that the real situation of radiation interacting with micron-sized particles is too complex for this simple model.

The apparent rate R_a depends on the intrinsic kinetics as well as on the pore structure of char (Gavalas (1980); Loewenberg *et al.* (1987)). From the standpoint of parameter estimation, however, all that is needed is a functional form as given by Eq.(5.1), where A_a and E_a are treated as apparent rate parameters.

Equations (5.9) and (5.10) are coupled to the equations of diffusion and heat transfer from the particle surface to the free stream. The latter equations, which include bulk flow and temperature-dependent properties, are given in Lowenberg *et al.* (1987). The coupled system of equations is solved to yield the radius and temperature of the particle and the oxygen partial pressure, p_s, at the surface of the particle, all as functions of time.

A comparision between calculated and experimental temperatures is shown for a particle in air at 1500K in Figure 5.4. The calculated curve was obtained by using the optimal parameters $\hat{E}_a$, $A_{ai}(\hat{E}_a)$, and $r_{0i}(\hat{E}_a)$. The fits are good, indicating the ability of the simple model to describe particle combustion from the estimated rate parameters.

5.5 Conclusions

Single-particle temperature-time traces measured by optical pyrometry show considerable variability because of differing sizes, shapes, pore structures and mineral contents of individual particles. A novel technique is introduced to analyze the traces by treating size and pre-exponential factor of each particle as random vari-

ables. This technique was used in conjunction with a particle combustion model, assuming that the heterogenous reaction is limited to a thin surface layer of the particle in order to estimate the apparent kinetic parameters. The estimated values of the apparent pre-exponential factor varied significantly from particle to particle. Using the estimated parameters provided good agreement between calculated and experimental temperature-time traces.

The effect of preoxidizing the material was to lower the observed rates unexpectedly. This may be due to the fact that the amount of active surface area (as measured by oxygen chemisorption) is lowered by this treatment.

REFERENCES

Ayling, A.B., and Smith I.W. (1972). Measured Temperature of Burning Pulverized Fuel Particles and the Nature of the Primary Reaction Product. *Combust. Flame* **18**, 173.

Field, M.A. (1969). Rate of Combustion of Size-Graded Fractions of Char from a Low-Rank Coal Between 1200K and 2000K. *Combust. Flame* **13**, 237.

Flagan, R.C. and Friedlander, S.K. (1978). in *Recent Developments in Aerosol Science*, D.T. Shaw, Ed., John Wiley and Sons, New York, p. 25.

Gavalas, G.R. (1980). Analysis of Char Combustion Including the Effect of Pore Enlargement. *Comb. Sci. Tech.* **24**, 197.

Hamor, R.J., and Smith, I.W. (1973). Kinetics of Combustion of a Pulverized Brown Coal Char Between 830 and 2200K. *Combust. Flame* **21**, 153.

Jorgensen, F.R.A. and Zuiderwyk, M. J. (1985). Two-Color Pyrometer Measurement of the Temperature of Individual Combusting Particles. *J. Phys. E: Sci. Instrum.* **18**, 486.

Levendis, Y.A. and Flagan, R.C. (1987). Combustion of Uniformly Sized Glassy Carbon Particles. *Comb. Sci. Tech.* **53**, 117.

Loewenberg, M., Bellan, J., and Gavalas, G.R. (1987). A Simplified Description of Char Combustion. *Chem. Eng. Comm.*, **58**, 89.

McLean, W.J., Hardesty, D.R., and Pohl, J.H. (1981). Direct Observations of Devolatilizing Pulverized Coal Particles in a Combustion Environment. *Eighteenth Symposium (Int.) on Combustion, the Combustion Institute*, p. 1239.

Mitchell, R.E., and McLean, W.J. (1982). On the Temperature and Reaction Rate of Burning Pulverized Fuels. *Nineteenth Symposium (Int.) on Combustion, the Combustion Institute*, p. 1113.

Senior, C.L. and Flagan, R.C. (1984). Synthetic Chars for the Study of Ash Vaporization. *Twentieth Symposium (Int.) on Combustion, the Combustion Institute*, p. 921.

Smith, I.W. and Tyler, R.J. (1974). The Reactivity of a Porous Brown Coal Char to Oxygen Between 630 and 1812K. *Comb. Sci. Tech.* **9**, 87.

Smith, I.W. (1982). The Combustion Rates of Coal Chars: A Review. *Nineteenth Symposium (Int.) on Combustion, the Combustion Institute*, p. 1045.

Timothy, L.D., Sarofim, A.F., and Beer, J.M. (1982). *Nineteenth Symposium (Int.) on Combustion, the Combustion Institute*, p. 1123.

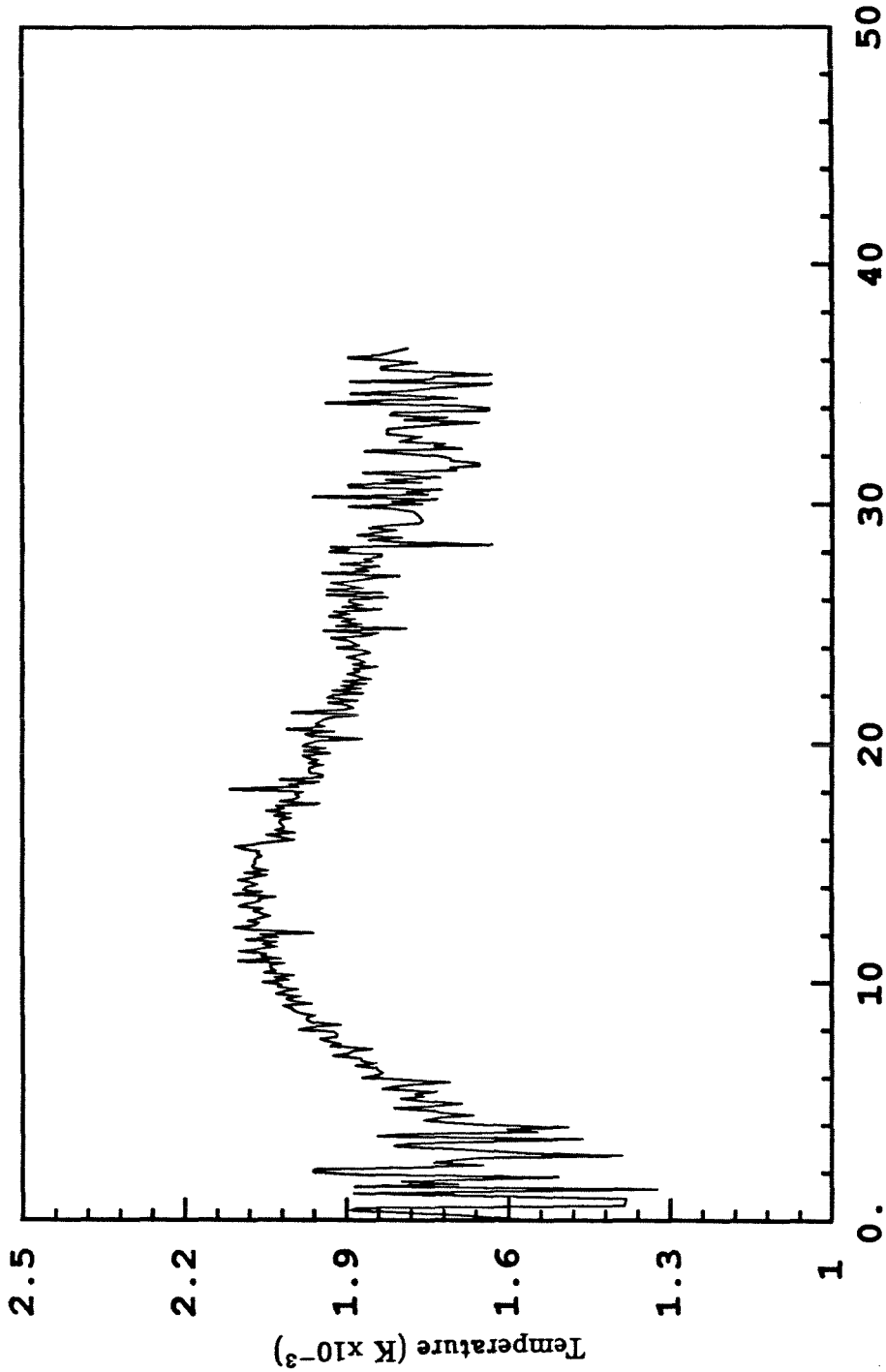

Figure 5.1. Temperature-time history for a lignite char particle in air at a reactor wall temperature of 1500K.

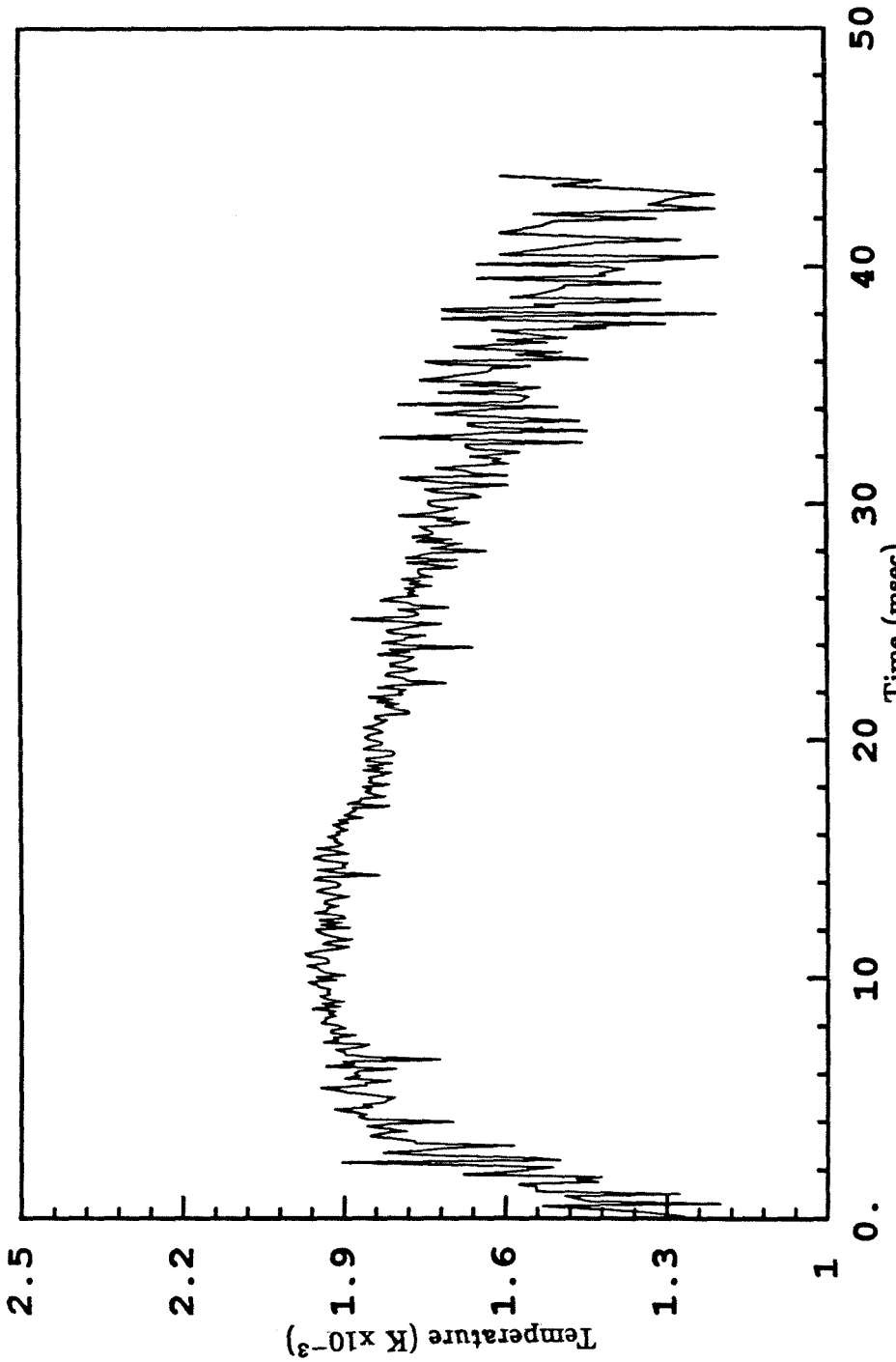

Figure 5.2. Temperature-time history for a lignite char particle in air at a reactor wall temperature of 1500K.

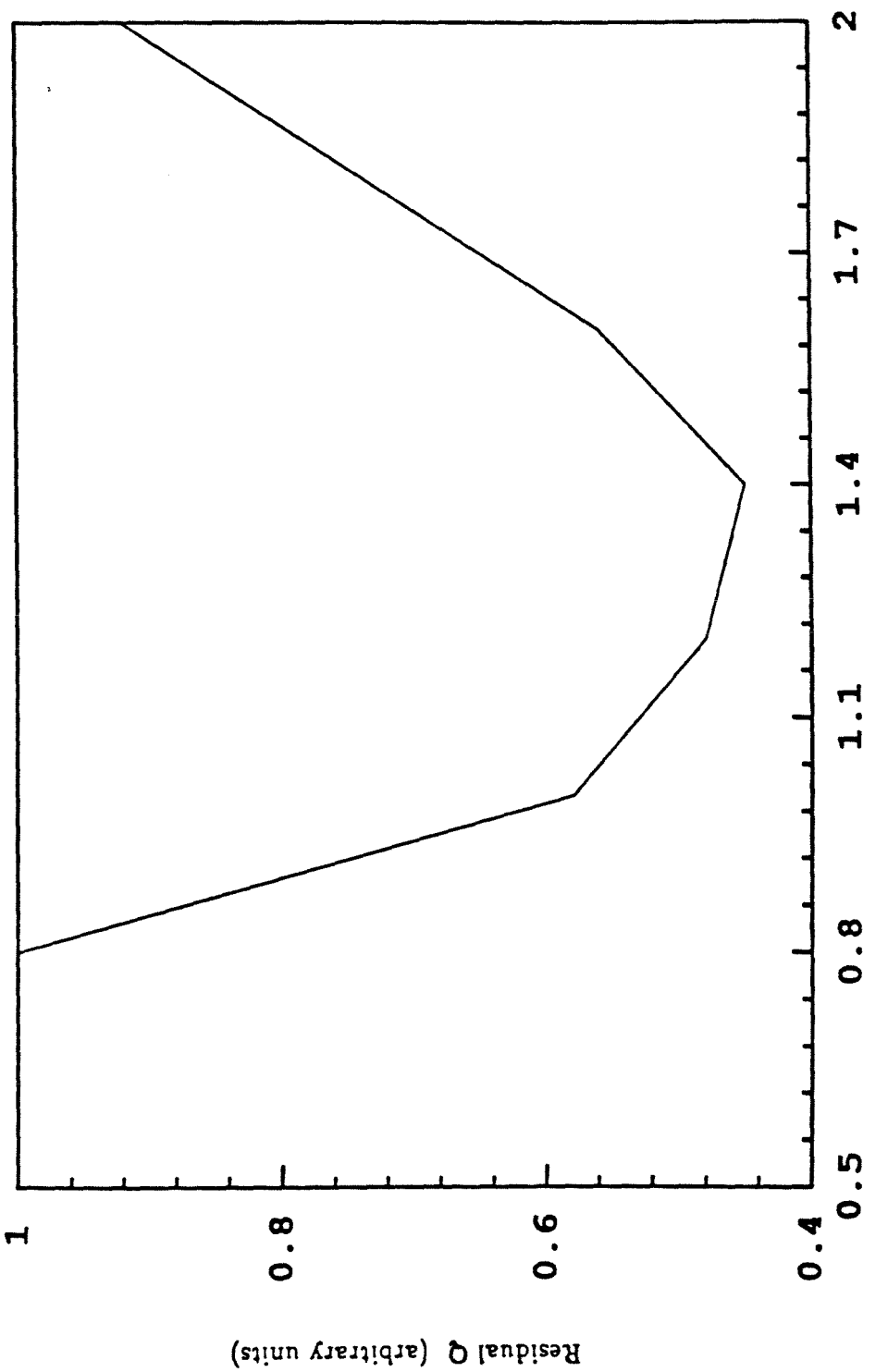

Figure 5.3. Minimization of the sum of residuals with respect to activation energy for lignite char.

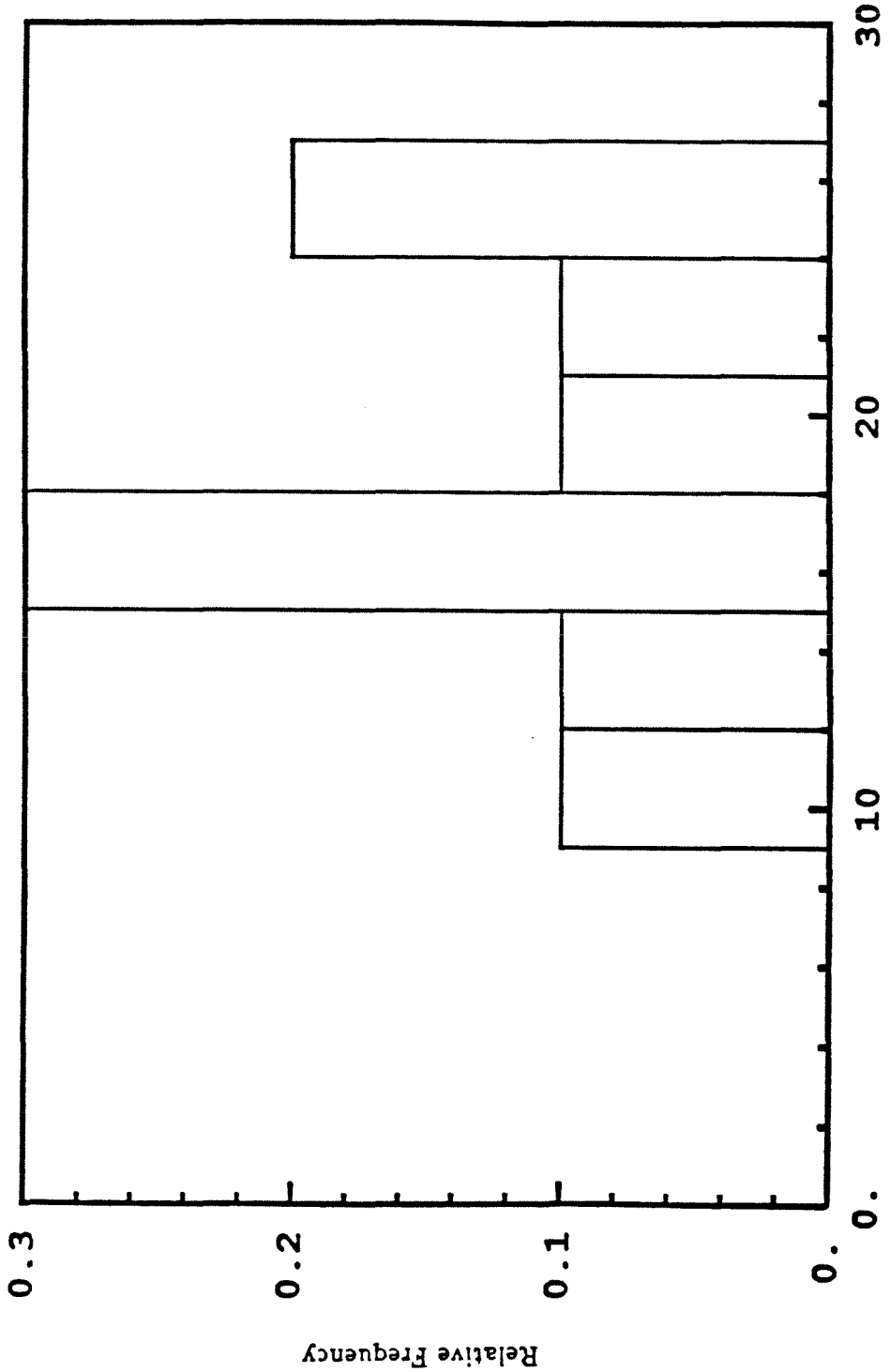

Figure 5.4. Histogram of preexponential factors for lignite char.

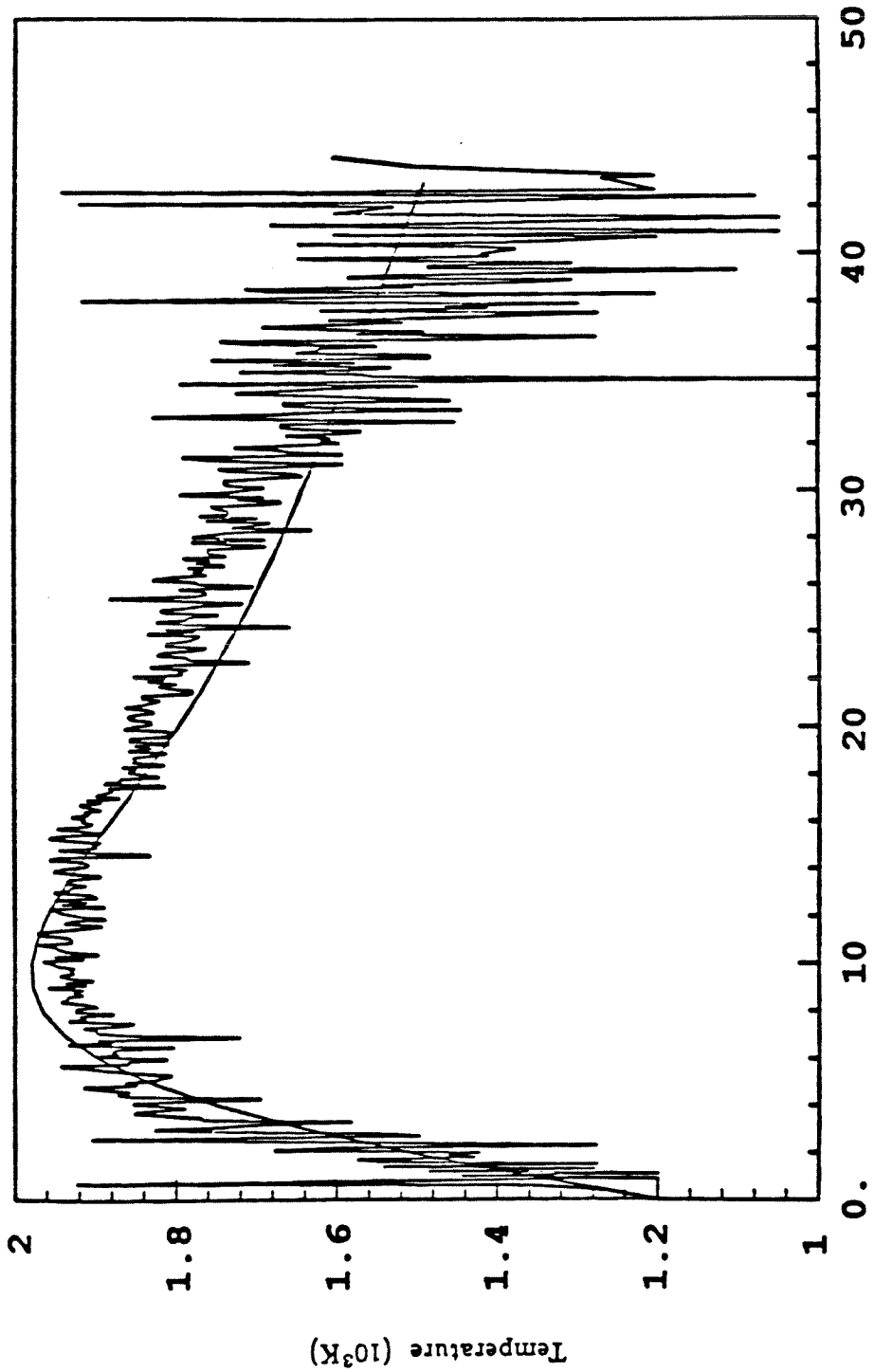

Figure 5.5. Comparision of experimental and calculated temperature-time history for a lignite char particle.

CHAPTER 6

MODELING SINGLE PARTICLE COMBUSTION

6.1 Introduction

This chapter describes the details of a numerical model for char particle combustion. The model simulates a char particle being injected into a furnace by assuming that the particle has an uniform initial temperature and is surrounded by an ambient of a different specified temperature. Mon and Amundson (1978); Libby and Blake (1979); and Sundaresan and Amundson (1980) are among many who have considered various aspects of single-particle-combustion modelling.

Field *et al.* (1967) have indicated that combusting carbon particles less than 100μm in diameter have a maximum temperature difference of 40K between the outside and the center. Therefore, in this model, we have assumed that the particle is isothermal.

The sole heterogeneous reaction is taken as $C + O_2 \rightarrow 2CO$, since Mitchell (1986) has shown that the direct oxidation of carbon to carbon dioxide is negligible for temperatures above 1000K. The oxidation of the carbon monoxide produced from this reaction is assumed to take place far from the particle (Field *et al.* (1967)). Thus, the gas surrounding the particle is assumed to consist of three species: 1-O_2, 2-CO and 3-N_2.

In addition to convective and conductive heat transfer, radiative heat transfer is accounted for; the gas is assumed to be transparent to this radiation. The gas phase is also assumed to be quasi-steady relative to the solid; *i.e.*, temperature and concentration profiles are established immediately for a given particle size and temperature.

For the detailed solid model, the particle voidage is described by the ran-

dom capillary model of Gavalas (1980, 1981). This continuum approach treats the interior of the particles as having spherical symmetry, *i.e.*; properties like local conversion, surface area, and void fraction are functions only of particle radius.

The mass and energy balance differential equations are formulated and then solved with suitable boundary and initial conditions. Particle temperature and radius are predicted as a function of time, while surface area is predicted as a function of conversion.

6.2 Shrinking Core Model

The solid is modeled as a shrinking sphere containing an initially uniform distribution of voids and ash particles. The details of the internal structure are not considered in this limiting case, since the reaction is assumed to be so fast that no reaction occurs on the pore walls. The voids affect only the apparent density of the particle.

As the carbonaceous material is oxidized, the ash particles are exposed at, then accumulate on, the surface. The thickness of the ash layer increases as combustion proceeds (Scanning electron micrographs of partially oxidized material have indicated that this is a realistic representation – see Chapter 4). This porous ash layer presents a diffusional resistance to the oxygen transport to the particle surface in series with the gas-phase diffusional resistance. The presence of ash also manifests itself in the energy balance of the particle, increasing the thermal inertia of the particle and altering its radiative properties. A detailed study of the radiative properties of the combined carbon-ash layer has not been undertaken. Instead, an overall emissivity of the particle is used. The catalytic effects of ash are not

considered.

6.2.1 Derivation of Model Equations

The particle mass balance is given by

$$\frac{dm_c}{dt} = 4\pi r_c^2 \rho_c (1 - \epsilon - v_{ash}) \frac{dr_c}{dt} = -4\pi r_p^2 N_p, \tag{6.1}$$

where m_c is the mass of carbon, r_c is the core radius, r_p is is the particle radius which includes the ash layer (see Figure 6.1), ρ_c is the density of solid carbon, ϵ is the void fraction, v_{ash} is the volume fraction of ash in the core, and N_p is the mass flux of carbon at the particle surface. If the rate of reaction is represented by the Arrhenius form and the rate is first order in oxygen, (6.1) becomes

$$\frac{dm_c}{dt} = -4\pi r_c^2 A_a \exp(-E_a/RT) Y_{1*}, \tag{6.2}$$

where A_a and E_a are the apparent Arrhenius kinetic parameters, T_p is the particle temperature, and Y_{1*} is the oxygen mass fraction at the carbon surface.

The particle energy balance is:

$$\frac{d}{dt}\{m_c H_c(T) + m_{ash} H_{ash}(T)\} = 4\pi r_p^2 (\sum_{i=1}^{3} N_{ip} H_i(T) - e_c - e_{rad}), \tag{6.3}$$

with

$$e_c = k \frac{dT}{dr}|_{r=r_p}, \tag{6.4}$$

and

$$e_{rad} = \sigma\{\varepsilon_p T_p^4 - \varepsilon_\infty T_\infty^4\}, \tag{6.5}$$

where m_{ash} is the mass of ash, $H_c(T)$ and $H_{ash}(T)$ are the enthalpies of solid carbon and ash, N_{ip} is the mass flux of the gas phase species i at the particle surface, $H_i(T)$

is the specific enthalpy of the component i, k is the gas phase thermal conductivity, σ is the Stefan-Boltzmann constant of radiation, ε_p is the overall emissivity of the particle, and ε_∞ is the emissivity of the radiating environment far from the particle. The term on the left-hand side of (6.3) is the energy accumulation term of the solid; the terms on the right-hand side represent heat generation from chemical reaction, energy transport via conduction, and energy transport via radiation, respectively. Given that

$$H_i(T) = H_i(T^0) + \int_{T^0}^{T} C_{p_i} dT, \tag{6.6}$$

where T^0 is the standard state reference temperature, (6.5) can be manipulated to yield:

$$\{m_c c_{pc} + m_{ash} c_{p_{ash}}\} \frac{dT}{dt} = 4\pi r_p^2 (N_p H_c(T) + e_p - e_{rad}). \tag{6.7}$$

Mass transport in the gas phase is described by the Stefan-Maxwell equations:

$$\frac{dY_i}{dr} = \sum_j \frac{(Y_i N_j - Y_j N_i)}{\rho_g \mathcal{D}_{ij}}, \tag{6.8}$$

where Y_i is the mass fraction of species i, N_i is the mass flux of i, ρ_g is the density of gas, and $\mathcal{D}_{ij}$ is the diffusivity of component i in component j. Since the molecules of interest are similar in size, the binary diffusion coefficients $\mathcal{D}_{ij}$ are assumed equal to $\mathcal{D}$. This simplifies (6.8) to

$$N_i = -\rho_g \mathcal{D} \frac{dY_i}{dr} + N Y_i, \tag{6.9}$$

where N is the overall mass flux $\sum_{i=1}^{3} N_i$, which satisfies

$$r^2 N = r_p^2 N_p, \tag{6.10}$$

where the subscript p denotes values at the surface of the particle. The single heterogeneous reaction yields the following stoichiometric relations:

$$N_{1p} = -\frac{4}{3}N_p, \quad N_{2p} = \frac{7}{3}N_p, \quad N_{3p} = 0. \tag{6.11}$$

Loewenberg *et al.* (1987) have shown that the equations (6.9) for all species can be combined to give

$$\frac{d(Y_1/4 + Y_2/7)}{dY_3} = \frac{Y_1/4 + Y_2/7}{Y_3} \tag{6.12}$$

Using (6.12) and the fact that $\sum_{i=1}^{3} Y_i = 1$, along with appropriate boundary conditions far from the particle,

$$Y_3 = \frac{3/28Y_1 + 1/7}{1/Y_{3\infty}(Y_{1\infty}/4 + Y_{2\infty}/7) + 1/7}, \tag{6.13}$$

$$Y_2 = 1 - Y_1 - Y_3, \tag{6.14}$$

where the subscript ∞ denotes values far from the particle.

The energy balance for the gas phase is

$$r^2\{-k\frac{dT}{dr} + \sum_i N_i H_i(T)\} = r_p^2 e_p. \tag{6.15}$$

From the stoichiometric relations (6.11) and overall mass balance (6.10), (6.14) becomes

$$r^2 k\frac{dT}{dr} = r_p^2\left(\frac{N_p}{3}(h(T) - e_p)\right), \tag{6.16}$$

with $h(T) = \{7H_2(T) - 4H_1(T)\}/3$. The boundary conditions are:

$$r = r_p : T = T_p; r \to \infty : T \to T_\infty. \tag{6.17}$$

Integrating (6.16) gives

$$r_p N_p = \int_{T_\infty}^{T} \frac{k dT}{\gamma_p - h(T)}, \tag{6.18}$$

where $\gamma_p = e_p/N_p$. This is an algebraic expression for mass flux at the surface. Combining (6.18) with the mass balance for oxygen (6.8) yields

$$r^2 \rho_g \mathcal{D} \frac{dY_1}{dr} = r_p^2 N_p \{Y_1 + \frac{4}{3}\}. \tag{6.19}$$

Dividing (6.19) by (6.16) gives

$$\frac{\rho_g \mathcal{D}}{k} \frac{dY_1}{dT} = \frac{Y_1 + 4/3}{h(T) - \gamma_p}, \tag{6.20}$$

with the initial condition $T = T_\infty : Y_1 = Y_{1\infty}$. Integration of (6.20) yields

$$\ln \frac{Y_{1\infty} + 4/3}{Y_{1p} + 4/3} = \int_{T_\infty}^{T_p} \frac{k dT}{\rho_g \mathcal{D}\{\gamma_p - h(T)\}}. \tag{6.21}$$

This is a quadrature for energy flux at the particle surface. Equations (6.18) and (6.21) were solved numerically to obtain the particle temperature and the oxygen mass fraction at the external surface of the particle as a function of time.

Once the oxygen mass fraction outside the ash layer, Y_{1p}, is obtained, the mass fraction of oxygen at the carbon surface, Y_{1*}, can be calculated. The mass-transfer coefficient in the ash layer (h_{mash}), assuming spherical geometry and negligible Reynolds number, is given by

$$h_{mash} = \frac{\epsilon_{int} \mathcal{D}}{\tau t} \ln\left(1 + \frac{t}{r}\right), \tag{6.22}$$

where ϵ_{int} is the void fraction of the ash layer (taken as 0.35) and τ is the tortuosity (taken as 2.0). The bulk diffusivity ($\mathcal{D}$) in the ash layer is calculated at the particle temperature. The thickness of the ash layer, t, is calculated from a mass balance of the total ash in the particle, assuming that none of it is lost:

$$t = \left[\frac{r^3 + v_{ash}(r_0^3 - r^3)}{1 - \epsilon_{int}}\right]^{0.33} - r, \tag{6.23}$$

where r_0 is the initial particle radius.

Mass conservation in the ash layer dictates that

$$4\pi r_c^2 A_a \exp(-E_a/RT) Y_{1*} = 4\pi r_c^2 h_{mash}(Y_{1p} - Y_{1*})(24/RT_p), \tag{6.24}$$

where R is the ideal gas constant, and the numerical factor is the number of grams of carbon removed per mole of oxygen. Solving (6.24) for Y_{1*} yields

$$Y_{1*} = \frac{Y_{1p}}{1 + RT_p A_a \exp(-E_a/RT)/24h_{mash}}. \tag{6.25}$$

The mass fraction Y_{1*} is used in the flux calculation (6.1).

6.2.2 Parametric Studies

Calculations were carried out to determine the influence of various parameters on the predicted particle-temperature histories. A "base" case was used for comparison with the other simulations. For the base case, the apparent activation energy (E_a) and apparent frequency factor (A_a) were taken as 16800 cal gmol^{-1} and 46 g cm^{-2}s^{-1}, respectively. The ambient was assumed to be air ($Y_{1\infty} = 0.22$). The initial particle temperature (T_0) was 1000K, and the wall temperature (T_∞) was set at 1600K. The wall emissivity (ε_∞) and particle emissivity (ε_p) were both taken to be 0.8, while the initial void fraction (ϵ) was set at 0.4. The carbon density (ρ_c) was 1.5 gcm^{-3}, and the ash volume fraction (v_{ash}) was 0.01 . The initial particle radius (r_{p_0}) was 25 μm.

Figure 6.2 shows simulations for three different initial particle radii. The effect of increasing the initial particle radius is to increase the burn time and slightly decrease the maximum temperature. The burnout time varies approximately as

the square of the particle radius, as expected from the imposed 'shrinking core' behavior.

The wall temperature has a strong influence on both the maximum particle temperature and the burnout time, as shown in Figure 6.3. Decreasing the wall temperature to 1200K reduces maximum particle temperature by nearly 500K and increases burnout time by more than 100%. In this case, the particle burns at a temperature close to 1200K for the last 50 msec of its life. This particle has undergone extinction. An explanation of this phenomenon is as follows: The transient process of single particle combustion can be described in terms of a succession of pseudo-steady states. As the particle shrinks, heat transfer via conduction ultimately causes it to pass from a high-temperature steady state to a low-temperature steady state. In this particular case, the particle temperature has fallen to 1400K at 48 msec. The particle radius at this time is 8.5 μm, corresponding to a conversion of over 95%.

The burnout time increases for decreasing void fraction of the particle, as seen in Figure 6.4. This is not surprising, because particles with a lower void fraction have a higher carbon mass. Varying the void fraction of the particle does not affect the maximum temperature reached.

The presence of ash affects the shape of the temperature trace significantly (Figure 6.5). The ash-containing particles reach slightly lower maximum temperatures because of the increased resistance to mass transfer of oxygen because of the ash layer. However, the temperature of the particle containing ash does not fall as quickly as it does for the ash-free particle. The reason for this is that the particle

containing ash has a greater thermal inertia due to the presence of ash. The total burnout times are not greatly affected.

The influence of carbon emissivity on predicted time-temperature histories is straightforward (see Figure 6.6): for a fixed wall emissivity, a particle with higher carbon emissivity burns at a lower maximum temperature due to increased radiative loss. However, the decrease in temperature is not dramatic and the burn time increases only marginally.

The temperature traces are most sensitive to adjustment of the reaction rate parameters. The effect of changing the frequency factor at constant activation energy is shown in Figure 6.7. The maximum temperature is increased and the burnout time is decreased for an increase in the apparent frequency factor. For a fixed frequency factor, increasing the activation energy results in lower maximum temperatures and higher burnout times, as shown in Figure 6.8.

6.3 Detailed Solid Model

This model considers the problem of diffusion and reaction inside the particle, in addition to transport in the gas phase. The porosity is described by a random capillary model (Gavalas (1981)). This model of porosity relates local void fraction and surface area to a local burnoff variable described below. Ash is not considered in this model.

The gas phase equations described in the previous section act as a non-linear boundary condition to the solid-phase equation. Both oxygen mass fraction and carbon mass flux must be matched at the particle surface to find the oxygen concentration profile inside the particle.

6.3.1 Solid Phase Equations

According to the random capillary model (Gavalas (1981)), void fraction (ϵ) and surface area (S) are related to a local burnoff variable ($q(r,t)$), which is given by

$$q(r,t) = \frac{1}{\rho_c}\int_0^t R_{in}(Y_1, T_p)dt, \tag{6.26}$$

where r is the radial position, t is time, ρ_c is the solid carbon density, and R_{in} is the intrinsic reaction rate, which depends on local oxygen mass fraction Y_1 and particle temperature T_p. For cylindrical voids,

$$\epsilon(q) = 1 - \exp[-2\pi\int_{r_{min}}^{r_{max}} \lambda(r)(r+q)^2 dr], \tag{6.27}$$

$$S(q) = [1-\epsilon(q)]4\pi\int_{r_{min}}^{r_{max}} \lambda(r)(r+q)dr. \tag{6.28}$$

For spherical voids,

$$\epsilon(q) = 1 - \exp[\frac{-4\pi}{3}\int_{r_{min}}^{r_{max}} \lambda(r)(r+q)^3 dr], \tag{6.29}$$

$$S(q) = [1-\epsilon(q)]4\pi\int_{r_{min}}^{r_{max}} \lambda(r)(r+q)^2 dr, \tag{6.30}$$

where $\lambda(r)$ is the distribution function for pores of radius r, while r_{min} and r_{max} are the radii of the smallest and largest pores, respectively. At a specified void fraction, ϵ^*, the pore walls are assumed to coalesce to the point where fragmentation of the solid takes place. The fragments are assumed to burn far away from the particle, and are not expected to influence it in any way.

Mass transport of oxygen in the solid is described by:

$$\frac{1}{r^2}\frac{\partial}{\partial r}(r^2 D_{eff}(q)\frac{\partial Y_1}{\partial r}) = R_{in}(Y_1, T_p)S(q), \tag{6.31}$$

where the effective diffusivity D_{eff} was calculated from

$$D_{eff}(q) = \mathcal{D}\epsilon(q)/\tau. \tag{6.32}$$

Here, $\mathcal{D}$ is the bulk gas phase diffusivity and τ is the tortuosity. The initial condition is

$$t = 0 \quad : \quad q(r,t) = 0, \tag{6.33}$$

while the boundary conditions are

$$r = 0 \quad : \frac{\partial Y_1}{\partial r} = 0, \frac{\partial q}{\partial r} = 0, \tag{6.34}$$

$$r = r_p(t) \quad : Y_1 = Y_{1s}, \frac{dr}{dt} = -(\frac{\partial \epsilon/\partial t}{\partial \epsilon/\partial r})|_{\epsilon=\epsilon^*}. \tag{6.35}$$

The last boundary condition relates the rate of change of the radius to ϵ^*, which is the critical void fraction at which point shedding begins. For the cases presented here, ϵ^* was taken to be 0.8.

Unless otherwise specified, the intrinsic rate was taken from Smith (1978):

$$R_{in} = 305 \exp(-41000/RT) Y_1 (\mathrm{gcm^{-2}s^{-1}}). \tag{6.36}$$

6.3.2 Solution of Model Equations

The particle is divided into fifty spherical shells of equal thickness, inside each of which concentration is assumed to be uniform. For a given time step (typically 0.1 msec), the conservation equation for oxygen (6.31) is solved as an initial value problem (IVP), using the conditions $\frac{\partial Y_1}{\partial r} = 0$ and $Y_1 = Y_{10}$ at r=0. The value of Y_{10} is a reasonable but arbitrary estimate of the oxygen mass fraction at the center of the particle. The IVP is solved along the fifty-one point grid, using a standard

fourth-order Runge-Kutta routine. Since (6.31) is linear in oxygen mass fraction, the resulting profile can be multiplied by $\mathcal{F}$ to obtain a profile that satisfies the matching condition of oxygen mass fraction at the surface. $\mathcal{F}$ is simply the ratio of the mass fraction of oxygen at the particle surface from the gas-phase equations (Y_{1p}) to that from the solid-phase equation (Y_{1s}).

The mass flux of carbon is calculated from the concentration gradient of O_2 at the surface. This flux is used to calculate a new gas-phase surface mass fraction Y_{1p}. This is used to adjust the internal mass fraction profile, and a new flux is computed. This process is continued until the "internal" and "external" fluxes and mass fractions match to within 0.1%.

The total mass loss during the time step is calculated from the mass flux of carbon at the surface of the particle. The overall conversion is computed from the total mass loss from zero time. The concentration profile inside the particle is used to calculate the local carbon conversion at each grid point; the local conversion for each shell is taken to be the average of the conversions of the grid points on either side. The local void fraction and local specific surface area are determined for each shell. The total surface area of the particle is obtained from the sum of the areas of the individual shells. Dividing the total area by the particle mass yields the specific area. The position of the external surface is calculated as a function of time by interpolations between the two grid points which bracket ϵ^*.

The particle energy balance is used to calculate the new particle temperature; a new particle radius is also calculated, based on the shedding condition. Another time step is taken and the entire process is repeated until the particle radius is less

than 2 μm.

6.3.3 Monodisperse Internal Voids

For this case, the integrals in (6.29) and (6.30) are replaced by a single mean pore radius a_0 and number density $\lambda(a_0)$. For spherical voids, the resulting expressions for ϵ and S are

$$\epsilon(q) = 1 - \exp[\frac{-4\pi}{3}\lambda(a_0)(a_0+q)^3], \tag{6.37}$$

$$S(q) = [1-\epsilon(q)]4\pi\lambda(a_0)(a_0+q)^2. \tag{6.38}$$

For the simulations that follow, initial void radius and void fraction were specified; the number density was calculated from a recast version of (6.37) by setting q=0:

$$\lambda(a_0) = [\frac{4\pi a_0^3}{3}\ln(1-\epsilon_0)]^{-1}. \tag{6.39}$$

Let us briefly consider the relationship between ϵ^* and its corresponding critical local burnoff q^*. Solving (6.37) in terms of q yields:

$$q = [\frac{4\pi}{3}\lambda(a_0)\ln(1-\epsilon)]^{-1/3} - a_0. \tag{6.40}$$

Substituting (6.39) into (6.40) at the critical condition gives:

$$q^* = a_0[\ln(1-\epsilon_0)/\ln(1-\epsilon^*)]^{1/3} - a_0. \tag{6.41}$$

For this "base" case, the mean pore radius was taken to be 0.05 μm, and the number density was based on an initial void fraction of 0.10. The initial particle radius was 25 μm, and the emissivity of the particle and wall were taken to be

0.8. The ambient was air. In the examples that follow, both the initial and wall temperature were 1500K, and the solid density (ρ_c) was 2.0 gcm^{-3}.

Figure 6.9 shows the model prediction for temperature versus time. The temperature increases from 1500K to 2100K in approximately 20 msec. The temperature remains rather constant for another 20 msec; it then falls abruptly to about 1550K, and burns for an additional 6 msec. It undergoes extinction, and falls to a new steady state with a temperature close to that of the wall. The drop in temperature is much faster than in the case of the shrinking core model. Note, however, that the total conversion is greater than 99% at this point.

The model prediction for particle radius versus time is shown in Figure 6.10. Initially, the particle radius remains constant at 25 μm. At about 11 msec, the material at the edge of the particle has reached the critical void fraction ϵ^*; the particle begins to shrink by fragmentation. The rate of shrinkage slows down when the particle temperature drops at 44 msec. During this period of low-temperature reaction, oxygen penetrates the pores of the particle more effectively; hence, reaction is not confined to the exterior shell of the particle. At about 51 msec, the entire particle reaches the critcal void fraction and disintegrates.

The oxygen partial pressure at the surface of the particle is plotted as a function of time in Figure 6.11. At a temperature of 1500K and radius of 25 μm, the partial pressure is already less than 0.15 (the ambient is 0.21) because of the diffusional resistance in the boundary layer. As particle temperature increases, the partial pressure of oxygen decreases to a level of 0.02. In the final few milliseconds, the partial pressure of oxygen at the surface approaches that of the ambient.

Figure 6.12 shows oxygen partial pressure profiles inside the particle at 2 msec intervals during the simulation. In all but the last two traces, the oxygen concentration falls to zero in a rather short distance. This indicates that the reaction zone is confined to a thin outer shell of the particle during most of the particle's history.

Figure 6.13 shows void fraction at the surface of the particle, as well as overall void fraction of the particle as a function of time. As the reaction proceeds, the void fraction of the outer edge of the particle increases to its critical value of 0.8. Initially, the overall void fraction increases as the outer part of the particle is oxidized. Once the fragmentation criterion is reached at the outer edge, material with a high value of void fraction is shed. Thus, the overall void fraction drops. This continues as material with a locally higher void fraction is consumed. The overall void fraction levels off, then increases as oxygen more effectively penetrates the particle.

Several parameters were adjusted to observe their influence on the model. Doubling the particle radius results in an approximately fourfold increase in burnout time, as seen in Figure 6.14. The larger particle burns at a slightly lower average temperature than the smaller one, as observed in the shrinking core model.

Figure 6.15 shows model behavior for two different solid densities. As expected, the burnout time is roughly proportional to solid density. The maximum temperature is about the same in each case.

As in the case of the shrinking core model, lowering particle emissivity increases the maximum particle temperature. This is shown in Figure 6.16. Interestingly, total burnout time is not significantly affected.

Variation of the Arrhenius pre-exponential factor has a strong effect on pre-

dicted combustion behavior. Figure 6.17 shows the temperature time history for three different pre-exponential factors. Increasing the pre-exponential factor by 67% increased the maximum particle temperature by about 50K and decreased the pre-extinction burnout time by only 2 to 3 msec. Decreasing the pre-exponential factor by 67% has a greater effect: the maximum temperature decreases by about 100K and the pre-extinction burnout time increases by about 7 msec. There is a large increase in postextinction oxidation time. (Again, conversion is greater than 99% at this point.)

Figure 6.18 shows the influence of initial void size for a fixed void fraction. Decreasing the initial void radius to 0.01 μm increases maximum particle temperature by nearly 100K, and shortens burnout time by almost 12 msec. Interestingly, postextinction burning does not appear to take place in this case. Increasing the initial void radius to 0.10 μm decreases maximum particle temperature by about 50K and increases total burnout time by 12 msec, much of this being due to postextinction oxidation. The reason for this is that the larger voids result in a smaller local surface area, S, for a fixed initial void fraction.

The influence of initial void fraction (for fixed initial void size) is demonstrated in Figure 6.19. Decreasing the initial void fraction decreases maximum particle temperature slightly, but increases total burnout time by about 10 msec. This is due to a twofold effect: (i) the local surface area S is smaller in this case; (ii) lower void fraction results in higher solid fraction. Increasing the initial void fraction has the opposite effect.

The effect of wall temperature is shown in Figure 6.20. For this series of

simulations, the initial particle temperature was 1300K in all cases. Increasing the wall temperature to 1700K results in a maximum particle temperature of nearly 2500K. Decreasing the wall temperature to 1300K results in a maximum particle temperature of about 2000K. The greatest effect is the increase in postextiction burn time at the lowest temperature.

The effect of initial pore geometry was explored. A simulation was done using cylindrical voids in place of spherical voids. The void sizes and void fractions were the same in both cases, and the solid density was taken as 1.5 g/cm^3. Figure 6.21 shows that there is not much difference in the predicted temperature-time histories.

6.3.4 Polydisperse Internal Voids

This model is an extension of the above one to include a more realistic internal structure. Three different initial void radii were used (spherical voids): a_{01}=0.1 μm, a_{02}=0.01 μm, and a_{03}=0.001 μm with corresponding initial void fractions of ϵ_1, ϵ_2, and ϵ_3. The integrals in (6.29) and (6.30) are replaced by sums. The resulting expressions for total void fraction ϵ_t and S are

$$\epsilon_t(q) = 1 - \exp[\frac{-4\pi}{3} \sum_{i=1}^{3} \lambda(a_{0i})(a_{0i} + q)^3], \tag{6.42}$$

$$S(q) = [1 - \epsilon(q)]4\pi \sum_{i=1}^{3} \lambda(a_{0i})(a_{0i} + q)^2. \tag{6.43}$$

Care was taken to calculate the number density of voids of each size. The smallest pores were considered first:

$$\lambda(a_{03}) = [\frac{4\pi}{3} a_{03}^3 \ln(1 - \epsilon_3)]^{-1}. \tag{6.44}$$

Since the random capillary model accounts for overlapping pores, we must write:

$$\epsilon_2 + \epsilon_3 = 1 - \exp[\frac{-4\pi}{3}\sum_{i=2}^{3}\lambda(a_{0i})(a_{0i}+q)^3]. \tag{6.45}$$

Subtracting the expression for ϵ_3 gives

$$\epsilon_2 = \exp[\frac{-4\pi}{3}\lambda(a_{03})(a_{03}+q)^3] - \exp[\frac{-4\pi}{3}\sum_{i=2}^{3}\lambda(a_{0i})(a_{0i}+q)^3]. \tag{6.46}$$

Pulling out the common factor $\exp[\frac{-4\pi}{3}\lambda(a_{03})(a_{03}+q)^3]$ and noting that it equals $1-\epsilon_3$, we arrive at the expression for $\lambda(a_{02})$ (for $q=0$):

$$\lambda(a_{02}) = [\frac{4\pi a_{02}^3}{3}\ln\{1-\epsilon_2/(1-\epsilon_3)\}]^{-1}. \tag{6.47}$$

The expression for $\lambda(a_{01})$ is derived analogously:

$$\lambda(a_{01}) = [\frac{4\pi a_{01}^3}{3}\ln\{1-\epsilon_1/(1-\epsilon_2-\epsilon_3)\}]^{-1}. \tag{6.48}$$

The results of varying the different void fractions in the various sizes is shown in Figure 6.22. Because of the amount of computer time required, the runs were stopped when a conversion of about 98% was acheived. As a result, the extinction phenomenon was cut short. The trend is clear: the greater the number of smallest voids, the higher the maximum temperature and the shorter the time to reach 98% conversion.

Figure 6.23 shows the specific surface area of the particles as a function of carbon conversion for the same cases shown in Figure 6.22. The shapes of the curves are generally similar to one another. There is an initial increase in surface area during the heating of the particle. When shedding occurs, material with locally

high surface area is lost; hence, the specific surface area decreases. Beyond 20% conversion, the surface areas remain quite constant, except for some numerical noise.

6.3.5 Non-linear Kinetics

The condition of first-order Arrhenius kinetics was relaxed to test the effects of various non-linear reaction rate expressions on the combustion history. The presence of ash was neglected in these formulations. The introduction of non-linearity makes the problem more difficult to solve numerically. A shooting technique was necessary to solve the intraparticle problem.

The first non-linear expression used was of the Langmuir-Hinschelwood type. The intrinsic reaction rate was assumed to be of the form

$$R_{in} = A_{in} e^{-E_{in}/RT} \frac{Y_{1p}}{1 + C Y_{1p}}, \tag{6.49}$$

where Y_{1p} is the surface oxygen mass fraction and C is a constant. A_{in} and E_{in} were taken to be the same as in the previous cases. The result of the simulation for $C = 1$ is compared to the result obtained from linear kinetics in Figure 6.24. The curves are virtually indistinguishable for these sets of parameters. The shooting technique causes the observed noise in the non-linear case.

The effect of varying C is shown in Figure 6.25. For the values used here, C did not have a strong effect on the predicted burntime history. A better expression for C might be an Arrhenius form, which would more appropriately describe the adsorption step. This was not considered.

An alternative rate form which was considered was:

$$R_{in} = A_{in} e^{-E_{in}/RT} {Y_{1p}}^{m}, \tag{6.50}$$

where m is between 0 and 1. For this case, it is possible for both the gradient and concentration to be zero at a radius greater than zero. The numerical routines are required to find the point at which this occurs, if it occurs at all. If m is smaller than 0.8, the problem becomes numerically stiff and difficult to solve. Because of this, no simulations could be completed. In these cases, the penetration of oxygen is confined to a very thin shell on the outside of the particle. In such situations, the asymptotic formulation given by Gavalas (1981) can be used without much error (Loewenberg *et al.* (1987)). Figure 6.26 shows initial internal oxygen partial pressure profiles for a few different values of m. In all cases, A is 305 $gcm^{-2}s^{-1}$ and E is 40000 cal/gmol. Other parameters are the same as the base case. It is evident that oxygen partial pressures drop to zero in a very short distance, even at the relatively low temperature of 1500K.

6.3.5 Incorporation of Characterization Data

So far, the random capillary model has been used for a dicrete set of pore sizes, which have been somewhat arbitrarily determined. In this section, the results from the characterization experiments will be used to develop a more realistic view of the solid in terms of this model. The model will then be used to predict the specific surface area as a function of conversion at low temperature. The results will be compared to measurements found in Chapter 3.

The lignite char was deemed to have a structure most well-suited for description in terms of the random capillary model. In this case, cylindrical voids will be considered. First, we must determine $\lambda(r)$ from the characterization experiments. In this case, the results from the porosimetry will be used to obtain $\lambda(r)$ for pores

with radii of 32Å to 17600Å. The initial surface area will be matched by giving the 32-17600Å pores an appropriate roughness factor.

In order to obtain $\lambda(r)$, we must begin with the expression for void fraction of pores with radii greater than r. From (6.27), with $q = 0$,

$$\epsilon(r) = 1 - \exp[-2\pi \int_r^{r_{max}} \lambda(\acute{r})\acute{r}^2 d\acute{r}]. \tag{6.50}$$

By differentiating (6.50) with respect to r, we obtain

$$\frac{d\epsilon(r)}{dr} = -2\pi\lambda(r)r^2 \exp[-2\pi \int_r^{r_{max}} \lambda(\acute{r})\acute{r}^2 d\acute{r}]. \tag{6.51}$$

Substituting (6.50) and rearranging,

$$\lambda(r) = -\frac{d\epsilon(r)}{dr}[2\pi r^2(1 - \epsilon(r))]^{-1}. \tag{6.52}$$

So, given $\epsilon(r)$ as a function of r, $\lambda(r)$ is obtained. For the unburned lignite char, $\epsilon(r)$ is plotted as a function of r in Figure 6.27. A log-log plot of $\lambda(r)$ versus r is given in Figure 6.28. The data were fit with a straight line (solid line Figure 6.28) by the method of least squares. The slope and intercept of this line are -3.02270 and -1.8677, respectively. Interestingly, lignite chars partially oxidized at low temperature gave similar results.

A particularly simple form for $\lambda(r)$ results by rounding the slope to -3. The intercept was adjusted so that $\epsilon(r_{min})$ matched the experimental void fraction. The resulting intercept is -1.9246, and the dashed line in Figure 6.28 shows that the fit is quite good. Thus, the expression for $\lambda(r)$ is

$$\lambda(r) = 0.0118953r^{-3}. \tag{6.53}$$

In order to compare the predictions of this model with the experimental results of the partially oxidized char, we need a relationship between the local burnoff (q) and conversion ($x(q)$). Gavalas (1980) has shown that, neglecting the change of particle radius,

$$x(q) = 1 - \frac{1 - \epsilon(q)}{1 - \epsilon_0}, \tag{6.54}$$

where ϵ_0 is the initial porosity. Using (6.27), the conversion can be expressed as

$$x(q) = 1 - \exp[-2\pi(B_0 q^2 + 2B_1 q)], \tag{6.55}$$

where B_0 and B_1 are given by:

$$B_0 = \int_{r_{min}}^{r_{max}} \lambda(r) dr, \tag{6.56}$$

$$B_1 = \int_{r_{min}}^{r_{max}} \lambda(r) r dr. \tag{6.57}$$

From (6.53), B_0=922.6 μm^{-2} and B_1=3.7105 μm^{-1}. Ultimately, we wish to obtain surface area as a function of conversion. Combining (6.54), (6.56), (6.57) and (6.28), we find

$$S(q) = (1 - \epsilon_0)(1 - x(q))4\pi(B_0 q + B_1). \tag{6.58}$$

Solving (6.55) for q yields

$$q = \left(-\frac{1}{2\pi B_0} \ln(1 - x(q)) + \frac{B_1^2}{B_0^2}\right)^{1/2} - \frac{B_1}{B_0}. \tag{6.59}$$

Substituting (6.59) into (6.58), and dividing by $(1 - x(q))$,

$$\frac{S(x(q))}{1 - x(q)} = 4\pi(1 - \epsilon_0)\left(-\frac{B_0}{2\pi} \ln(1 - x(q)) + B_1^2\right)^{1/2}. \tag{6.60}$$

Finally, the predicted specific area is simply

$$S_g(x) = \frac{\varsigma S(x)}{(\rho_{p_0}(1-x))}, \tag{6.61}$$

where ρ_{p_0} is the initial particle density (1.1 gcm^{-3}) and ς is the roughness factor. At zero conversion, $S(0) = 4\pi B_0(1-\epsilon_0) = 29.1\mu\text{m}^{-1}$. Dividing by the particle density and converting to appropriate units, $S_g(0)$= 26.5 m^2/g. In order to match the experimental value of 385 m^2/g, a roughness factor of 14.53 is required.

The predicted specific surface area is compared to the measured area in Figure 6.29. Interestingly, the calculated specific surface area was nearly linear for this case. As a result, the fit is not very good, especially for conversions beyond 50%. Actually, the calculated surface area will monotonically increase for any values of B_0 and B_1. Thus, the model cannot adequately describe the low-temperature combustion behavior of this char.

REFERENCES

Field, M.A., Gill, D.W., Morgan, B.B., and Hawksley, P.G.W. (1967). it Combustion of Pulverized Coal, The British Coal Utilisation Research Association, Leatherhead, England, p. 315.

Gavalas, G.R. (1980). A Random Capillary Model with Application to Char Combustion at Chemically Controlled Rates. *AIChE J.*, **26**, 577.

Gavalas, G.R. (1981). Analysis of Char Combustion Including the Effect of Pore Enlargement. *Comb. Sci. Tech.*, **24**, 197.

Libby, P.A., and Blake, T.R. (1979). Theoretical Study of Burning Char Particles. *Comb. Flame*, **36**, 139.

Loewenberg, M., Bellan, J., and Gavalas, G.R. (1987). A Simplified Description of Char Combustion. *Chem. Eng. Comm.*, **58**, 89.

Mitchell, R.E., (1976). Experimentally Determined Overall Burning Rates of Coal Chars, *Combined Canadian and Western States Section Tech. Mtg. of the Combustion Institute*, Banff, Canada.

Mon, E.,and Amundson, N.R. (1978). Diffusion and Reaction in a Stagnant Boundary Layer About a Carbon Particle 2. An Extension. *Ind. Eng. Chem. Fund.*, **17**, 33.

Smith, I.W. and Tyler, R.J. (1974). The Reactivity of a Porous Brown Coal Char to Oxygen Between 630 and 1812K. *Comb. Sci. Tech.*, **9**, 87.

Smith, I.W. (1978). The Intrinsic Reactivity of Carbons to Oxygen. *Fuel*, **57**, 409.

Smith, I.W. (1982). The Combustion Rates of Coal Chars: A Review. *Nineteenth Symposium (International) on Combustion, the Combustion Institute*, 1045.

Sotirchos, S.V.,and Amundson, N.R. (1984). Dynamic Behavior of a Porous Char Particle Burning in an Oxygen-Containing Environment. 1. Constant Particle Radius. *AIChE J.*, **30**, 537.

Sotirchos, S.V.,and Amundson, N.R. (1984). Dynamic Behavior of a Porous Char Particle Burning in an Oxygen-Containing Environment. 2. Transient Analysis of a Shrinking Particle. *AIChE J.*, **30**, 549.

Sundaresan, S.,and Amundson, N.R. (1980). Diffusion and Reaction in a Stagnant Boundary Layer About a Carbon Particle 5. Pseudosteady State Structure and Parameter Sensitivity. *Ind. Eng. Chem. Fund.*, **19**, 344.

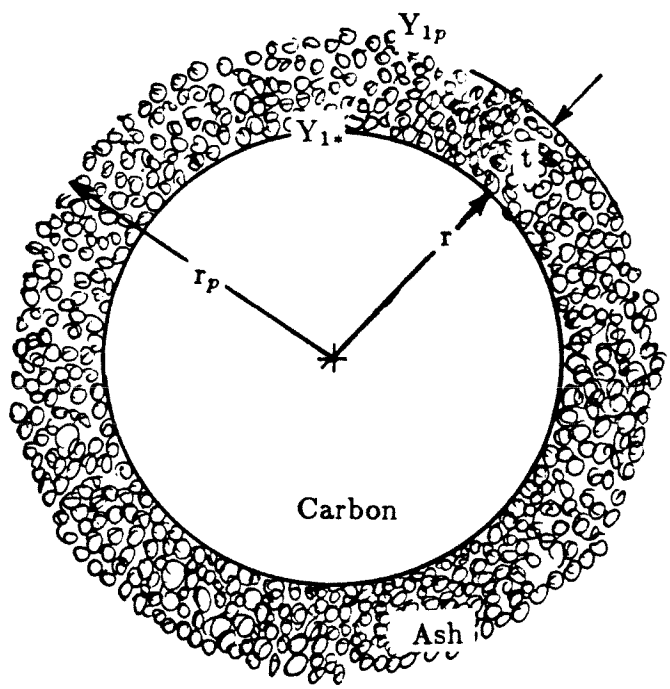

Figure 6.1. Schematic diagram of a single char particle with ash.

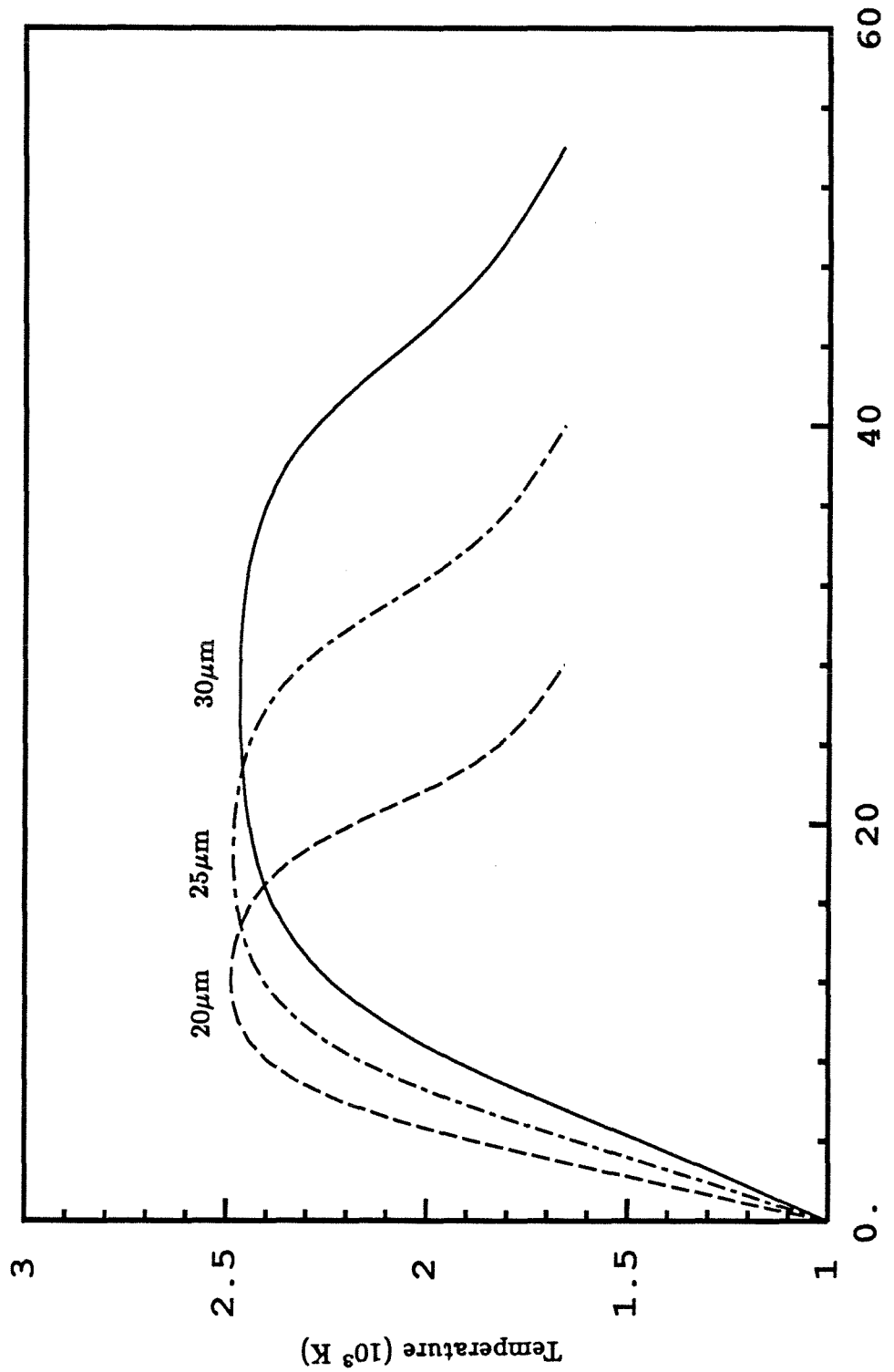

Figure 6.2. The effect of initial particle radius as predicted by the shrinking core model. ρ_c=1.5 gcm^{-3}, T_0=1000K, T_∞=1600K, $Y_{1\infty}$=0.22, A_a=46 gcm^{-2}s^{-1}, E_a=16800 cal gmol^{-1}, ϵ=0.4, v_{ash}=0.01, $\epsilon_p = \epsilon_\infty$=0.8.

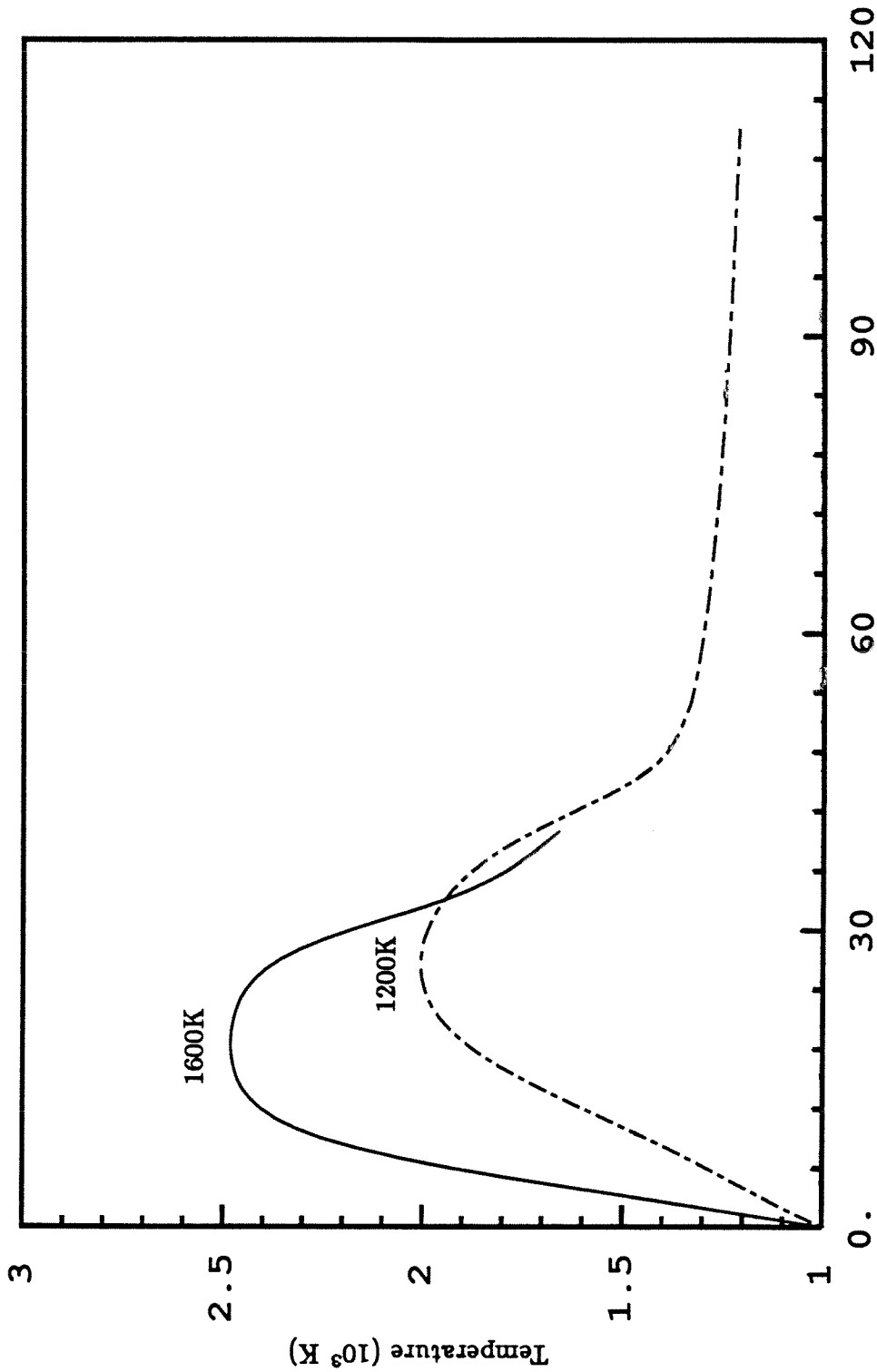

Figure 6.3. The effect of wall temperature as predicted by the shrinking core model. ρ_c=1.5 gcm^{-3}, T_0=1000K, r_{p0}=25 μm, $Y_{1\infty}$=0.22, A_a=46 gcm^{-2}s^{-1}, E_a=16800 cal gmol^{-1}, ϵ=0.4, v_{ash}=0.01, $\varepsilon_p = \varepsilon_\infty$=0.8.

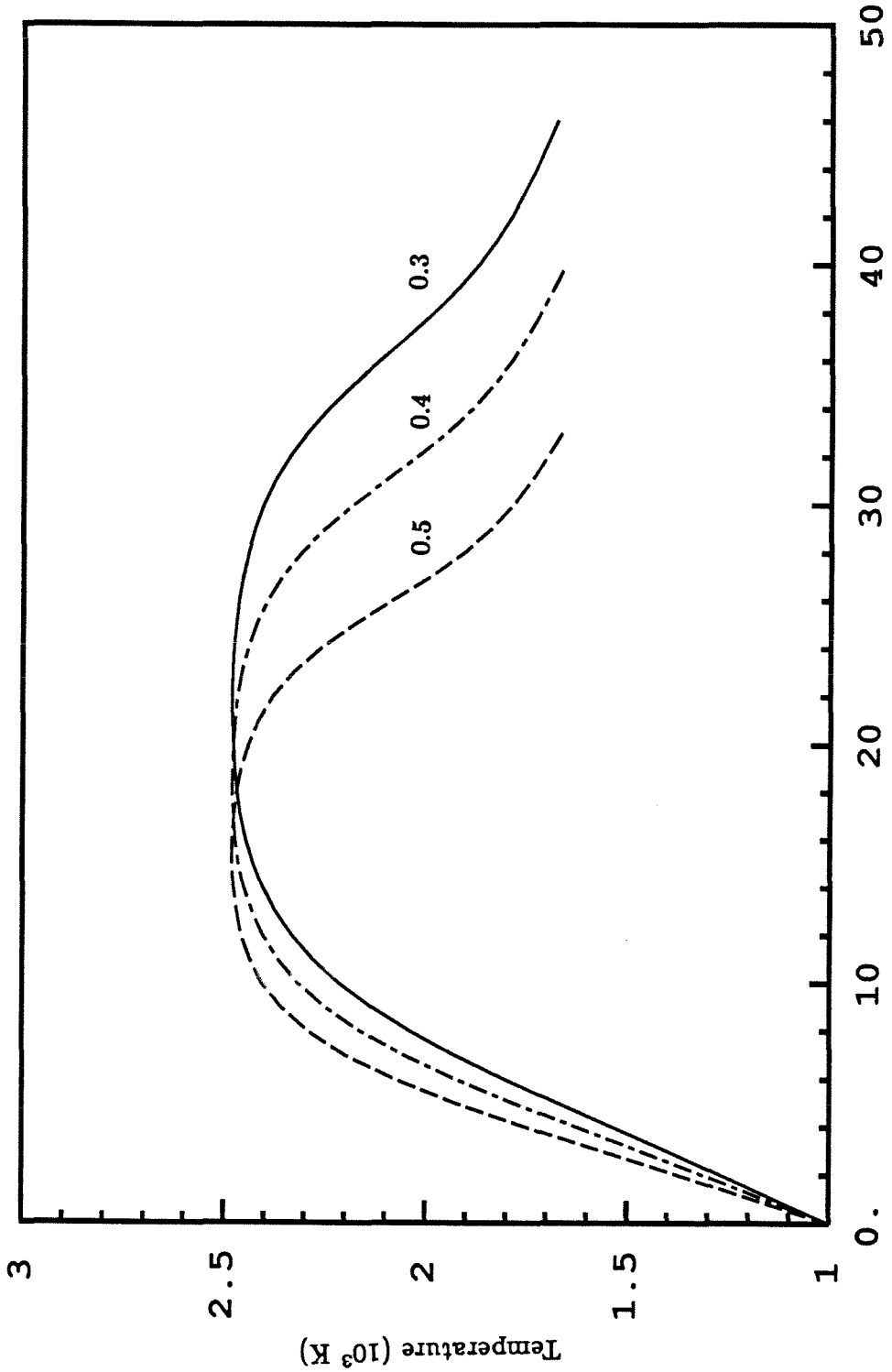

Figure 6.4. The effect of void fraction as predicted by the shrinking core model. ρ_c=1.5 gcm^{-3}, T_0=1000K, T_∞=1600K, r_{p_0}=25 μm, $Y_{1\infty}$=0.22, A_a=46 gcm^{-2}s^{-1}, E_a=16800 cal gmol^{-1}, v_{ash}=0.01, $\varepsilon_p = \varepsilon_\infty$=0.8.

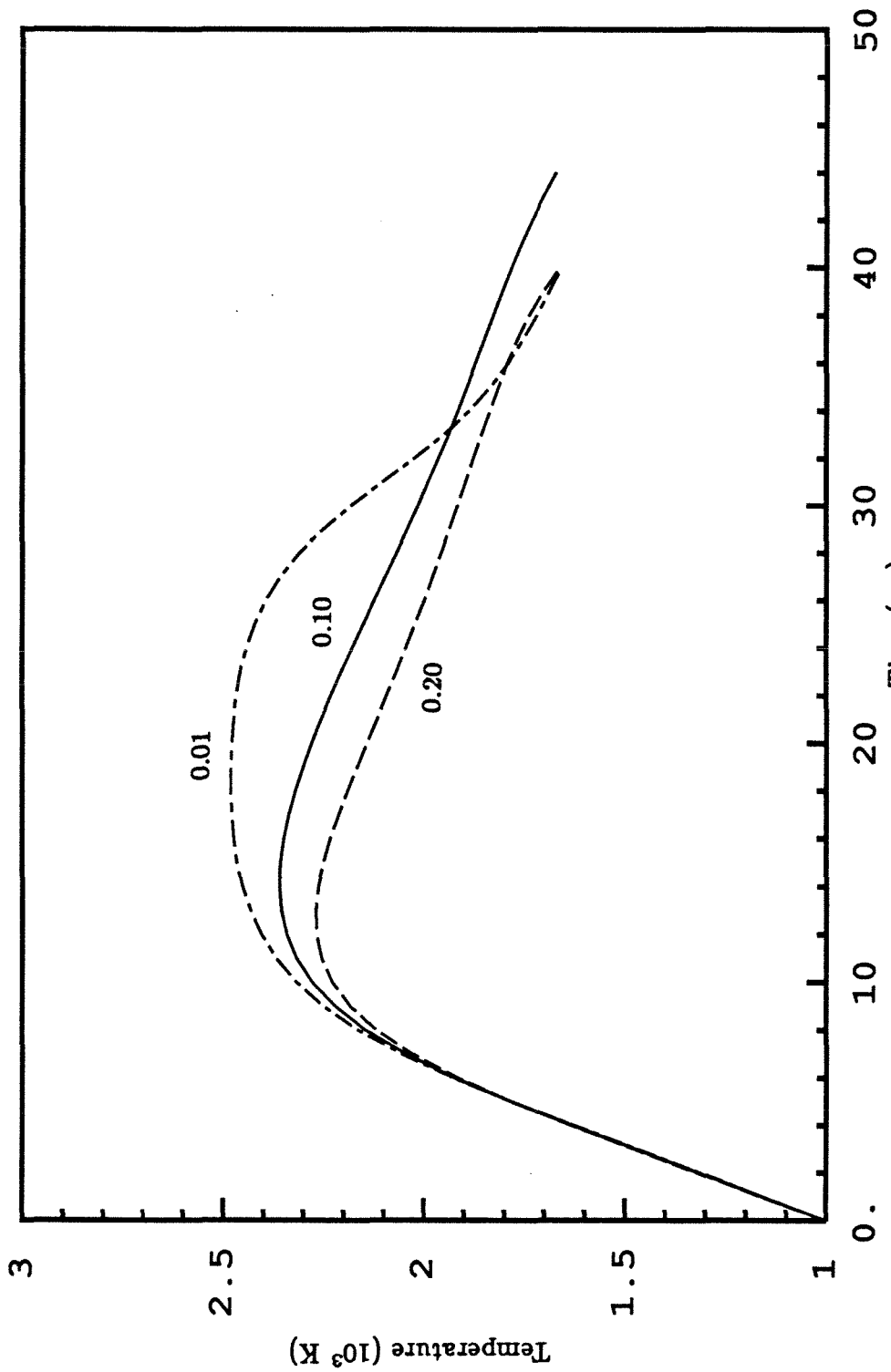

Figure 6.5. The effect of initial ash content as predicted by the shrinking core model. ρ_c=1.5 gcm^{-3}, T_0=1000K, T_∞=1600K, r_{p0}=25 μm, $Y_{1\infty}$=0.22, A_a=46 gcm^{-2}s^{-1}, E_a=16800 cal gmol^{-1}, ϵ=0.4, $\epsilon_p = \epsilon_\infty$=0.8.

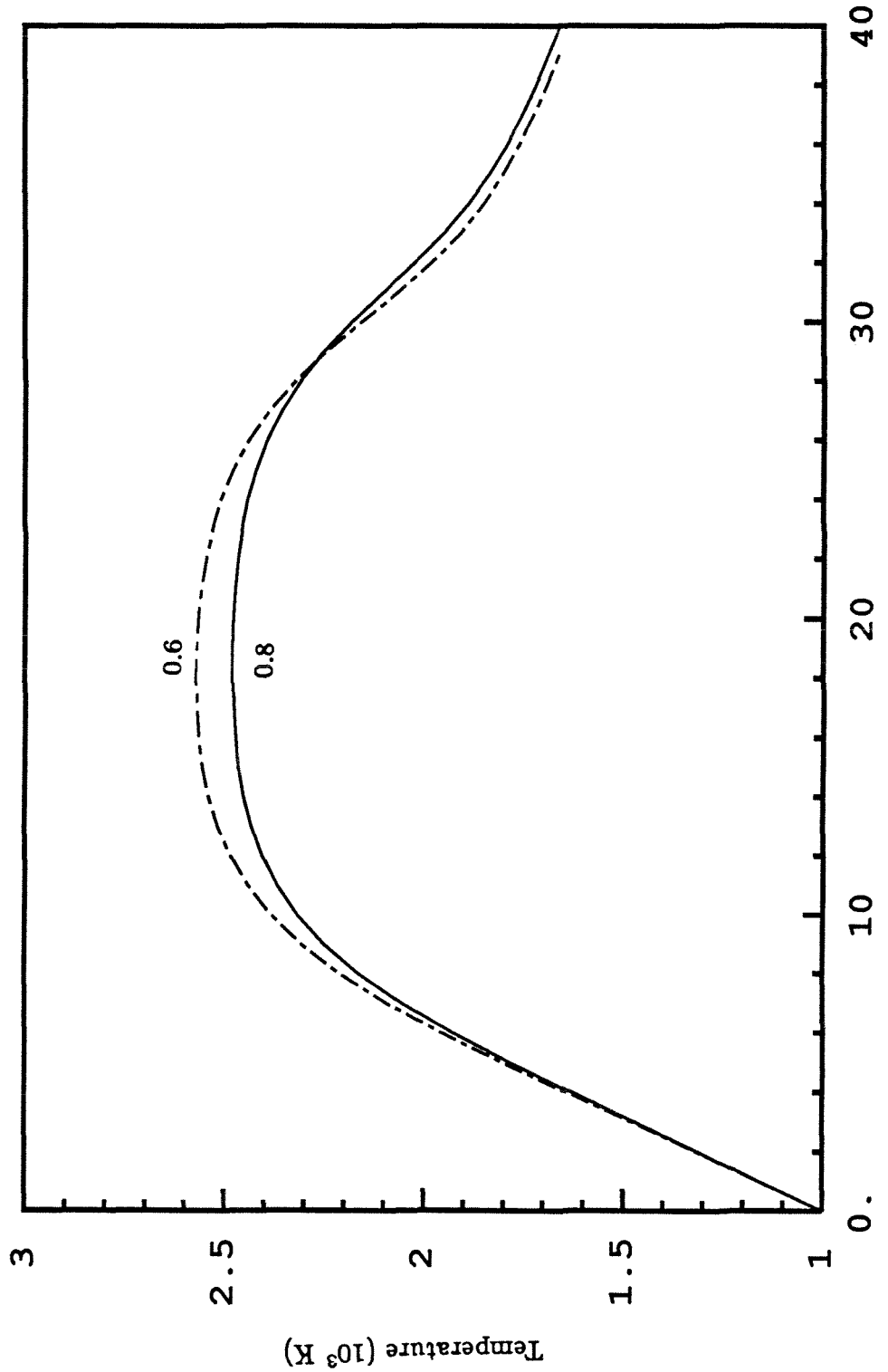

Figure 6.6. The effect of carbon emissivity as predicted by the shrinking core model. ρ_c=1.5 gcm^{-3}, T_0=1000K, T_∞=1600K, r_{p0}=25 μm, $Y_{1\infty}$=0.22, A_a=46 gcm^{-2}s^{-1}, E_a=16800 cal gmol^{-1}, ϵ=0.4, v_{ash}=0.01.

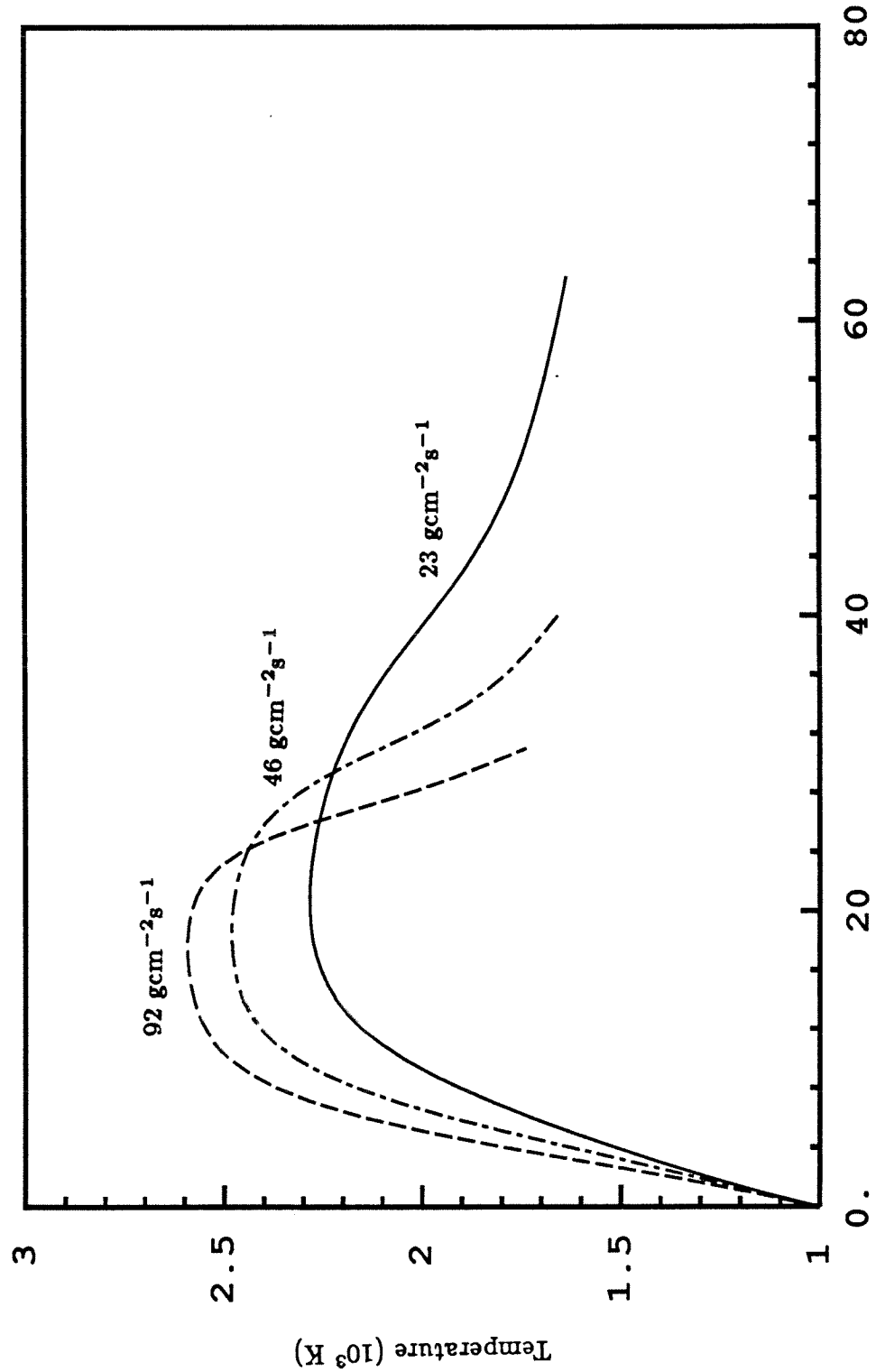

Figure 6.7. The effect of pre-exponential factor as predicted by the shrinking core model. ρ_c=1.5 gcm^{-3}, T_∞=1000K, T_0=1600K, r_{p0}=25 μm, $Y_{1\infty}$=0.22, E_a=16800 cal gmol^{-1}, ϵ=0.4, ν_{ash}=0.01, $\varepsilon_p = \varepsilon_\infty$=0.8.

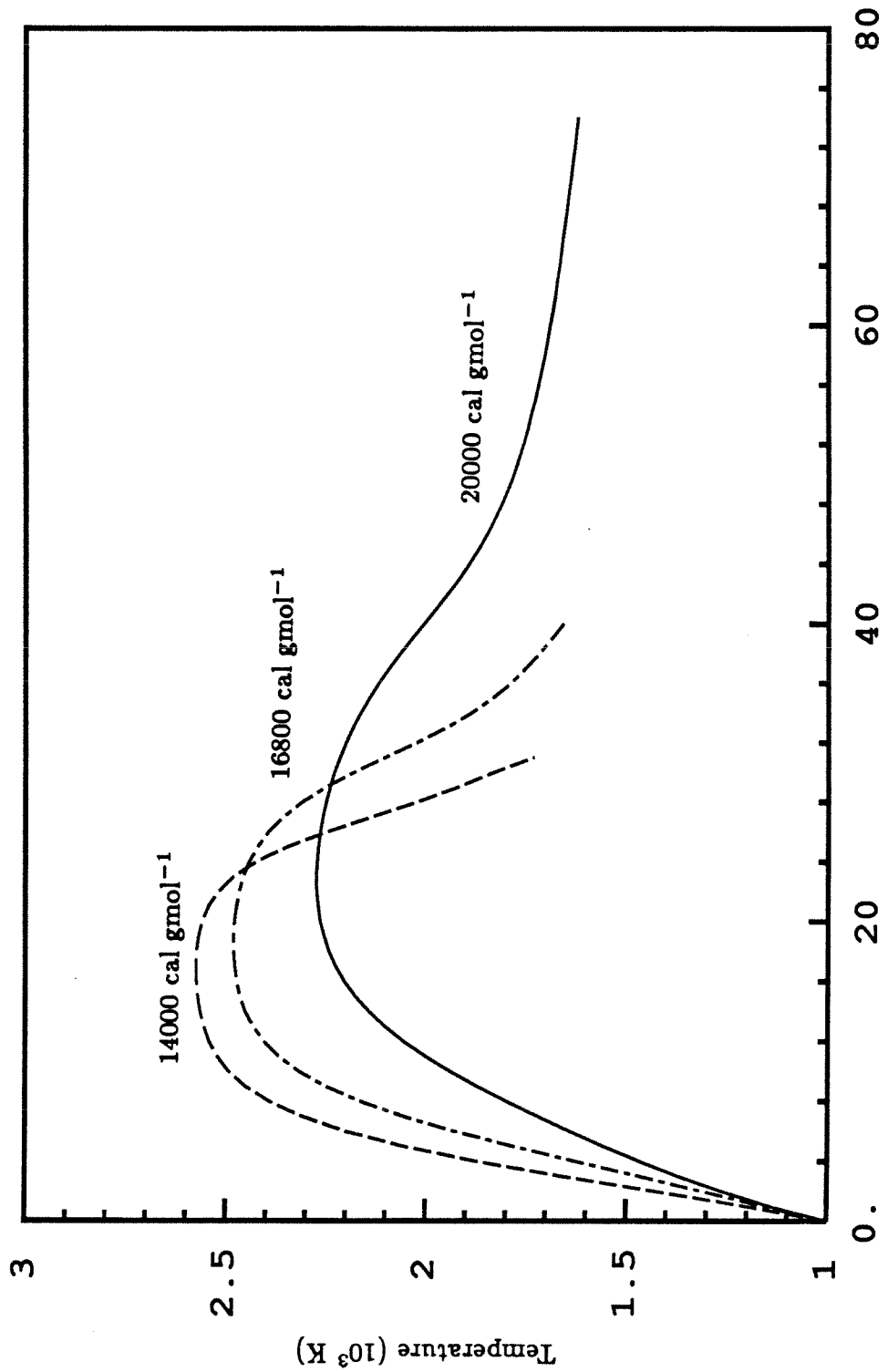

Figure 6.8. The effect of activation energy as predicted by the shrinking core model. ρ_c=1.5 gcm^{-3}, T_0=1000K, T_∞=1600K, r_{p0}=25 μm, $Y_{1\infty}$=0.22, A_a=46 gcm^{-2}s^{-1}, ϵ=0.4, v_{ash}=0.01, $\varepsilon_p = \varepsilon_\infty$=0.8.

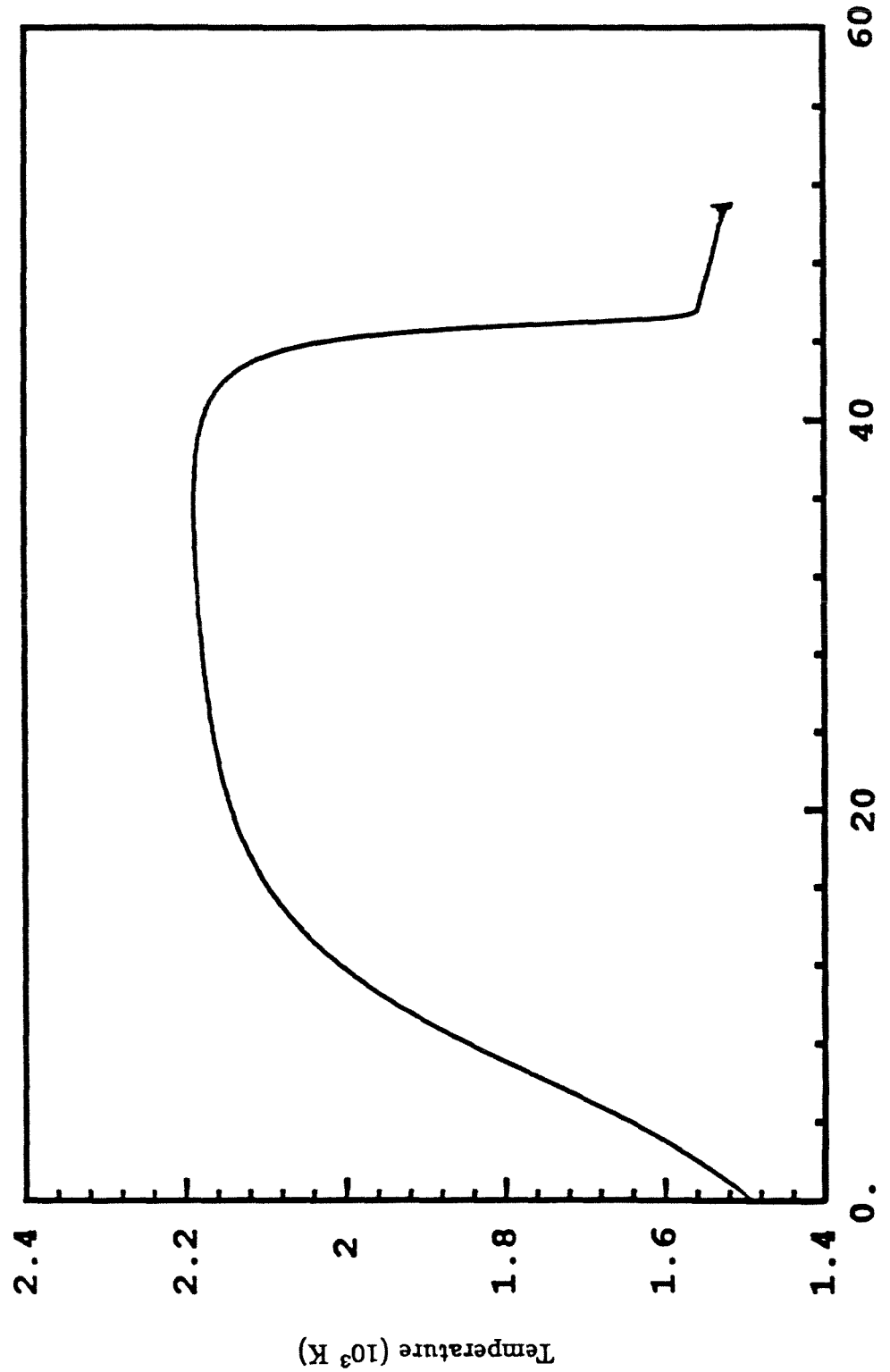

Figure 6.9. Particle temperature versus time as predicted by the monodisperse void model. ρ_c=2.0 gcm^{-3}, T_0=1500K, T_∞=1500K, r_{p0}=25 μm, $Y_{1\infty}$=0.22, A_{in}=305 gcm^{-2}s^{-1}, E_{in}=41000 cal gmol^{-1}, ϵ_0=0.1, a_0=0.05 μm, v_{ash}=0, $\epsilon_p = \epsilon_\infty$=0.8.

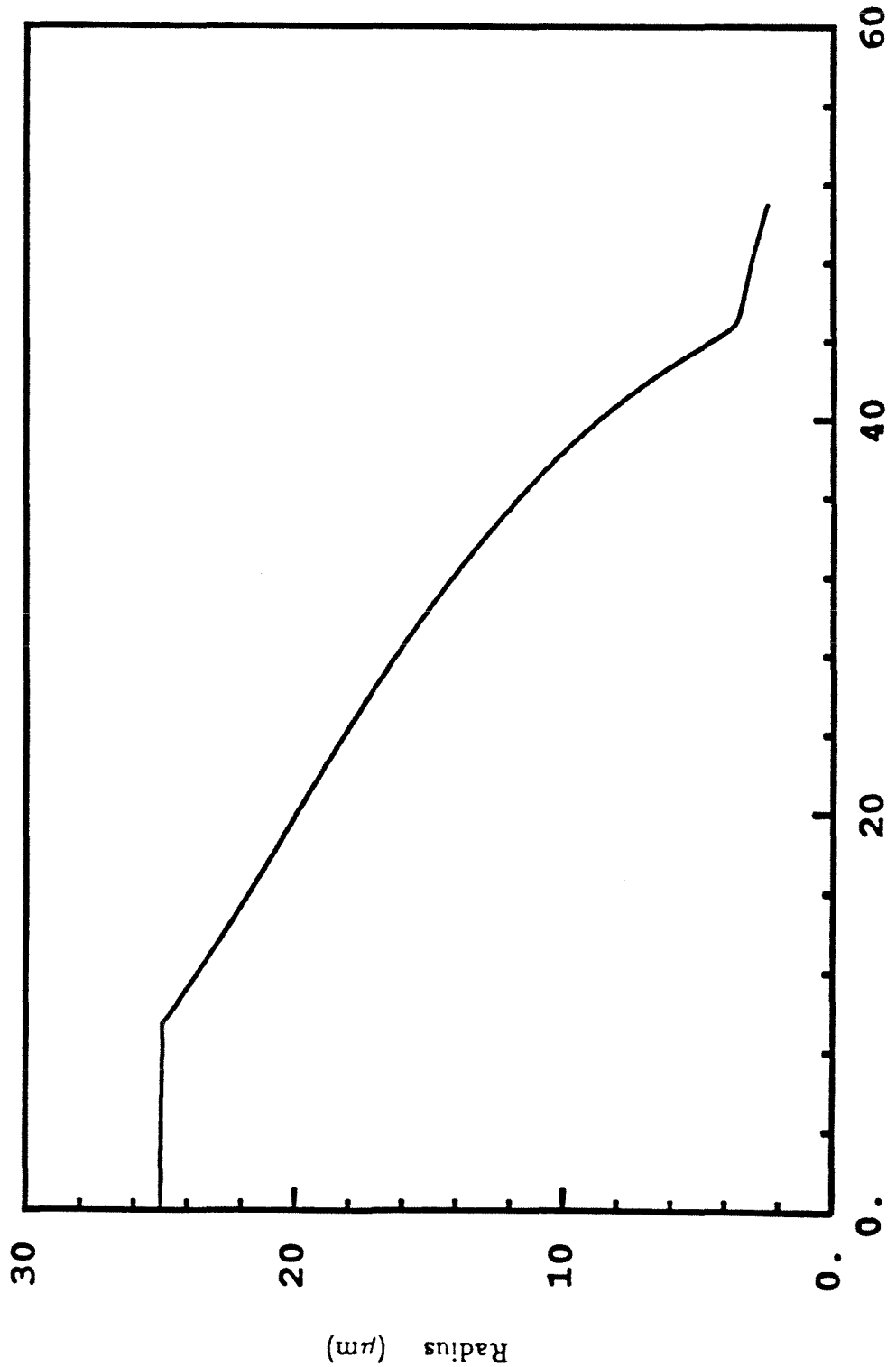

Figure 6.10. Particle radius versus time as predicted by the monodisperse void model. ρ_c=2.0 gcm^{-3}, T_0=1500K, T_∞=1500K, r_{p_0}=25 μm, $Y_{1\infty}$=0.22, A_{in}=305 gcm^{-2}s^{-1}, E_{in}=41000 cal gmol^{-1}, ϵ_0=0.1, a_0=0.05 μm, v_{ash}=0, $\varepsilon_p = \varepsilon_\infty$=0.8.

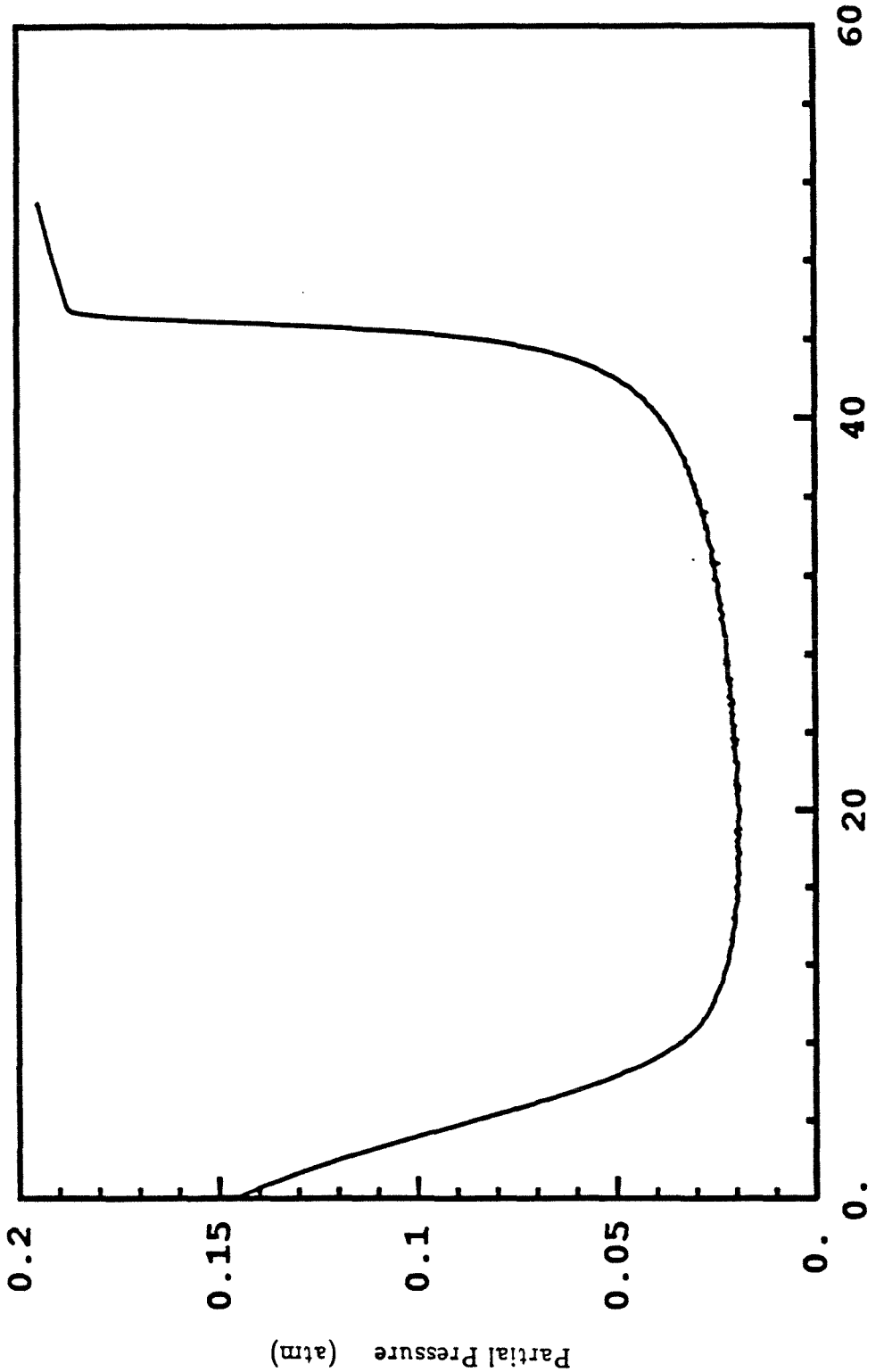

Figure 6.11. Oxygen partial pressure at the surface versus time as predicted by the monodisperse void model. ρ_c=2.0 gcm^{-3}, T_0=1500K, T_∞=1500K, r_{p0}=25 μm, $Y_{1\infty}$=0.22, A_{in}=305 gcm^{-2}s^{-1}, E_{in}=41000 cal gmol^{-1}, ϵ_0=0.1, a_0=0.05 μm, ν_{ash}=0, $\varepsilon_p = \varepsilon_\infty$=0.8.

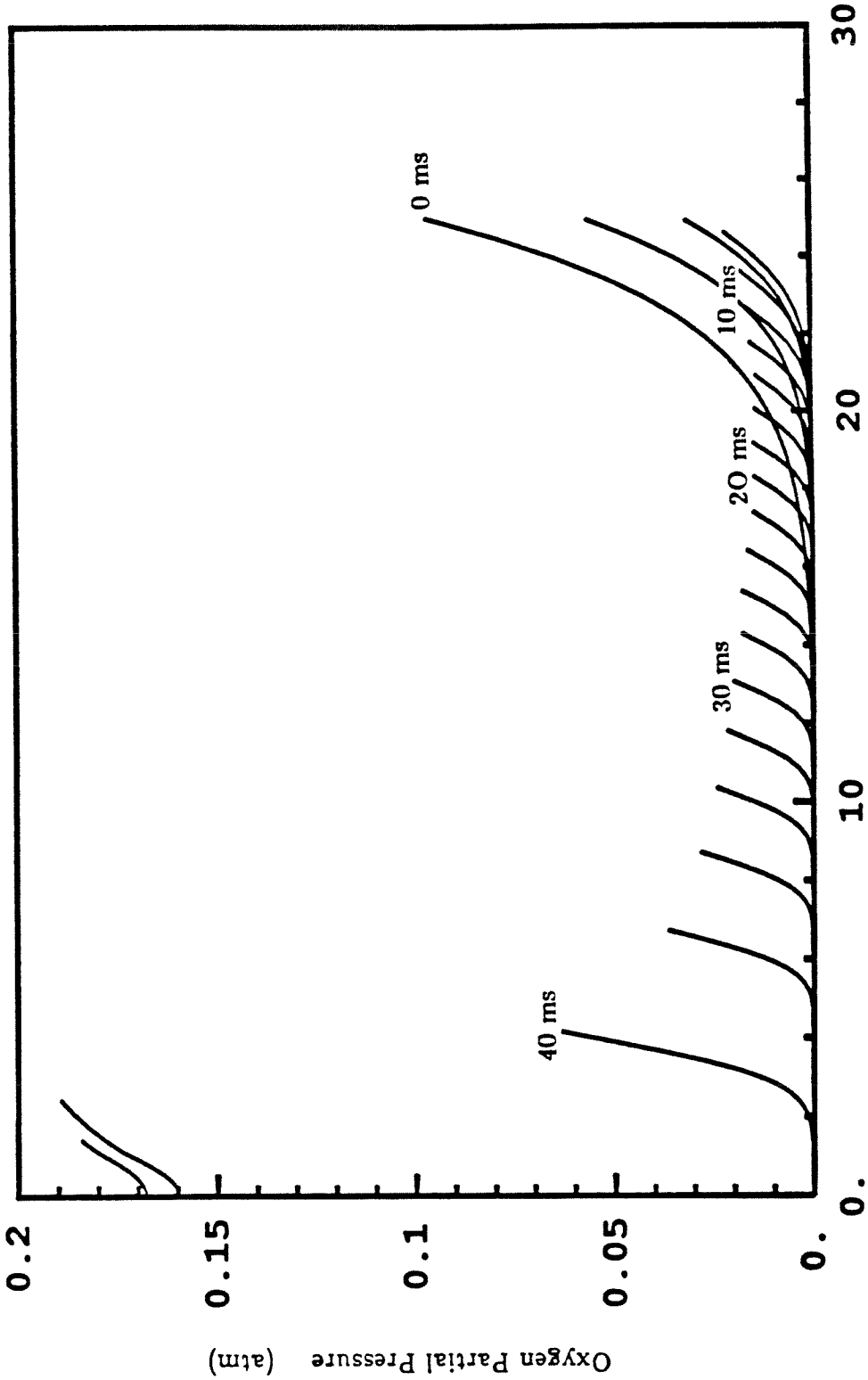

Figure 6.12. Oxygen partial pressure versus radius for various times (monodisperse void model). ρ_c=2.0 gcm^{-3}, T_0=1500K, T_∞=1500K, r_{p_0}=25 μm, $Y_{1\infty}$=0.22, A_{in}=305 gcm^{-2}s^{-1}, E_{in}=41000 cal gmol^{-1}, ϵ_0=0.1, a_0=0.05 μm, v_{ash}=0, $\varepsilon_p = \varepsilon_\infty$=0.8.

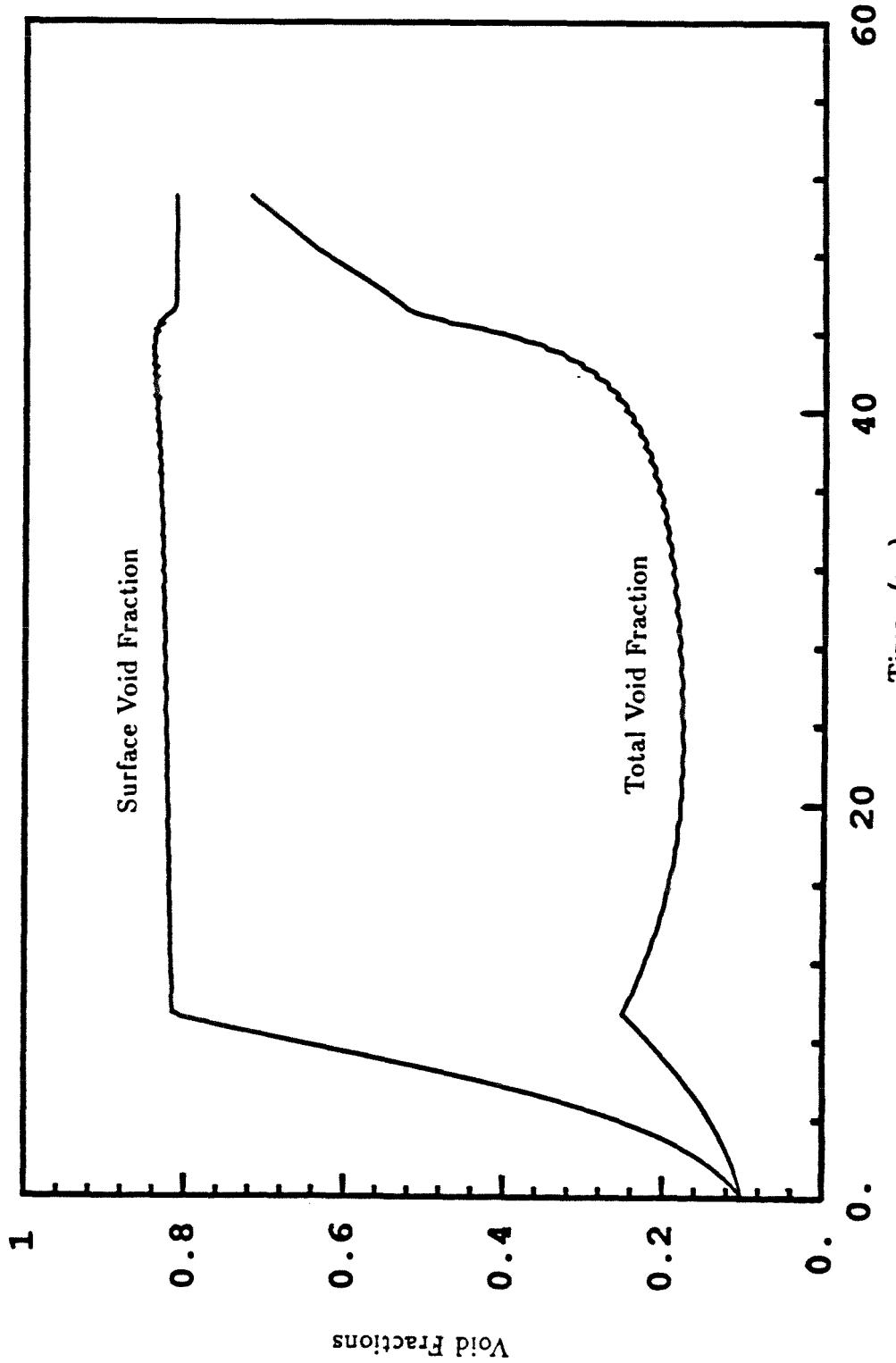

Figure 6.13. Surface void fraction and total void fraction versus time as predicted by the monodisperse void model. ρ_c=2.0 gcm^{-3}, T_0=1500K, T_∞=1500K, r_{p_0}=25 μm, $Y_{1\infty}$=0.22, A_{in}=305 gcm^{-2}s^{-1}, E_{in}=41000 cal gmol^{-1}, ϵ_0=0.1, a_0=0.05μm, v_{ash}=0, $\epsilon_p = \epsilon_\infty$=0.8.

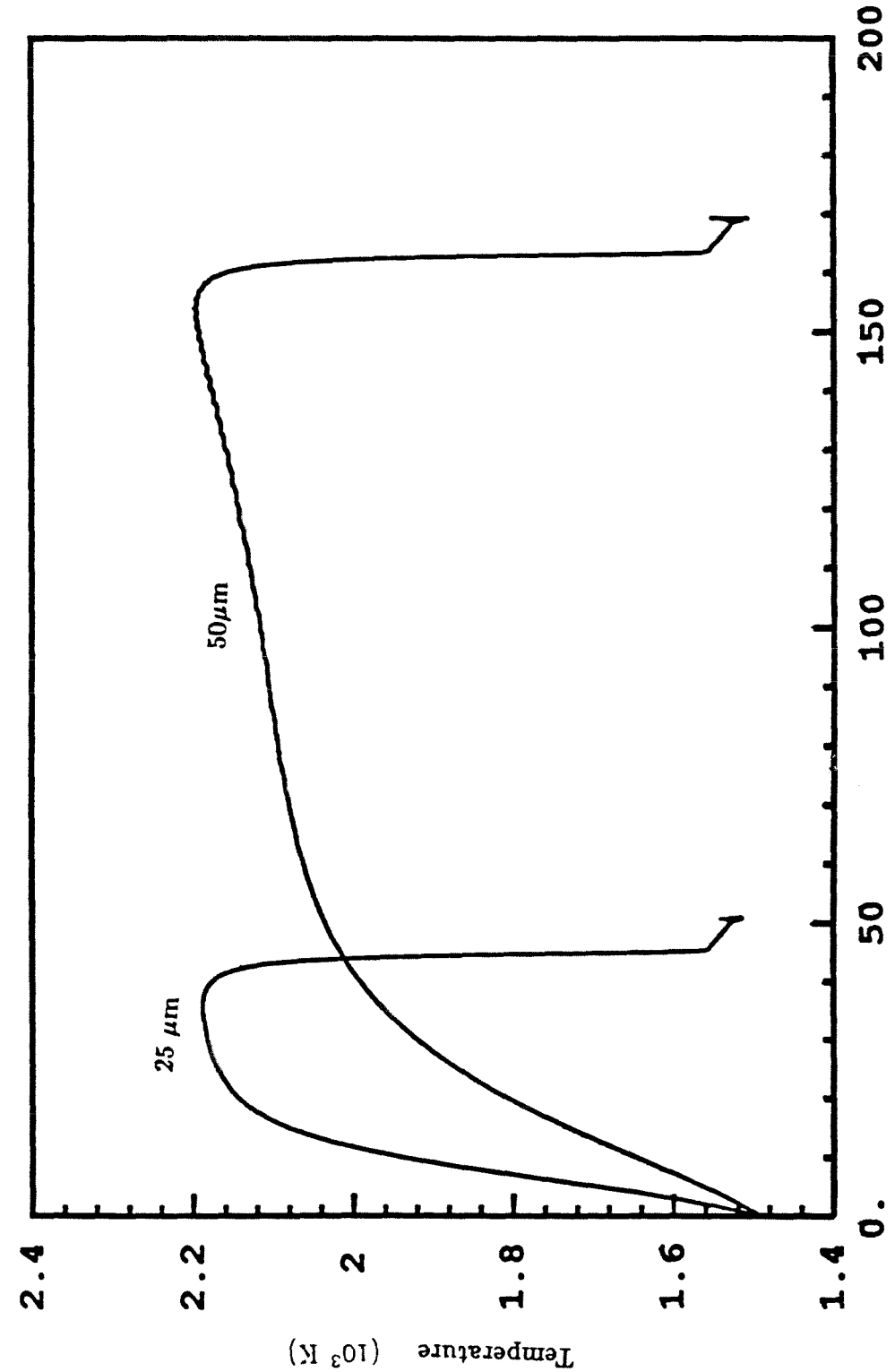

Figure 6.14. The effect of initial particle radius as predicted by the monodisperse void model. ρ_c=2.0 gcm^{-3}, T_0=1500K, T_∞=1500K, $Y_{1\infty}$=0.22, A_{in}=305 gcm^{-2}s^{-1}, E_{in}=41000 cal gmol^{-1}, ϵ_0=0.1, a_0=0.05 μm, v_{ash}=0, $\varepsilon_p = \varepsilon_\infty$=0.8.

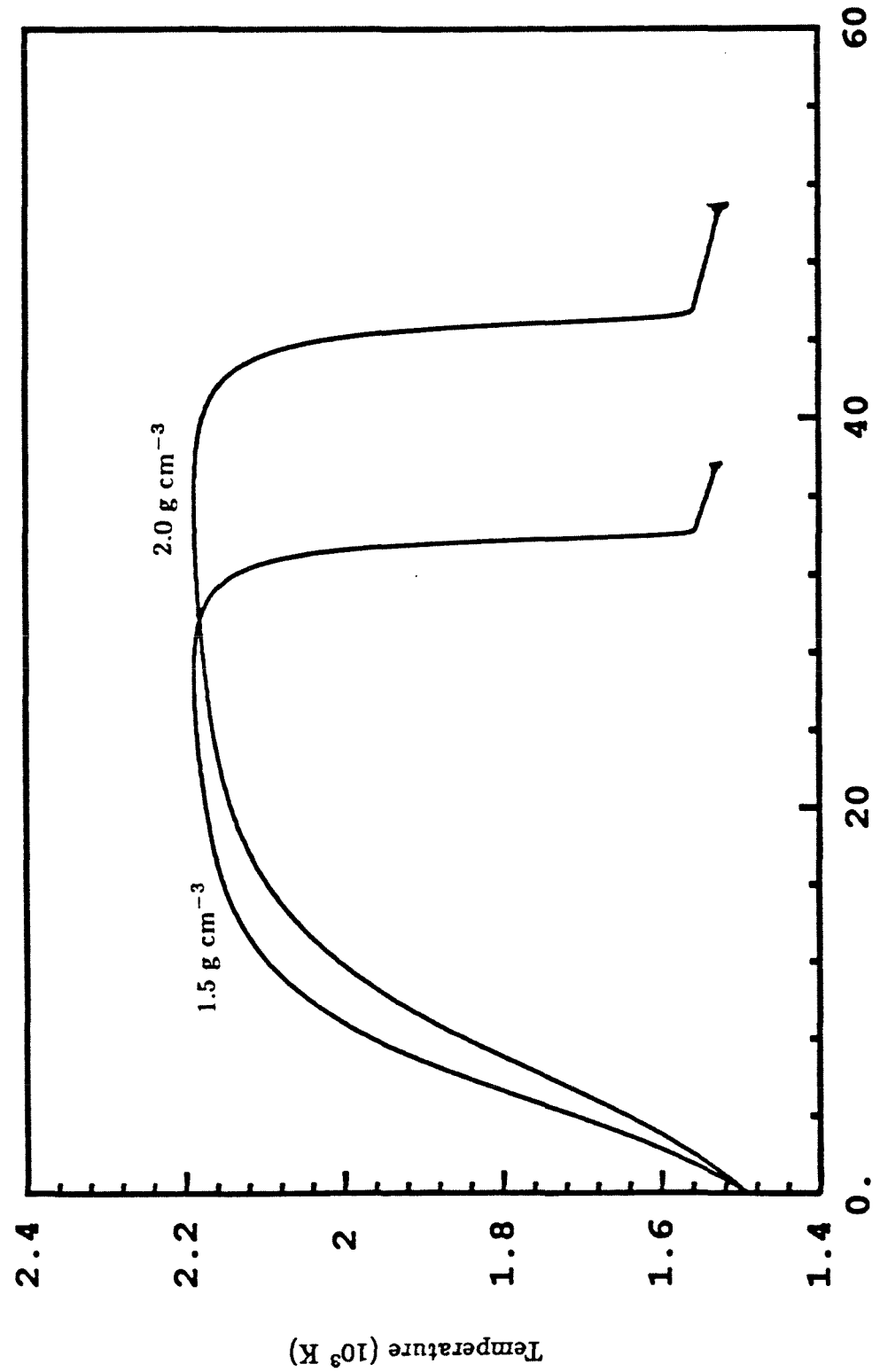

Figure 6.15. The effect of solid density as predicted by the monodisperse void model. T_0=1500K, T_∞=1500K, r_{p_0}=25 μm, $Y_{1\infty}$=0.22, A_{in}=305 gcm^{-2}s^{-1}, E_{in}=41000 cal gmol^{-1}, ϵ_0=0.1, a_0=0.05 μm, v_{ash}=0, $\epsilon_p = \epsilon_\infty$=0.8.

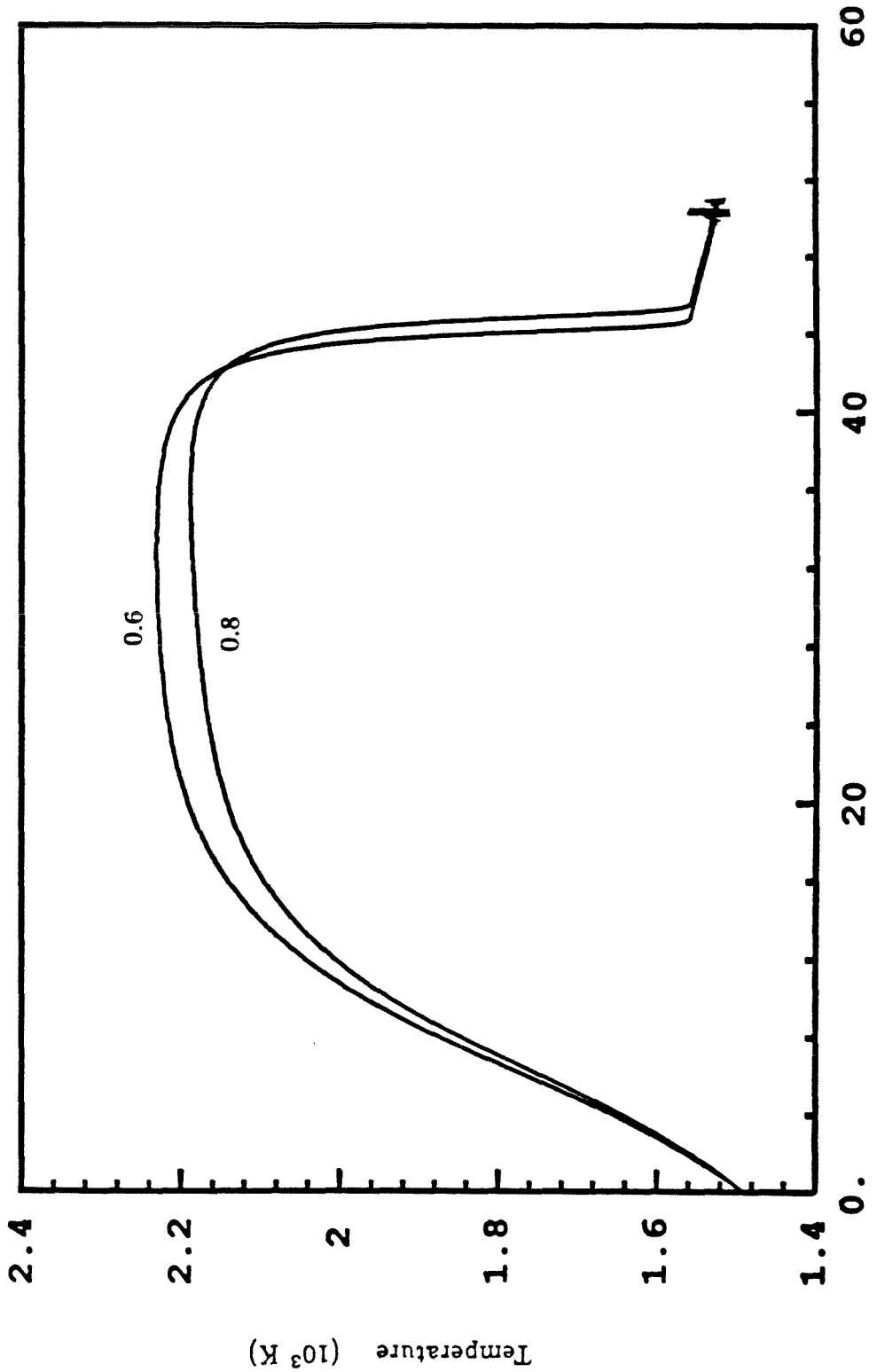

Figure 6.16. The effect of carbon emissivity as predicted by the monodisperse void model. ρ_c=2.0 gcm^{-3}, T_0=1500K, T_∞=1500K, r_{p0}=25 μm, $Y_{1\infty}$=0.22, A_{in}=305 gcm^{-2}s^{-1}, E_{in}=41000 cal gmol^{-1}, ϵ_0=0.1, a_0=0.05 μm, v_{ash}=0.

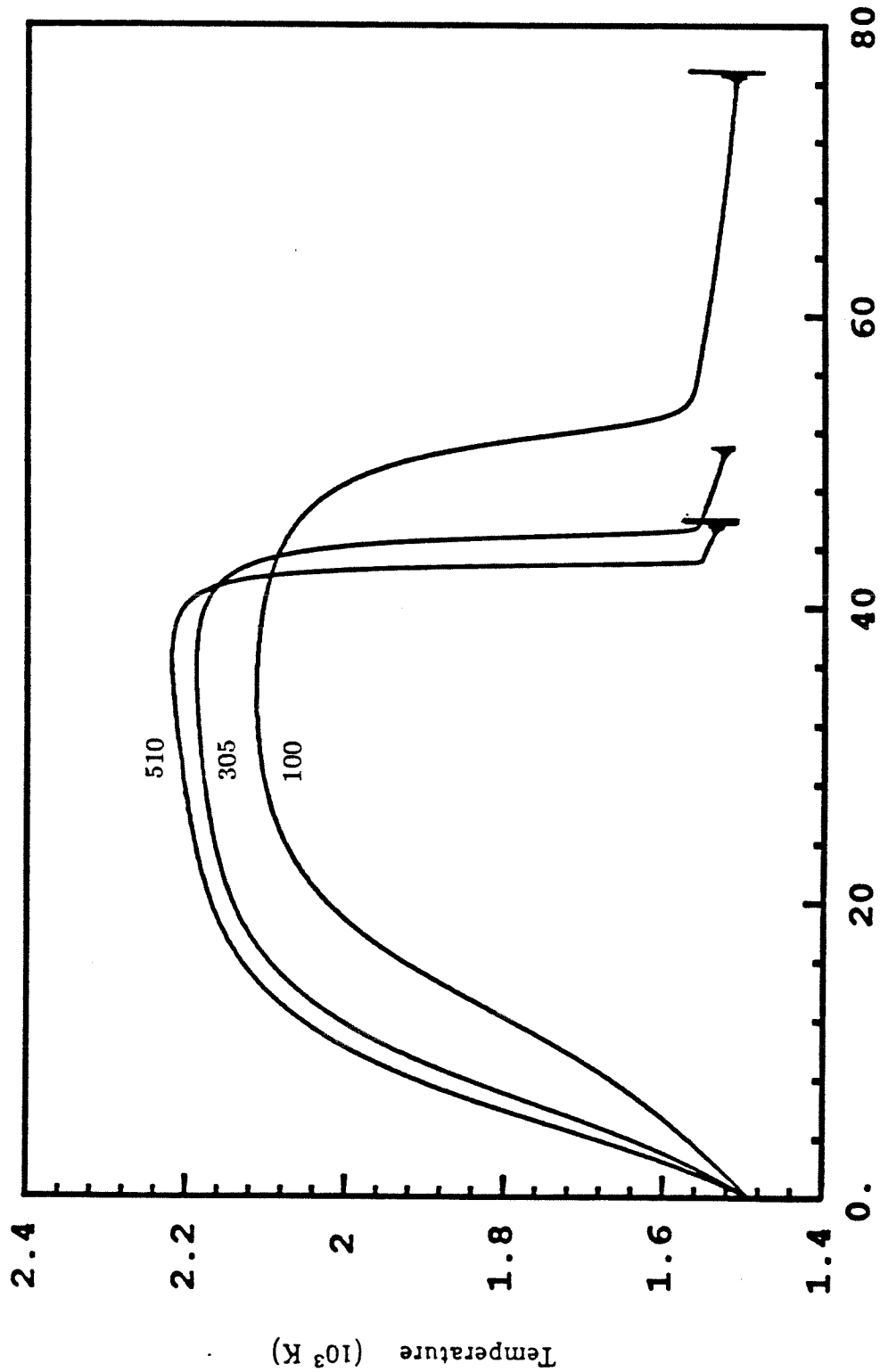

Figure 6.17. The effect of pre-exponential factor as predicted by the monodisperse void model. ρ_c=2.0 gcm^{-3}, T_0=1500K, T_∞=1500K, r_{p_0}=25 μm, $Y_{1\infty}$=0.22, E_{in}=41000 cal gmol^{-1}, ϵ_0=0.1, a_0=0.05 μm, v_{ash}=0, $\epsilon_p = \epsilon_\infty$=0.8.

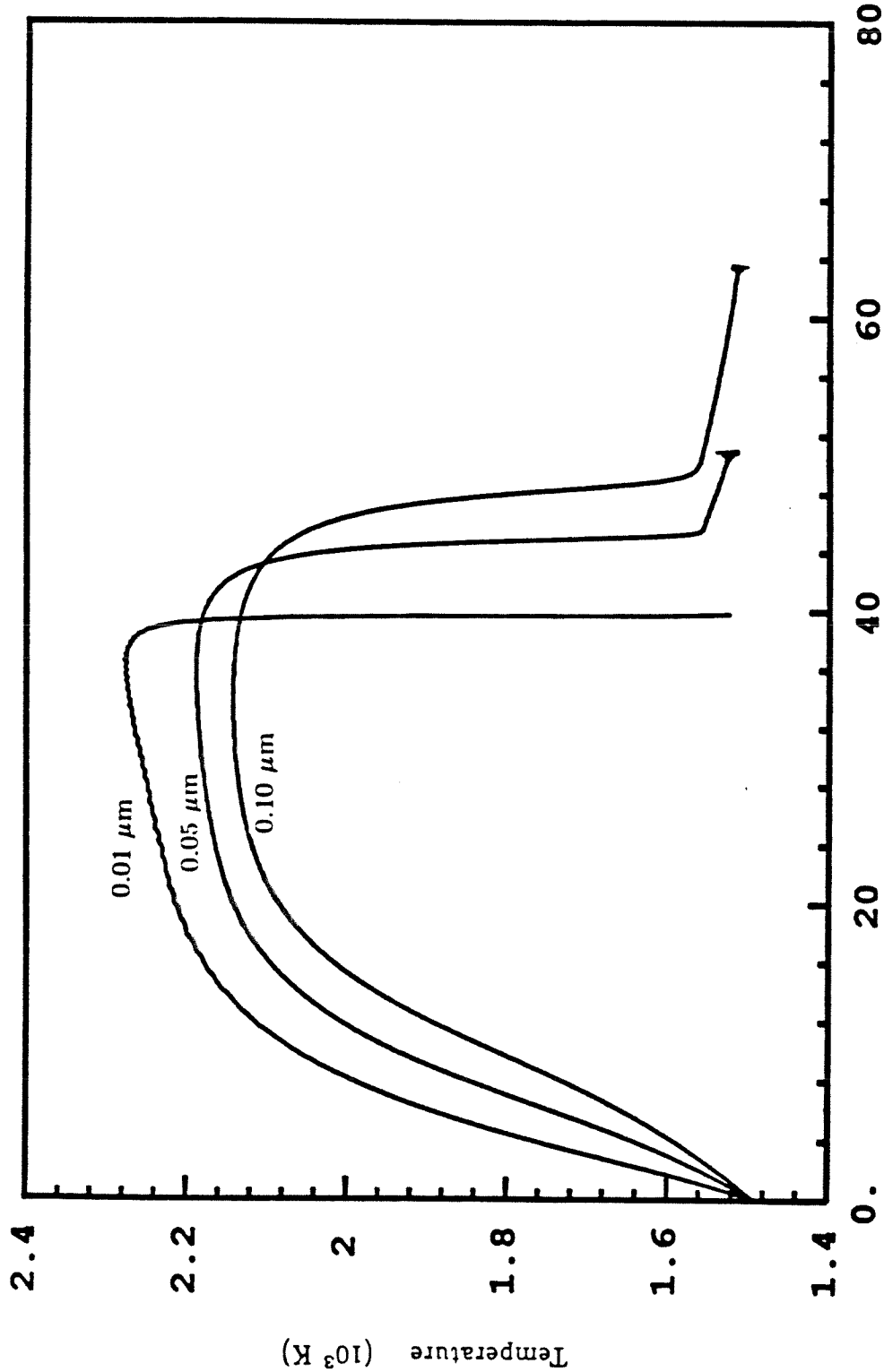

Figure 6.18. The effect of initial void size as predicted by the monodisperse void model. ρ_c=2.0 gcm^{-3}, T_0=1500K, T_∞=1500K, r_{p_0}=25 μm, Y_{1_∞}=0.22, A_{in}=305 gcm^{-2}s^{-1}, E_{in}=41000 cal gmol^{-1}, ϵ_0=0.1, v_{ash}=0, $\varepsilon_p = \varepsilon_\infty$=0.8.

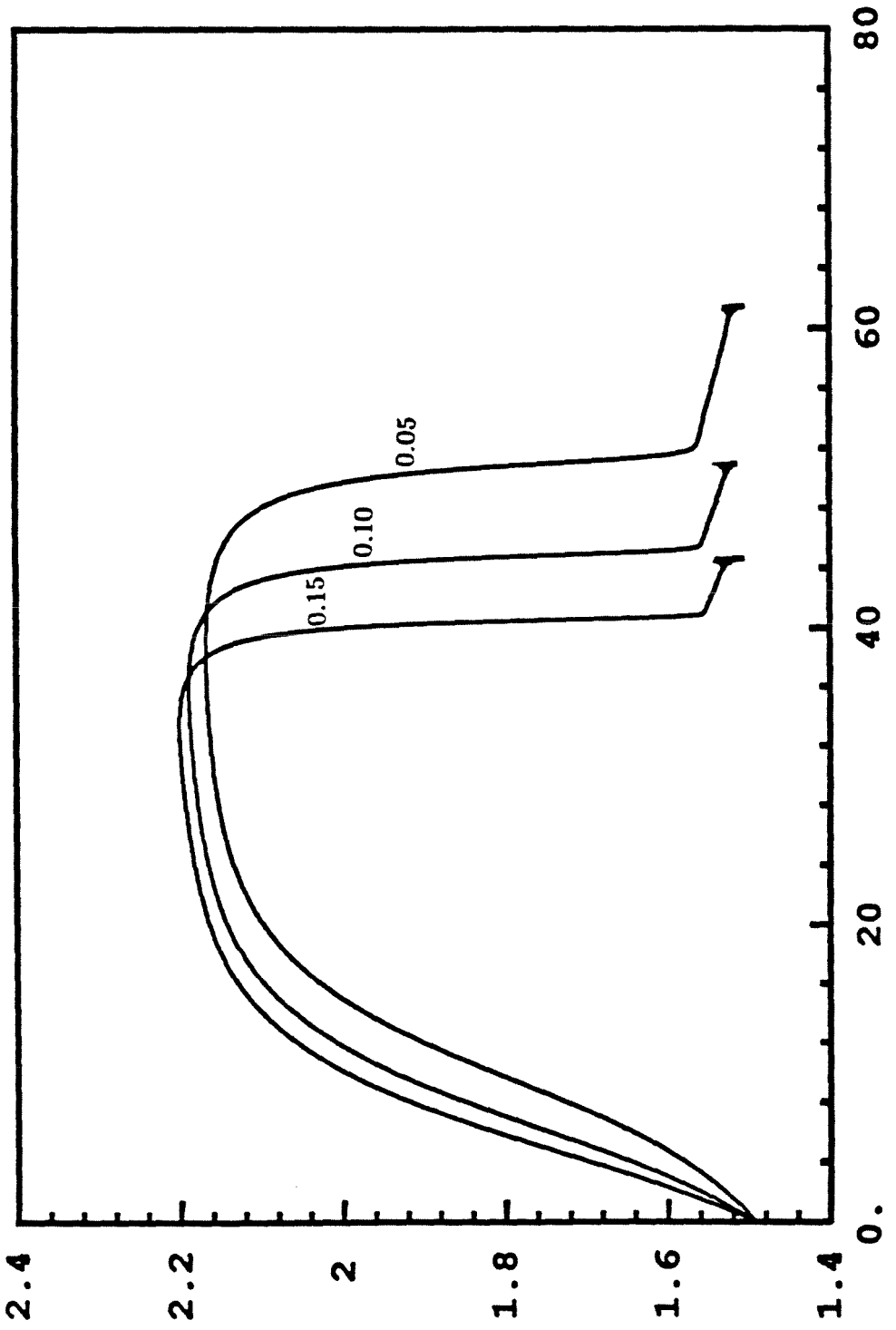

Figure 6.19. The effect of initial void fraction as predicted by the monodisperse void model. ρ_c=2.0 gcm^{-3}, T_0=1500K, T_∞=1500K, r_{p0}=25 μm, $Y_{1\infty}$=0.22, A_{in}=305 gcm^{-2}s^{-1}, E_{in}=41000 cal gmol^{-1}, a_0=0.05 μm, v_{ash}=0, $\epsilon_p = \epsilon_\infty$=0.8.

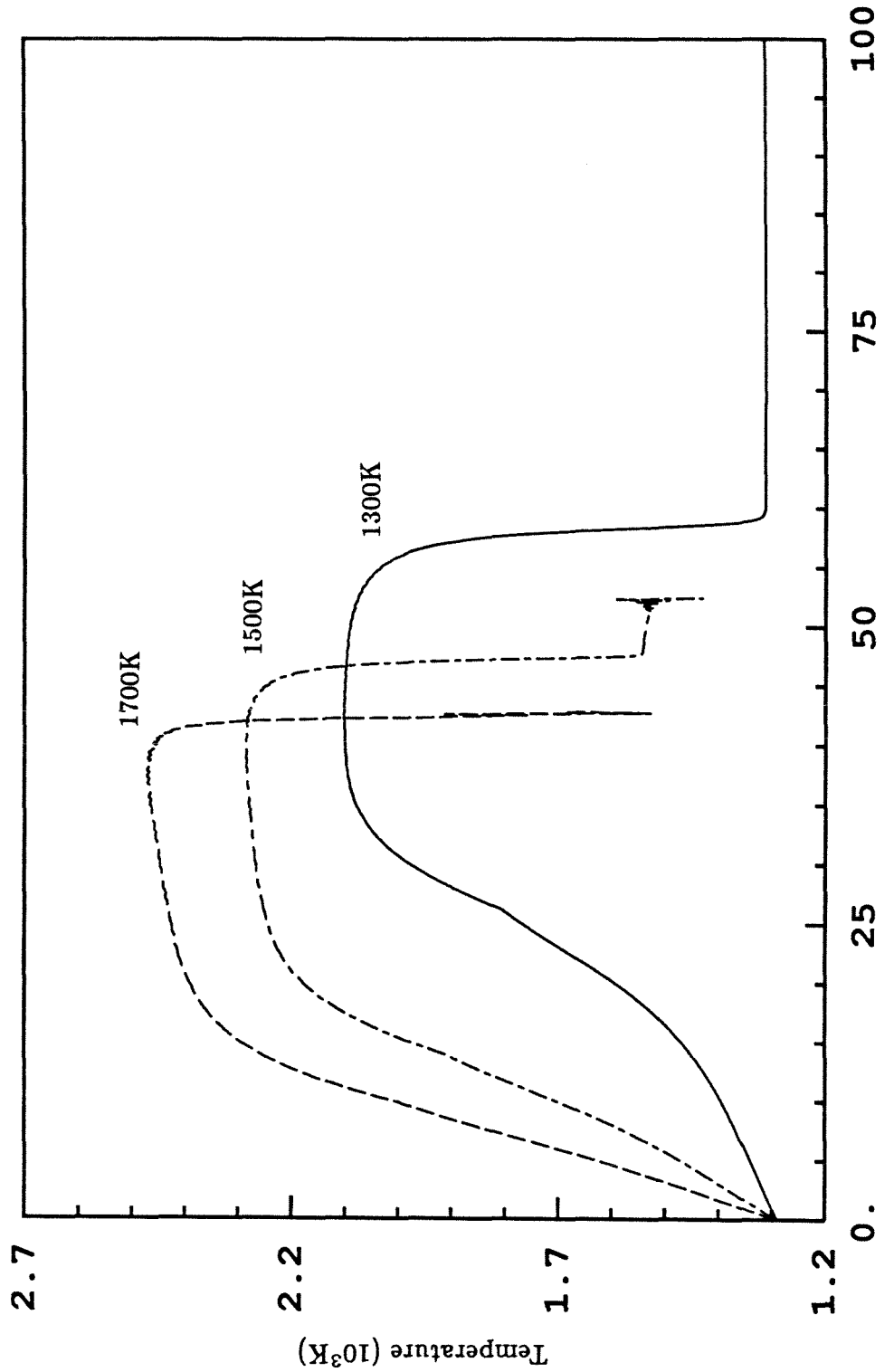

Figure 6.20. The effect of wall temperature as predicted by the monodisperse void model. ρ_c=2.0 gcm^{-3}, T_0=1500K, r_{p0}=25 μm, $Y_{1\infty}$=0.22, A_{in}=305 gcm^{-2}s^{-1}, E_{in}=41000 cal gmol^{-1}, ϵ_0=0.1, a_0=0.05 μm, v_{ash}=0, $\varepsilon_p = \varepsilon_\infty$=0.8.

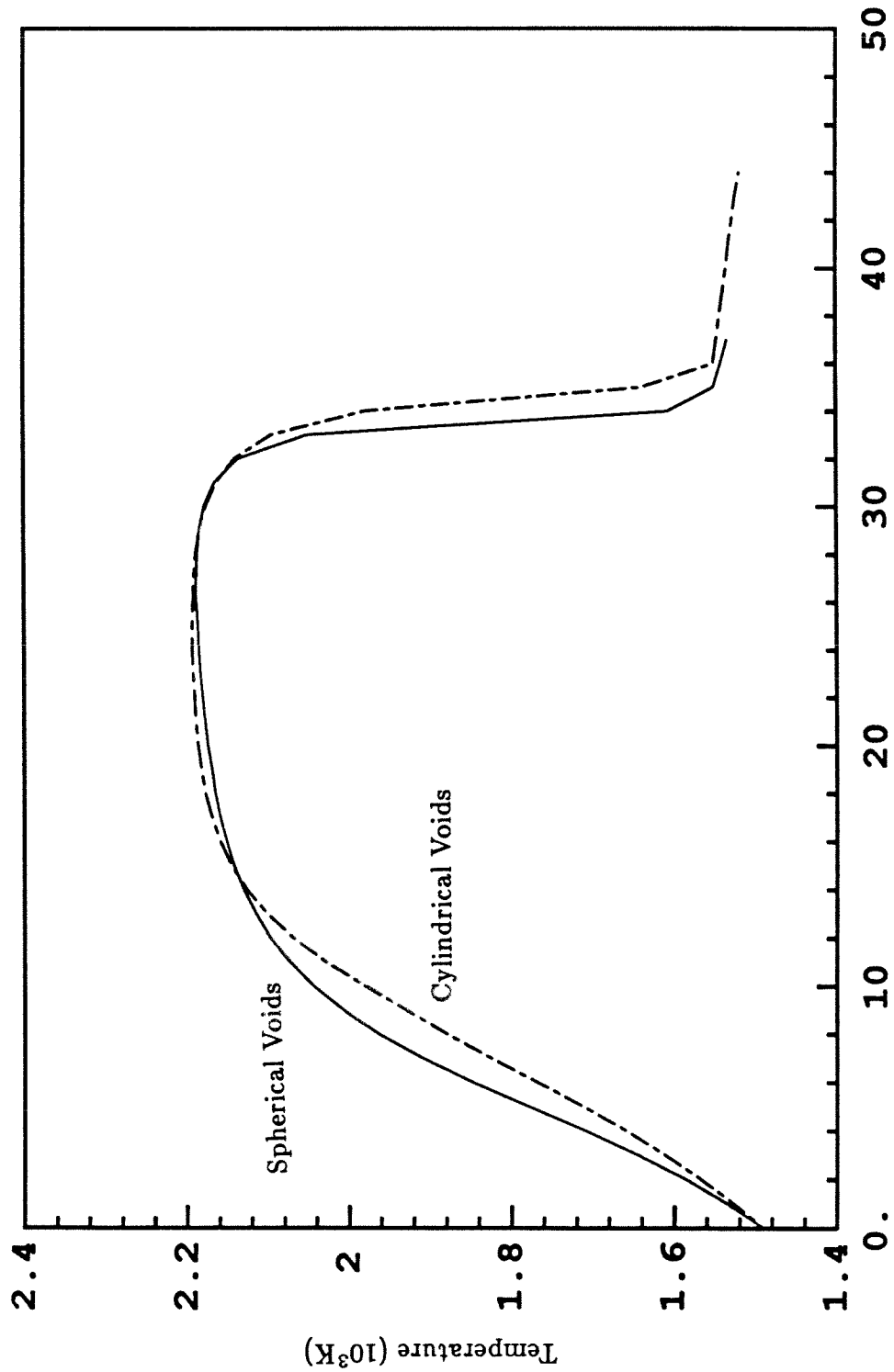

Figure 6.21. The effect of void type as predicted by the monodisperse void model. ρ_c=1.5 gcm^{-3}, T_0=1500K, T_∞=1500K, r_{p_0}=25 μm, $Y_{1\infty}$=0.22, A_{in}=305 gcm^{-2}s^{-1}, E_{in}=41000 cal gmol^{-1}, ϵ_0=0.1, a_0=0.05 μm, v_{ash}=0, $\varepsilon_p = \varepsilon_\infty$=0.8.

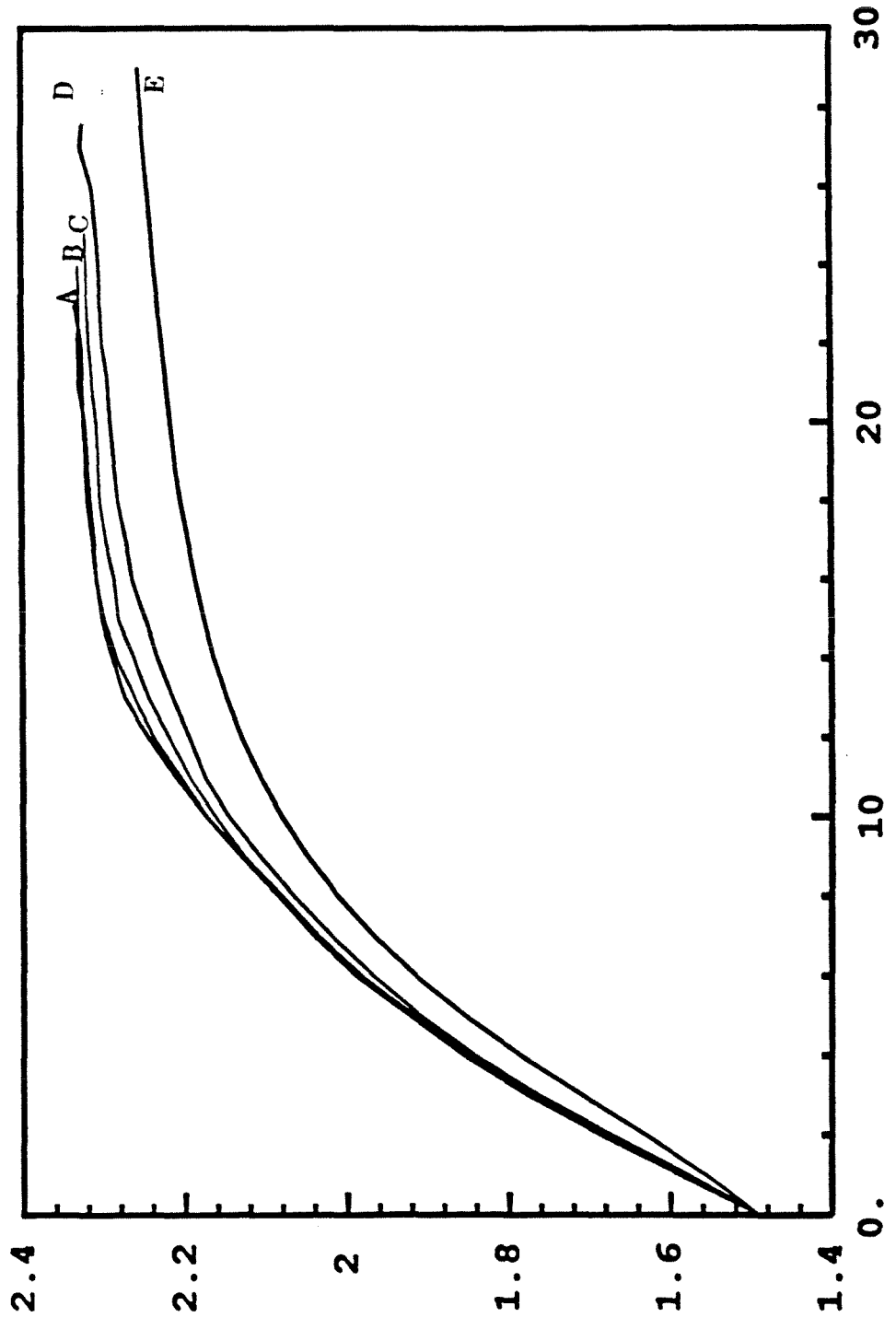

Figure 6.22. The effect of initial void fraction distribution as predicted by the polydisperse void model for the following sets of ϵ_1, ϵ_2, and ϵ_3 - A:0.05,0.09,0.03; B:0.10,0.04,0.03; C:0.10,0.05,0.02;D:0.10,0.06,0.01;E:0.10,0.07,0.00. ρ_c=1.5 gcm^{-3}, T_0=1500K, T_∞=1500K, r_{p_0}=25 μm, $Y_{1\infty}$=0.22, A_{in}=305 gcm^{-2}s^{-1}, E_{in}=41000 cal gmol^{-1}, v_{ash}=0, $\epsilon_p = \epsilon_\infty$=0.8.

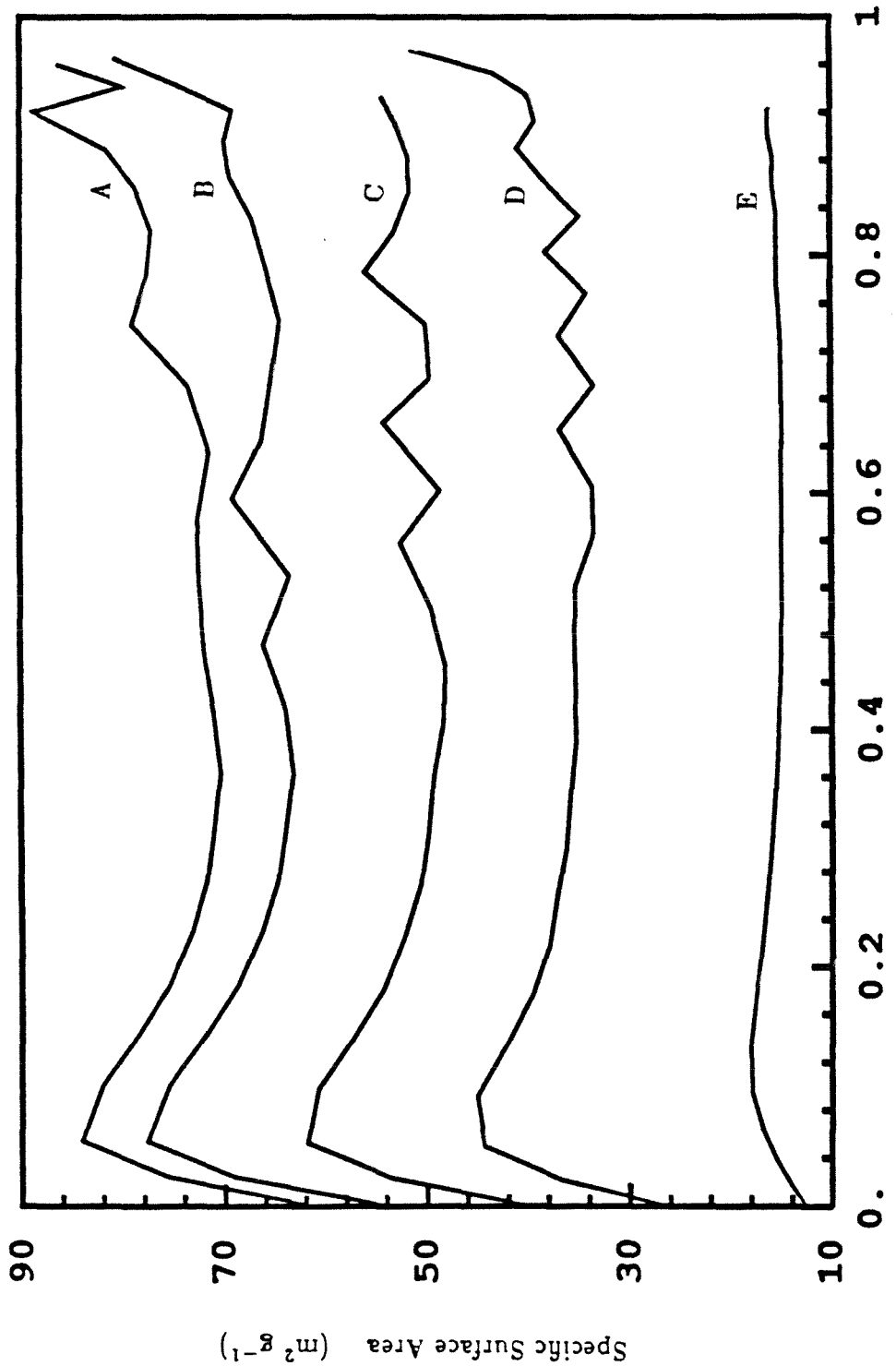

Figure 6.23. Specific surface area versus conversion as predicted by the polydisperse void model for the following sets of ϵ_1, ϵ_2, and ϵ_3 – A:0.05,0.09,0.03; B:0.10,0.04,0.03; C:0.10,0.05,0.02;D:0.10,0.06,0.01;E:0.10,0.07,0.00. ρ_c=1.5 gcm^{-3}, T_0=1500K, T_∞=1500K, r_{p0}=25 μm, $Y_{1\infty}$=0.22, A_{in}=305 $gcm^{-2}s^{-1}$, E_{in}=41000 cal $gmol^{-1}$, v_{ash}=0, $\epsilon_p = \epsilon_\infty$=0.8.

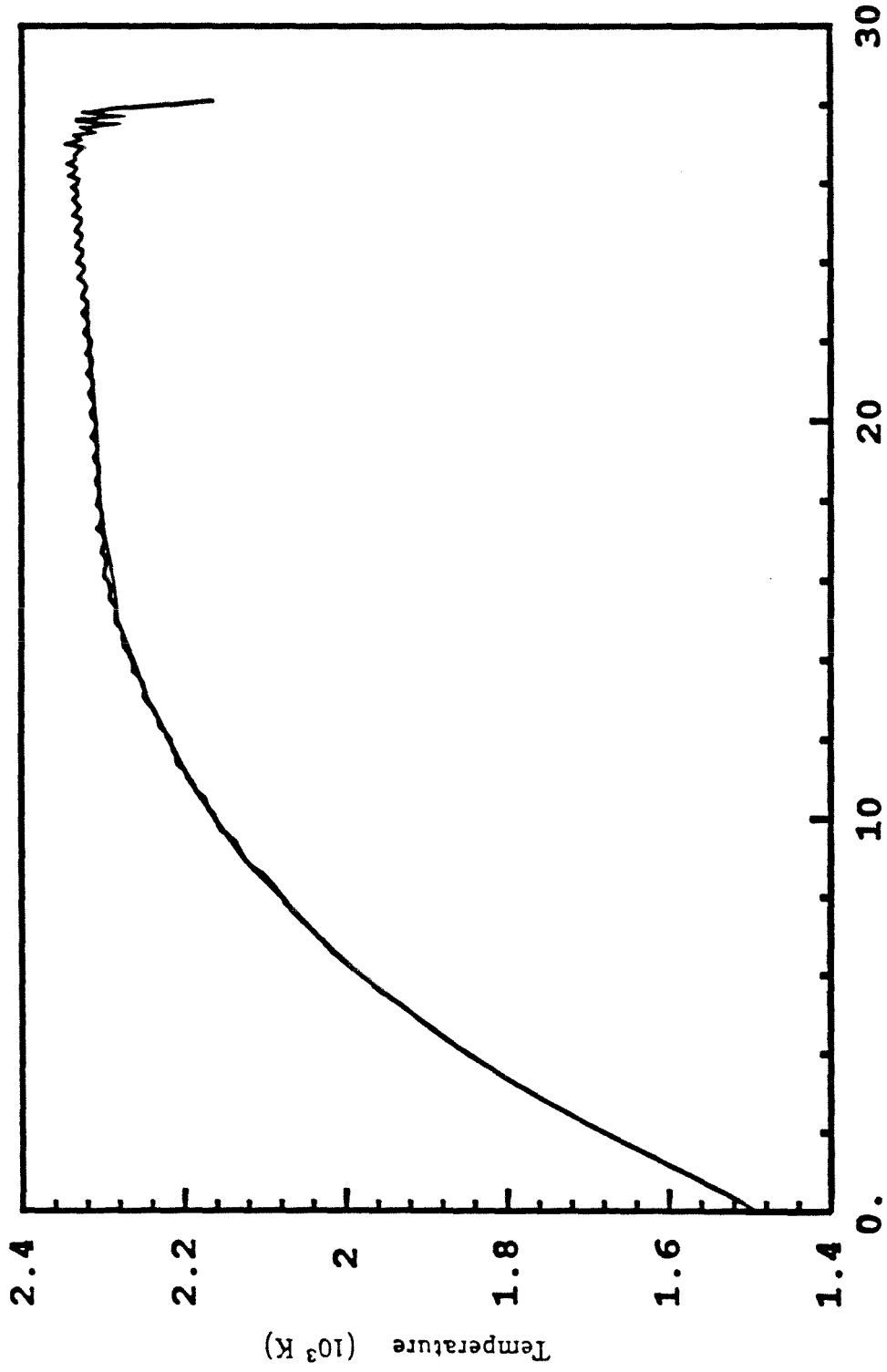

Figure 6.24. Comparison of the Langmuir-Hinschelwood model to the linear kinetic model. (Polydisperse case A). ρ_c=1.5 gcm^{-3}, T_0=1500K, T_∞=1500K, r_{p_0}=25 μm, $Y_{1\infty}$=0.22, A_{in}=305 gcm^{-2}s^{-1}, E_{in}=41000 cal gmol^{-1}, v_{ash}=0, $\epsilon_p = \epsilon_\infty$=0.8.

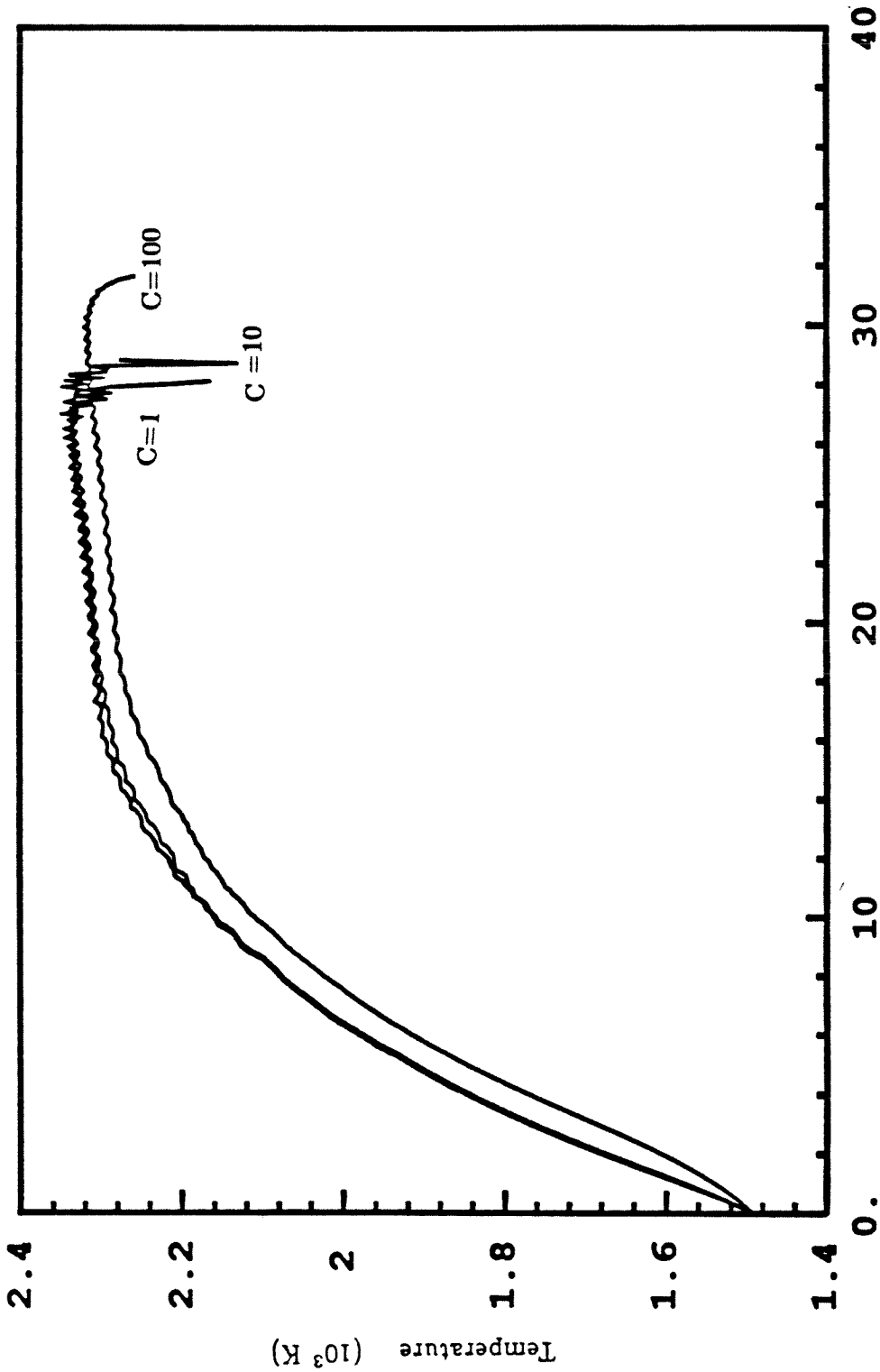

Figure 6.25. The effect of C on the Langmuir-Hinschelwood model. ρ_c=1.5 gcm^{-3}, T_0=1500K, T_∞=1500K, r_{p_0}=25 μm, $Y_{1\infty}$=0.22, A_{in}=305 gcm^{-2}s^{-1}, E_{in}=41000 cal gmol^{-1}, v_{ash}=0, $\varepsilon_p = \varepsilon_\infty$=0.8.

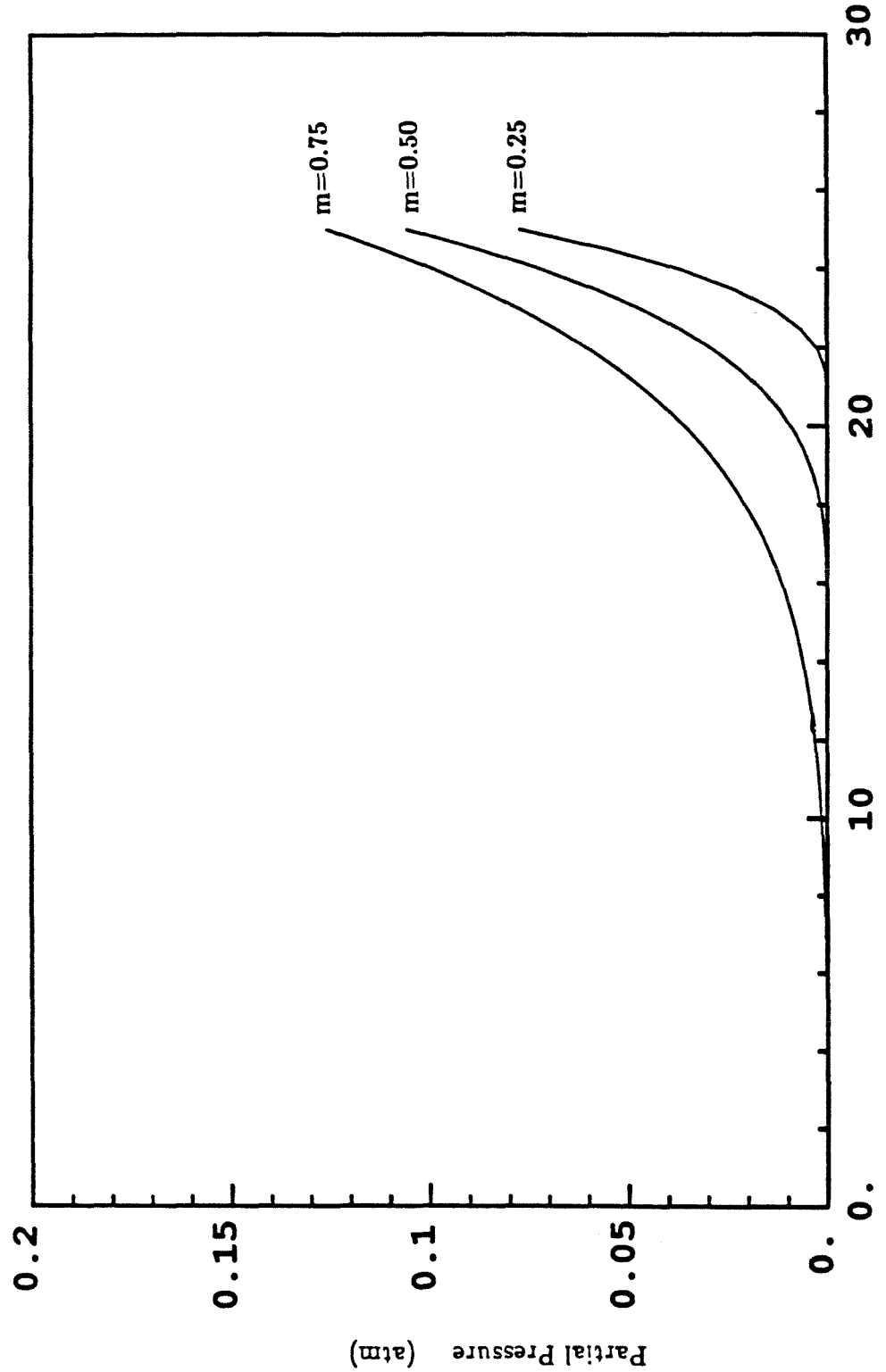

Figure 6.26. Initial internal oxygen partial pressure profiles for the power law expression with the indicated value of m. ρ_c=1.5 gcm^{-3}, T_0=1500K, T_∞=1500K, r_{p0}=25 μm, $Y_{1\infty}$=0.22, A_{in}=305 gcm^{-2}s^{-1}, E_{in}=41000 cal gmol^{-1}, ϵ_0=0.1, a_0=0.05 μm, v_{ash}=0, $\varepsilon_p = \varepsilon_\infty$=0.8.

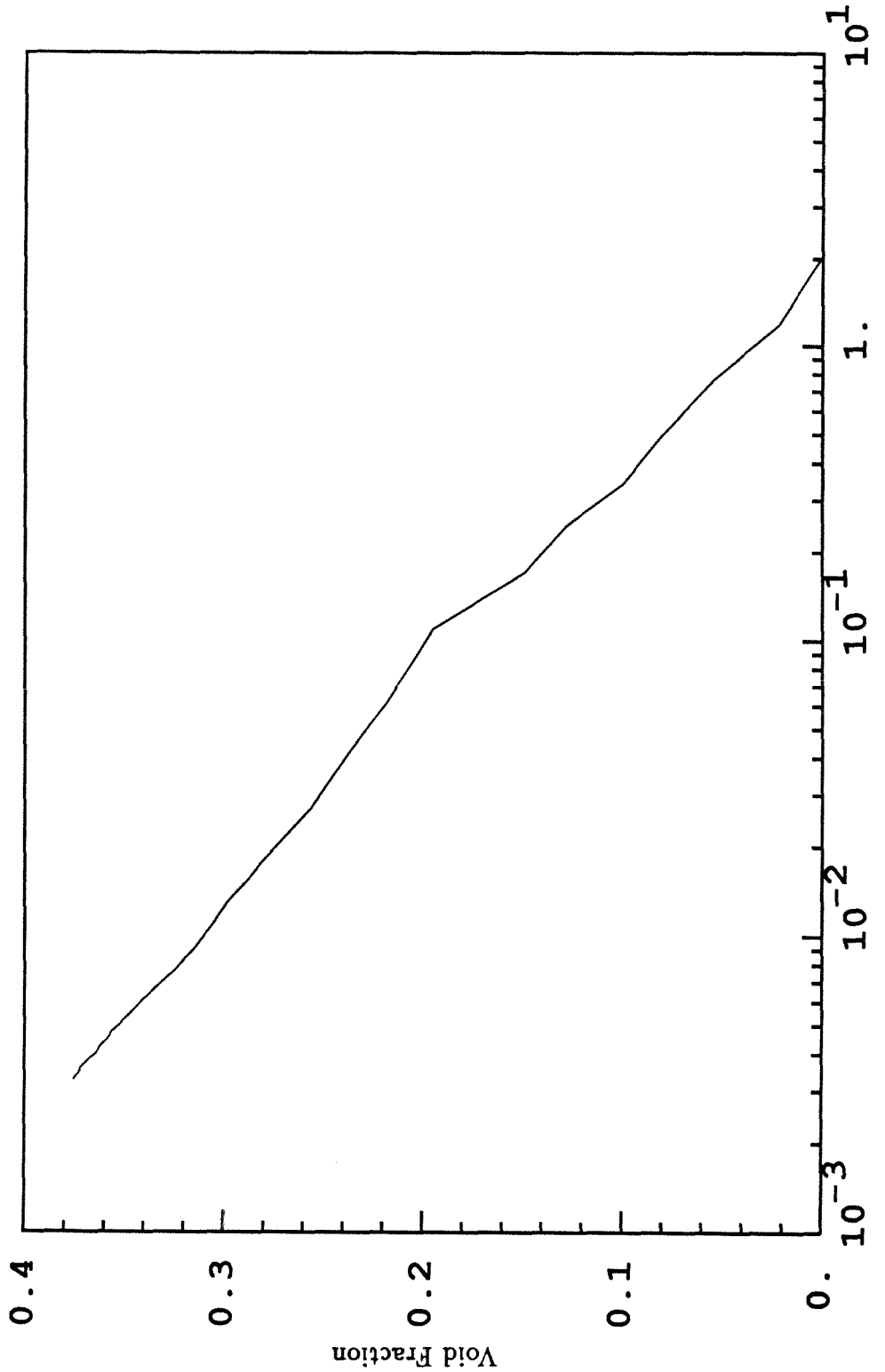

Figure 6.27. Cumulative void fraction versus radius for unburned lignite char.

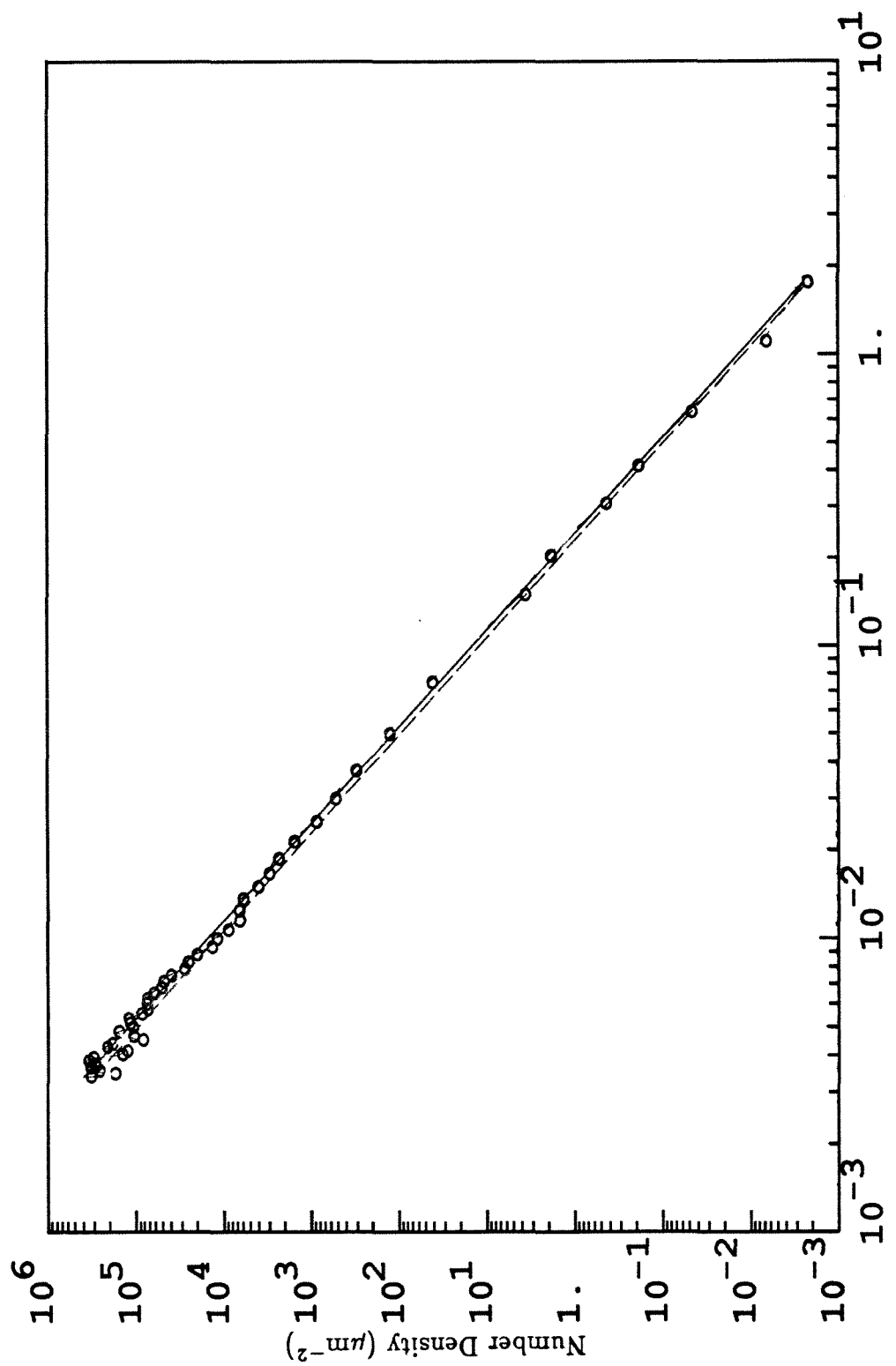

Figure 6.28. Number density of pores versus radius for unburned lignite char.

0-from porosimetry, — least squares fit, - - - emperical fit.

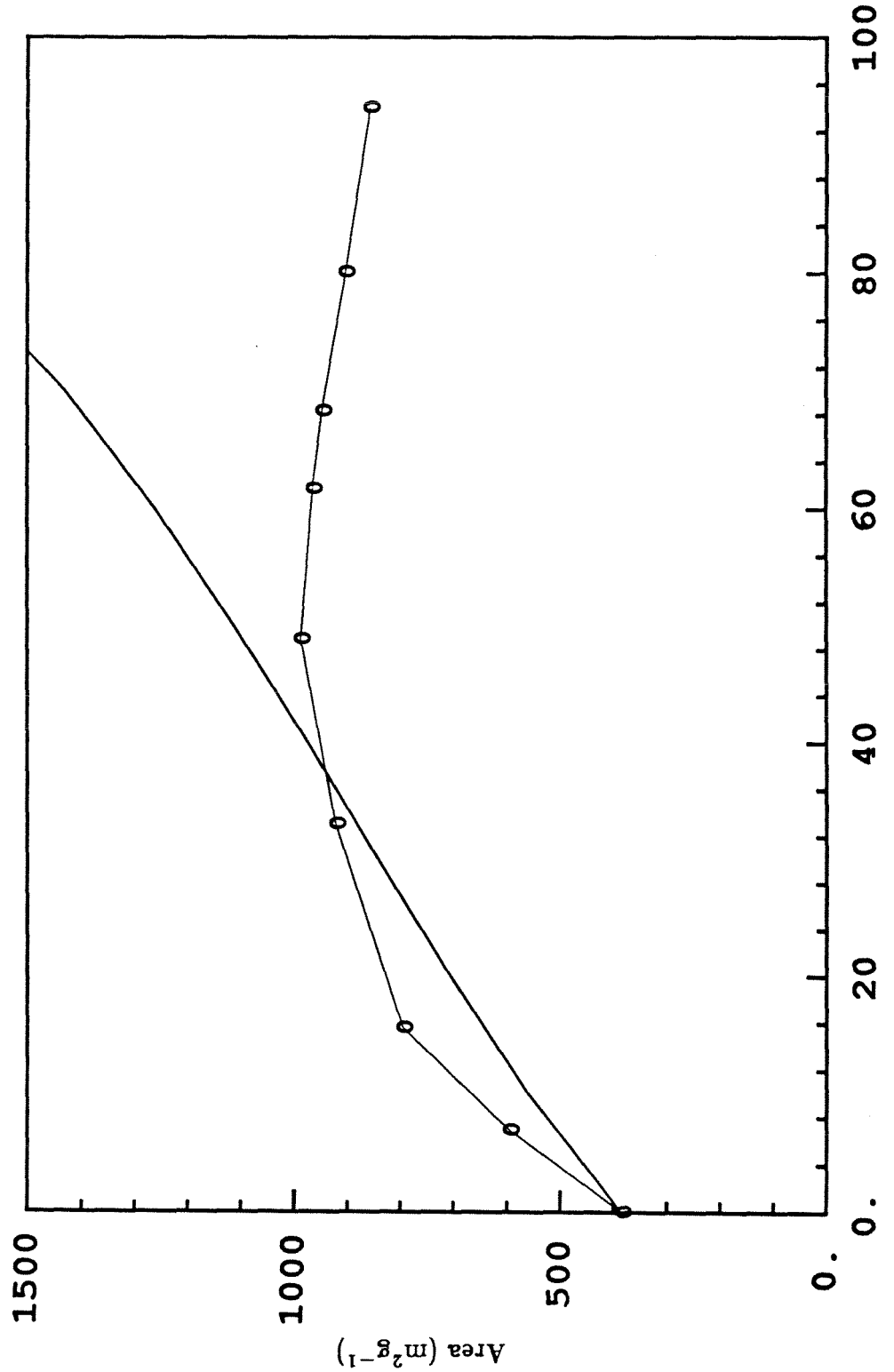

Figure 6.29. Specific surface area versus conversion for lignite char. 0-measured, — model prediction.

CHAPTER 7

CONCLUSIONS

7.1 Significance

In this study, we have attempted to characterize the porous microstructures of coal chars in sufficient detail to understand the influence of that microstructure on the kinetics of the reaction of the char with oxygen. The effects of coal type and pyrolysis conditions on the reactivity of and on the physical structure of chars were examined. Measurements of the changes in certain physical and chemical properties after low- and high- temperature reaction were also made. This experimental investigation was coupled to theoretical studies of the role of the porous microstructure in char oxidation.

The major developments and conclusions of this study are:

1. An improved method for measuring gas adsorption isotherms by continuous addition of the adsorbate gas has been developed. This continuous flow method compares well with the traditional incremental addition of adsorbate gas and has proven to be extremely efficient for the measurement of total surface area and for obtaining pore-volume distributions by the capillary-condensation method.

2. The properties of a coal char depend strongly upon the conditions of pyrolysis. Beginning with size-classified coals, a broad range of char-particle sizes can be generated, indicating substantial differences in density. While this effect is most pronounced for the swelling bituminous coal, a broad particle size distribution was observed for all of the coals studied, in spite of sizing the coal particles before pyrolysis. This indicates that there are substantial variations in the char properties from one particle to another.

Interesting differences and similarities in morphology were observed between these chars. The bituminous char was largely cenospheric, indicating that it underwent plasticization during pyrolysis. Partial oxidation of this material revealed an extensive network of micropores. The lignite char had a very rough surface, and did not undergo plasticization. The subbituminous char had certain characteristics in common with each of the other two chars. The precursor coal strongly resembled the lignite coal in appearance. There was no swelling during pyrolysis; however, micrographs showed that these char particles had a round, bubbly appearance similar to that of the bituminous char.

3. Apparent low-temperature reaction rates of chars generated from the bituminous coal vary significantly with pyrolysis condition and conversion. The specific surface area of the char also changes dramatically with conversion, increasing by more than an order of magnitude as the first 20% of the char is consumed, and remaining relatively constant thereafter. When the apparent reaction rates are normalized with respect to the nitrogen surface area, the intrinsic rate decreases during the first 20% of the conversion and is approximately constant thereafter. The variation of reactivity between chars produced at different temperatures is greatly reduced by this normalization. The remainder of the variation is due to chemical effects. Apparently, the higher hydrogen content of the char pyrolyzed at the lowest temperature leads to a higher active surface area.

4. During high-temperature combustion, there was little change in the pore-

volume distribution with increasing conversion. However, while much of the reaction appeared to take place at the external surface of the particle, there was evidence that some internal burning occurred.

5. When the temperature-time histories of individual burning char particles were measured, substantial particle-to-particle variations were observed. A method of statistical analysis of the reaction profiles of individual particles has been developed to facilitate reaction rate parameter estimation in the face of this variability. The initial particle radius and pre-exponential factor was allowed to vary from one particle to another, but a single apparent activation energy was determined that best fit the set of all traces for a particular char. The rate parameters derived from this analysis were consistent with those obtained from low-temperature oxidation. It is not certain why char particles that were pre-oxidized to about 30% conversion at low temperature showed lower reactivities than untreated particles.

6. A detailed model of char combustion was used to predict the effect of various parameters on the time-temperature history of single char particles. This model included the effect of intraparticle transport and the changing pore structure of the particle. Not surprisingly, the imposed structure had a significant effect on both the predicted maximum temperature and predicted burnout time of the particle.

The results of the characterization experiments were used to develop a picture of the lignite char in terms of the random capillary model. A simple empirical form was found to fit the data very well. However, comparison of the pre-

dicted specific surface area to the area measured after partial oxidation at low temperature showed that the model was not adequate in this situation.

7.2 Recommendations for Future Work

While several forms of physical characterization were performed on these chars, it may be of interest to utilize other methods in order to obtain a more complete picture of the physico-chemical structure of these chars. For example, small angle x-ray scattering and transmission electron microscopy could be used to probe the chars on the micropore level. X-ray scattering data could also be used to find the state of graphitization of the chars. While these techniques have been used in isolated cases, there appears to be no complete study of a single coal char.

The inversion of data from these techniques must also be considered. Improper inversion will lead to conflicting data, and erroneous visualization of the solid. These inversions should be developed to obtain the most complete collection of information possible. In this study, only the first intrusion of the mercury porosimetry experiments was used to obtain pore-volume distributions. However, in Chapter 2 it was pointed out that extrusion and subsequent intrusion-extrusion cycles have potential for obtaining data regarding the shape of and connectivity of the pores.

The results in Chapter 3 indicate that a differential reactor would be a useful tool to obtain data on the relative production of carbon oxides in the char at temperatures between 700 and 900K. This would be very helpful in determining mechanisms for these two heterogeneous reactions.

The difficulty in determining properties of the lignite char were partly due to the presence of large amounts of ash. This could be largely eliminated by acid

washing of the char. While some studies of demineralized chars have been done (*e.g.*, Jenkins *et al.*(1973); Hengel and Walker (1984)), they have concentrated on the low-temperature reactivity of these chars. It would be of great interest to see the effect of ash on the developing morphology and on the relative production of carbon oxides during low-temperature oxidation. It would also be useful to study the combustion of demineralized chars at high temperature.

One of the most interesting findings of the high-temperature experiments was that the surface area of the lignite char actually began to decrease after partial oxidation at high temperature. This may be due to annealing of the microporous structure. This could be examined by further pyrolysis of the char at relevant temperatures. Also, the effect of ash on this process could be examined by using demineralized chars.

In view of the findings of Chapter 6, it may be worthwhile to modify the random capillary model. In reality, the Theile Modulus depends on pore size. Based on this, it may be possible to describe the local burnoff, q, in terms of three variables: time, radial postion in the particle, and pore radius. This will necessarily complicate the analysis, but the problem will remain tractable.

REFERENCES

Hengel, T.P., and Walker, P.L.,Jr. (1984). Catalysis of Lignite Char by Exchangeable Calcium and Magnesium. *Fuel*, **63**, 1214.

Jenkins, R.G., Nandi, S.P. and Walker, P.L.,Jr. (1973). Reactivity of Heat-Treated Coals in Air at 500°C. *Fuel*, **52**, 288.

Tseng, H.P. and Edgar, T.F. (1985). Combustion Behavior of Bituminous and Anthracite Coal Char Between 425 and 900°. *Fuel*, **64**, 373.

APPENDIX A

RAW COAL DATA

A.1 Results of Characterization Experiments

Selected characterization experiments were performed on the raw coals. The purpose of this was to understand more clearly the changes that took place in the coals during pyrolysis.

Figures A.1 to A.3 show electron micrographs of the bituminous, lignite and subbituminous coals, respectively. The bituminous coal particles are very irregular, with smooth surfaces and sharp edges. Ash particles are visible on the surface of the particles.

The lignite and subbituminous chars have similar, rough surfaces. Particles of ash are visible on the surface.

Mercury porosimetry was done on the raw coals, with the resulting pore volume distributions in Figures A.4 to A.6. The bituminous coal has very little micro- and transitional porosity. Some of the apparent porosity may be due to the compressibility of the solid, which has not been accounted for here. The volume for pores greater than 1 μm in diameter is largely due to interparticle voids. The lignite coal contains significant porosity over the entire range of sizes. In this respect, it is similar to the char derived from it. The subbituminous coal possess relatively little transitional and macroporosity. There is a significant amount of porosity in the 32-100 Å radius range.

Surface areas were measured with nitrogen at 77K. In all cases, surface areas were quite low: for the bituminous, it was 1.4 m^2/g; for the lignite, it was 2.25 m^2/g; for the subbituminous, it was 3.2 m^2/g.

A. Data from the Penn State Office of Coal Research

Data sheets were provided by the PSOCR, who also provided the coals for this study. Included are the results from a variety of analyses.

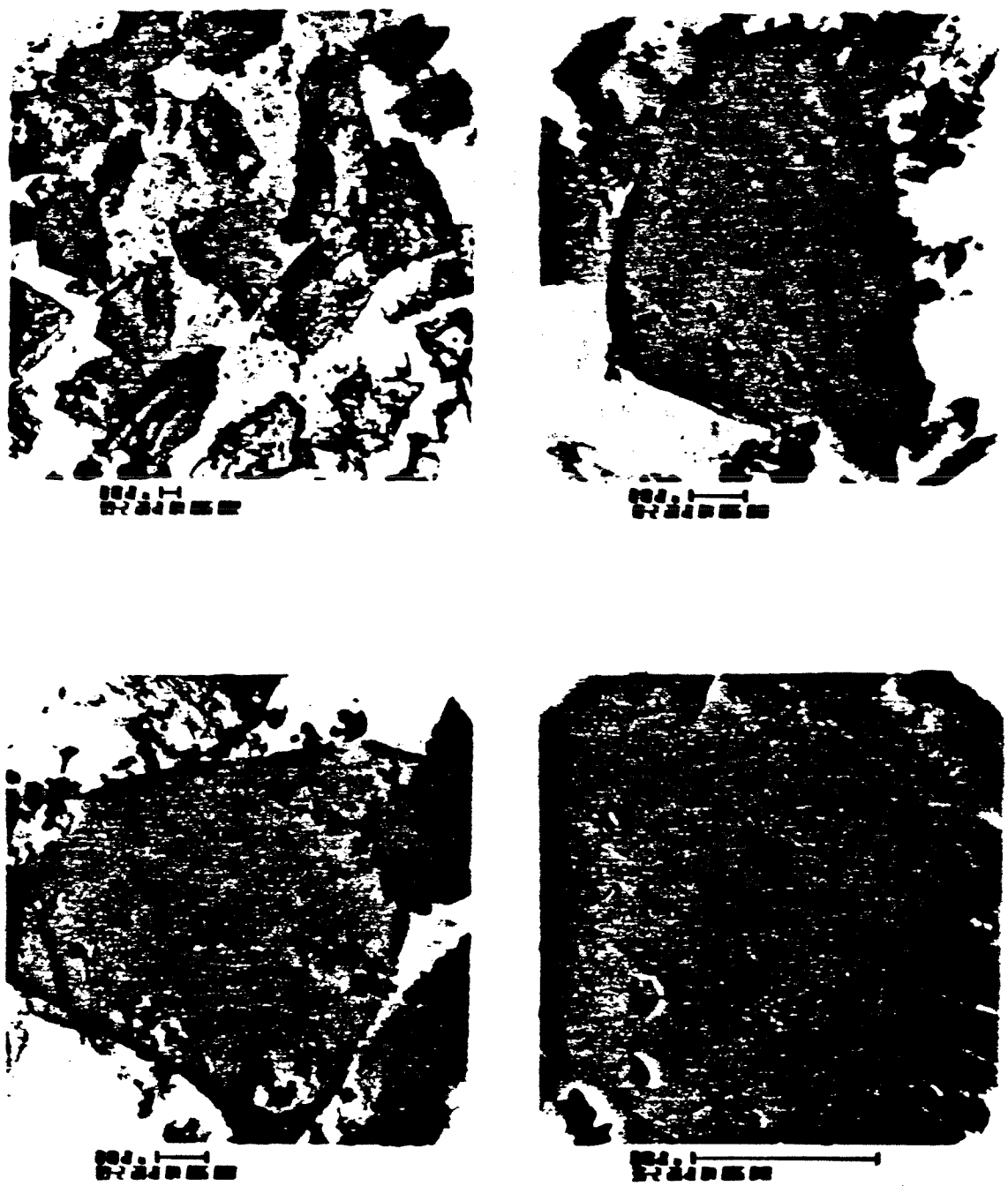

Figure A.1. Electron micrographs of raw PSOC 1451 coal.

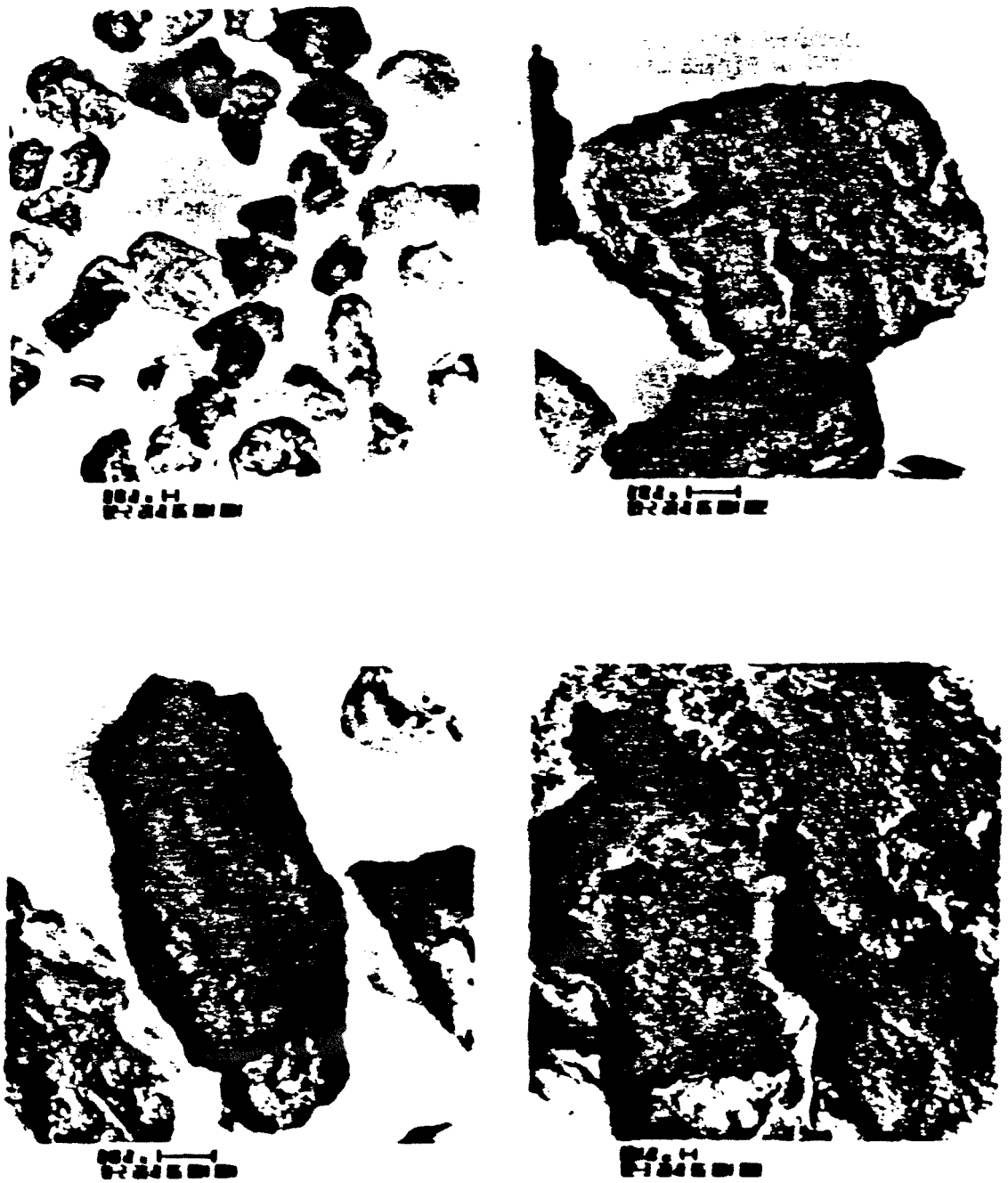

Figure A.2. Electron micrographs of raw PSOC 1443 coal.

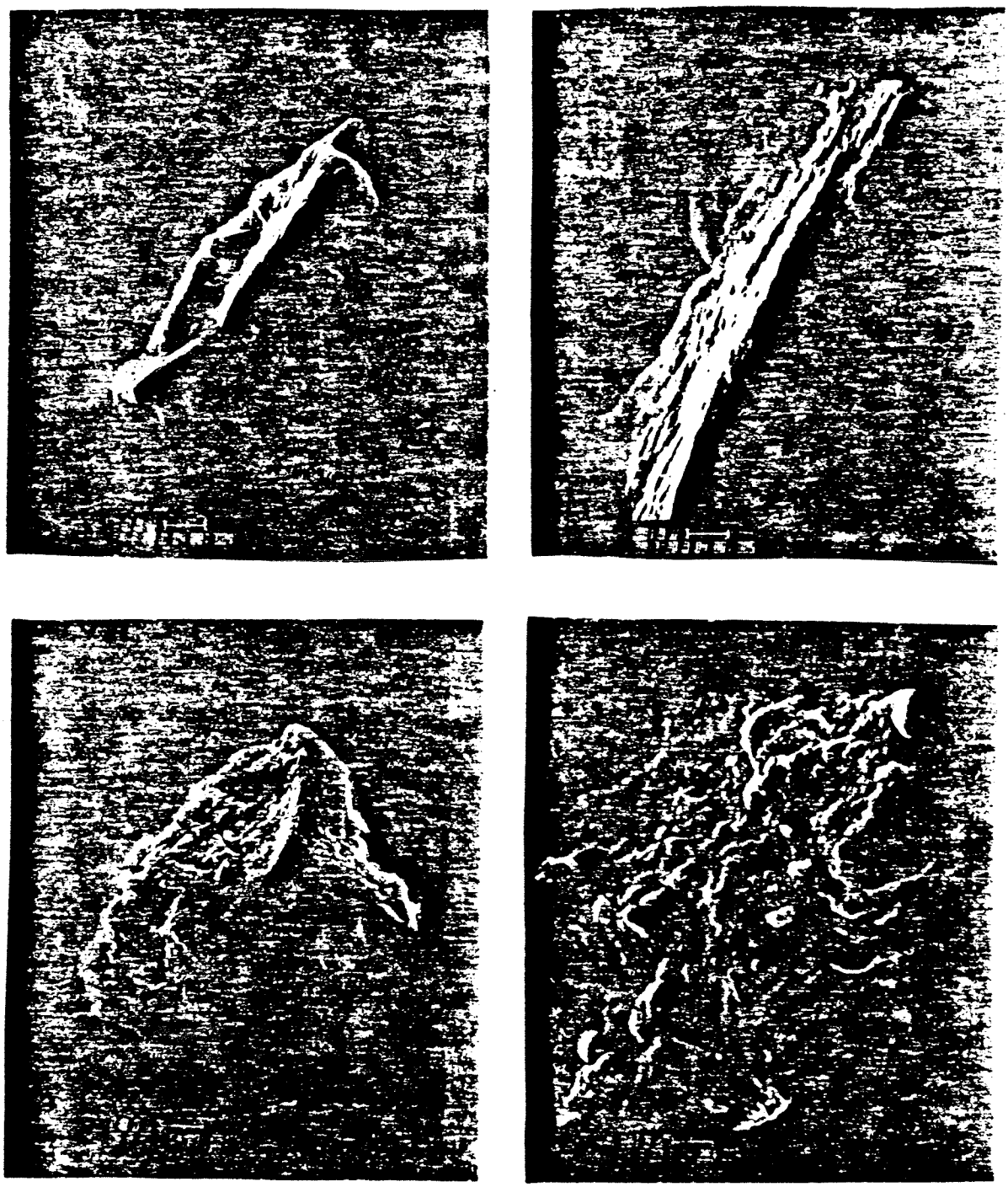

Figure A.3. Electron micrographs of raw PSOC 1488 coal.

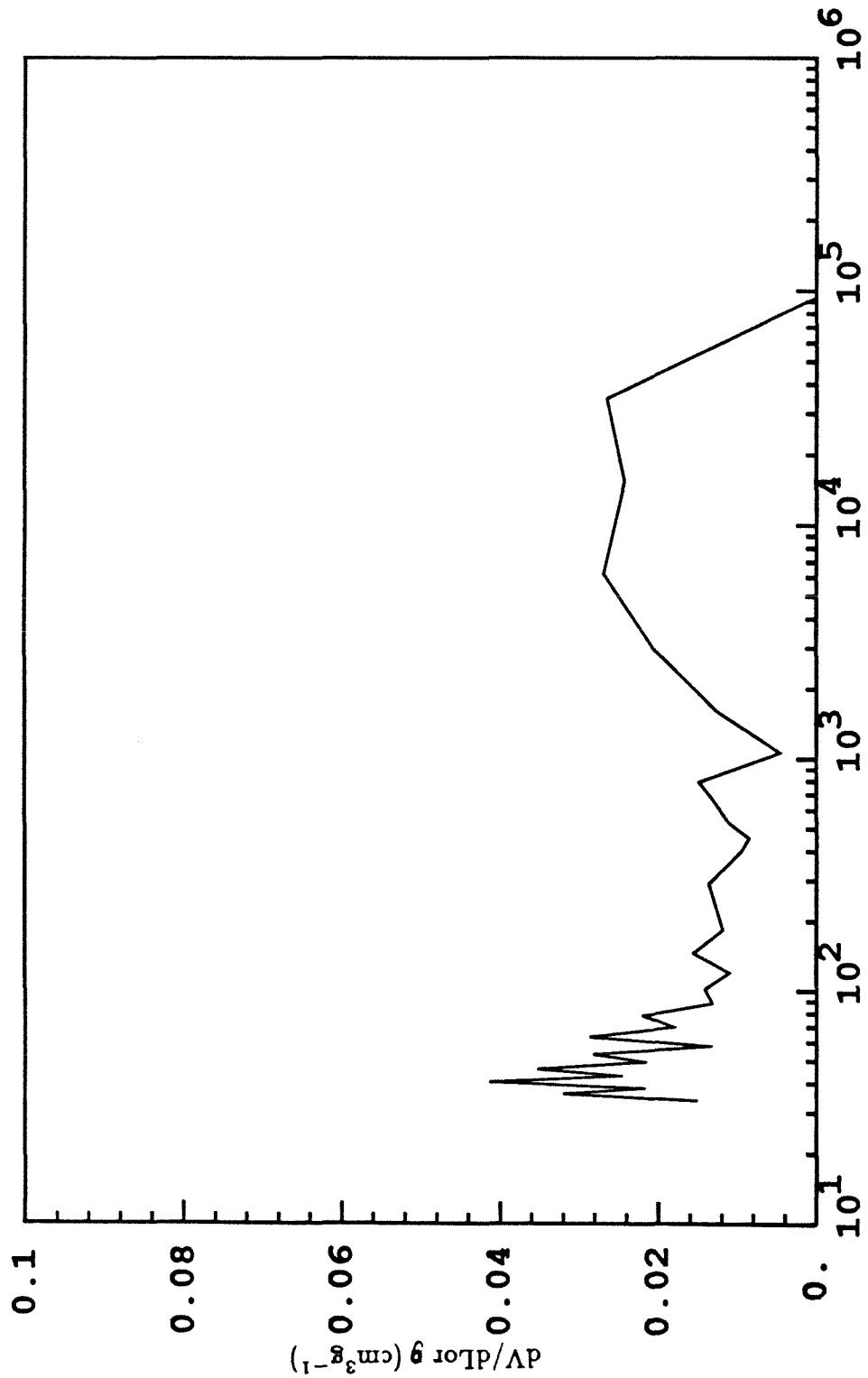

Figure A.4. Pore volume distribution for raw PSOC 1451 coal.

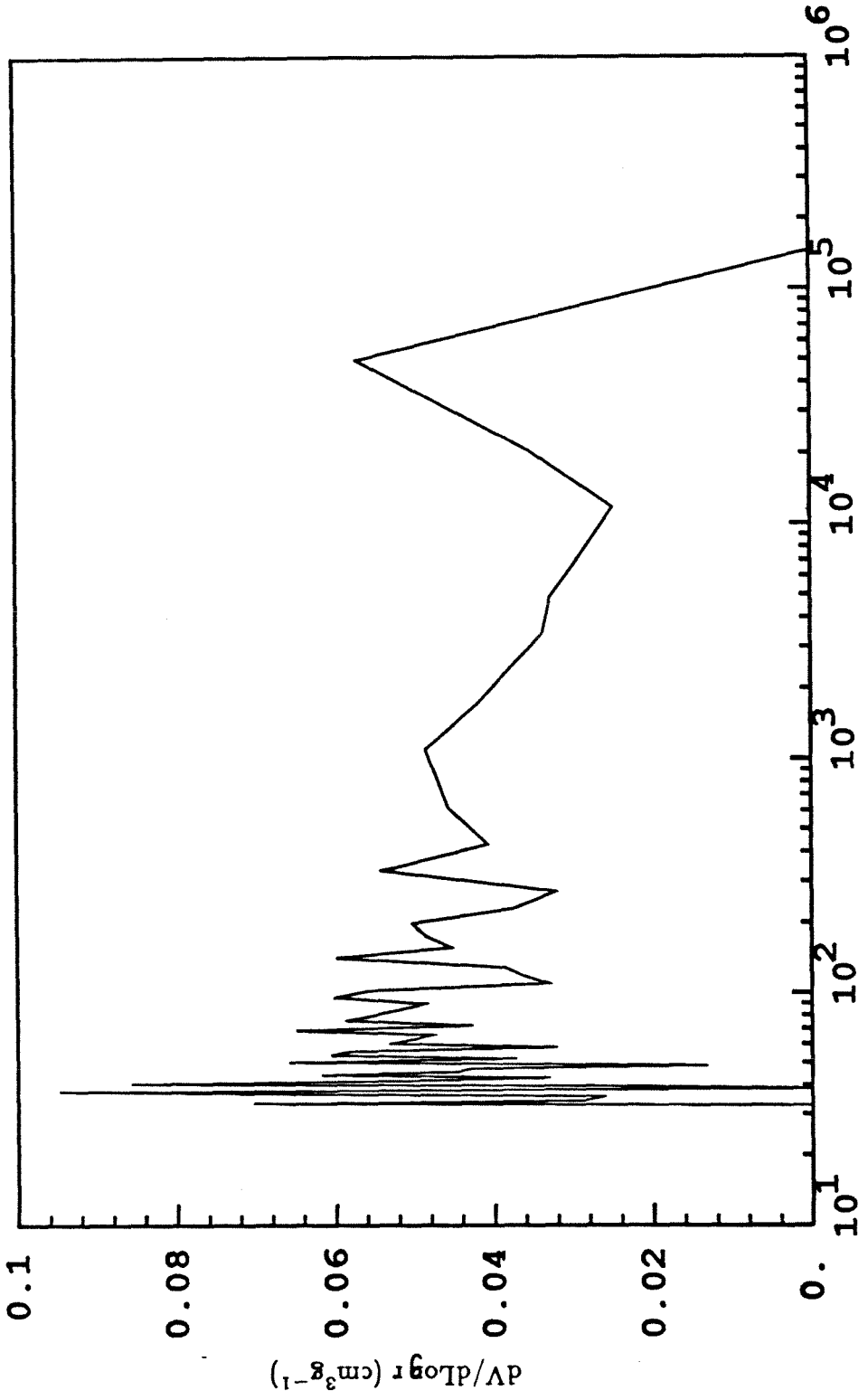

Figure A.5. Pore volume distribution for raw PSOC 1443 coal.

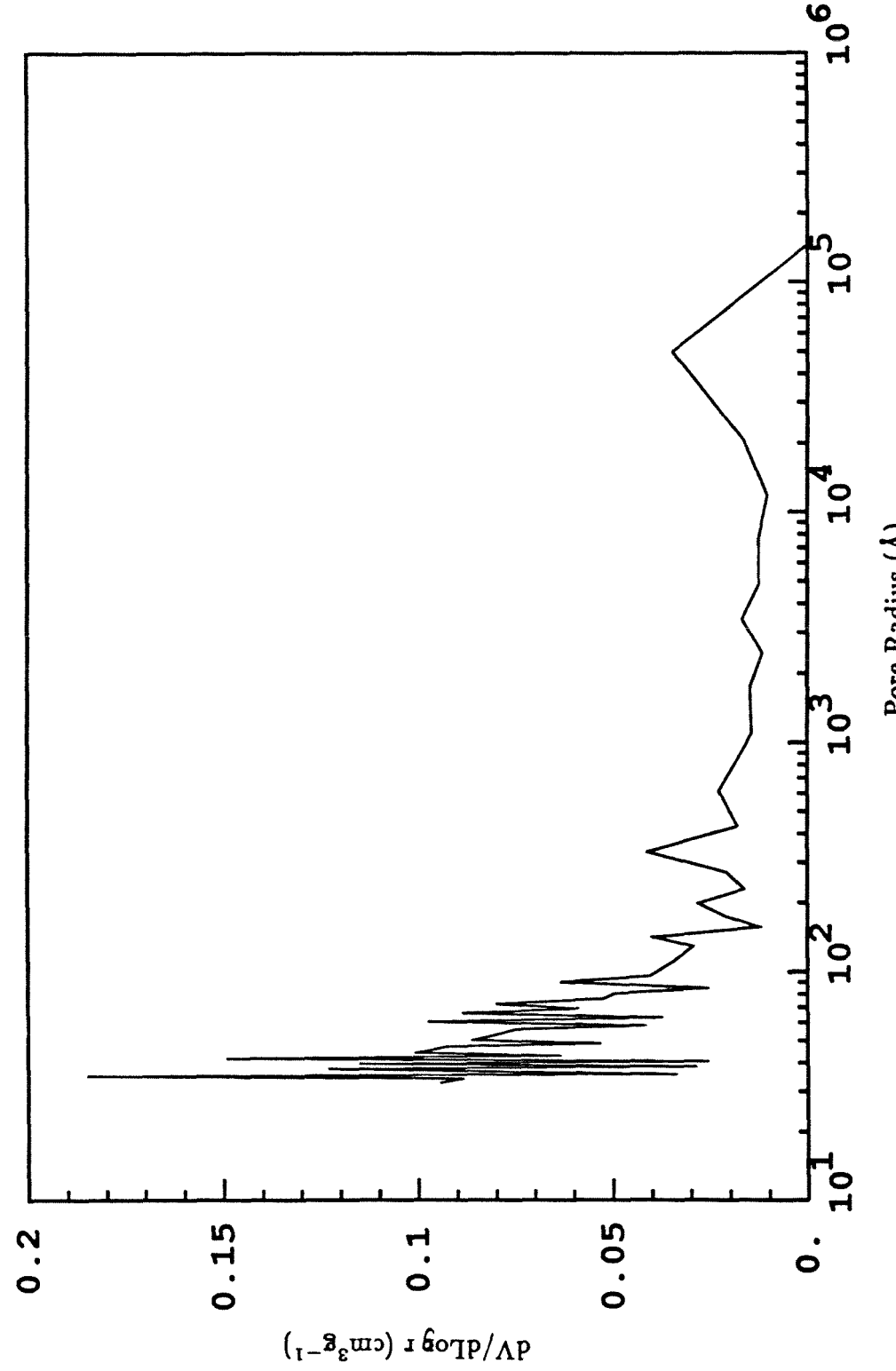

Figure A.6. Pore volume distribution for raw PSOC 1488 coal.

** PENN STATE COAL DATA BASE **

****
* *
* SAMPLE HISTORY *
* *
****

PENN STATE NUMBER	PSOC-1451
COLLECTED BY	PENNSYLVANIA STATE UNIVERSITY
COLLECTION DATE	5/ 1/85
COLLECTOR'S NUMBER	
REPORTED RANK	HIGH VOLATILE A BITUMINOUS (HVAB)
SAMPLE TYPE	CHANNEL WHOLE SEAM
OTHER SAMPLE INFORMATION	
SAMPLE RESERVE	
SEAM NAME	PITTSBURGH
ALTERNATE SEAM NAME	#8
TOTAL SEAM THICKNESS	6 FT. 5 IN.
THICKNESS OF SEAM SAMPLED	6 FT. 5 IN.
PORTION RECOVERED IN CORE	
DIAMETER OF CORE	

****
* *
* SAMPLE LOCATION *
* *
****

COUNTRY	U.S.A.
STATE	PENNSYLVANIA
COUNTY	WASHINGTON
TOWNSHIP	NORTH STRABANE
NEAREST TOWN	LINDEN
COAL PROVINCE	EASTERN
COAL REGION	APPALACHIAN
COAL FIELD	MAIN BITUMINOUS
MAP REFERENCE: LATITUDE	80D 8M 20S
LONGITUDE	40D 14M 00S
QUADRANGLE	WASHINGTON EAST (7.5')

** PENN STATE COAL DATA BASE **

SEAM NAME PITTSBURGH
APPARENT RANK HIGH VOLATILE A BITUMINOUS (HVAB)

****
* *
* GEOLOGIC INFORMATION *
* *
****

SYSTEM (AGE) PENNSYLVANIAN
SERIES
GROUP MONONGAHELA
FORMATION

OVERBURDEN LITHOLOGY SHALE
FLOOR LITHOLOGY SHALE

****
* *
* SEAM STRATA INFORMATION *
* *
****

THICKNESS	LITHOTYPE

****
* *
* MINE INFORMATION *
* *
****

MINE NAME MATHIES
MINING METHOD UNDERGROUND
MINE RESERVES
MINE PRODUCTION 700 THOUSAND TONS/YEAR
MINE LIFE EXPECTANCY 15 YEAR
OVERBURDEN THICKNESS 230 FT.

** PENN STATE COAL DATA BASE **

SEAM NAME PITTSBURGH
APPARENT RANK HIGH VOLATILE A BITUMINOUS (HVAB)

CHEMICAL DATA 1

PROXIMATE ANALYSIS	AS REC'D	DRY	DAF	DMMF (PARR)	DMMF (PARR-G)	DMMF (DIR MM)
% MOISTURE	2.54					
% ASH	13.32	13.67				
% VOLATILE MATTER	33.56	34.43	39.88	38.81	38.21	
% FIXED CARBON	50.58	51.90	60.12	61.19	61.79	

CALORIFIC VALUE (GROSS BTU/LB)	DRY	AS REC'D MOIST.	EQUIL. MOIST.
MM-FREE,DIRECT			
MM-CONTAINING	12855	12528	12541
MM-FREE (PARR)	15135	14682	14699
MM-FREE (MOD.P)	15227	14736	14754
BEST MM FREE		14736	14754
NET CV, DMMF BTU/LB	14713		
ASH-FREE	14891		

MOTT-SPOONER DIFFERENCE =

ASSOCIATED ANALYSES	DRY	MMF
% EQUILIBRIUM MOISTURE	2.44	2.89
% TOTAL SULFUR	1.36	

RANK CALCULATIONS

APPARENT RANK (AS REC'D MOIST)	HIGH VOLATILE A BITUMINOUS (HVAB)
ASTM RANK (EQUIL. MOIST.)	HIGH VOLATILE A BITUMINOUS (HVAB)
REFLECTANCE RANK CATEGORY	HIGH VOLATILE A BITUMINOUS (HVAB)
INTERNATIONAL RANK	
AS REC'D MOIST.	
EQUIL. MOIST.	
REPORTED RANK	HIGH VOLATILE A BITUMINOUS (HVAB)

** PENN STATE COAL DATA BASE **

SEAM NAME PITTSBURGH
APPARENT RANK HIGH VOLATILE A BITUMINOUS (HVAB)

CHEMICAL DATA 2

ULTIMATE ANALYSIS	AS REC'D	DRY	DAF	DMMF(PARR) (15.51 %MM)
% ASH	13.32	13.67		
% CARBON	70.05	71.88	83.26	85.08
% HYDROGEN	4.55*	4.67	5.41	5.53
% NITROGEN	1.33	1.36	1.58	1.61
% SULFUR	1.33	1.36	1.58	
% CHLORINE	0.07	0.08	0.09	0.09
% OXYGEN(DIFF)	6.81*	6.99	8.10	7.71

SULFUR FORMS	% PYRITIC	% SULFATIC	% ORGANIC	% TOTAL
DRY	0.82	0.01	0.53	1.36
DAF	0.95	0.01	0.61	1.58

OPTICAL

ELEMENTAL ANALYSIS	DRY	DMMF(MOD.P) (15.87%MM)	DMMF(DIR.) (%MM)
% CARBON	71.64	85.16	
% HYDROGEN	4.64	5.52	
% NITROGEN	1.36	1.61	
% ORGANIC SULFUR	0.53	0.63	
% OXYGEN(DIFF)	5.95	7.00	
% CHLORINE	0.08	0.09	
% MINERAL MATTER (INCLUDES 1.53 % FES2)	15.87		

ATOM RATIOS (DMMF)	PARR	MOD.PAR	DIRECT
ATOMIC H/C	0.780	0.778	
ATOMIC O/C	0.068	0.073	

MISC. CHEMICAL DATA	DRY	OF DMMF COAL	OF DMMF OXYGEN
% O AS COOH			
% O AS OH			
% S AS SO4,IN ASH			
% CARBONATE AS CO2	0.87		
% CHLORINE	0.15		

INFRA-RED ANALYSIS

(*)-EXCLUDES MOISTURE

** PENN STATE COAL DATA BASE **

SEAM NAME PITTSBURGH
APPARENT RANK HIGH VOLATILE A BITUMINOUS (HVAB)

****
* *
* CHEMICAL DATA 3 *
* *
****

% MOISTURE IN COAL = 1.52
% HIGH TEMPERATURE ASH = 13.20 AT 750 DEGREES C

TRACE ELEMENT ANALYSIS	PPM HTA	PPM TOTAL COAL
AG		
B		
BA	540	71
BE	7	1
BI		
CE		
CO		
CR	150	20
CU	80	11
GA		
GE		
LA		
LI		
MN	140	18
MO		
NI	65	9
NB		
PB		
RB	100	13
SC		
SN		
SR	590	78
TH		
U		
V	200	26
Y		
YB		
ZN	95	11
ZR	240	32

MAJOR ELEMENT ANALYSIS	OXIDE % OF HTA	ELEMENT % OF TOTAL DRY COAL
SIO2	54.40	3.36
AL2O3	24.50	1.71
TIO2	1.14	0.09
FE2O3	9.16	0.85
MGO	0.85	0.07
CAO	2.97	0.28
NA2O	0.61	0.06
K2O	2.02	0.22
P2O5	0.34	0.02
SO3	2.30	0.12

VOLATILES	PPM TOTAL COAL
AS	
BR	
CD	
CL	
F	
HG	
SB	
SE	

** PENN STATE COAL DATA BASE **

SEAM NAME PITTSBURGH
APPARENT RANK HIGH VOLATILE A BITUMINOUS (HVAB)

****
* *
* MINERALOGICAL DATA *
* *
****

TOTAL MINERAL MATTER

% MM-PARR	15.51
% MM-MODIFIED PARR	15.87
% MM-KMC	
% MM-DIRECT	
% MM-BEST AVAILABLE	15.87
VOL % MM-PARR	8.13

MINERAL COMPOSITION

% LOW TEMPERATURE ASH (MCL) =

	% OF LTA
QUARTZ	
PYRITE	
CALCITE	
GYPSUM	
KAOLINITE	
MONT + ILL + MLC	
MONT + ILL	
MONT + MLC	
ILLITE + MLC	
MONTMORILLONITE	
ILLITE	
MIXED LAYER CLAYS	
FELDSPAR	
MINOR FE SULFATES	

% LOW TEMPERATURE ASH (O'GORMAN)
(ALL DATA DETERMINED ON 65X100 MESH SIZE FRACTION)

	% OF LTA
KAOLINITE	
ILLITE	
MUSCOVITE	
CHLORITE	
MONTMORILLONITE	
MIXED CLAYS	
CALCITE	
ARAGONITE	
DOLOMITE	
ANKERITE	
SIDERITE	
QUARTZ	
GYPSUM	
PYRITE	
HEMATITE	
RUTILE	
THENARDITE	
PLAGIOCLASE	

** PENN STATE COAL DATA BASE **

SEAM NAME PITTSBURGH
APPARENT RANK HIGH VOLATILE A BITUMINOUS (HVAB)

****
* *
* PETROGRAPHIC DATA *
* *
****

MACERAL COMPOSITION WHITE ANALYSIS ONLY

	DRY VOLUME %	DMMF VOLUME %	DRY WEIGHT %
VITRINITE (CALC.)	80.1	87.2	73.7
INERTINITE (CALC.)	8.7	9.5	8.0
LIPTINITE (CALC.)	3.0	3.3	2.8
MINERAL MATTER (CALC.)	8.1		15.5
VITRINOIDS			
VITRINITE	80.1	87.2	73.7
PSEUDOVITRINITE	0.0	0.0	0.0
FUSINITE	1.8	2.0	1.7
SEMI-FUSINITE	4.2	4.6	3.9
MACRINITE	0.7	0.8	0.7
MICRINITE	1.9	2.1	1.8
SCLEROTINITE	0.0	0.0	0.0
SPORINITE			
CUTINITE			
EXINITE (ANAL.)	3.0	3.3	2.8
RESINITE	0.0	0.0	0.0
SUBERINITE			
EXUDATINITE			
FLUORINITE			
BITUMINITE			
ALGINITE	0.0	0.0	0.0
LIPTODETRINITE			
MINERAL MATTER(ANAL.)			
INERTINITE(ANAL.)			
LIPTINITE(ANAL.)			

REFLECTANCE DATA (%,IN OIL)	HIGH	LOW	RANGE	MEAN MAX	STAND.DEV.
VITRINITE	0.89	0.62	0.27	0.77	0.06
PSEUDOVITRINITE					
VITRINOIDS					

** PENN STATE COAL DATA BASE **

SEAM NAME PITTSBURGH
APPARENT RANK HIGH VOLATILE A BITUMINOUS (HVAB)

****
* *
* PETROGRAPHIC DATA *
* CONTINUED *
* *
****

% VITRINOID REFLECTANCE	HALF-TYPE	VOLUME PERCENT	% VITRINOID REFLECTANCE	V-TYPE	VOLUME PERCENT
0.60-0.64	VHT 0.625	3.00			
0.65-0.69	VHT 0.675	9.00	0.60-0.69	V6	12.00
0.70-0.74	VHT 0.725	18.00			
0.75-0.79	VHT 0.775	37.00	0.70-0.79	V7	55.00
0.80-0.84	VHT 0.825	25.00			
0.85-0.89	VHT 0.875	8.00	0.80-0.89	V8	33.00

** PENN STATE COAL DATA BASE **

SEAM NAME PITTSBURGH
APPARENT RANK HIGH VOLATILE A BITUMINOUS (HVAB)

PHYSICAL PROPERTIES

HARDGROVE GRINDABILITY	38.9
VICKER'S MICROHARDNESS	
FREE SWELLING INDEX	7.5
GRAY KING COKE TYPE	
SURFACE AREA (DETERMINED WITH NITROGEN)	
SURFACE AREA (DETERMINED WITH CARBON DIOXIDE)	
DENSITY (DETERMINED WITH HELIUM)	
DENSITY (DETERMINED WITH MERCURY)	
DENSITY (DETERMINED WITH WATER)	
SPECIFIC GRAVITY	
MICROPORE VOLUME	
MACROPORE VOLUME	
TOTAL PORE VOLUME	
PORE SIZE DISTRIBUTION	

GIESELER PLASTICITY DATA

MAXIMUM FLUIDITY	8525
MAXIMUM FLUIDITY TEMPERATURE	433
INITIAL SOFTENING TEMPERATURE	390
SOLIDIFICATION TEMPERATURE	470
FLUID TEMPERATURE RANGE	80
PLASTOMETER TYPE	GIESELER - PSU

ASH FUSION ANALYSIS (DEGREES F)	REDUCING	OXIDIZING
INITIAL DEFORMATION TEMPERATURE	2435	2570
SOFTENING TEMPERATURE	2580 - 1415 SC	2640
HEMISPHERE TEMPERATURE	2670	2690
FLUID TEMPERATURE	2685	2700

** PENN STATE COAL DATA BASE **

SEAM NAME PITTSBURGH
APPARENT RANK HIGH VOLATILE A BITUMINOUS (HVAB)

****
* *
* ANALYSIS LOG *
* *
****

ANALYSIS	DATE	PERFORMED BY
A.R. MOIST	2/14/86	WARNER LABORATORIES
EQUIL. MOIST.	6/ 4/85	WARNER LABORATORIES
PROXIMATE	2/14/86	WARNER LABORATORIES
ULTIMATE	2/14/86	WARNER LABORATORIES
SULFUR FORMS	6/ 4/85	WARNER LABORATORIES
FST	9/15/85	COAL PETROGRAPHY LABORATORIES - PSU
PLASTOMETER	5/29/85	COAL PETROGRAPHY LABORATORIES - PSU
DIRECT MM		
GRAY-KING		

****
* *
* PERFORMANCE DATA *
* *
****

PREPARATION DATA	YIELD	ASH	SULFUR	VITRINITE (HUMINITE)	LIPTINITE	INERTINITE
1.35 FLOAT						
1.35 X 1.45						
1.45 X 1.55						
1.55 X 1.65						
1.65 X SINK						

GASIFICATION DATA (MAX REACTIVITY OF 1000 DEGREES C,
40 X 100 MESH COAL CHARS)

	TEMPERATURE (DEGREES C)	PRESSURE (ATM)	REACTIVITY
AIR			
CO2			
H			

CARBONIZATION DATA

TOTAL REACTIVE MACERAL MATERIAL (USS)	
TOTAL REACTIVE MACERAL MATERIAL (BETH)	
TOTAL INERT MATERIAL	
EFFECTIVE INERT MATERIAL	
BALANCE INDEX	
STRENGTH INDEX	
PREDICTED STABILITY	
PREDICTED MICUM 40	
MEASURED STABILITY	
MEASURED MICUM 40	

** PENN STATE COAL DATA BASE **

SAMPLE HISTORY

PENN STATE NUMBER	PSOC-1443
COLLECTED BY	PENNSYLVANIA STATE UNIVERSITY
COLLECTION DATE	3/29/85
COLLECTOR'S NUMBER	
REPORTED RANK	LIGNITE
SAMPLE TYPE	CHANNEL WHOLE SEAM
OTHER SAMPLE INFORMATION	
SAMPLE RESERVE	
SEAM NAME	
ALTERNATE SEAM NAME	LOWER WILCOX SEAM
TOTAL SEAM THICKNESS	10 FT. 8 IN.
THICKNESS OF SEAM SAMPLED	10 FT. 8 IN.
PORTION RECOVERED IN CORE	
DIAMETER OF CORE	

SAMPLE LOCATION

COUNTRY	U.S.A.
STATE	TEXAS
COUNTY	TITUS
TOWNSHIP	
NEAREST TOWN	WINFIELD
COAL PROVINCE	GULF
COAL REGION	
COAL FIELD	
MAP REFERENCE: LATITUDE	33D 11M 40S
LONGITUDE	95D 4M 30S
QUADRANGLE	WINFIELD (7.5')

** PENN STATE COAL DATA BASE **

SEAM NAME
APPARENT RANK SUBBITUMINOUS C (SUBC)

CHEMICAL DATA 1

PROXIMATE ANALYSIS	AS REC'D	DRY	DAF	DMMF (PARR)	DMMF (PARR-G)
% MOISTURE	28.54				
% ASH	15.31	21.43			
% VOLATILE MATTER	44.17	61.81	78.67	78.22	77.15
% FIXED CARBON	11.98	16.76	21.33	21.78	22.85

CALORIFIC VALUE (GROSS BTU/LB)	DRY	AS REC'D MOIST.	EQUIL. MOIST.
MM-FREE,DIRECT			
MM-CONTAINING	9882	7062	6519
MM-FREE (PARR)	12878	9459	7689
MM-FREE (MOD.P)	13045	8510	7731
BEST MM FREE		8510	7731
NET CV, DMMF BTU/LB	12545		
ASH-FREE	12577		

MOTT-SPOONER DIFFERENCE = 202.

ASSOCIATED ANALYSES	DRY	MMF
% EQUILIBRIUM MOISTURE	34.03	44.51
% TOTAL SULFUR	0.74	

RANK CALCULATIONS

APPARENT RANK (AS REC'D MOIST) SUBBITUMINOUS C (SUBC)
ASTM RANK (EQUIL. MOIST.) LIGNITE A (LIGA)
REFLECTANCE RANK CATEGORY
INTERNATIONAL RANK
  AS REC'D MOIST.
  EQUIL. MOIST.
REPORTED RANK LIGNITE

** PENN STATE COAL DATA BASE **

SEAM NAME
APPARENT RANK SUBBITUMINOUS C (SUBC)

CHEMICAL DATA 2

ULTIMATE ANALYSIS	AS REC'D	DRY	DAF	DMMF(PARR)
				(23.55 %MM)
% ASH	15.31	21.43		
% CARBON	40.62	56.84	72.34	74.35
% HYDROGEN	2.92*	4.09	5.21	5.35
% NITROGEN	0.76	1.06	1.35	1.39
% SULFUR	0.53	0.74	0.94	
% CHLORINE	0.04	0.05	0.07	0.07
% OXYGEN(DIFF)	11.26*	15.78	20.11	18.86

SULFUR FORMS	% PYRITIC	% SULFATIC	% ORGANIC	% TOTAL
DRY	0.09	0.01	0.64	0.74
DAF	0.11	0.01	0.81	0.94

OPTICAL

ELEMENTAL ANALYSIS	DRY	DMMF(MOD.P)	DMMF(DIR.)
		(24.29%MM)	(%MM)
% CARBON	56.64	74.81	
% HYDROGEN	3.82	5.05	
% NITROGEN	1.06	1.39	
% ORGANIC SULFUR	0.64	0.85	
% OXYGEN(DIFF)	13.55	17.84	
% CHLORINE	0.05	0.07	
% MINERAL MATTER	24.29		
(INCLUDES 0.17 % FES2)			

ATOM RATIOS (DMMF)	PARR	MOD.PAR	DIRECT
ATOMIC H/C	0.864	0.810	
ATOMIC O/C	0.190	0.237	

MISC. CHEMICAL DATA	DRY	OF DMMF COAL	OF DMMF OXYGEN
% O AS COOH			
% O AS OH			
% S AS SO4,IN ASH			
% CARBONATE AS CO2	0.72		
% CHLORINE	0.11		

INFRA-RED ANALYSIS

(*)-EXCLUDES MOISTURE

** PENN STATE COAL DATA BASE **

SEAM NAME
APPARENT RANK SUBBITUMINOUS C (SUBC)

****
* *
* CHEMICAL DATA 3 *
* *
****

% MOISTURE IN COAL = 14.70
% HIGH TEMPERATURE ASH = 14.20 AT 750 DEGREES C

TRACE ELEMENT ANALYSIS	PPM HTA	PPM TOTAL COAL
AG		
B		
BA	1090	153
BE	4	1
BI		
CE		
CO		
CR	120	17
CU	160	23
GA		
GE		
LA		
LI		
MN	1500	213
MO		
NI	35	5
NB		
PB		
RB	25	4
SC		
SN		
SR	1100	156
TH		
U		
V	240	34
Y		
YB		
ZN	20	3
ZR	310	44

MAJOR ELEMENT ANALYSIS	OXIDE % OF HTA	ELEMENT % OF TOTAL DRY COAL
SIO2	47.90	3.18
AL2O3	22.20	1.67
TIO2	1.75	0.15
FE2O3	3.51	0.35
MGO	2.79	0.24
CAO	14.00	1.42
NA2O	0.37	0.04
K2O	0.55	0.06
P2O5	0.11	0.01
SO3	7.00	0.40

VOLATILES	PPM TOTAL COAL
AS	
BR	
CD	
CL	
F	
HG	
SB	
SE	

** PENN STATE COAL DATA BASE **

SEAM NAME
APPARENT RANK SUBBITUMINOUS C (SUBC)

****
* *
* PETROGRAPHIC DATA *
* *
****

MACERAL COMPOSITION WHITE ANALYSIS ONLY

	DRY VOLUME %	DMMF VOLUME %
HUMINITE	78.4	90.0
INERTINITE	6.0	6.9
LIPTINITE	2.7	3.1
MINERAL MATTER(CALC.)	12.9	
TEXTINITE	0.0	0.0
ULMINITE	70.1	80.5
ATTRINITE		
DENSINITE		
HUMODETRINITE(ANAL)	5.9	6.8
GELINITE	1.8	2.1
CORPOHUMINITE	0.5	0.6
SPORINITE		
CUTINITE		
EXINITE (ANAL.)	2.1	2.4
RESINITE	0.6	0.7
SUBERINITE	0.0	0.0
EXUDATINITE	0.0	0.0
FLUORINITE	0.0	0.0
BITUMINITE	0.0	0.0
ALGINITE	0.0	0.0
LIPTODETRINITE	0.0	0.0
FUSINITE	1.1	1.3
SEMI-FUSINITE	2.7	3.1
MACRINITE	2.2	2.5
MICRINITE	0.0	0.0
SCLEROTINITE	0.0	0.0
INERTODETRINITE	0.0	0.0
MINERAL MATTER(ANAL.)		
HUMINITE(ANAL.)		
INERTINITE(ANAL.)		
LIPTINITE(ANAL.)		

REFLECTANCE DATA (%,IN OIL)	HIGH	LOW	RANGE	MEAN MAX	STAND.DEV
ULMINITE	0.52	0.35	0.17	0.44	0.03

** PENN STATE COAL DATA BASE **

SAMPLE HISTORY

PENN STATE NUMBER	PSOC-1488
COLLECTED BY	PENNSYLVANIA STATE UNIVERSITY
COLLECTION DATE	7/17/85
COLLECTOR'S NUMBER	
REPORTED RANK	SUBBITUMINOUS
SAMPLE TYPE	CHANNEL BENCH
OTHER SAMPLE INFORMATION	
SAMPLE RESERVE	900
SEAM NAME	DIETZ
ALTERNATE SEAM NAME	
TOTAL SEAM THICKNESS	80 FT. 0 IN.
THICKNESS OF SEAM SAMPLED	40 FT. 0 IN.
PORTION RECOVERED IN CORE	
DIAMETER OF CORE	

SAMPLE LOCATION

COUNTRY	U.S.A.
STATE	MONTANA
COUNTY	BIGHORN
TOWNSHIP	
NEAREST TOWN	DECKER
COAL PROVINCE	NORTHERN GREAT PLAINS
COAL REGION	FORT UNION
COAL FIELD	
MAP REFERENCE: LATITUDE	45D 6M 40S
LONGITUDE	106D 53M 50S
QUADRANGLE	PEARL SCHOOL (7.5')

** PENN STATE COAL DATA BASE **

SEAM NAME DIETZ
APPARENT RANK SUBBITUMINOUS B (SUBB)

CHEMICAL DATA 1

PROXIMATE ANALYSIS	AS REC'D	DRY	DAF	DMMF (PARR)	DMMF (PARR-G)
% MOISTURE	23.66				
% ASH	4.08	5.35			
% VOLATILE MATTER	31.95	41.95	44.22	43.88	43.80
% FIXED CARBON	40.31	52.80	55.78	56.12	56.20

CALORIFIC VALUE (GROSS BTU/LB)	DRY	AS REC'D MOIST.	EQUIL. MOIST.
MM-FREE,DIRECT			
MM-CONTAINING	12519	9557	9508
MM-FREE (PARR)	13299	10000	9946
MM-FREE (MOD.P)	13327	10000	9946
BEST MM FREE		10000	9946
NET CV, DMMF BTU/LB	12839		
ASH-FREE	13227		

MOTT-SPOONER DIFFERENCE = 93.

ASSOCIATED ANALYSES	DRY	MMF
% EQUILIBRIUM MOISTURE	24.05	25.60
% TOTAL SULFUR	0.50	

RANK CALCULATIONS

APPARENT RANK (AS REC'D MOIST)	SUBBITUMINOUS B (SUBB)
ASTM RANK (EQUIL. MOIST.)	SUBBITUMINOUS B (SUBB)
REFLECTANCE RANK CATEGORY	
INTERNATIONAL RANK	
AS REC'D MOIST.	
EQUIL. MOIST.	
REPORTED RANK	SUBBITUMINOUS

** PENN STATE COAL DATA BASE **

SEAM NAME DIETZ
APPARENT RANK SUBBITUMINOUS B (SUBB)

****
* *
* CHEMICAL DATA 2 *
* *
****

ULTIMATE ANALYSIS	AS REC'D	DRY	DAF	DMMF(PARR) (6.05 %MM)
% ASH	4.08	5.35		
% CARBON	54.91	71.93	76.00	76.56
% HYDROGEN	3.78*	4.95	5.23	5.27
% NITROGEN	0.68	0.89	0.94	0.95
% SULFUR	0.38	0.50	0.53	
% CHLORINE	0.03	0.04	0.04	0.04
% OXYGEN(DIFF)	12.47*	16.35	17.27	17.18

SULFUR FORMS	% PYRITIC	% SULFATIC	% ORGANIC	% TOTAL
DRY	0.02	0.00	0.48	0.50
DAF	0.02	0.00	0.51	0.53
OPTICAL				

ELEMENTAL ANALYSIS	DRY	DMMF(MOD.P) (6.07%MM)	DMMF(DIR.) (%MM)
% CARBON	71.91	76.55	
% HYDROGEN	4.88	5.20	
% NITROGEN	0.89	0.95	
% ORGANIC SULFUR	0.48	0.51	
% OXYGEN(DIFF)	15.77	16.76	
% CHLORINE	0.04	0.04	
% MINERAL MATTER (INCLUDES 0.04 % FES2)	6.07		

ATOM RATIOS (DMMF)	PARR	MOD.PAR	DIRECT
ATOMIC H/C	0.827	0.815	
ATOMIC O/C	0.169	0.175	

MISC. CHEMICAL DATA	DRY	OF DMMF COAL	OF DMMF OXYGEN
% O AS COOH			
% O AS OH			
% S AS SO4,IN ASH			
% CARBONATE AS CO2	0.09		
% CHLORINE	0.07		

INFRA-RED ANALYSIS

(*)-EXCLUDES MOISTURE

** PENN STATE COAL DATA BASE **

SEAM NAME DIETZ
APPARENT RANK SUBBITUMINOUS B (SUBB)

CHEMICAL DATA 3

% MOISTURE IN COAL = 16.40
% HIGH TEMPERATURE ASH = 3.79 AT 750 DEGREES C

TRACE ELEMENT ANALYSIS	PPM HTA	PPM TOTAL COAL	MAJOR ELEMENT ANALYSIS	OXIDE % OF HTA	ELEMENT % OF TOTAL DRY COAL
AG			SIO2	32.50	0.58
B			AL203	19.60	0.39
BA	8010	304	TIO2	1.46	0.03
BE	7	0	FE203	5.33	0.14
BI			MGO	5.62	0.13
CE			CAO	16.20	0.44
CO			NA2O	3.17	0.09
CR	95	4	K2O	0.37	0.01
CU	190	7	P2O5	0.24	0.00
GA			SO3	12.50	0.19
GE					
LA					
LI					
MN	255	10			
MO			VOLATILES	PPM TOTAL COAL	
NI	65	2			
NB			AS		
PB			BR		
RB	20	1	CD		
SC			CL		
SN			F		
SR	5500	208	HG		
TH			SB		
U			SE		
V	260	10			
Y					
YB					
ZN	50	2			
ZR	410	16			

** PENN STATE COAL DATA BASE **

SEAM NAME DIETZ
APPARENT RANK SUBBITUMINOUS B (SUBB)

****
* *
* MINERALOGICAL DATA *
* *
****

TOTAL MINERAL MATTER

% MM-PARR	6.05
% MM-MODIFIED PARR	6.07
% MM-KMC	
% MM-DIRECT	
% MM-BEST AVAILABLE	6.07
VOL % MM-PARR	3.01

MINERAL COMPOSITION

% LOW TEMPERATURE ASH (MCL) =

	% OF LTA
QUARTZ	
PYRITE	
CALCITE	
GYPSUM	
KAOLINITE	
MONT + ILL + MLC	
MONT + ILL	
MONT + MLC	
ILLITE + MLC	
MONTMORILLONITE	
ILLITE	
MIXED LAYER CLAYS	
FELDSPAR	
MINOR FE SULFATES	

% LOW TEMPERATURE ASH (GLUSKORMAN)
(ALL DATA DETERMINED ON 65X100 MESH SIZE FRACTION)

	% OF LTA
KAOLINITE	
ILLITE	
MUSCOVITE	
CHLORITE	
MONTMORILLONITE	
MIXED CLAYS	
CALCITE	
ARAGONITE	
DOLOMITE	
ANKERITE	
SIDERITE	
QUARTZ	
GYPSUM	
PYRITE	
HEMATITE	
RUTILE	
THENARDITE	
PLAGIOCLASE	

** PENN STATE COAL DATA BASE **

SEAM NAME DIETZ
APPARENT RANK SUBBITUMINOUS B (SUBB)

PHYSICAL PROPERTIES

HARDGROVE GRINDABILITY	35.2
VICKER'S MICROHARDNESS	
FREE SWELLING INDEX	0.0
GRAY KING COKE TYPE	
SURFACE AREA (DETERMINED WITH NITROGEN)	
SURFACE AREA (DETERMINED WITH CARBON DIOXIDE)	
DENSITY (DETERMINED WITH HELIUM)	
DENSITY (DETERMINED WITH MERCURY)	
DENSITY (DETERMINED WITH WATER)	
SPECIFIC GRAVITY	
MICROPORE VOLUME	
MACROPORE VOLUME	
TOTAL PORE VOLUME	
PORE SIZE DISTRIBUTION	

GIESELER PLASTICITY DATA

MAXIMUM FLUIDITY	
MAXIMUM FLUIDITY TEMPERATURE	
INITIAL SOFTENING TEMPERATURE	
SOLIDIFICATION TEMPERATURE	
FLUID TEMPERATURE RANGE	
PLASTOMETER TYPE	

ASH FUSION ANALYSIS (DEGREES F)	REDUCING	OXIDIZING
INITIAL DEFORMATION TEMPERATURE	2085	2190
SOFTENING TEMPERATURE	2115	2320
HEMISPHERE TEMPERATURE	2175	2460
FLUID TEMPERATURE	2235	2470